PONTIFÍCIA UNIVERSIDADE CATÓLICA
DO RIO DE JANEIRO

Keyla Maria Mora Navarro

Rain Effects on Microwave and Millimeter Wave Radio Links

Tese de Doutorado

Thesis presented to the Programa de Pós–graduação em Engenharia Elétrica of PUC-Rio in partial fulfillment of the requirements for the degree of Doutor em Ciências – Engenharia Elétrica.

Advisor: Prof. Emanoel Paiva de Oliveira Costa

Rio de Janeiro

April 2017

PONTIFÍCIA UNIVERSIDADE CATÓLICA
DO RIO DE JANEIRO

Keyla Maria Mora Navarro

Rain effects on microwave and millimeter wave radio links

Thesis presented to the Programa de Pós–graduação em Engenharia Elétrica of PUC-Rio in partial fulfillment of the requirements for the degree of Doutor em Ciências – Engenharia Elétrica. Approved by the undersigned Examination Committee.

Prof. Emanoel Paiva de Oliveira Costa
Advisor
Centro de Estudos em Telecomunicações – PUC-Rio

Prof. Carlos Augusto Morales Rodriguez
Universidade de São Paulo

Prof. Fernando José da Silva Moreira
Universidade Federal de Minas Gerais

Prof. Luiz Alencar Reis da Silva Mello
Centro de Estudos em Telecomunicações – PUC-Rio

Prof. Flavio José Vieira Hasselmann
Centro de Estudos em Telecomunicações – PUC-Rio

Prof. Marcio da Silveira Carvalho
Coordenador Sectorial do Centro Técnico Científico – PUCRio

Rio de Janeiro, April 7th, 2017

Keyla Maria Mora Navarro

Received the B.S degree in electrical engineerting from the Univeridad Autonoma del Caribe of Barranquilla, Colombia, in 2009, and the M. S. degree in electrical engineering from the University of Puerto Rico, Mayagüez Campus in 2012.

Bibliographic data

Navarro, Keyla Maria Mora

Rain effects on microwave and millimeter wave radio links / Keyla Maria Mora Navarro ; advisor: Emanoel Paiva de Oliveira Costa. – 2017.

187 f. : il. color. ; 30 cm

Tese (doutorado)–Pontifícia Universidade Católica do Rio de Janeiro, Departamento de Engenharia Elétrica, 2017.

Inclui bibliografia

1. Engenharia Elétrica – Teses. 2. Chuva. 3. Espalhamento. 4. Ondas milimétricas. 5. Extended Boundary Condition Method (EBCM). 6. Interferência. I. Costa, Emanoel Paiva de Oliveira. II. Pontifícia Universidade Católica do Rio de Janeiro. Departamento de Engenharia Elétrica. III. Título.

CDD: 621.3

This work is dedicated to my family.

Acknowledgments

First, I would like to thank God Almighty for giving me the health, strength, knowledge and opportunity to undertake this research study. I specially want to thank my advisor, Dr. Emanoel Paiva de Oliveira Costa for his guidance and supervision during this research. Without his knowledge and assistance, this study would not have been possible and successful.

I would like to thanks to the memebers of my doctoral committee, Professors Carlos Augusto Morales Rodriguez, Fernando José da Silva Moreira, Luiz Alencar Reis da Silva Mello and Flavio José Vieira Hasselmann for their helpful suggestions. I also like to thanks to all my partners of the CETUC for their friendship and support.

I would like to thank my family members, specially Xiomara Navarro, Pedro Mora, and Alejandro Mora for supporting and encouraging me to pursue this degree. I would also like to express my gratitude to my friend Jose A. Ortiz for being there at times when I require motivation to pursue my research.

I thank Michael Mishchenko and Cory Davis for the development of original Fortran codes for the T-Matrix method and for gracefully and unselfshily making them available online. I would like to thank Conselho Nacional de Desenvolvimento Científico e Tecnológico (CNPq) and Coordenação de Aperfeiçoamento de Pessoal de Nível Superior (CAPES), for their financial support under the Grant 165330/2013-9. I would also like to thanks to the Collaborative Adaptive Sensing of the Atmosphere Engineering Research Center (CASA) and the research group Chuva Project, under the coordination of the Centro de Previsão de Tempo e Estudos Climáticos (CPTEC), Instituto Nacional de Pesquisas Espaciais (INPE) for their resources and information for this study.

Abstract

Mora Navarro, Keyla Maria; de Oliveira Costa, Emanoel Paiva (Advisor). **Rain Effects on Microwave and Millimeter Wave Radio Links.** Rio de Janeiro,2017.187p. Tese de Doutorado – Departamento de Engenharia Elétrica, Pontifícia Universidade Católica do Rio de Janeiro.

The main goal of this research is to study the rain effects on microwave and millimeter wave radio links. Thus, the rain-induced attenuation, depolarization and scattering are studied. To carry out this study, a realistic rain model is proposed, which consider a realistic rain medium composed by a cluster of raindrops with the shape-size relation proposed by Chuang and Beard, a raindrop size distribution given by de Wolf, index of refraction of water for a given temperature and frequency suggested by Ray and a distribution of the orientation angle of the symmetry axis. The realistic rain model is evaluated with two different applications of systems operating at microwave and millimeter wave frequencies. One of the applications involves wireless telecommunication systems, which are strongly affected by the presence of precipitation. To design an efficient radio communication system, the realistic rain model is applied for the analysis and quantification of rain-induced effects on links operating at millimeter-wave frequencies in urban environments. Another application involves weather radars (X-band radars in particular). Considering their relatively low cost and high resolution, X-band radars would be among the best options to monitor meteorological events. However, they are susceptible to attenuation by fog, snow or rain. To solve this problem, a realistic and improved rain model is implemented to compute backscattering cross sections and estimate rain attenuation at each range gate. The proposed method is evaluated using radar data provided by the CASA OTG X-band (λ = 3cm) radar located in Mayaguez, Puerto Rico, and X-band radar METEOR 50DX –Selex located in Belém, Brazil.

Keywords

Scattering, Interference, Millimeter Waves, Rain, Extended Boundary Condition Method (EBCM), X-band radar

Resumo

Mora Navarro, Keyla Maria; Oliveira Costa, Emanoel Paiva (Advisor). **Efeitos da Chuva em Rádio Enlaces Operando nas Faixas de Micro-ondas e Ondas Milimétricas.** Rio de Janeiro,2017.187p. Tese de Doutorado – Departamento de Engenharia Elétrica, Pontifícia Universidade Católica do Rio de Janeiro.

A principal meta desta tese é estudar os efeitos da chuva nos enlaces operando na faixa de micro-ondas e comprimentos de ondas milimétricas. Para realizar este estudo, é considerado o modelo de chuva que considera um meio de chuva realista composto por um conjunto de gotas com a relação formato-tamanho proposta por Chuang e Beard, uma distribuição de tamanho das gotas dada por de Wolf, o índice de refração complexo da água para uma frequência e temperatura dada sugerido por Ray e uma distribuição de orientação dos eixos de simetria da partícula. O Extended Boundary Condition Method (EBCM) foi aplicado ao modelo descrito para determinar a atenuação, depolarização e espalhamento devidos à chuva. O desenvolvimento foi validado com sucesso por intermédio de comparações de seus resultados com os correspondentes disponíveis na literatura. O modelo de chuva realista foi utilizado em duas aplicações diferentes. Na primeira, foi estudada a interferência devida à chuva entre enlaces de telecomunicações sem fio operando em frequências de ondas milimétricas em ambientes urbanos. Outra aplicação envolve a determinação da taxa de precipitação por intermédio de radares meteorológicos (em particular, radares banda-X). Considerando que seu custo é relativamente baixo e sua resolução elevada, os radares em banda-X estariam entre as melhores opções para monitorar eventos meteorológicos. Entretanto, são susceptíveis à atenuação devida a gases atmosféricos e chuva ao longo dos enlaces, que impedem que a taxa de precipitação seja estimada diretamente a partir da potência recebida correspondente a uma determinada posição. Desta forma, um modelo de chuva realista foi implementado para calcular a seção reta de retroespalhamento e estimar a atenuação específica por intermédio do EBCM em cada um dos volumes existentes entre o radar e a posição selecionada. Este desenvolvimento permite a correção dos efeitos da atenuação existente no enlace formado entre estas duas posições.

Palavras-chave

Chuva, Espalhamento, Ondas Milimétricas, Extended Boundary Condition Method (EBCM), Interferência, Radar Banda-X.

Table of contents

List of figures

List of tables

1 Introduction

1.1. Motivation

Recently, there has been a strong interest in the use of systems operating at millimeter wave frequencies for different applications such as fixed and next generation of cellular mobile wireless telecommunication systems, weather and surveillance radars, and television broadcast, among others. This interest has been due to the good performance and advantages that these systems may offer [91]. Primarily, that they may offer wide to ultra-wide bandwidths and high spatial resolution, while requiring lower power sources.

One of these applications are wireless telecommunication systems, which are challenged by a steadily increasing demand for more and better services, as well as by the introduction of new ones. These demands are initially met by a more efficient use of the traditional frequency spectrum, which will eventually saturate regardless of all efforts. One of the natural solutions for the evolution of wireless telecommunication systems is the use of unexplored bands of the frequency spectrum [94], [95]. This process is generally translated into the use of higher frequencies, new technologies and procedures.

One such transition is currently under way. It is anticipated that the microwave spectrum (below approximately 28 GHz) will saturate in the near future [94], [95]. Additionally, it will not be able to meet the requirements of new systems, including the Fifth Generation of cellular networks (5G). The use of millimeter waves (initially, in the more restricted band from 28 GHz to 86 GHz) are being considered to provide users with new and better services (for example higher data transmissions, using larger bandwidths). In addition, the transmission capacity can be doubled, with the transmission of different signals through the propagation of waves with orthogonal polarization. This will be combined with the use of appropriate semiconductor technology, adaptive antenna arrays in both the access points and the user terminals, as well as of massive multiple-input

multiple-output (massive MIMO) and novel medium access control and network operation techniques.

The wireless telecommunication systems operating at millimeter-wave frequencies are strongly affected by the presence of hydrometeor precipitation, among other effects that will not be further discussed (absorption by oxygen and water vapor, scattering by natural or man-made obstacles, multipath, etc.). Some of the rain effects on the propagation of a signal operating at millimeter-wave frequencies are severe attenuation, depolarization and scattering during intense rainfall rates. It is seen that the development of the 5G technology is led by countries in the northern hemisphere and Asia [94], [95]

. However, the listed rain effects are particularly important in tropical climates, where the rainfall rates substantially exceed those of the temperate climates, typical of most of these countries.

There are previous studies on the limitations of millimeter-wave communication systems [1]-[5]. These studies were a motivation to the present thesis of a more realistic and improved model for the analysis and quantification of rain-induced effects on links operating at millimeter-wave frequencies. The proposed model will provide useful information for the efficient planning of radio communication systems. This research will be an extension of the studies presented by [6]. The cited reference focused on the study of the rain-induced interference at 28 GHz and 42 GHz, taking into account the scattering of raindrops for a maximum rainfall rate of 30 mm/h. The scattering properties were analyzed through the classical Mie scattering theory due to homogeneous spheres with an arbitrary size [7].

Another application to systems operating at microwave and millimeter wave frequencies involves weather radars (X-band radars in particular). Considering their relatively low cost and high resolution, X-band radars would be among the best options to monitor meteorological events. However, they are susceptible to attenuation by atmospheric gases, snow or rain. To solve this problem, a realistic and improved rain model is implemented to compute backscattering cross sections and estimate rain attenuation at each range gate. The proposed method will be evaluated using radar data provided by the CASA OTG X-band (λ = 3cm) radar located in Mayaguez, Puerto Rico, and X-band radar METEOR 50DX –Selex located in Belém, Brazil.

1.2. Scientific Contribution of the Thesis

The contribution of this thesis is based on the analysis of rain-induced attenuation, depolarization and scattering. Thus, it takes into account the rain cross-polarization effects that were not considered in a previous study [6]. To reach this goal, the raindrops are modeled by the shape-size relation suggested by [8], which display a symmetry axis and a flattened bottom. It is important to emphasize that the assumed raindrop shape is different from spherical (or even spheroidal), which leads to considerations of canting angle and drop orientation effects. These are random variables, which will be modeled with basis on available measurements.

Another contribution is related with the fact that the rain-induced effects have been analyzed only for frequencies below about 40 GHz and moderate rainfall rates, as has been demonstrated by several studies available in [6] and [9]. Where applicable, the present study is focused on the higher frequency band between 30 GHz and 90 GHz and more intense rainfall rates. It should be noted that the rainfall rates exceeded during 0.01% of the average year are approximately equal to: (1) 75 mm/h in the cities of Rio de Janeiro and São Paulo, Brazil; and (2) 120 mm/h at the city of Belém, Brazil [97]. These rainfall rates are substantially greater than the one assumed by [6].

With respect to the computational method necessary to calculate the scattering properties of raindrops, a required literature review was performed to identify the advantages and disadvantages of the different methods that exist for solving electromagnetic scattering problems involving non-spherical particles. The Extended Boundary Condition Method (EBCM) was selected for this research, because it is the most suitable method with respect to the particle shapes and size parameters of interest. It was also decided to adapt the code for computing electromagnetic scattering by non-spherical particles provided by [10] and [11]. This code was carefully analyzed and modified to conform to the present and future needs. The introduced modifications will be described in the next section.

An additional contribution of this thesis is the implementation of a realistic and extended rain model for X-band radars to compute the radar backscattering cross section, taking attenuation effects into account. This model considers a realistic rain medium,

which is composed by a cluster of raindrops with the shape-size relation proposed by Chuang and Beard [8], a raindrop size distribution given by de Wolf [12], index of refraction of water for a given temperature and frequency suggested by Ray [13] and a distribution of the orientation angle of the symmetry axis [14]. Note that the original procedure applied to the processing of meteorological radar data to acquire the reflectivity or rainfall rate normally assume the Marshall and Palmer drop size distribution (DSD) and the Rayleigh approximation to scattering by spherical particles. The most straightforward procedures do not take rain attenuation effects into account.

1.3. Research Objectives

The main objective of this thesis is to study the effects of scattering by precipitation, taking into account a realistic rain model. This includes a cluster of raindrops with the shape-size relation proposed by [8], combined with appropriate distributions for the drop size distribution [12] and the orientation of the symmetry axis of the particles [14]. The results from this model will be applied to the calculation of: (1) the power of the interference signal received by radio links operating in the millimeter-wave frequency band, considering depolarization effects; and (2) the attenuation-corrected estimates of the rainfall rate using X-band radar data.

To achieve the main objective, it has been necessary to identify and reach specific objectives that include:

- Develop a subroutine for the calculation of function r = f (θ), which describes the raindrop shapes given by [8];
- Implement a subroutine to determine the complex index of refraction of water, considering the frequency and temperature, as proposed by [12];
- Implement a model to compute the scattering properties of a single raindrop;
- Determine the scattering properties due to a cluster of raindrops, considering appropriate drop size distribution (DSD) and orientation distribution of the symmetry axis of the droplets;

- Apply the radar equation together with the above computation of scattering properties to quantify the interference levels into a radio receiver operating in the millimeter-wave frequency band, considering the depolarization effects due to rain;

- Compute the backscattering cross section as a function of rainfall rate by the realistic rain model based on the EBCM;

- Apply the EBCM to calculate the specific attenuation at each range gate to the corresponding rainfall rate;

- Evaluate the realistic rain model using X-band radar data to estimate the rainfall rate.

1.4. Description of the Following Chapters

This thesis is organized into eight chapters.

Chapter 1: Introduction

It has been seen that the first chapter provides an overview of the problem, the principal motivation, the objectives, and the main steps that were carry out in this research work, as well as its contributions.

Chapter 2: Literature review

This chapter includes a review of the related work and a brief description of the different computational method previously adopted to calculate the scattered fields due to raindrops. This chapter provides a clearer framework for this thesis and highlight its relevance and original contribution.

Chapter 3: Description of the enviroment

This chapter describes the propagation medium of the electromagnetic waves, which is composed by rain. Some important characteristics and models of the medium that are required for the calculation of the scattering properties of raindrops are summarized.

Chapter 4: Methodology

This chapter describes all the procedures that are required to calculate rain scatter effects on an incident plane wave.

Chapter 5: Validation

This chapter contains the validation of the realistic rain model based on the EBCM and evaluate the reliability of this method in comparison with scattering results obtained from previous works.

Chapter 6: Estimation of the rainfall rate from radar measurements

This chapter applies the realistic rain model developed to estimate the backscattering cross section and rain attenuation. Results and comparisons using radar measurements are presented.

Chapter 7: Calculation of the interference power into a receiver operating in millimeter wave frequencies

This chapter provides the results from the application of the procedures described in Chapter 4 to calculate the interference power into a receiver operating in millimeter wave frequencies in an urban environment.

Chapter 8: Conclusion and future work

This chapter summarizes the main results from the thesis and suggests extensions to them.

2 Literature Review

2.1. Related Works

Rain scatter interference between two stations has been the subject of study since the early 1960's. This interference problem is considered relevant because it affects decision-making during the planning and installation process of a telecommunication system. Within the possible decisions, those involving the position of transmitter and receiving antennas, polarizations, widths and directions of beams can be found. Additionally, Olsen et al. [15] emphasize that the scattering due to rainfall can be the primary source of interference on communication systems operating at millimeter-wave frequencies. To overcome this problem, several models and techniques have been proposed to quantify the corresponding effects.

The prediction of interference was first motivated by the observation of experimental results of a scatter link in the presence of rain, which revealed the increased fading rate and decreased bandwidth [16]. Thus, the performance deterioration of radio links brings up the long studied interference problem, which was formally recognized since 1971 by the Radio Regulations [15]. More surveys indicating that scattering by rain is the cause of such interference are described below.

Setzer [17] calculated the interference between satellite communication links and terrestrial radio-relay systems due to scattering by rain. The author assumed a spherical raindrop shape and unpolarized waves and showed that the angular dependence of Mie scattering is close to that of Rayleigh scattering at frequencies below 30 GHz.

Other related work was developed by Crane[18], who used the radar equation and a model for the scattering properties per unit rain volume based on Rayleigh scattering in the analysis of interference. Rain interference was also analyzed by Chu [19], who estimated the rain-scatter coupling between multiple beams of an earth-station antenna, assuming single scattering by spherical raindrops.

The study developed by Tingye et al. [20] presented experimental results of forward scattering, which were interpreted with basis on a single scattering theory and the bistatic radar equation. The study carry out by Delogne and Lobelle [21] was based on the calculation of bistatic scattering by uncanted oblate spheroids in the frequency range from 10 GHz to 100 GHz.

Within recent researches focused on the prediction of interference levels, the ones described in the next paragraphs are particularly relevant to the present work.

Bose et al. [22] presented a study based on the estimation of the interference levels within a local multipoint distribution system (LMDS) as a function of the half-power beamwidth of the customer-site antennas for the downlink. This analysis was made to solve the problem of propagation losses due to co-channel and adjacent channel interference. Panangopoulos and Kanellopoulos [23] proposed a method to compute the cumulative distribution of differential rain attenuation on two converging microwave link. It is important to point out that rain scattering was not considered in the two studies.

Enjamio et al. [6] also studied the effects of rain interference in the lower end of the millimeter-wave frequency band. In contrast with the previous studies, their interference predictions considered rain scattering through a combination of the Mie theory for spherical drops with the bistatic radar equation, taking into account realistic variations of rainfall along the propagation path.

Having the previous studies as references, the present work will extend the one by Enjamio et al. [6]. The current analysis differs from the previous one by providing a more complete and detailed scattering model that will consider the physical properties of raindrop, as well as realistic shapes, drop size and symmetry axis distributions. These assumptions allow the development of depolarization studies. The scattering properties of raindrops will be calculated with basis on the Extended Boundary Condition Method (EBCM) initially proposed by Waterman [24].

The Radiocommunication Sector of the International Telecommunication Union (ITU-R) recommended a method for interference calculations [25] based on the bistatic radar equation, which can be expressed as:

$$P_r = \frac{\lambda^2}{P_t(4\pi)^3} \iiint\limits_{all\ space} \frac{G_t G_r \eta A}{r_t^2 r_r^2}\, dV. \tag{2.1}$$

where λ is the wavelength; G_t is the gain of the transmitting antenna; G_r is the gain of the receiving antenna; η is the scattering cross-section per unit volume δV; A is the attenuation along the path from transmitter to receiver (in linear terms); r_t is the distance from the transmitter to the scattering volume element and r_r is the distance from the scattering volume element to the receiver. Note in the above equation that the product of the scattering cross section by other terms is numerically integrated over the three-dimensional rain cell to determine the interference power. This formulation will be applied to the scattering cross section resulting from the calculations described in the previous paragraph.

2.2. Numerical Techniques used to Compute the Scattering Properties of Rain

Calculations of rain scatter interference between two terrestrial systems imply the previous knowledge of the scattering properties of the raindrops to be associated with the bistatic radar equation. It is important to point out that the raindrop geometry for the calculation of the scattering properties of interest in this proposal is given by Chuang and Beard [8].

Initially, the electromagnetic interaction with particles is physically described through Maxwell's equations, as outlined in the literature [7], [26], [27].

The frequency-domain analysis of the scattering problem due to a three-dimensional particle can be performed with the help of solutions to the scalar Helmholtz equation, as will be seen later. The scattering calculations depend on the physical characteristics of the particles, such as size, shape, and composition, as well as on the frequency and direction of the incident electromagnetic wave. The solution of the scalar Helmholtz equation can also be tailored to the assumed coordinate system.

For the case of small particles (in comparison with the wavelength), the Rayleigh theory provides a suitable approximation to the exact solution [7]. On the other hand, for the case of a particle with an arbitrary radius, the scattering properties can be obtained from the Mie theory. A detailed explanation of the Mie theory for spherical particles and the corresponding mathematical developments and explanations can be found in [7], [24], [25].

The above theories began to be applied to the solution of practical problems related with rain attenuation and rain scattered interference at millimeter-wave frequencies. As result of experimental study carry out by Magono [28], the shape of raindrop was found not to be spherical or even spheroidal in general. To improve predictions of attenuation and rain induced interference, several authors assumed nonspherical raindrop shapes. In particular, some authors assumed the oblateness of the raindrop in their scattering calculations [29], [30].

The literature lists several methods that are suitable to solve electromagnetic scattering problems for nonspherical particles. The main purpose of most of the numerical techniques is to compute the scattered and internal fields due to a single particle, and not to a cluster of particles. A summary of the most important analytical and numerical methods and techniques that have been developed for the analysis of scattering problems involving single nonspherical particles [31] follows:

- **The separation of variables method**

This method proposes to solve the scalar Helmholtz equation through a set of differential equation for each component function. This solution implies the expansion of the incident, scattered and internal fields in vector spherical (or spheroidal) wave functions. Thus, the geometry of the scattering particle should not substantially depent from the above forms. The corresponding scalar Helmholtz equation to be solved is

$$\nabla^2\psi + k^2\psi = 0, \tag{2.2}$$

In spherical coordinates, equation (2.2) can be expressed as follow

$$\frac{1}{r^2}\frac{d}{dr}\left(r^2\frac{d\psi}{dr}\right)+\frac{1}{r^2\sin\theta}\frac{d}{d\theta}\left(\sin\theta\frac{d\psi}{d\theta}\right)+\frac{1}{r^2\sin\theta}\frac{d^2\psi}{d\phi^2}+k^2\psi=0, \tag{2.3}$$

Assuming a solution of the form

$$\psi(r,\theta,\phi)=R(r)\Theta(\theta)\Phi(\phi), \tag{2.4}$$

that is substituted into equation (2.3), one obtains the following three ordinary differential equations

$$\frac{d^2(rR)}{dr^2}+\left(k^2-\frac{n(n+1)}{r^2}\right)rR=0, \tag{2.5}$$

$$\frac{1}{\sin\theta}\frac{d}{d\theta}\left(\sin\theta\frac{d\Theta}{d\theta}\right)+\left(n(n+1)-\frac{m^2}{\sin^2\theta}\right)\Theta=0, \tag{2.6}$$

$$\frac{d^2\Phi}{d\phi}+m^2\Phi=0. \tag{2.7}$$

The incident, scattered and internal field are expressed by linear combinations of modes expressed by solutions of the above equations. The coefficients of these expansions are obtained from the boundary conditions. This method provides exact solutions for particles conforming to coordinate systems which allow the separation of scalar Helmholtz equation. Despite the high numerical accuracy, the separation of variables has been restricted for large size parameters (*kD*) of the particle and large index of refractive, since ill-conditioned problems may occur. Literature examples of the application of this technique can be found in [32], [33], [34].

- **The finite element method**

The method is based on solving the electromagnetic scattering problem in the frequency domain by discretizing the Helmholtz equation in the three-dimensional space and solving it numerically as a weighted-residual problem. The field in the interior of each discrete element is represented by a linear combination of known expansion

functions. This method is applicable to arbitrarily shaped particles, but its implementation requires elevated computational resources and the accuracy of computations strongly depends on the spatial discretization, being difficult to control. A detailed explanation of this method is presented in [35].

- **The finite difference time domain method (FDTD)**

This method proposes to solve the electromagnetic scattering problem in the time domain by directly discretizing Maxwell's equations in time and space and solving them numerically. The scattering problem is solved in a finite spatial region that is discretized into a large number of mesh cells. One of the features of this method is the high flexibility in terms of particle geometries, but this can result in time-consuming computation. A detailed explanation of this method is given in [36].

- **Volume integral equation methods**

This class of methods solves scattering problems with basis on the determination of equivalent currents that appear in an integral equation. That is, it assumes an inhomogeneous vector Helmholtz equation defined as

$$\nabla \times \nabla \times \vec{E}(\vec{r}) - k_o^2 \vec{E}(\vec{r}) = j\omega\mu_o \vec{J}(\vec{r}), \tag{2.8}$$

where $\vec{J}(\vec{r})$represents the volume current density. The solution to the above equation can be written as

$$\vec{E}(\vec{r}) = \vec{E}^{inc}(\vec{r}) + \int_V \bar{\bar{G}}_o(\vec{r},\vec{r}') \cdot \vec{J}(\vec{r}')dV'. \tag{2.9}$$

where $\bar{\bar{G}}_o(\vec{r},\vec{r}')$ is the free-space dyadic Green's function. This class of methods is applicable to arbitrary shaped and inhomogeneous particles. One of its disadvantages of some version of this method is that computations may need to be repeated for each new angle of incidence of the external field. Different methods can be used for the solution of equation (2.9). One of those will be briefly described next.

• The method of moment

This method proposes to solve equation (2.9) by initially rewriting it as

$$\vec{E}(\vec{r}) = \vec{E}^{inc}(\vec{r}) + \int_V [\varepsilon_r(\vec{r}') - 1]\bar{\bar{G}}_o(\vec{r}, \vec{r}') \cdot \vec{E}^{int}(\vec{r}')dV'. \tag{2.10}$$

The straightforward solution of the new equation discretizes the volume *V* into a very large number of three-dimensional elements. The assumption that field remains constant within each volume element transforms the integral equation into a system of linear equations. A detailed explanation of this method, which is applicable to irregular shapes, can be found in [37].

• Point matching method

In this method, the electric and magnetic fields inside and outside of the particle are represented as truncated expansions of spherical vector wave functions. This method is ideal to compute the scattering properties of particles with arbitrary size. The boundary condition is imposed at a number of points on the surface. The previous procedure yields to a set of linear equations.

This method is applicable in the computation of scattering properties of perfectly conducting and lossy dielectric spheres, spheroids, or particles with arbitrary sizes. Some surveys related with its implementation are presented by [30] and [38]. This is a simple method, but its application is limited by the uncertain convergence presented when the particle geometry departs from the spherical shape [29].

• Perturbation method

This method can be used to compute the scattering properties of non-spherical particles, as the point matching method described in [29]. Initially, the particle is assumed to be geometrically perturbed with a small deformation. The scattering properties can be

calculated by the Taylor expansion of the boundary conditions. Thus, the shape of a perturbed sphere can be expressed as

$$r_p = r_o(1 + \delta f_1(\theta, \varphi) + \delta^2 f_2(\theta, \varphi) + \cdots). \quad (2.11)$$

where r_o is the radius of the unperturbed sphere, δ represents a smallness parameter and $f_n(\theta, \varphi)$ are arbitrary single valued functions.

The incident, scattered and transmitted field are expanded in elementary spherical vector solutions, with known and unknown expansion coefficients. The determination of the unknown coefficients is obtained by applying the special boundary perturbation technique together with orthogonality properties. As a result, a set of four simultaneous linear algebraic equations for the *l*th-order perturbation coefficients $(\mathrm{a}, \mathrm{b}, \mathrm{c}, \mathrm{d})_{\pm mn^l}$ is obtained. All scattering quantities can be calculated in terms of these coefficients. The principal disadvantages of this method are the problem of uncertain convergence and the approximations involved in modelling the exact particle shape. By this method, scattering properties were calculated by [39],[40],[41],[42].

- **Extended Boundary Condition Method**

The Extended Boundary Condition Method (EBCM) is widely used to calculate the electromagnetic scattering by nonspherical particles, such as arbitrary bodies of revolution. This method involves a matrix solution of the scattering problem and could be classified as a surface integral equation method. It was initially proposed by Waterman [24] and is derived in detail by Tsang et al. [44] and Mishchenko et al. [45].

This method initially expands the incident, scattered and internal electromagnetic fields in vector spherical wave functions with known expansion coefficients for the incident field and unknown expansion coefficients for the internal and scattered fields. A surface integral which involves induced surface currents on the particle and the free-space Green's function represent the scattered field. The solution of this equation leads to an infinite system of linear equations which relates the coefficients of the incident field with those of the scattered field. The corresponding matrix (System Transfer Operator or

Transition Matrix, usually shortened as T-matrix) depends only on the characteristics of the particle (size, shape and index of refraction) and on the operating frequency. The EBCM method is especially attractive because the T-matrix does not depend on the direction or polarization of the incident field.

Some of the relevant works based on this method are: Barber and Yeh [46] calculated the scattering properties of spheres, spheroids and finite cylinders; Warner and Hizal [47] calculated the scattering properties of Pruppacher and Pitter raindrops [48] and found that their scattering properties are not very different from those of oblate spheroidal raindrops in the microwave frequency band. The T-matrix approach has been recently reviewed by Mishchenko et al. [49], [50]. Their implementations include randomly oriented and rotationally symmetric particles.

After surveying the above methods, it has been found that the EBCM version implemented by Mishchenko and Travis [10] would be a suitable method for the computation of the scattering properties of a cluster of more realistic raindrops in this research. Thus the drop shape determined by Chuang and Beard [8] will be used to improve the reliability of the procedure for calculating the scattering properties due to a rain-filled medium. The shape preserves the axial symmetry, but considers particles with relatively flattened bottoms. These concepts will be further explored in chapter IV of the present thesis. Then, after proper validation of the model by comparison of its results with the ones available in the literature, results will be used in two applications.

3 Description of the Enviroment

This chapter describes in detail the characteristics of the scattering environment, composed of raindrops, because they are essential for the analysis of rain effects on microwave and millimeter wave propagation. The characteristics of rain that will be covered in this research are the following:

- Raindrop shape;
- Raindrop size distribution;
- Index of refraction of water;
- Canting angle;
- Distribution of the orientation angle of the symmetry axis;
- Terminal velocity.

3.1. Rain

Rain can be considered as a meteorological phenomenon in which drops of liquid water fall toward the surface of the earth [51]. Rain can be classified as convective or stratiform. The convective rain is generally more intense and of short duration than the stratiform, which is caused when moist air is forced upwards over rising terrain [93]. In this research, the rain medium is represented by a volume composed by rotationally-symmetric raindrops at any position. Some properties of the raindrops are:

• **Shape:** the rotationally-symmetric drop shape is described by the equilibrium shape derived by [8], where the size also defines the shape.

• **Size:** rain consists of a distribution of drops with diameters ranging from 0.01 mm to 8 mm.

• **The complex index of refraction of water:** is considered a constant for a given temperature and frequency [13].

• **Orientation:** it is assumed that the axes of the raindrops are not aligned. The axes of symmetry of the particles are partially oriented by the local horizontal component of

air flow, as suggested in [14]. The orientation of symmetry axis of a raindrop is described by the zenith angle β and the azimuth angle γ, in response to the effects of the horizontal component of the wind. More generally, the angles α, β and γ represent the Eulerian angles of rotation which specify the raindrop orientations with respect to the principal reference frame (with a vertical z axis). Due to oscillations, these angles will be treated as random variable, with distributions to be specified.

3.2. Raindrop Shape

Previous authors modeled raindrops by oblate spheroids, arguing that the assumed shape were very close to the observed ones [43] [32], [30], [52]. To analyze the effects and scattering properties of the rain medium with a more realistic shape, the raindrop shape is described by the model proposed by [8], which takes into account factors such as: surface tension, hydrostatic pressure, dynamic pressure and electrostatic stress. According to this numerical model, the drop size defines the drop shape. That is, small drops are considered spherical, but the larger drops tend to have an oblate shape with flattened bottom. The drops are axially symmetric, but there are no symmetry planes perpendicularly to the axis. The possible role of truly asymmetric particles will not be discussed here. The radius of the raindrop is modeled through the following linear combination of Chebyshev polynomials:

$$r_k(\theta) = \frac{D_k}{2}\left(1 + \sum_{n=0}^{10} c_{nk}\cos(n\theta)\right). \tag{3.1}$$

where $D_k = 0.5\,k$ (mm) is the equivalent diameter of an undistorted drop, c_{nk} (n = 1, …, 10; k = 2, 3, …, 14, 16, 18) are the coefficients for raindrops shape definition, listed in Table 3.1 [8] for drops with equivalent diameters from 1.0 mm to 9.0 mm. Drops with equivalent diameter D < 1 mm are spherical. The radii of drops with equivalent diameter D in the interval (D_k, D_{k+1}) is obtained by linear interpolation $r(\theta) = (1-\alpha)\, r_k(\theta) + \alpha\, r_{k+1}(\theta)$, with $\alpha = (D-D_k)/(D_{k+1}-D_k)$. A computer routine was implemented to verify the provided theory for the modeled raindrop equilibrium shapes, which are shown in Figure 3.1.

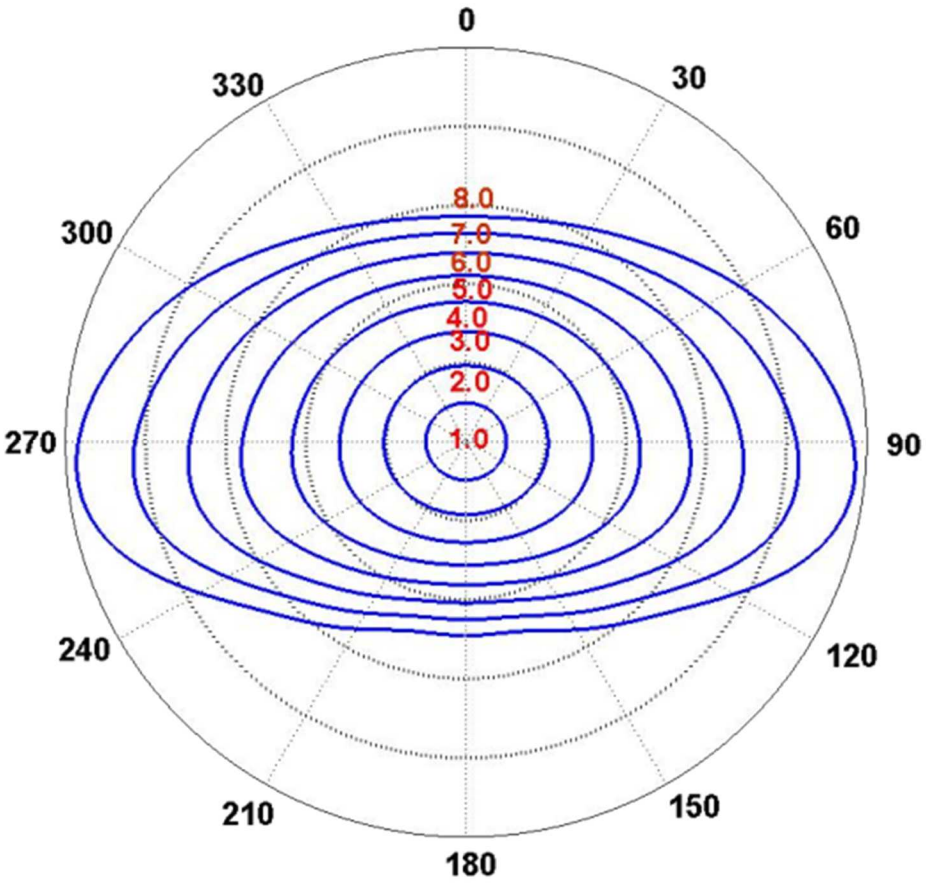

Figure 3.1: Chuang and Beard equilibrium drop shapes [8] for drop diameters from 1.0 mm to 8.0 mm.

The axial ratio (between the minimum and maximum radii) was calculated by [8] as a function of the equivalent diameter D (mm) and represented by the following regression curve.

$$\alpha(D) = 1.01668 - 0.098055D - 0.00252686D^2 + 0.000375061D^3 - 0.000168692D^4. \quad (3.2)$$

Figure 3.2 plots the axial ratio represented by the above equation. It is observed that smaller raindrops tend to be spherical (b/a ≈ 1) and that the larger ones tend to be more oblate (b/a approaching 0.5).

Table 3.1: Set of coefficients for raindrop shape definition given by Chuang and Beard [8].

	Shape coefficient (c_{nk} ×10^4) for n = 0, …, 10; k = 2, 3, …, 14, 16, 18											
k	**D(mm)**	0	1	2	3	4	5	6	7	8	9	10
2	**1.0**	-28	-30	-83	-22	-3	2	1	0	0	0	0
3	**1.5**	-72	-70	-210	-57	-6	7	3	0	-1	0	1
4	**2.0**	-134	-118	-385	-100	-5	17	6	-1	-3	-1	1
5	**2.5**	-211	-180	-592	-147	4	32	10	-3	-5	-1	2
6	**3.0**	-297	-247	-816	-188	24	52	13	-8	-8	-1	4
7	**3.5**	-388	-309	-1042	-221	53	75	15	-15	-12	0	7
8	**4.0**	-481	-359	-1263	-244	91	99	15	-25	-16	2	10
9	**4.5**	-573	-401	-1474	-255	137	121	11	-36	-19	6	13
10	**5.0**	-665	-435	-1674	-258	187	141	4	-48	-21	11	17
11	**5.5**	-755	-465	-1863	-251	242	157	-7	-61	-21	17	21
12	**6.0**	-843	-472	-2040	-240	299	168	-21	-73	-20	25	24
13	**6.5**	-930	-487	-2207	-222	358	175	-37	-84	-16	34	27
14	**7.0**	-1014	-492	-2364	-199	419	178	-56	-93	-12	43	30
16	**8.0**	-1187	-482	-2650	-148	543	171	-100	-107	2	64	32
18	**9.0**	-1328	-403	-2899	-106	662	153	-146	-111	18	81	31

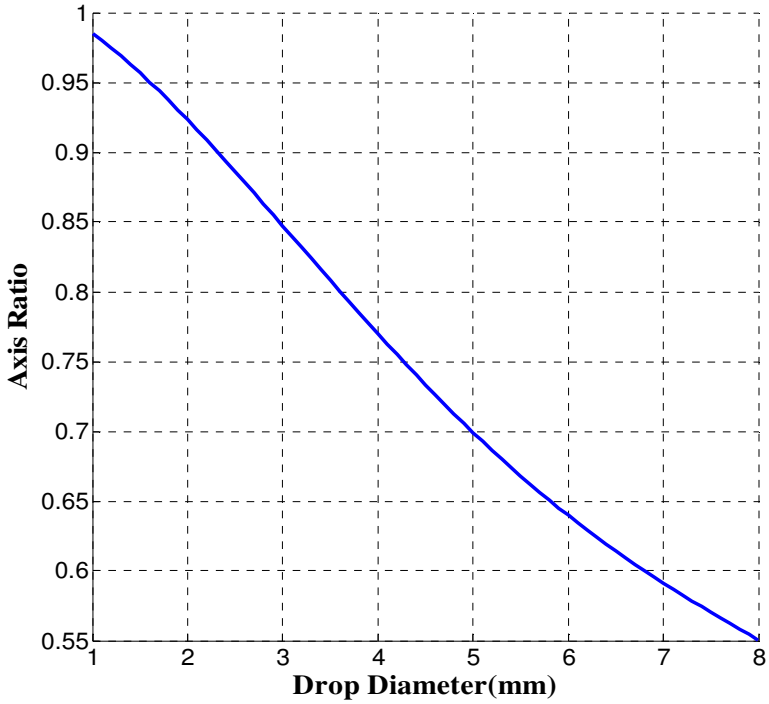

Figure 3.2: Axis ratio for the Beard-Chuang [8] numerical model for D from 1.0 mm to 8.0 mm.

3.3. Raindrop Size Distribution

The drop size distribution is also of central importance to determining the scattering properties due to rainfall. The drop size distribution *N(D)* (m^{-3} mm^{-1}) is the number of particles with diameters within the interval *D* and *D*+*dD* that are present in the unit volume. In the current study, the drop size distribution (DSD) model is based on a gamma approximation to the [53] data and [54] function, derived by [12]. The DSD can be written in the form

$$N(D) = N_O D^p \exp(-\Lambda D^q), \tag{3.3}$$

where N_O and Λ, with dimensions inferred from the above expression, are functions of the rainfall rate R (mm/h):

$$N_O = 1.98 \times 10^4 R^{-0.384}, \tag{3.4}$$

$$\Lambda = 5.38 \times 10^3 R^{-0.186}. \tag{3.5}$$

Additionally, D is the drop equivalent diameter (mm), p = 2.93 and q = 1. As indicated by [12], equations (3.3) to (3.5) remain consistent with the [53] data. However, it eliminates two difficulties of the exponential distribution proposed by Marshall and Palmer [54], which is not consistent with the evaluation of the rain rate R, as indicated by [55], and predicts maximum value for zero-diameter droplets. Figure 3.3 depicts the rain drop size distribution derived by [12] for the rainfall rates R = 25 mm/h, 50 mm/h, 75 mm/h, and 100 mm/h.

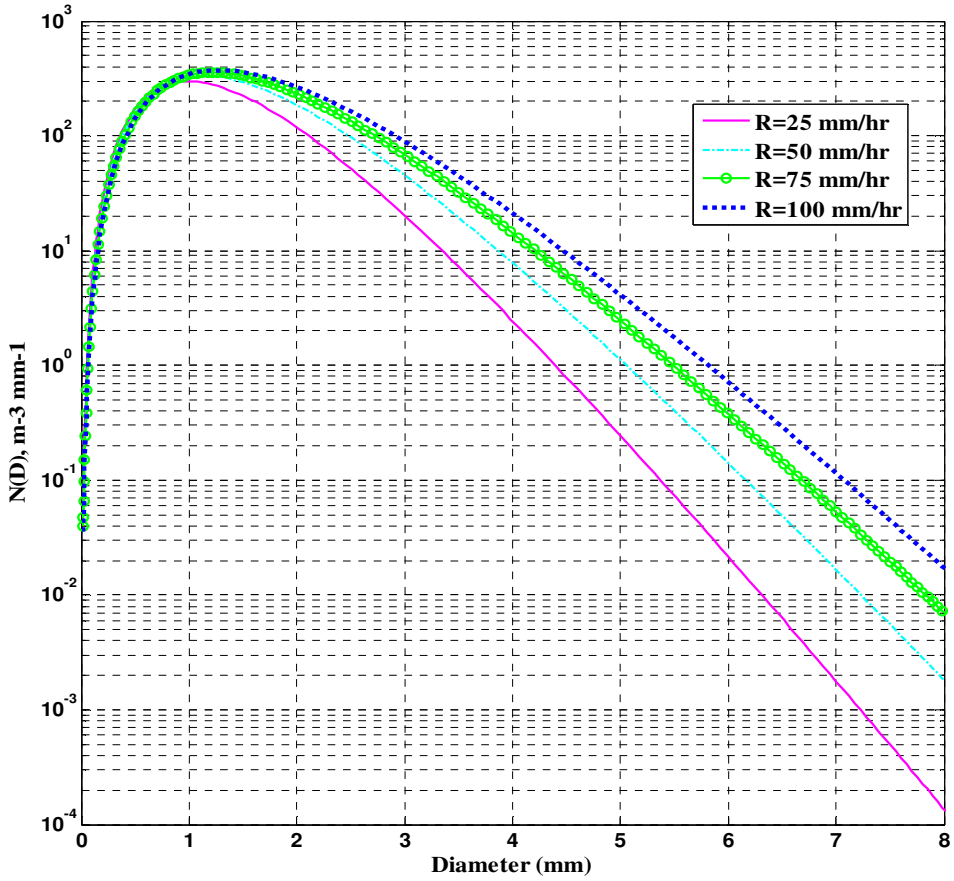

Figure 3.3: Rain drop size distribution by de Wolf [12].

3.4 Complex Index of Refraction

The determination of the scattering properties of raindrops depends on the characteristics of the index of refraction of water, which is strongly dependent on frequency and temperature, especially in the millimeter-wave frequency band. The index of refraction model of Ray [13] for liquid water was implemented in this research to

describe its behavior as a function of temperature and frequency, which implicitly assumed the harmonic time variation $e^{-i\omega t}$. The expressions of the index of refraction model given by [13] are as follow:

$$\varepsilon_r = \varepsilon_r' + i\varepsilon_r'', \tag{3.6}$$

where ε_r is the complex relative permittivity and is related to the complex index of refraction by:

$$\varepsilon_r = m^2, \tag{3.7}$$

$$\varepsilon_r' = Re[m]^2 - Im[m]^2, \tag{3.8}$$

$$\varepsilon_r'' = 2Re[m]Im[m], \tag{3.9}$$

and ε_r' and ε_r'' are the real and imaginary parts of ε_r, respectively, that can be expressed as:

$$\varepsilon_r' = \varepsilon_r^{\infty} + \frac{[\varepsilon_r^s - \varepsilon_r^{\infty}]}{\left[1 + \left(\frac{\lambda_s}{\lambda}\right)^2\right]}, \tag{3.10}$$

$$\varepsilon_r'' = \frac{\left[(\varepsilon_r^s - \varepsilon_r^{\infty})\left(\frac{\lambda_s}{\lambda}\right)\right]}{\left[1 + \left(\frac{\lambda_s}{\lambda}\right)^2\right]}. \tag{3.11}$$

where ε_r^{∞} is the high frequency dielectric constant, ε_r^s is the static constant and λ_s is the relaxation wavelength. For details, see [13].

Figure 3.4 illustrates the results from the theory implementation of this model for different values of temperature. In this study, the complex index of refraction *m = Re[m] + i Im[m]* is kept constant for a given frequency and temperature. Thus, the following index of refraction were used: *m = 8.21+i1.76, m=5.037+i2.76* and *m=3.96+i2.367* for the frequencies of 9.41 GHz, 42 GHz and 70 GHz, respectively.

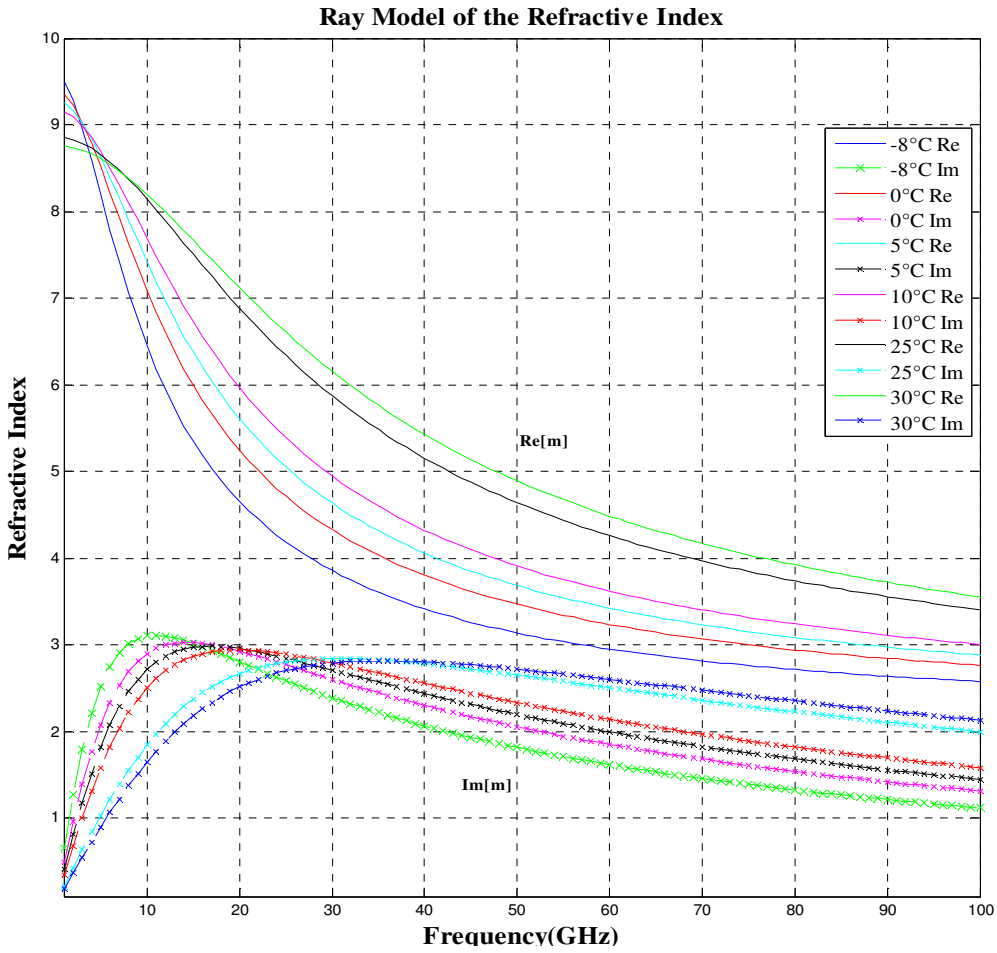

Figure 3.4: Real and imaginary parts of the index of refraction of water using the Ray model [13].

3.5. Canting Angle

The canting angle model assumed in this study is described by [52]. This model, defined by Brussaard, was considered in other studies [56], [57], [58], and [59].

The author defines the canting angle as: “the angle of rotation of the drop image around the propagation direction, which is in fact the projection of the canting angle in a plane perpendicular to the propagation direction”. Figure 3.5 illustrates the concept.

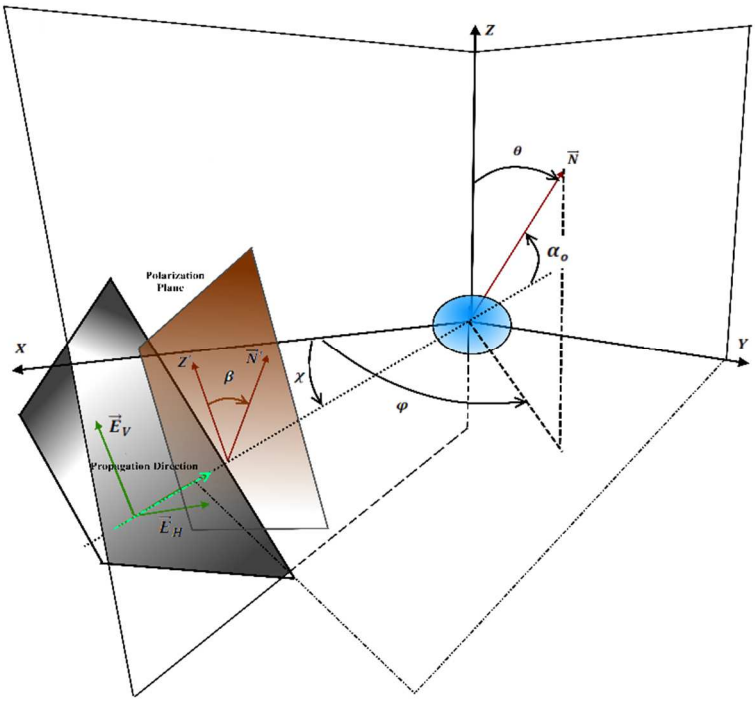

Figure 3.5: Drop canting angle representation.

The mean canting angle $\beta(h)$ of raindrops as a function of the drop size at the observation height h (n) is given by [14] as

$$\tan\beta(h) = \frac{V_v U'(h)}{g} x^{(1-n)} e^{x} \Gamma(n,x), \tag{3.12}$$

where V_v is the vertical drop speed, assumed to be constant and equal to the terminal velocity in stagnant air [60], n is a constant dependent on the roughness of the terrain ranging from 0.1 for sea to 0.3-0.4 for large cities, and $\Gamma(n,x)$ is the incomplete Gamma function

$$\Gamma(n,x) = \int_{x}^{\infty} e^{-p} p^{(n-1)} dp, \tag{3.13}$$

The quantity $U'(h)$ is the wind gradient, defined as

$$U(h) = \left(\frac{h}{h_r}\right)^q U_r \quad \rightarrow \quad U'(h) = \frac{dU}{dh} = q h^{q-1} \frac{U_r}{{h_r}^2}, \tag{3.14}$$

where U_r (typically 15 m/s) is the mean horizontal wind velocity measured at reference height h_r (typically 10 m) and x is the correction function defined by [61]

$$x = \frac{gh}{{V_v}^2}. \tag{3.15}$$

where g = 9.8 m/s^2 is the acceleration of gravity, $h\ (m)$ is the height of observation and $V_v\ (\mathrm{m/s})$ is the terminal velocity. Equation (3.15) shows the considerable dependence of the canting angle on the drop size, since the terminal velocity V_v is related with the diameter of the raindrop.

On the other hand, authors such as [62] and [63] assume that the canting angle may be considered to independ from the drop size. In order to verify this assumption, the model of [14] for the canting angle was implemented for different observation heights. The resulting curves are plotted in Figure 3.6, which shows that the assumption considered in different literatures applies only for larger drops. For the case of raindrops with sizes smaller than approximately 2 mm, the canting angle increases as the drop size increases. However, the assumption in [62] may be explained by taking into account that the typical shapes of smaller raindrops tend to be spherical. Thus, any arbitrary axis can be the axis of rotationally symmetry of the drop and it is reasonable to assume that the canting angle is independ from the drop size.

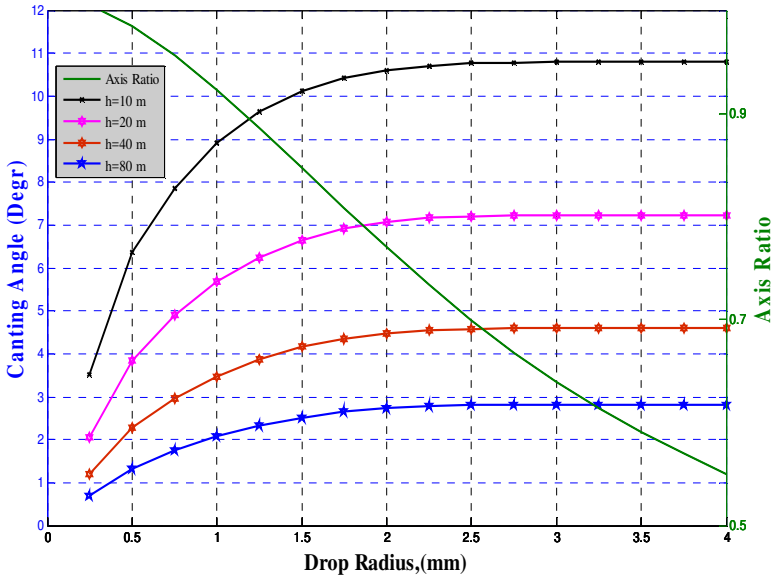

Figure 3.6: Canting angle as a function of drop size and height. It is assumed that m = 0.2, g = 9.8 m/s^2, U_r = 15 m/s (wind velocity) measured at the height h_r = 10 m.

3.6. Orientation Distribution

Due to random fluctuations of the wind intensity and direction, the medium contains a collection of also randomly-oriented axis-symmetric raindrops. Thus, a probability density function (pdf) for the orientation of the symmetry axis is needed. It will be described on a spherical surface by $P_\Omega(\beta,\gamma)$. The probability that the symmetry axis be oriented within an elementary solid angle dΩ centered at Ω = (β, γ) is $P_\Omega(\beta,\gamma)\mathrm{d}\Omega = P_{B\Gamma}(\beta,\gamma)\sin\beta d\beta d\gamma$, where

$$P_{B\,\Gamma}(\beta,\gamma) = \begin{cases} \dfrac{1}{\mathcal{F}}\dfrac{1}{\delta\gamma}\dfrac{1}{\sqrt{2\pi}\Delta\beta}\, e^{-\frac{1}{2}\left(\frac{\beta-\beta_o}{\Delta\beta}\right)^2} & |\gamma-\gamma_o| < \dfrac{\delta\gamma}{2}, \\ \dfrac{1}{\mathcal{F}}\dfrac{1}{\delta\gamma}\dfrac{1}{\sqrt{2\pi}\Delta\beta}\, e^{-\frac{1}{2}\left(\frac{\beta+\beta_o}{\Delta\beta}\right)^2} & |\gamma-(\gamma_o+\pi)| < \dfrac{\delta\gamma}{2}. \end{cases} \tag{3.16}$$

In the above equation, β represents the angle between the symmetry axis of the particle and the vertical, which varies in the [0, π] interval. Additionally, the distribution of the orientation angle γ is uniform in the provide intervals. The average value β_o can vary between 5° and 10° [61] and $\Delta\beta \approx 30°$ [59]. Figure 3.7 shows the geometric relations between the propagation and wind directions, as well as the orientation angle of the raindrop with respect to the reference frame. In this Figure, $\vec{N}$ is the symmetry axis of the

raindrop, $\vec{Z}$ represents the true vertical, and β is the angle between the vertical and $\vec{N}$. Additionally, $\vec{W}$ is the wind direction, γ_o is the angle between the wind direction and the Y axis (horizontal and perpendicular to the plane defined by vertical and the propagation direction). The coordinate system (X_b, Y_b, Z_b) represents the "body reference frame" fixed to the particle, and the coordinate system (X, Y, Z) represents the "principal reference frame" or "laboratory reference frame" fixed in space. The X, Y and X_b, Y_b planes intersect along the line of the nodes. A detailed discussion of reference frames and Eulerian angles transformation can be found in [44].

According to measurements, the orientation of the symmetry axis would be well represented by a Gaussian distribution with parameters β_o and $\Delta\beta$. Considering their values indicated above, one sees that there would be a non-negligible probability associated with a negative value for β, as illustrated by Figure 3.8. However, the zenith angle β should be restricted to the interval [0, π]. To reconcile the two conflicting requirements, it is necessary to redefine the integration intervals of the azimuthal angle γ as is illustrated in Figure 3.9 and slightly modify the representation of the Gaussian distribution as indicated in expression (3.16). This expression remains continuous in the region of interest (within the dotted lines), as explained by Figure 3.10.

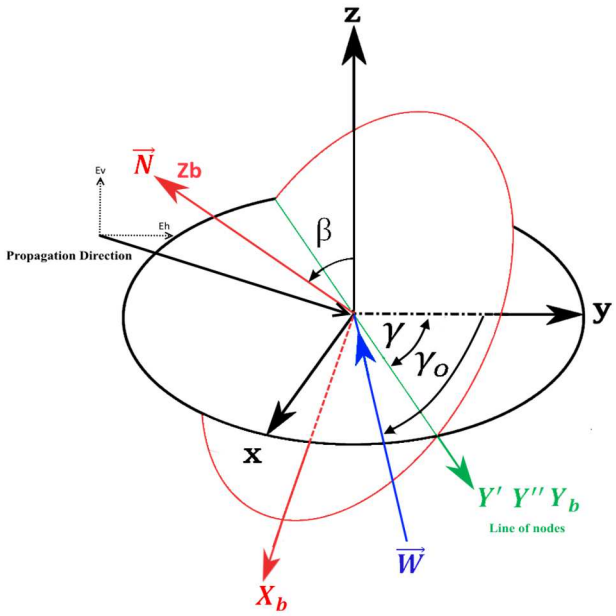

Figure 3.7: Relation between wind direction and geometric illustration of the raindrop orientation.

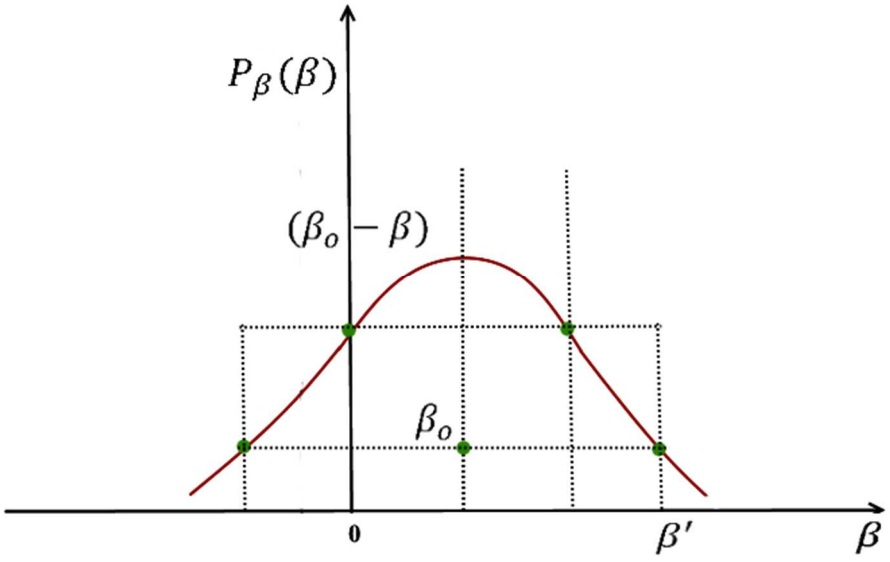

Figure 3.8: Gaussian probability density function of the zenith angle β.

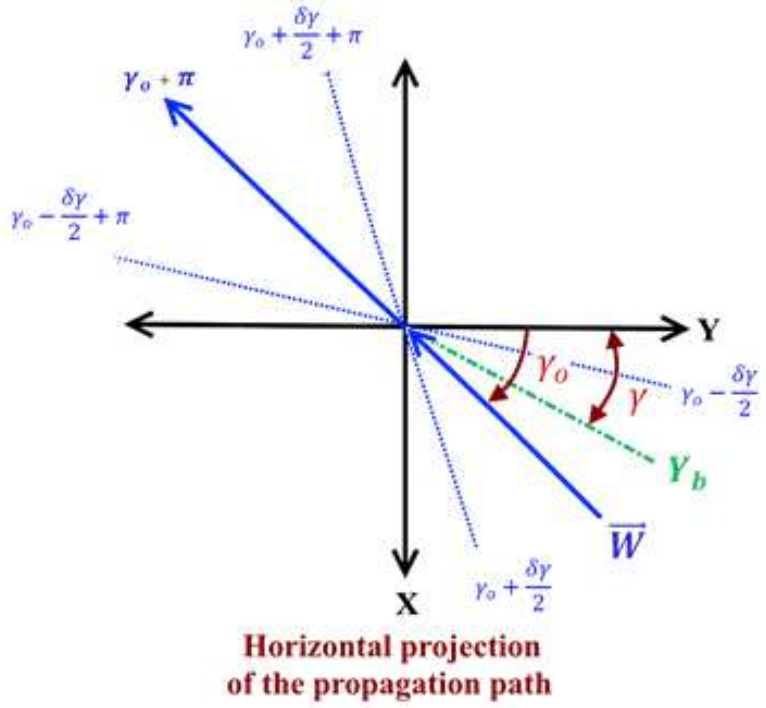

Figure 3.9: Geometric illustration of the raindrop orientation in the horizontal plane (X,Y).

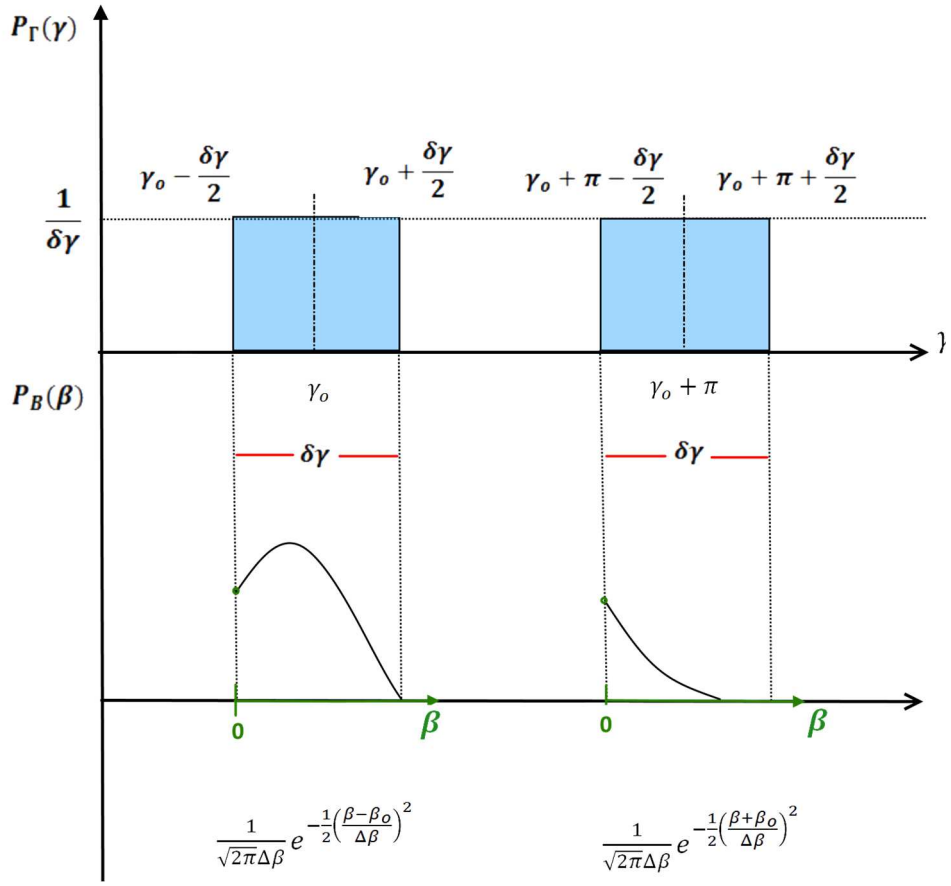

Figure 3.10: Description of the probability density functions $\boldsymbol{P_B(\beta)}$and $\boldsymbol{P_\Gamma(\gamma)}$.

From expression (3.16), one has [43]

$$\int_0^{2\pi}\int_0^{\pi} P_{B\,\Gamma}(\beta,\gamma)\,\sin\beta d\beta d\gamma =$$

$$= \frac{1}{\sqrt{2\pi}\Delta\beta\mathcal{F}\delta\gamma}\left\{\int_{\gamma_o-\frac{\delta\gamma}{2}}^{\gamma_o+\frac{\delta\gamma}{2}}\int_0^{\pi} e^{-\frac{1}{2}\left(\frac{\beta-\beta_o}{\Delta\beta}\right)^2}\sin\beta d\beta d\gamma + \right.$$

$$\left. + \int_{\gamma_o+\pi-\frac{\delta\gamma}{2}}^{\gamma_o+\pi+\frac{\delta\gamma}{2}}\int_0^{\pi} e^{-\frac{1}{2}\left(\frac{\beta+\beta_o}{\Delta\beta}\right)^2}\sin\beta d\beta d\gamma\right\} =$$

$$= \frac{1}{\sqrt{2\pi}\Delta\beta\mathcal{F}}\left\{\int_0^{\pi} e^{-\frac{1}{2}\left(\frac{\beta-\beta_o}{\Delta\beta}\right)^2}\sin\beta d\beta + \int_0^{\pi} e^{-\frac{1}{2}\left(\frac{\beta+\beta_o}{\Delta\beta}\right)^2}\sin\beta d\beta\right\}, \qquad (3.17)$$

The change of variables β´ = - β in the second integral lead to

$$\int_0^{2\pi}\int_0^{\pi} P_{\mathrm{B\Gamma}}(\beta,\gamma)\,\sin\beta d\beta d\gamma = \frac{1}{\sqrt{2\pi}\Delta\beta\mathcal{F}}\left\{\int_{-\pi}^{\pi} e^{-\frac{1}{2}\left(\frac{\beta-\beta_o}{\Delta\beta}\right)^2}|\sin\beta|\,d\beta\right\}, \tag{3.18}$$

which is equal to one for the following value of the normalization parameter

$$\mathcal{F} = \frac{1}{\sqrt{2\pi}\Delta\beta}\int_{-\pi}^{\pi} e^{-\frac{1}{2}\left(\frac{\beta-\beta_o}{\Delta\beta}\right)^2}|\sin\beta|\,d\beta. \tag{3.19}$$

3.7. Terminal Velocity

The drop terminal velocity *v(D)* is necessary to determine the rainfall rate. It is calculated from the equilibrium equation

$$F_{net} = mg - \gamma v. \tag{3.20}$$

where mg represent the gravitational force, γv represent the air resistance force, the friction coefficient is $\gamma = 3\pi D\eta$, D is the diameter of the raindrop (in mm) and η is viscosity of the air ($17.1\text{x}10^{-6}$ Pa.s). The solution to equation (3.20) for a constant velocity v is obtained by setting $F_{net} = 0$. Figure 3.11 shows the forces acting on a raindrop.

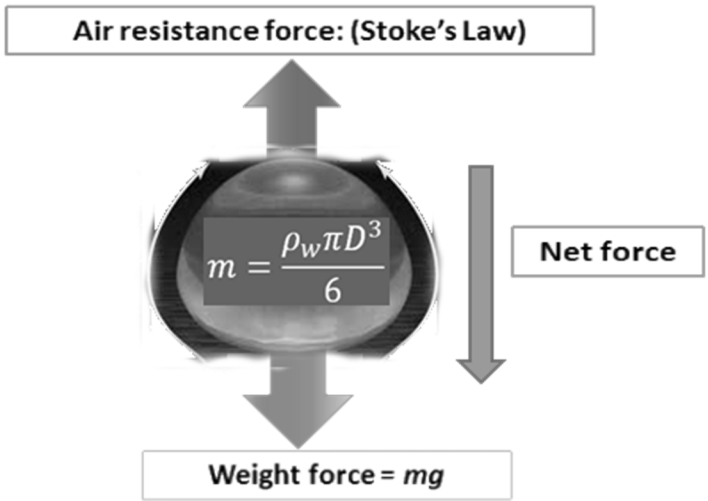

Figure 3.11: Representation of the forces acting on a raindrop falling.

To model the terminal velocity variation as a function of drop radius, the values listed in Table 3.2 [60] have been used to obtain the following regression curve

$$v(D) = -0.00279686D^4 + 0.08789383D^3 - 1.01376794D^2 + 5.08201572D - 0.20586810. \quad (3.21)$$

that is plotted in Figure 3.12.

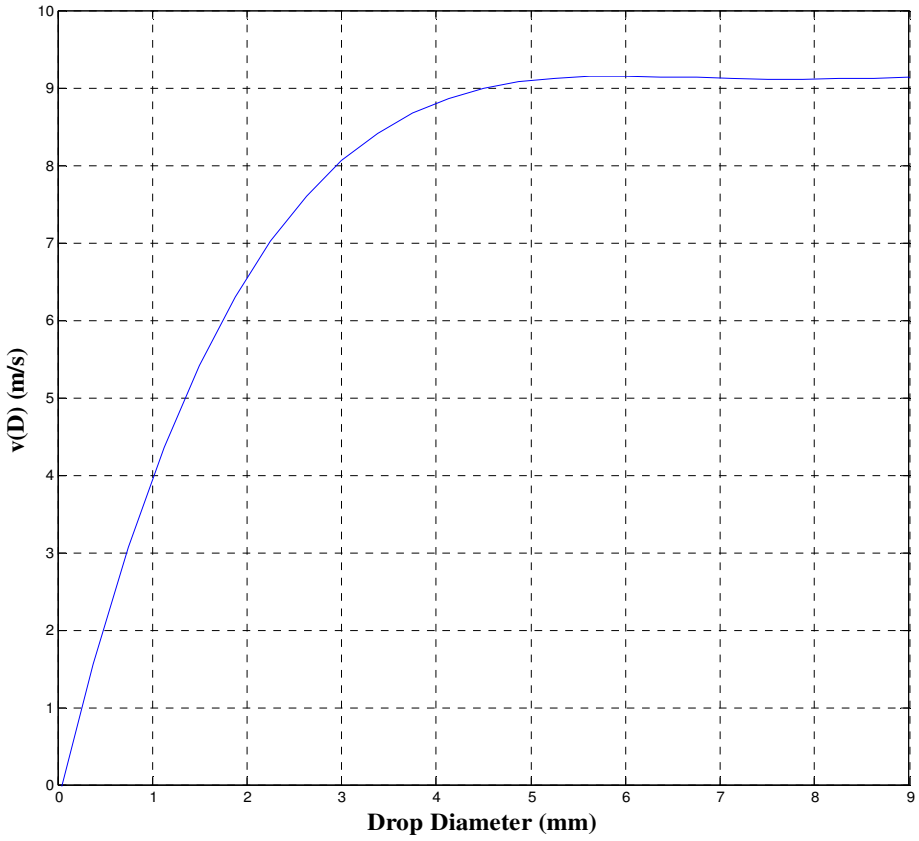

Figure 3.12: Terminal velocity of raindrop as a function of drop diameter.

Table 3.2: Terminal velocities of drops of various sizes [60].

D(mm)	v(D)
0.5	2.06
1.0	4.03
1.5	5.40
2.0	6.49
2.5	7.45
3.0	8.06
3.5	8.53
4.0	8.83
4.5	9.00
5.0	9.09
5.5	9.13
6.0	9.14
6.5	9.14
7.0	9.14
7.5	9.14
8.0	9.14
8.5	9.14
9.0	9.14

The above data can also be partially fitted by the following equations [64]:

$$v(D) = \begin{cases} 28D^2 & for\ D \leq 0.075\ mm, \\ 4.5D - 0.18 & for\ 0.075\ mm < D \leq 0.5\ mm, \\ 4.0D + 0.07 & for\ 0.5\ mm < D \leq 1.0\ mm, \\ -0.425D^2 + 3.695D + 0.8 & for\ 1.0\ mm < D \leq 3.6\ mm. \end{cases} \quad (3.21)$$

4 Methodology

This chapter outlines the set of methods that are used to calculate the scattered field due to a cluster of raindrops. The results will then be used in interference computations. The procedures will be divided into four macro stages, each further described in the next sections. In particular, the scattering formulation by a single particle is based on the extended boundary condition method (EBCM) initially proposed in [24]. The theoretical development that will be described is based on [45], which is very similar to the one previously presented in [44].

4.1. Characteristics of Rainfall

Initially, it is necessary to model the physical properties of the medium, defined by a cluster of raindrops. The characteristics and models considered herein were described in Chapter 3. In particular, the DSD, the particle shapes for each equivalent diameter, the index of refraction, and the symmetry axis orientation distribution are known.

4.2. Description of the Scattering Problem for a Single Particle

Let a known isotropic, homogeneous, and nonmagnetic particle centered at the origin, as shown in Figure 4.1, be illuminated by an incident electromagnetic field. Figure 4.1 also shows: (i) an internal region V_{int} bounded by the closed surface S that limits the particle; and (ii) the region V_{ext}, bounded by the surfaces S_∞ (of infinite radius) and S, representing the infinite region exterior to the particle, which is circumscribed by the sphere with radius $r_>$ and circumscribes another sphere with radius $r_<$.

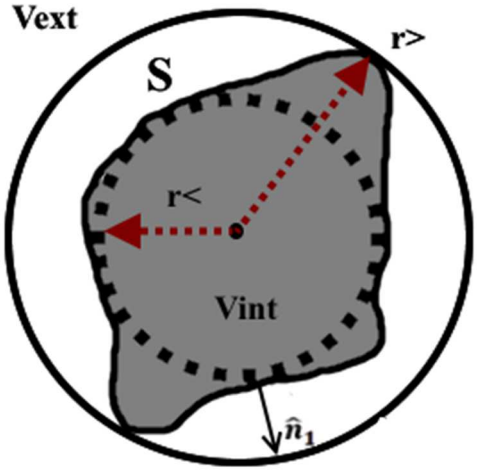

Figure 4.1: Homogeneous scattering particle.

For each region, the electric field satisfies the following equations:

$$\begin{aligned} \nabla \times \nabla \times \vec{E} - {k_o}^2 \vec{E} = 0 \quad r \in V_{ext}, \\ \nabla \times \nabla \times \vec{E} - {k_1}^2 \vec{E} = 0 \quad r \in V_{int}. \end{aligned} \tag{4.1}$$

where k_o and k_1 are the wave number of the exterior and interior regions. Here, $k_o = \omega\sqrt{\mu_o \varepsilon_o}$ and $k_1 = k_o m$, where $m = \left[\varepsilon_r + i\left(\frac{\sigma}{\omega \varepsilon_o}\right)\right]^{1/2}$ is the complex index of refraction of water at the assumed frequency and temperature. The harmonic time variation $e^{-i\omega t}$ is implicitly assumed.

Next, the vector Green's theorem will be applied to the volume V_{ext}. The vector Green's theorem allows one to express the vector quantities $\vec{E}$ and $\vec{H}$ inside the volume V_{ext} as functions of the fields $\vec{E}$ and $\vec{H}$ over the limiting closed surface. According to [68], this theorem is ideal to "solve equations in space which contains sources as well as regions where the constitutive parameters differ from those of the medium in the surrounding space". The vector Green's theorem is given by

$$\int_{V_{ext}} \left[\vec{a} \cdot \left(\nabla \times \nabla \times \vec{b}\right) - \vec{b} \cdot \left(\nabla \times \nabla \times \vec{a}\right)\right] dV = \tag{4.2}$$

$$= \int_{S+S_\infty} \hat{n} \cdot \left[\vec{b} \times (\nabla \times \vec{a}) - \vec{a} \times \left(\nabla \times \vec{b}\right)\right] dS.$$

where the unit vector $\hat{n}$ is perpendicular to surfaces S and S_∞ and directed away from V_{ext}. Thus, $\hat{n} = -\hat{n}_1$ along S. Suppose $\vec{a} = \vec{E}$ and $\vec{b} = \bar{\bar{G}}_o(\vec{r}, \vec{r}\,') \cdot \vec{c}$, where $\vec{c}$ is an arbitrary constant vector and $\bar{\bar{G}}_o(\vec{r}, \vec{r}\,')$ is the free-space dyadic Green´s function [69]. Taking into account that the total field throughout the entire exterior space is equal to the sum of the incident and scattered field

$$\vec{E}(\vec{r}\,') = \vec{E}_i(\vec{r}\,') + \vec{E}_s(\vec{r}\,'), \tag{4.3}$$

the application of the vector Green's theorem provides

$$\vec{E}(\vec{r}\,') = \vec{E}_i(\vec{r}\,') + \int_S \left\{ i\omega\mu_o \left[\hat{n}_1 \times \vec{H}_+(\vec{r})\right] \cdot \bar{\bar{G}}_o(\vec{r}, \vec{r}\,') + \left[\hat{n}_1 \times \vec{E}_+(\vec{r})\right] \cdot \nabla \times \right. \\ \left. \times \bar{\bar{G}}_o(\vec{r}, \vec{r}\,') \right\} dS, \tag{4.4}$$

for $\vec{r}\,' \in V_{ext}$ and

$$\vec{E}_i(\vec{r}\,') = -\int_S \left\{ i\omega\mu_o \left[\hat{n}_1 \times \vec{H}_+(\vec{r})\right] \cdot \bar{\bar{G}}_o(\vec{r}, \vec{r}\,') + \left[\hat{n}_1 \times \vec{E}_+(\vec{r})\right] \cdot \nabla \times \bar{\bar{G}}_o(\vec{r}, \vec{r}\,') \right\} dS, \tag{4.5}$$

for $\vec{r}\,' \in V_{int}$.

Note that the unit vector $\hat{n}_1$ is perpendicular to surface S and directed away from the particle, as indicated in Figure 4.1. The plus sign (+) indicates that the electric and magnetic fields just outside the surface S should be use in equations (4.4) and (4.5). The complete procedure for the application of the vector Green's theorem is detailed in Appendix A. It can be seen that only the incident field exists for all the points $\vec{r}\,' \in V_{ext}$ in the particle absence ($V_{int} \rightarrow 0$ and $S \rightarrow 0$). This result is confirmed by equation (4.4) and justifies the identification of the integral over S_∞ with $-\vec{E}_i(\vec{r}\,')$.

Equation (4.5) is called the Extended Boundary Condition Method (EBCM), because it analytically extends $\vec{r}'$ to the internal region. As explained in [45], the essence of the EBCM is based on the possibility of obtaining the fields $\vec{E}_+(\vec{r})$ and $\vec{H}_+(\vec{r})$ outside the particle surface by using this equation. It is applied under the assumption that the incident field is known. Then, the scattered field can be computed.

According to equation (C.61) of [45], the free-space dyadic Green´s function $\bar{\bar{G}}_o(\vec{r},\vec{r}')$ can be expressed in terms of vector spherical harmonic wave functions (VSWFs) as follow

$$\bar{\bar{G}}_o(\vec{r},\vec{r}') = ik_o \sum_{n=1}^{\infty}\sum_{m=-n}^{+n}(-1)^m \times$$

$$\times \begin{cases} \vec{M}_{-mn}(k_o r,\theta,\varphi) Rg\vec{M}_{mn}(k_o r',\theta',\varphi') + \\ +\vec{N}_{-mn}(k_o r,\theta,\varphi) Rg\vec{N}_{mn}(k_o r',\theta',\varphi') \qquad r > r', \\ \\ Rg\vec{M}_{-mn}(k_o r,\theta,\varphi)\vec{M}_{mn}(k_o r',\theta',\varphi') + \\ +Rg\vec{N}_{-mn}(k_o r,\theta,\varphi)\vec{N}_{mn}(k_o r',\theta',\varphi') \qquad r < r'. \end{cases} \tag{4.6}$$

In the above equation,

$$\vec{M}_{mn}(k_o r,\theta,\varphi) = \sqrt{\frac{(2n+1)}{4\pi n(n+1)}}\, h_n^{(1)}(k_o r)\{i\pi_{mn}(\theta)\hat{\theta} - \tau_{mn}(\theta)\hat{\varphi}\}e^{im\varphi},$$

$$\vec{N}_{mn}(k_o r,\theta,\varphi) = \sqrt{\frac{(2n+1)}{4\pi n(n+1)}} \times \left\{\left[\frac{h_n^{(1)}(k_o r)}{k_o r}\right] n(n+1) d_{om}^n(\theta)\hat{R} + \right.$$

$$\left. \frac{\left[u h_n^{(1)}(u)\right]'}{u}\bigg|_{k_o r} \left[\tau_{mn}(\theta)\hat{\theta} + i\pi_{mn}(\theta)\hat{\varphi}\right]\right\} e^{im\varphi},$$

$$\pi_{mn}(\theta) = m\frac{d_{om}^{n}(\theta)}{\sin\theta},$$

$$\tau_{mn}(\theta) = \frac{d}{d\theta}[d_{om}^{n}(\theta)],$$

$$d_{0m}^{n}(\theta) = \sqrt{\frac{(n-m)!}{(n+m)!}}P_{n}^{m}(cos\theta),$$

where $h_n^{(1)}(x)$ is the spherical Hankel function of first kind, $d_{0m}^{n}(\theta)$ is the Wigner d function, and $P_n^m(cos\theta)$ is the associated Legendre function of the first kind. Additionally, the regular VSWFs $Rg\vec{M}_{mn}(k_o r', \theta', \varphi')$ and $Rg\vec{N}_{mn}(k_o r', \theta', \varphi')$ are obtained by substituting the spherical Bessel function $j_n(x)$ for $h_n^{(1)}(x)$ in the above equations for $\vec{M}_{mn}(k_o r', \theta', \varphi')$ and $\vec{N}_{mn}(k_o r', \theta', \varphi')$, respectively.

From equation (4.6) and the properties $\nabla \times \vec{M}_{mn} = k_o\vec{N}_{mn}$ and $\nabla \times \vec{N}_{mn} = k_o\vec{M}_{mn}$, also valid for the pair $\left(Rg\vec{M}_{mn}, Rg\vec{N}_{mn}\right)$, it can be directly shown that

$$\nabla \times \bar{\bar{G}}_o(\vec{r}, \vec{r}') =$$

$$= ik_o{}^2 \sum_{n=1}^{\infty}\sum_{m=-n}^{+n}(-1)^m \begin{cases} \vec{N}_{-mn}(k_o r, \theta, \varphi)Rg\vec{M}_{mn}(k_o r', \theta', \varphi') + \\ +\vec{M}_{-mn}(k_o r, \theta, \varphi)Rg\vec{N}_{mn}(k_o r', \theta', \varphi') \qquad r > r', \\ \\ Rg\vec{N}_{-mn}(k_o r, \theta, \varphi)\vec{M}_{mn}(k_o r', \theta', \varphi') + \\ +Rg\vec{M}_{-mn}(k_o r, \theta, \varphi)\vec{N}_{mn}(k_o r', \theta', \varphi') \qquad r < r'. \end{cases} \tag{4.7}$$

Let the incident field be represented by an expansion of VSWFs as

$$\vec{E}_i(\vec{r}') = \sum_{n=1}^{\infty}\sum_{m=-n}^{+n} a_{mn}Rg\vec{M}_{mn}(k_o r', \theta', \varphi') + b_{mn}Rg\vec{N}_{mn}(k_o r', \theta', \varphi'), \tag{4.8}$$

Expressions for the coefficients a_{mn} and b_{mn} due to an incident plane wave are provided in Appendix B.

Assume a pair of position vectors $(\vec{r},\vec{r}\,')$ such that $r' < r_<$ and $\vec{r} \in S$. Since $r > r'$, $\bar{\bar{G}}_o(\vec{r},\vec{r}\,')$ and $\nabla \times \bar{\bar{G}}_o(\vec{r},\vec{r}\,')$ are represented by the upper parts of equations (4.6) and (4.7), respectively. Inserting these upper parts and the right-hand side of equation (4.8) into equation (4.5), one gets

$$\sum_{n=1}^{\infty}\sum_{m=-n}^{+n} a_{mn} Rg\vec{M}_{mn}(k_o r',\theta',\varphi') + b_{mn} Rg\vec{N}_{mn}(k_o r',\theta',\varphi') = \tag{4.9}$$

$$= \sum_{n=1}^{\infty}\sum_{m=-n}^{+n} \Bigg\{ k_o(-1)^m \int_S \{\omega\mu_o[\hat{n}_1 \times \vec{H}_+(\vec{r})] \cdot \vec{M}_{-mn}(k_o r,\theta,\varphi)] -$$

$$-ik_o[\hat{n}_1 \times \vec{E}_+(\vec{r})] \cdot \vec{N}_{-mn}(k_o r,\theta,\varphi)\}dS\} Rg\vec{M}_{mn}(k_o r',\theta',\varphi') +$$

$$+ \Bigg\{ k_o(-1)^m \int_S \{\omega\mu_o [\hat{n}_1 \times \vec{H}_+(\vec{r})] \cdot \vec{N}_{-mn}(k_o r,\theta,\varphi) -$$

$$-ik_o[\hat{n}_1 \times \vec{E}_+(\vec{r})] \cdot \vec{M}_{-mn}(k_o r,\theta,\varphi)\}dS\} Rg\vec{N}_{mn}(k_o r',\theta',\varphi')\}.$$

Comparing the two sides of equation (4.9), it follows that

$$a_{mn} = (-1)^m k_o \int_S \{\omega\mu_o[\hat{n}_1 \times \vec{H}_+(\vec{r})] \cdot \vec{M}_{-mn}(k_o r,\theta,\varphi) - \tag{4.10}$$
$$-ik_o[\hat{n}_1 \times \vec{E}_+(\vec{r})] \cdot \vec{N}_{-mn}(k_o r,\theta,\varphi)\}dS,$$

$$b_{mn} = (-1)^m k_o \int_S \{\omega\mu_o[\hat{n}_1 \times \vec{H}_+(\vec{r})] \cdot \vec{N}_{-mn}(k_o r,\theta,\varphi) -$$
$$-ik_o[\hat{n}_1 \times \vec{E}_+(\vec{r})] \cdot \vec{M}_{-mn}(k_o r,\theta,\varphi)\}dS. \tag{4.11}$$

Similarly, the scattered field can also be represented by another expansion of VSWFs

$$\vec{E}_s(\vec{r}\,') = \sum_{n=1}^{\infty}\sum_{m=-n}^{+n} p_{mn}\vec{M}_{mn}(k_o r', \theta', \varphi') + q_{mn}\vec{N}_{mn}(k_o r', \theta', \varphi'). \tag{4.12}$$

Now, let the pair of position vectors $(\vec{r}, \vec{r}\,')$ be such that $r' > r_>$ and $\vec{r} \in S$. Since $r' > r$, $\bar{\bar{G}}_o(\vec{r}, \vec{r}\,')$ and $\nabla \times \bar{\bar{G}}_o(\vec{r}, \vec{r}\,')$ are represented by the lower parts of equations (4.6) and (4.7), respectively. Inserting these lower parts and the right-hand side of equation (4.12) into equation (4.4) and following a similar procedure to the one that led to equations (4.10) and (4.11), one gets

$$\begin{aligned} p_{mn} = -(-1)^m k_o \int_S \{\omega\mu_o[\hat{n}_1 \times \vec{H}_+(\vec{r})] \cdot Rg\vec{M}_{-mn}(k_o r, \theta, \varphi) - \\ - ik_o[\hat{n}_1 \times \vec{E}_+(\vec{r})] \cdot Rg\vec{N}_{-mn}(k_o r, \theta, \varphi)\} dS, \end{aligned} \tag{4.13}$$

$$\begin{aligned} q_{mn} = -(-1)^m k_o \int_S \{\omega\mu_o[\hat{n}_1 \times \vec{H}_+(\vec{r})] \cdot Rg\vec{N}_{-mn}(k_o r, \theta, \varphi) - \\ - ik_o[\hat{n}_1 \times \vec{E}_+(\vec{r})] \cdot Rg\vec{M}_{-mn}(k_o r, \theta, \varphi)\} dS. \end{aligned} \tag{4.14}$$

On the other hand, the fields $\vec{E}_t(\vec{r})$ and $\vec{H}_t(\vec{r})$ at an arbitrary point in the interior of the particle ($\vec{r} \in V_{int}$) can be represented by the following expressions

$$\vec{E}_t(\vec{r}) = \sum_{n'=1}^{\infty}\sum_{m=-n'}^{+n'} c_{m'n'}Rg\vec{M}_{m'n'}(k_1 r, \theta, \varphi) + d_{m'n'}Rg\vec{N}_{m'n'}(k_1 r, \theta, \varphi), \tag{4.15}$$

$$\vec{H}_t(\vec{r}) = \frac{k_1}{i\omega\mu_o}\sum_{n=1}^{\infty}\sum_{m=-n'}^{+n'} d_{m'n'}Rg\vec{M}_{m'n'}(k_1 r, \theta, \varphi) + c_{m'n'}Rg\vec{N}_{m'n'}(k_1 r, \theta, \varphi). \tag{4.16}$$

The following boundary conditions should be applied at the surface *S* of the particle

$$\hat{n}_1 \times \vec{E}_+(\vec{r}) = \hat{n}_1 \times \vec{E}_-(\vec{r}) \tag{4.17}$$

$$\hat{n}_1 \times \vec{H}_+(\vec{r}) = \hat{n}_1 \times \vec{H}_-(\vec{r}) \tag{4.18}$$

where the minus sign $(-)$ indicates the interior of the particle and expressions (4.15) and (4.16) provide the values of $\vec{E}_-(\vec{r})$ and $\vec{H}_-(\vec{r})$ as $\vec{r} \to S$. Thus, $\hat{n}_1 \times \vec{E}_+(\vec{r})$ and $\hat{n}_1 \times \vec{H}_+(\vec{r})$ can be expressed in terms of the right-hand sides of equations (4.15) and (4.16) and the results substituted into equations (4.10), (4.11), (4.13), and (4.14). After time-consuming derivations that are detailed in Appendix C, the following relationships are obtained

$$a_{mn} = \sum_{n'=1}^{\infty} \sum_{m=-n'}^{+n'} Q^{11}_{mnm'n'} c_{m'n'} + Q^{12}_{mnm'n'} d_{m'n'}, \tag{4.19}$$

$$b_{mn} = \sum_{n'=1}^{\infty} \sum_{m=-n'}^{+n'} Q^{21}_{mnm'n'} c_{m'n'} + Q^{22}_{mnm'n'} d_{m'n'}, \tag{4.20}$$

$$p_{mn} = -\sum_{n'=1}^{\infty} \sum_{m=-n'}^{+n'} RgQ^{11}_{mnm'n'} c_{m'n'} + RgQ^{12}_{mnm'n'} d_{m'n'}, \tag{4.21}$$

$$q_{mn} = -\sum_{n'=1}^{\infty} \sum_{m=-n'}^{+n'} RgQ^{21}_{mnm'n'} c_{m'n'} + RgQ^{22}_{mnm'n'} d_{m'n'}. \tag{4.22}$$

In the above expressions

$$Q^{11}_{mnm'n'} = (-1)^m (-ik_o)\left(k_1 J^{21}_{mnm'n'} + k_o J^{12}_{mnm'n'}\right), \tag{4.23}$$

$$Q^{12}_{mnm'n'} = (-1)^m (-ik_o)\left(k_1 J^{11}_{mnm'n'} + k_o J^{22}_{mnm'n'}\right), \tag{4.24}$$

$$Q^{21}_{mnm'n'} = (-1)^m (-ik_o)\left(k_1 J^{22}_{mnm'n'} + k_o J^{11}_{mnm'n'}\right), \tag{4.25}$$

$$Q^{22}_{mnm'n'} = (-1)^m(-ik_o)\left(k_1 J^{12}_{mnm'n'} + k_o J^{21}_{mnm'n'}\right). \tag{4.26}$$

The integrals $J^{kl}_{mnm'n'}$ (k,l = 1,2) are defined in Appendix C. Additionally,

$$RgQ^{11}_{mnm'n'} = (-1)^m(-ik_o)\left(k_1 RgJ^{21}_{mnm'n'} + k_o RgJ^{12}_{mnm'n'}\right), \tag{4.27}$$

$$RgQ^{12}_{mnm'n'} = (-1)^m(-ik_o)\left(k_1 RgJ^{11}_{mnm'n'} + k_o RgJ^{22}_{mnm'n'}\right), \tag{4.28}$$

$$RgQ^{21}_{mnm'n'} = (-1)^m(-ik_o)\left(k_1 RgJ^{22}_{mnm'n'} + k_o RgJ^{11}_{mnm'n'}\right), \tag{4.29}$$

$$RgQ^{22}_{mnm'\,n'} = (-1)^m(-ik_o)\left(k_1 RgJ^{12}_{mnm'n'} + k_o RgJ^{21}_{mnm'n'}\right). \tag{4.30}$$

The integrals $RgJ^{kl}_{mnm'n'}$ (k,l = 1,2) are also defined in Appendix C. They are obtained by substituting $j_n(x)$ for $h^{(1)}_n(x)$ in the expressions for $J^{kl}_{mnm'n'}$, respectively. Simplified expressions for the integrals $J^{kl}_{mnm'n'}$ and $RgJ^{kl}_{mnm'n'}$ are derived in Appendix D.

Each of the equations (4.19) to (4.22) represent a row (for a specific combination of indices mn) of a truncated system of linear equations ($1 \le n, n' \le N_{max}$). Each row mn ($|m| \le n$) contains the coefficients for all possible combinations of indices $m'n'$ ($|m'| \le n'$). Thus, the systems of linear equations can be written in block matrix notation as follows

$$\begin{pmatrix} \underline{Q}_{11} & \underline{Q}_{12} \\ \underline{Q}_{21} & \underline{Q}_{22} \end{pmatrix}\begin{pmatrix} \vec{c} \\ \vec{d} \end{pmatrix} = \begin{pmatrix} \vec{a} \\ \vec{b} \end{pmatrix}; \quad -\begin{pmatrix} Rg\underline{Q}_{11} & Rg\underline{Q}_{12} \\ Rg\underline{Q}_{21} & Rg\underline{Q}_{22} \end{pmatrix}\begin{pmatrix} \vec{c} \\ \vec{d} \end{pmatrix} = \begin{pmatrix} \vec{p} \\ \vec{q} \end{pmatrix} \tag{4.31}$$

Since

$$\begin{pmatrix} \vec{c} \\ \vec{d} \end{pmatrix} = \begin{pmatrix} \underline{Q}_{11} & \underline{Q}_{12} \\ \underline{Q}_{21} & \underline{Q}_{22} \end{pmatrix}^{-1}\begin{pmatrix} \vec{a} \\ \vec{b} \end{pmatrix},$$

one finally gets

$$\begin{pmatrix}\vec{p}\\ \vec{q}\end{pmatrix} = -\begin{pmatrix}Rg\underline{Q}_{11} & Rg\underline{Q}_{12}\\ Rg\underline{Q}_{21} & Rg\underline{Q}_{22}\end{pmatrix}\begin{pmatrix}\underline{Q}_{11} & \underline{Q}_{12}\\ \underline{Q}_{21} & \underline{Q}_{22}\end{pmatrix}^{-1}\begin{pmatrix}\vec{a}\\ \vec{b}\end{pmatrix} = \begin{pmatrix}\underline{\hat{T}}_{11} & \underline{\hat{T}}_{12}\\ \underline{\hat{T}}_{21} & \underline{\hat{T}}_{22}\end{pmatrix}\begin{pmatrix}\vec{a}\\ \vec{b}\end{pmatrix}. \tag{4.32}$$

From a comparison between terms in equation (4.32), a compact form can be written for the System Transfer Operator [44] or Transition Matrix [45] $\underline{\hat{T}}(P)$, usually shortened as T-matrix, in the body reference frame

$$\underline{\hat{T}}(P) = -\left(Rg\underline{Q}\right)\underline{Q}^{-1}. \tag{4.33}$$

It is observed that the T-matrix relates the coefficients of the representation of the incident field in terms of VSWFs to those of the scattered field. However, the T-matrix does not depend on them. It depends only on the frequency of operation, characteristics of the particle and on the reference frame. So far, it has been assumed that the origin of the reference frame is the center of the particle. Furthermore, it has been seen that the particles of interest display a symmetry axis, which is aligned with the Z_b axis to simplify calculations of the $J^{kl}_{mnm'n'}$ and $RgJ^{kl}_{mnm'n'}$ integrals.

4.3. Computation of the T-Matrix for an Axially Symmetric Particle of Equivalent Diameter D in the Principal Reference Frame

In the present section, the rotation transformation rule for the T-matrix described by Tsang et al. [44] and Mishchenko et al. [45] is used to determine the scattering properties of the particle in the principal reference frame. The Eulerian angles α, β and γ specifies the rotation of the corresponding axes into those aligned with the symmetry axis of the raindrop of equivalent diameter *D*. It has been shown by the above authors that the vector spherical wave functions in the two reference frames can be related as follow

$$\vec{M}_{mn}(k_o r, \theta_b, \varphi_b) = \sum_{m'=-n}^{+n} \vec{M}_{m'n}(k_o r, \theta, \varphi) D^n_{m'm}(\alpha, \beta, \gamma), \tag{4.34}$$

$$\vec{N}_{mn}(k_o r, \theta_b, \varphi_b) = \sum_{m'=-n}^{+n} \vec{N}_{m'n}(k_o r, \theta, \varphi) D^n_{m'm}(\alpha, \beta, \gamma), \tag{4.35}$$

$$\vec{M}_{mn}(k_o r, \theta, \varphi) = \sum_{m'=-n}^{+n} \vec{M}_{m'n}(k_o r, \theta_b, \varphi_b) D^n_{m'm}(-\gamma, -\beta, -\alpha), \tag{4.36}$$

$$\vec{N}_{mn}(k_o r, \theta, \varphi) = \sum_{m'=-n}^{+n} \vec{N}_{m'n}(k_o r, \theta_b, \varphi_b) D^n_{m'm}(-\gamma, -\beta, -\alpha), \tag{4.37}$$

where the *b* subscript indicates the body reference frame, the distance from the origin to any observation point is invariant under rotations and $D^n_{m'm}(\alpha, \beta, \gamma)$ are the Wigner D functions

$$D^n_{m'm}(\alpha, \beta, \gamma) = e^{-im'\alpha} d^n_{m'm}(\beta) e^{-im\gamma} \tag{4.38}$$

The regular vector spherical wave functions $Rg\vec{M}_{mn}(kr, \theta_b, \varphi_b)$ and $Rg\vec{N}_{mn}(kr, \theta_b, \varphi_b)$ can be similarly transformed using the Wigner D function. As shown in Appendix E, the above transformations lead to the following general relation between the T-matrix elements $T^{kl}_{mnm'n'}$ in the principal reference frame and $\hat{T}^{kl}_{mnm'n'}$ in the body reference frame

$$T^{kl}_{mnm'n'} = \sum_{m_1=-n}^{+n} \sum_{m_2=-n'}^{+n'} D^n_{mm_1}(\alpha, \beta, \gamma) \hat{T}^{kl}_{m_1 n m_2 n'} D^{n'}_{m_2 m'}(-\gamma, -\beta, -\alpha), \tag{4.39}$$

where k,l = 1,2. It is immediate from the results in Appendix D, in combination with the above development, that

$$\hat{T}^{kl}_{m_1 n m_2 n'} = \delta_{m_1 m_2} \hat{T}^{kl}_{m_1 n m_1 n'}, \tag{4.40}$$

for axially-symmetric raindrops. Thus, equation (4.39) can be simplified for the case of interest as follows

$$T_{mnm'n'}^{kl} = \sum_{m_1=-N_{min}}^{+N_{min}} D_{mm_1}^{n}(\alpha,\beta,\gamma)\hat{T}_{m_1nm_1n'}^{kl} D_{m_1m'}^{n'}(-\gamma,-\beta,-\alpha), \tag{4.41}$$

where $N_{min} = min(n, n')$.

Therefore, by implementing equation (4.41), it is possible to compute the orientation-averaged scattering characteristics with respect to the laboratory reference frame for a raindrop of equivalent diameter *D*.

4.4 Computation of the Orientation-Averaged T-Matrix for a Raindrop of Equivalent Diameter *D*

In the principal reference frame, the scattered field by a particle of equivalent diameter *D* can be expanded in terms of VSWFs as

$$\vec{E}_s^D(\vec{r}) = \sum_{n=1}^{\infty}\sum_{m=-n}^{+n} p_{mn}^D \vec{M}_{mn}(k_o\vec{r}) + q_{mn}^D \vec{N}_{mn}(k_o\vec{r}) \tag{4.42}$$

where

$$\begin{pmatrix}\vec{p}\\ \vec{q}\end{pmatrix}_D = \begin{pmatrix}\underline{T}_{11} & \underline{T}_{12}\\ \underline{T}_{21} & \underline{T}_{22}\end{pmatrix}_D \begin{pmatrix}\vec{a}\\ \vec{b}\end{pmatrix}, \tag{4.43}$$

That is,

$$p_{mn}^D = \sum_{n\prime=1}^{\infty}\sum_{m=-n\prime}^{+n\prime} T_{mnm\prime n\prime}^{11D} a_{m\prime n\prime} + T_{mnm\prime n\prime}^{12D} b_{m\prime n\prime}, \tag{4.44}$$

and

$$q_{mn}^D = \sum_{n\prime=1}^{\infty}\sum_{m=-n\prime}^{+n\prime} T_{mnm\prime n\prime}^{21D} a_{m\prime n\prime} + T_{mnm\prime n\prime}^{22D} b_{m\prime n\prime}, \tag{4.45}$$

Substituting the right-hand side of expression (4.41) for $T_{mnm'n'}^{klD}$ in the above expressions, one gets

$$p_{mn}^{D} = \\ = \sum_{n'=1}^{\infty}\sum_{m=-n'}^{+n'}\left\{\sum_{m_1=-N_{min}}^{+N_{min}} D_{mm_1}^{n}(\alpha,\beta,\gamma)\hat{T}_{m_1nm_1n'}^{11D}D_{m_1m'}^{n'}(-\gamma,-\beta,-\alpha)\right\}a_{m'n'} \\ +\left\{\sum_{m_1=-N_{min}}^{+N_{min}} D_{mm_1}^{n}(\alpha,\beta,\gamma)\hat{T}_{m_1nm_1n'}^{12D}D_{m_1m'}^{n'}(-\gamma,-\beta,-\alpha)\right\}b_{m'n'}, \tag{4.46}$$

and

$$q_{mn}^{D} = \\ = \sum_{n'=1}^{\infty}\sum_{m=-n'}^{+n'}\left\{\sum_{m_1=-N_{min}}^{+N_{min}} D_{mm_1}^{n}(\alpha,\beta,\gamma)\hat{T}_{m_1nm_1n'}^{21D}D_{m_1m'}^{n'}(-\gamma,-\beta,-\alpha)\right\}a_{m'n'} \\ +\left\{\sum_{m_1=-N_{min}}^{+N_{min}} D_{mm_1}^{n}(\alpha,\beta,\gamma)\hat{T}_{m_1nm_1n'}^{22D}D_{m_1m'}^{n'}(-\gamma,-\beta,-\alpha)\right\}b_{m'n'} \tag{4.47}$$

The average scattered field due a particle of equivalent diameter D and randomly-oriented symmetry axis is

$$\langle\vec{E}_s^{D}(\vec{r})\rangle = \int_{\Omega'}\vec{E}_s^{D}(\vec{r})p_{\mathrm{AB\Gamma}}^{D}(\alpha,\beta,\gamma)d\Omega', \tag{4.48}$$

where $p_{\mathrm{AB\Gamma}}^{D}(\alpha,\beta,\gamma)$ is the known probability density function of orientation of the symmetry axis of the particle with equivalent diameter D and the region of integration Ω' is limited by $0 \le \alpha \le 2\pi$, $0 \le \beta \le \pi$, and $0 \le \gamma \le 2\pi$.

It is evident from expressions (4.42) to (4.45) that the averaging procedure indicated in expression (4.48) is finally applied to the T-matrix terms. That is,

$$\langle \vec{E}_s^D(\vec{r}) \rangle = \sum_{n=1}^{\infty} \sum_{m=-n}^{+n} \langle p_{mn}^D \rangle \vec{M}_{mn}(k_o \vec{r}) + \langle q_{mn}^D \rangle \vec{N}_{mn}(k_o \vec{r}), \tag{4.49}$$

where

$$\langle p_{mn}^D \rangle = \sum_{n'=1}^{\infty} \sum_{m=-n'}^{+n'} \langle \hat{T}_{mnm'n'}^{11D} \rangle a_{m'n'} + \langle \hat{T}_{mnm'n'}^{12D} \rangle b_{m'n'}, \tag{4.50}$$

$$\langle q_{mn}^D \rangle = \sum_{n'=1}^{\infty} \sum_{m=-n'}^{+n'} \langle \hat{T}_{mnm'n'}^{21D} \rangle a_{m'n'} + \langle \hat{T}_{mnm'n'}^{22D} \rangle b_{m'n'}, \tag{4.51}$$

and

$$\langle \hat{T}_{mnm'n'}^{klD} \rangle = \int_{\Omega'} \hat{T}_{mnm'n'}^{klD} p_{\mathrm{AB\Gamma}}^D(\alpha, \beta, \gamma) d\Omega' \tag{4.52}$$

Substituting the right-hand side of expression (4.41) for $\hat{T}_{mnm'n'}^{klD}$ in the above result, one gets

$$\langle \hat{T}_{mnm'n'}^{klD} \rangle = \tag{4.53}$$
$$= \sum_{m_1=-N_{min}}^{+N_{min}} \int_{\Omega'} D_{mm_1}^{n}(\alpha, \beta, \gamma) \hat{T}_{m_1 n m_1 n'}^{klD} D_{m_1 m'}^{n'}(-\gamma, -\beta, -\alpha) p_{\mathrm{AB\Gamma}}^D(\alpha, \beta, \gamma) \mathrm{d}\Omega',$$

The above integral can be expanded into a summation through the use of the Wigner D functions, the rotationally symmetric properties of the T-matrix and the Clebsch-Gordan expansion, to finally yield

$$\langle \hat{T}_{mnm'n'}^{klD} \rangle = \frac{\delta_{mm'}}{2\pi} (-1)^m \sum_{n_1=|n-n'|}^{n+n'} \left[1 + (-1)^{n+n'+n_1+k+l}\right] C_{nmn'(-m)}^{n_1 0} \times \tag{4.54}$$

$$\times \underline{P}_{n_1}\left[\sum_{m_1=0}^{+N_{min}}(-1)^{m_1}\left(1-\frac{1}{2}\delta_{m_1 0}\right)C^{n_1 0}_{nm_1 n'(-m_1)}\hat{T}^{klD}_{m_1 n m_1 n'}\right]=\delta_{mm'}\tilde{T}^{klD}_{mnn'}.$$

Detailed derivation of equation (4.54), as well as the definition of the coefficients $\underline{P}_{n_1}$, can be found in Appendix F. A summary of the T-matrix formulation is presented in Appendix I. It should be remarked that no evidence of singularities or ill-conditionings of the model were detected during its use, to be described in the next Chapters.

5 Validation

This chapter presents the validation results of the proposed rain and scattering model. This model is used to compute the scattering properties of rain, as described in Chapter 4. The validation procedures presented herein were performed by comparison of scattering results with the ones obtained from previous works [7], [31], [32], [41], [73], [74], and [75].

The theoretical study of scattering by individual raindrops has usually been carried out assuming spherical or spheroidal raindrop shapes. The latter shape is characterized in Figure 5.1. The realistic raindrop shape from Chuang and Beard [8] has been adopted in this thesis because it takes into account hydrostatic pressure, friction, surface tension and electric fields. The following Figures 5.2 to 5.4 compare spheres and equal-volume spheroids with the corresponding equilibrium drop shapes of Chuang and Beard [8] with equivalent diameters D = 1.0 mm, 3.0 mm, and 6.0 mm. Figure 5.1 shows the description of a spheroid with axial ratio $\epsilon = a/b$, for which the surface of the spheroid is modeled by

$$r(\theta) = a[\sin^2\theta + \epsilon^2\cos^2\theta]^{-1/2}$$

$$\frac{1}{r}\frac{dr}{d\theta} = \frac{(\epsilon^2 - 1)\sin\theta\cos\theta}{\sin^2\theta + \epsilon^2\cos^2\theta} \tag{5.1}$$

The differences between the spheroidal and the Chuang and Beard [8] raindrop shapes are displayed in Figures 5.3 and 5.4. It is also clear from these Figures that the raindrop shape depends on the equivalent drop size. Thus, the scattering properties could change depending on the assumed raindrop shape. Several tests have been carried out to validate the performance of the code for computing electromagnetic scattering based on Extended Boundary Condition Method (EBCM).

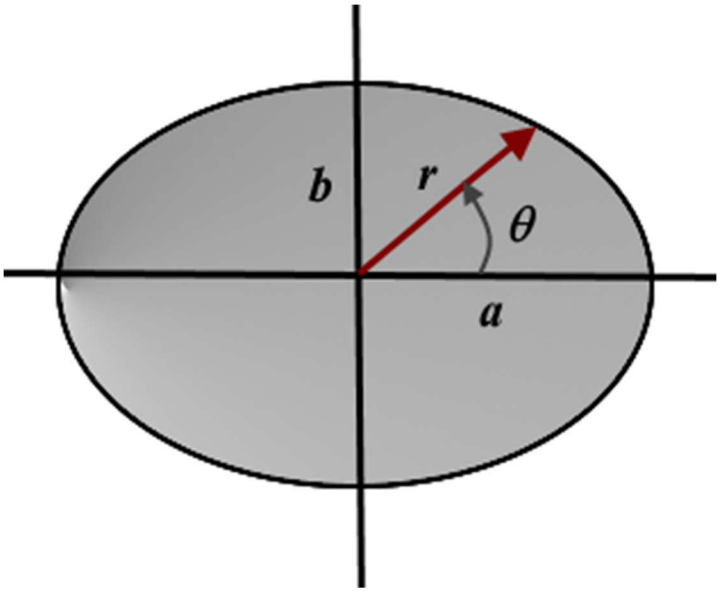

Figure 5.1: Geometric description of a spheroid, which displays horizontal and vertical symmetry planes.

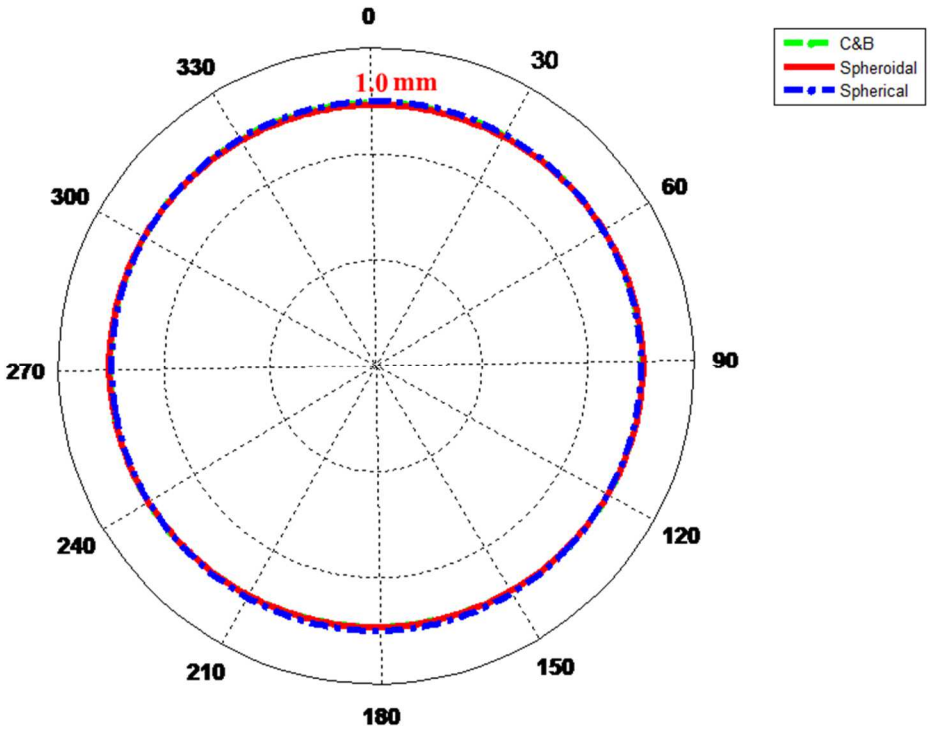

Figure 5.2: Comparison of the modeled drop shapes for D = 1.0 mm.

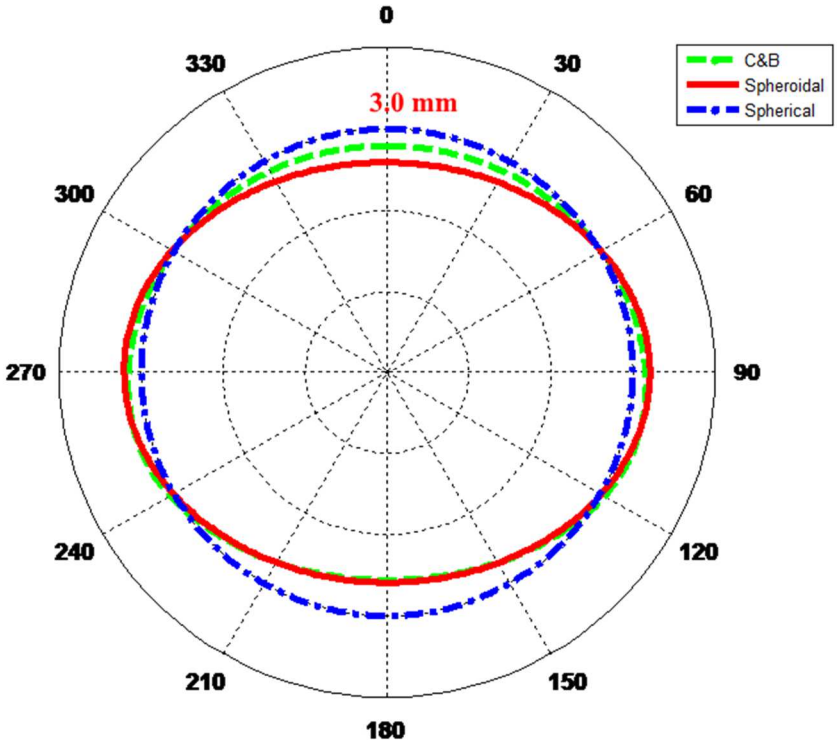

Figure 5.3: Comparison of the modeled drop shapes for D = 3.0 mm.

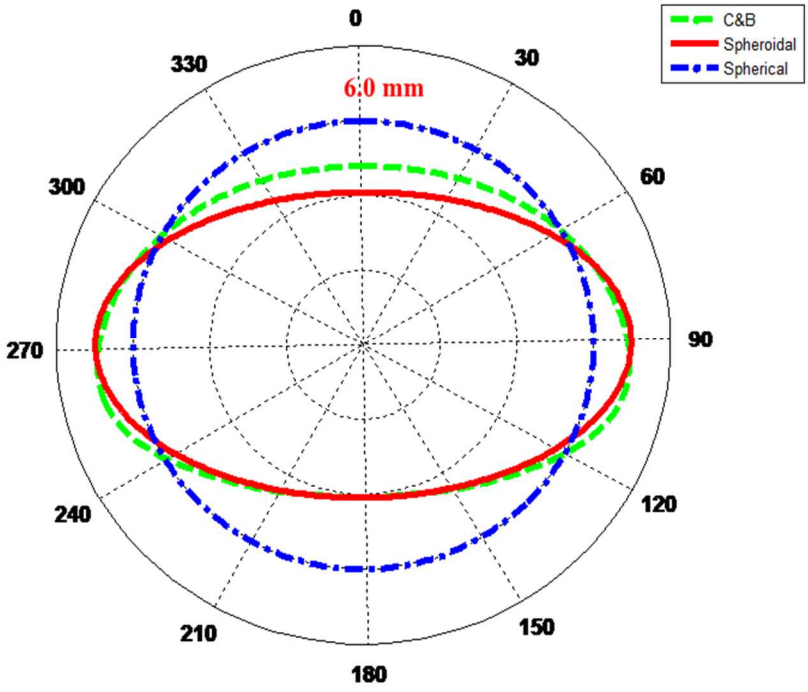

Figure 5.4: Comparison of the modeled drop shapes for D = 6.0 mm.

The initial test considered the simplest case of the scattering characteristics of a sphere with size parameter x (= $2\pi a/\lambda$, where a is the particle radius) equal to 3.0 and refractive index m = $1.33+i10^{-8}$. That is, the same parameters used by reference [7] to generate the results of the scattering amplitude given in its Figure 4.9 were adopted here to reproduce the corresponding results. It should be observed that this approach will be used in all the other comparisons discussed in in the present Chapter. Figure 5.5 shows the co-polar elements S11 and S22 of the scattering matrix as functions of the scattering angle (between the direction of the incident wave and that of interest). Note that the two directions define the scattering plane. The elements S11 or S22 are related to components perpendicular or parallel to the scattering plane, respectively [72]. To compare the results, the open source program WebPlotDigitizer was used to extract the numerical data from Figure 4.9 of reference [7]. The solid and dotted curves correspond to the EBCM and the digitized curves from Figure 4.9 of reference [7], respectively. This Figure shows that the two results are in very good agreement.

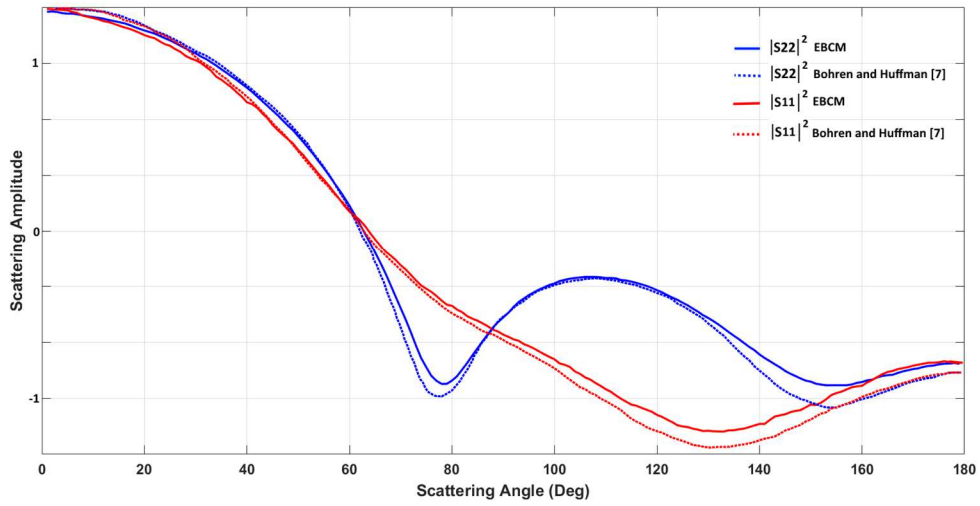

Figure 5.5: Scattering by a sphere with size parameter x (= $2\pi a/\lambda$, where a is the particle radius) equal to 3.0 and refractive index m = $1.33+i10^{-8}$, which were originally used by reference [7] to produce its Figure 4.9. The open source program WebPlotDigitizer was used to extract the numerical data from the original data referenced immediately above.

Another test of the EBCM computer program was done by comparison of calculated scattering parameters due to different spheres with the corresponding ones shown in Figures 14, 15a, 15c, and 15d of Chapter 2 of reference [72]. Each one of the Figures

wwas again reproduced using the open source program WebPlotDigitizer. Figure 5.6 compares the corresponding results obtained with the EBCM and by the immediately above reference. The EBCM results are in good agreement with the corresponding ones reported by reference [72].

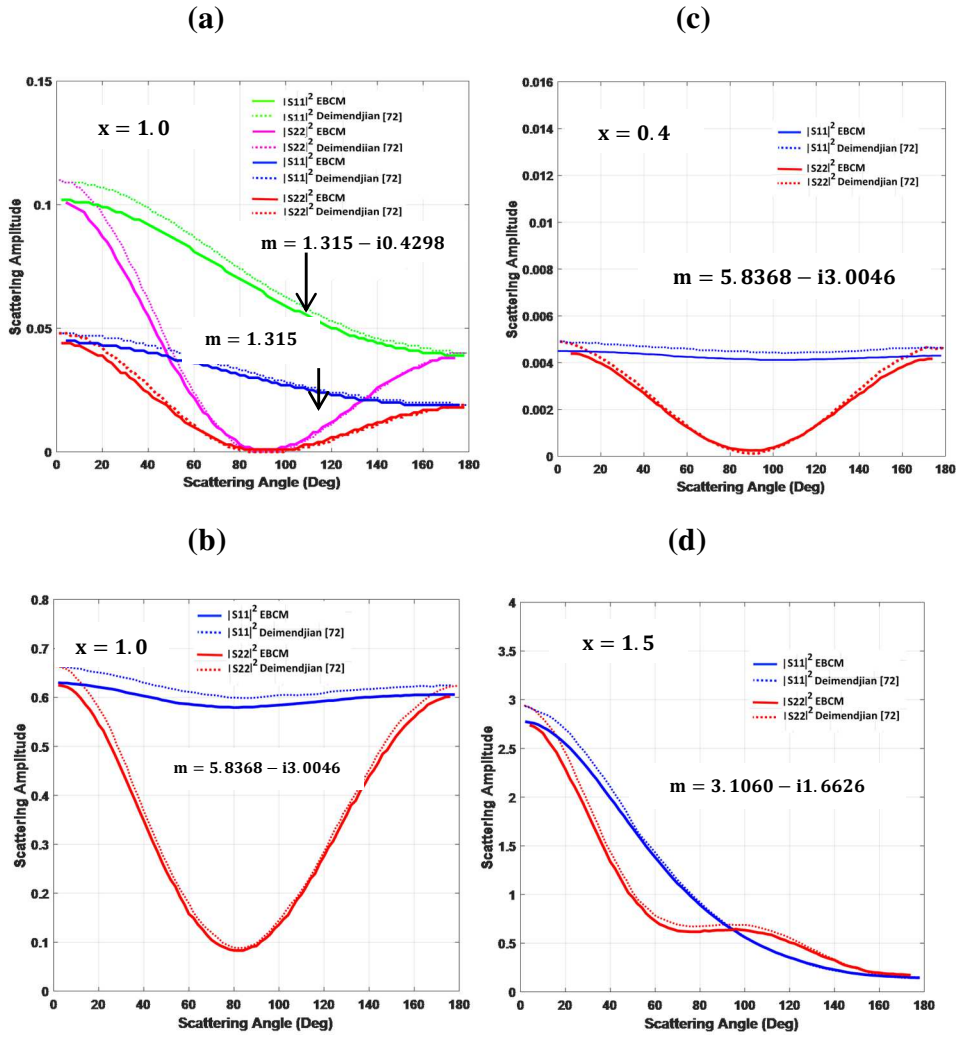

Figure 5.6: Angular distributions of the matrix elements $|S11|^2$ and $|S22|^2$ for a sphere computed by the EBCM scattering code, assuming: (a) size parameter x = 1.0 and two different refractive indices m= $\mathbf{1.315 - i0.4298}$ and m = $\mathbf{1.315}$; (b) size parameter x = 1.0 and refractive index m = $\mathbf{5.8368 - i3.0046}$; (c) size parameter x = 0.4 and refractive index m = $\mathbf{5.8368 - i3.0046}$; and (d) size parameter x = 1.5 and refractive index m = $\mathbf{3.1060 - i1.6626}$. These results (continuous lines) agree with the corresponding ones reproduced from reference [72] (dotted lines), using the open source program WebPlotDigitizer.

Additionally, the scattering code was tested for a case in which higher frequencies are considered. The test was made through the calculation of scattering by a homogeneous spherical particle with radius a = 4.999 mm and refraction index $m \approx 2.517 + i0.017$ at 80 GHz, corresponding to the size parameter x = 1.333, as described in Chapter 13 of reference [73]. It should be observed that 80 GHz is located in the upper frequency band of the millimeter wave spectrum being considered for 5G applications [94]. The calculations of the angular distribution of the matrix elements $|S11|^2$ and $|S22|^2$ were obtained by the present EBCM scattering code, as well as by the BHMIE code listed in Appendix A of reference [7]. While the EBCM code is able to consider general axially-symmetric particles, the BHMIE code, based on the Mie Theory, is specialized to spherical particles. The results are shown in Figure 5.7. This Figure is in good agreement with the results illustrated in Figure 4 in Chapter 13 of reference [73] , as noted by the superposition of the associated curves (blue curves from the EBCM scattering code and red symbols from the BHMIE code). Thus, the very good agreement between corresponding results show the applicability of the code for cases of scattering computation at millimeter-wave frequencies.

The above class of tests using spheres confirms the applicability of the code for this particular shape of particles at low and high frequencies.

Continuing the validation procedure, the present EBCM code was used to reproduce the scattering calculations associated with the oblate spheroidal particles that are commonly used in the literature. The first example of this class was used to test the EBCM code with basis on reference [33], considering the case of an oblate spheroid with symmetry axis along the Z axis, as shown in Figure 5.8 (a). The incident wave propagates in the direction $\hat{k}_i$. The angle of incidence θ_i is defined by that between $\hat{k}_i$ and the Z axis and φ_i represents the corresponding azimuth angle. In the present example, $\theta_i = 0°, 45°, \text{and } 90°$, but the azimuth φ_i was kept fixed at 0°. The spherical coordinate system (θ, φ) refers to the direction of a far-field observation point.

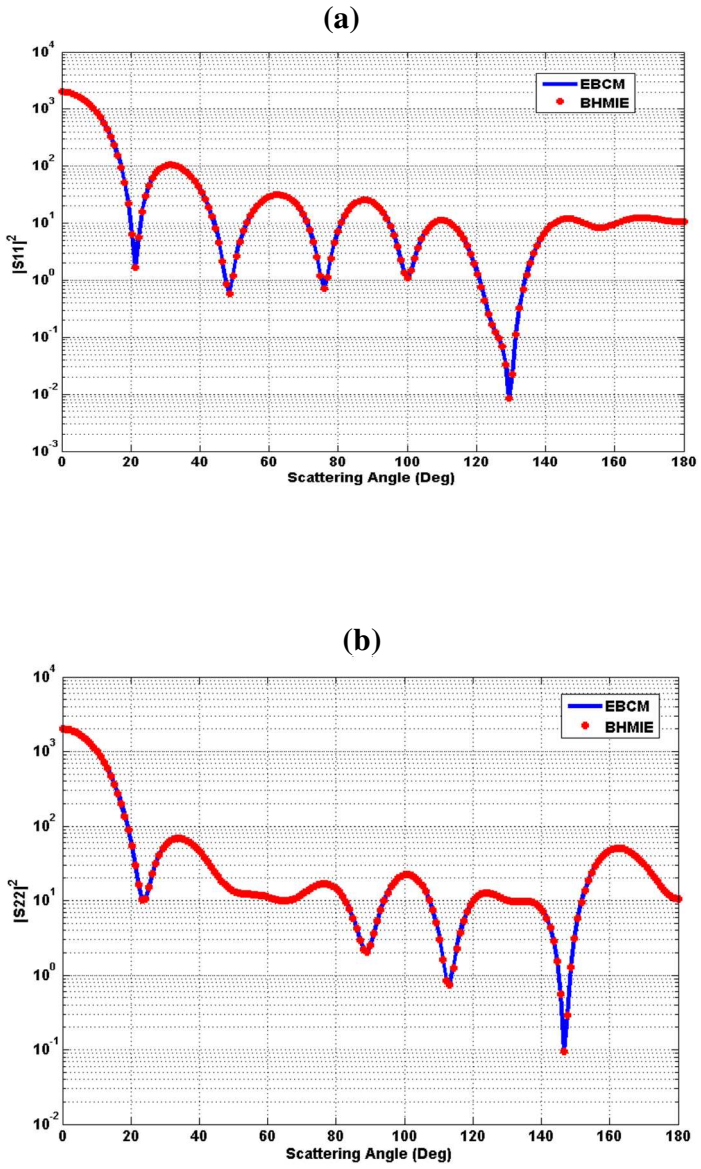

Figure 5.7: Comparison of between the results from the EBCM scattering code (blue curves) and the BHMIE code (red symbols, based on the Mie solution for spherical particles; available in **Appendix A of reference [7]**) to compute matrix elements: (a) $|\boldsymbol{S11}|^2$ and (b) $|\boldsymbol{S22}|^2$ for a sphere with radius a = 4.999 mm and refraction index $\boldsymbol{m \approx 2.517 + i0.017}$ at 80 GHz.

The right side of the Figure 5.8 (b) (scattering angle θ+180º, with 0º ≤ θ ≤ 180º) shows the corresponding intensity function $1/2(|S_{11}|^2 + |S_{12}|^2 + |S_{21}|^2 + |S_{22}|^2)$ for the unpolarized light (with the electric field randomly oscillating in all directions perpendicular to $\hat{k}_i$) and the three different incidence angles $\theta_i = 0°, 45°, \text{and } 90°$, and fixed azimuth angle $\varphi = 0°$, indicating that the scattering unit vector $\hat{k}_s$ points upward,

toward the positive X direction of the X-Z plane, or downward. The left side of the Figure 5.8 (b) (scattering angle θ, with $0^o \leq \theta \leq 180^o$) shows the corresponding scattering curves of the oblate spheroid for the same three different incidence angle of unpolarized light $\theta_i = 0°, 45°, \text{and } 90°$, and fixed azimuth angle $\varphi = 180°$, indicating that the scattering unit vector $\hat{k}_s$ points upward, toward the negative X direction of the X-Z plane, or downward. The code was run using the same parameters specified in [33], where the refractive index is *m* = 1.33, the axial ratio is *a/b* = 3 (*a* is the semi-major axis and *b* is the semi-minor axis) and the size parameter is x = 10. This Figure shows that the resulting curves are in good agreement with the ones displayed in Figure 13 of reference [33]. In particular, the symmetry of the curve corresponding to $\theta_i = 0°$ around the scattering angle 180^o should be noted. It should be noted that, while the EBCM code is able to consider general axially-symmetric particles with flattened bottoms, the formulation of reference [33], based on the Mie Theory, is specialized to spheroidal particles (that is, developed in terms of vector spheroidal wave functions).

As another example of the present class of tests, the present EBCM code was used to generate scattering curves shown in Figure 5 of reference [34] for an oblate spheroid with axial ratio *a/b* = 2.0, several size parameters *x = 1.0*, *5.0*, and *7.0* and angle of incidence $\theta_i = 0°$. Figures 5.9 (a) to 5.9 (c) shows the results of scattering by the oblate spheroids, which are in good agreement with those in the original reference, reproduced in Figures 5.9 (d) to 5.9 (f).

The third example of the present class of tests used in the verification procedure considers the computation of scattering by an oblate spheroid of size parameter $x = 5.0$, axial ratio $a/b = 2.0$ and refraction index $m = 1.33$ for an incident angle $\theta_i = 45°$. Figure 5.10 (a) shows the angular distribution of the intensity function for the unpolarized light $1/2(|S_{11}|^2 + |S_{12}|^2 + |S_{21}|^2 + |S_{22}|^2)$ given in [34]. The Figure shows the resulting angular distribution in three different scattering planes with respect to the incident plane by the present EBCM code, using the same convention adopted by Figure 5.8 (b). The right and left sides of the solid blue line represent the scattering curve in a plane parallel

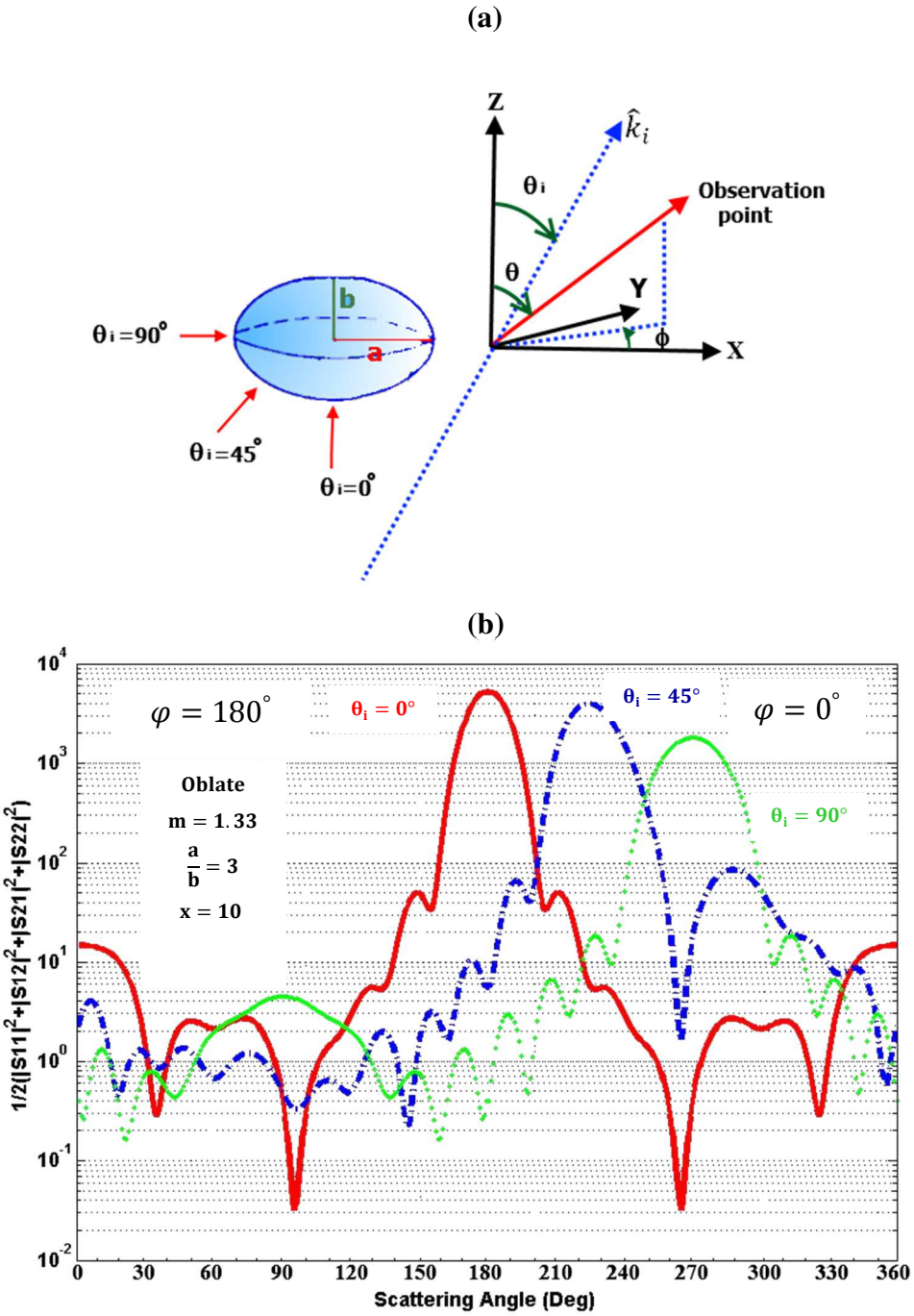

Figure 5.8: (a) Scattering geometry for an oblate spheroidal particle; and (b) Results from the present EBCM scattering code for the angular distribution of the intensities for three different incident waves with incident angles $\boldsymbol{\theta_i = 0°, 45°, \text{and } 90°}$ with scattering plane parallel to the incident plane (φ = 0° and φ = 180°) for an oblate spheroid with refractive index *m* = 1.33, axial ratio *a/b* = 3, and size parameter x = 10. These results are in good agreement with the ones displayed by Figure 13 of reference [33], reproduced in panel (c).

to the incidence plane ($\varphi = 0°$ and $180°$). The right and left sides of the short dashed red line represent the scattering curve in a plane that is inclined from the incidence plane by an angle of $45°$ ($\varphi = 45°$ and $225°$). Finally, the right and left sides of the long dashed green line represent the scattering curve in a plane that is normal to the incident plane ($\varphi = 90°$ and $270°$). It is evident that the original curves in Figure 16 of reference [34], reproduced in Figure 5.10 (b), are in good agreement with the EBCM results.

The same case described in Figure 5.10 was implemented for a particle with the shape suggested by Chuang and Beard [8]. The scattering curves were generated using the specifications given in the above example for incident angles $\theta_i = 45°$ and $135°$. The results are shown in Figure 5.11 for each particle shape. The Figure demonstrates the differences between the scattering properties of the oblate spheroidal and Chuang and Beard particles. Note that many cases [9], [28], [36], [45] of scattering calculations model the particle shapes by oblate spheroids. Figure 5.11 shows that the scattering amplitudes of equal-volume (and relatively large) oblate spheroidal and Chuang and Beard particles may differ by non negligible factors or even orders of magnitude for particular scattering angles. Combined with theoretical calculations and observations of realistic raindrop shapes, these results justify the adopted model of rainfall in the present work.

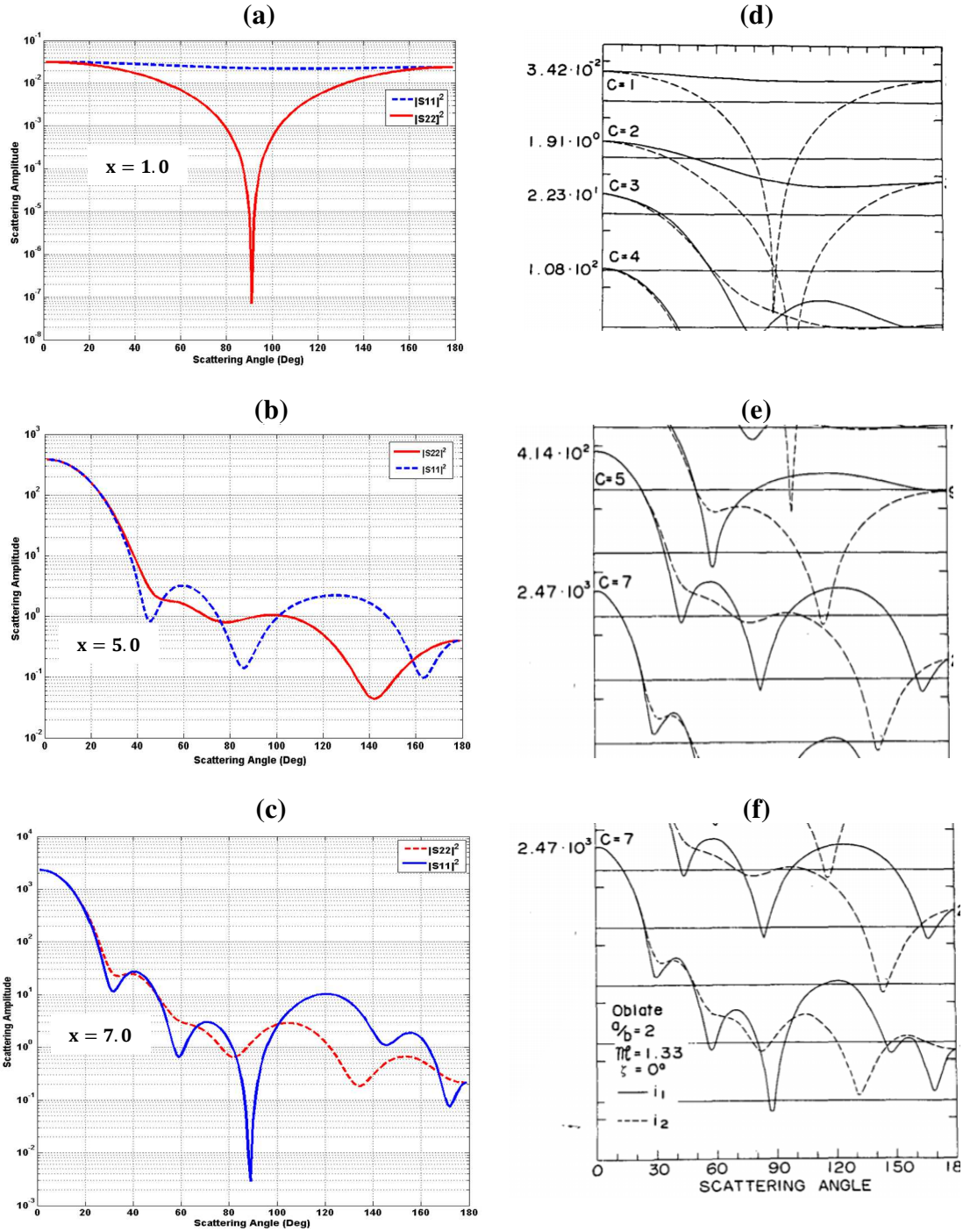

Figure 5.9: Results obtained by the present EBCM scattering code for an oblate spheroid of axial ratio *a/b* = 2, refraction index $\boldsymbol{m = 1.33}$ and size parameters: (a) $\boldsymbol{x = 1.0}$; (b) $\boldsymbol{x = 5.0}$; and (c) $\boldsymbol{x = 7}$, which are in good agreement with the corresponding results (d) to (f), respectively, reproduced from Figure 5 of reference [34]**.**

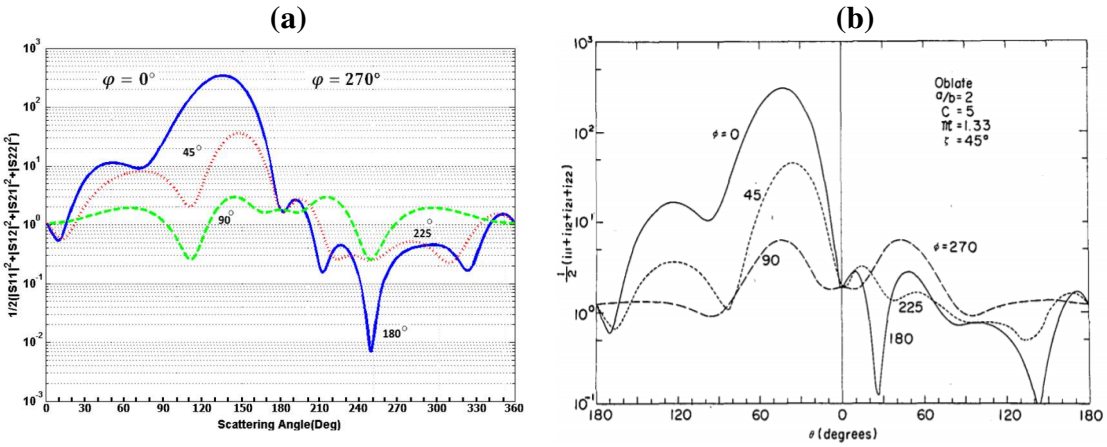

Figure 5.10: (a) Results obtained by the implementation of the EBCM code for the scattering by an oblate spheroid of size parameter x = 5.0, axial ratio *a/b* = 2.0, refraction index m = 1.33, assuming different scattering planes through the Z axis. The results are in good agreement with the original curves in Figure 16 of reference [34], reproduced in panel (b).

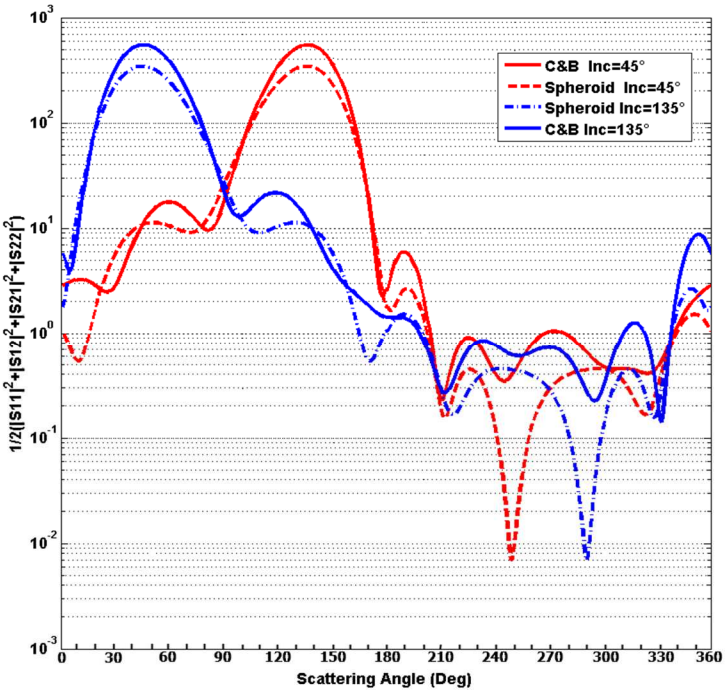

Figure 5.11: Results obtained by the implementation of the EBCM code for the scattering by an oblate spheroid of size parameter x = 5.0, axial ratio *a/b* = 2.0, and refraction index m = 1.33, as well as by the corresponding Chuang and Beard particle [8], assuming different directions of incidence.

So far, the validity check of the computational procedure was made for cases of individual spheres and oblate spheroids, with very good results. Another aspect to test is the applicability of the present EBCM code to compute scattering properties of a cluster of raindrops, a procedure which requires a drop size distribution (DSD). To carry out this test, the case described in Figure 2 of reference [74] was implemented. That is, the scattering cross section per unit volume of a cluster of spherical drops conforming to the Marshall-Palmer DSD was calculated using the EBCM at 19.5 GHz.

Figure 5.12 shows the scattering cross section $|S11|^2$ and $|S22|^2$ for the above cluster and frequency (cm^2/m^3) for different rainfall rates: 5 mm/h, 25 mm/h, 50 mm/h, 100 mm/h, and 200 mm/h. The present results were compared with the ones provided by the Mie theory using the BHMIE code of Appendix A of reference [7]. Note that the BHMIE code, developed to study the scattering properties of a single spherical particle, was extended by the author to also analyze the scattering properties of a cluster of spherical particles which conforms to a specified DSD. The results from both codes are identical. Indeed, the solid and dashed-dotted lines in Figure 5.12 represent the results generated by the EBCM and BHMIE (based on the Mie Theory) codes, respectively. The corresponding results clearly overlap. These results are also in good agreement with the ones obtained in Figure 2 of reference [74], based on an extension of the Rayleigh scattering approximation for frequencies less than 27 GHz. Additionally, the approximations of reference [74] were tested for frequencies higher than 30 GHz, but it was found that they are in fact limited to the frequency range from 10 GHz to 27 GHz, as originally intended. Indeed, the expressions for the coefficients of the approximation $C_{kj}(k = 1 - 4, j = 1 - 4)$ described in [74] were implemented and directly extended to the frequency range 10 GHz to 59 GHz, as graphically shown in Figure 5.13. The fast variations displayed by some of the curves confirm that the original set of coefficients, based on the Rayleigh scattering approximation, is not a suitable solution for scattering problems for frequencies higher than 27 GHz.

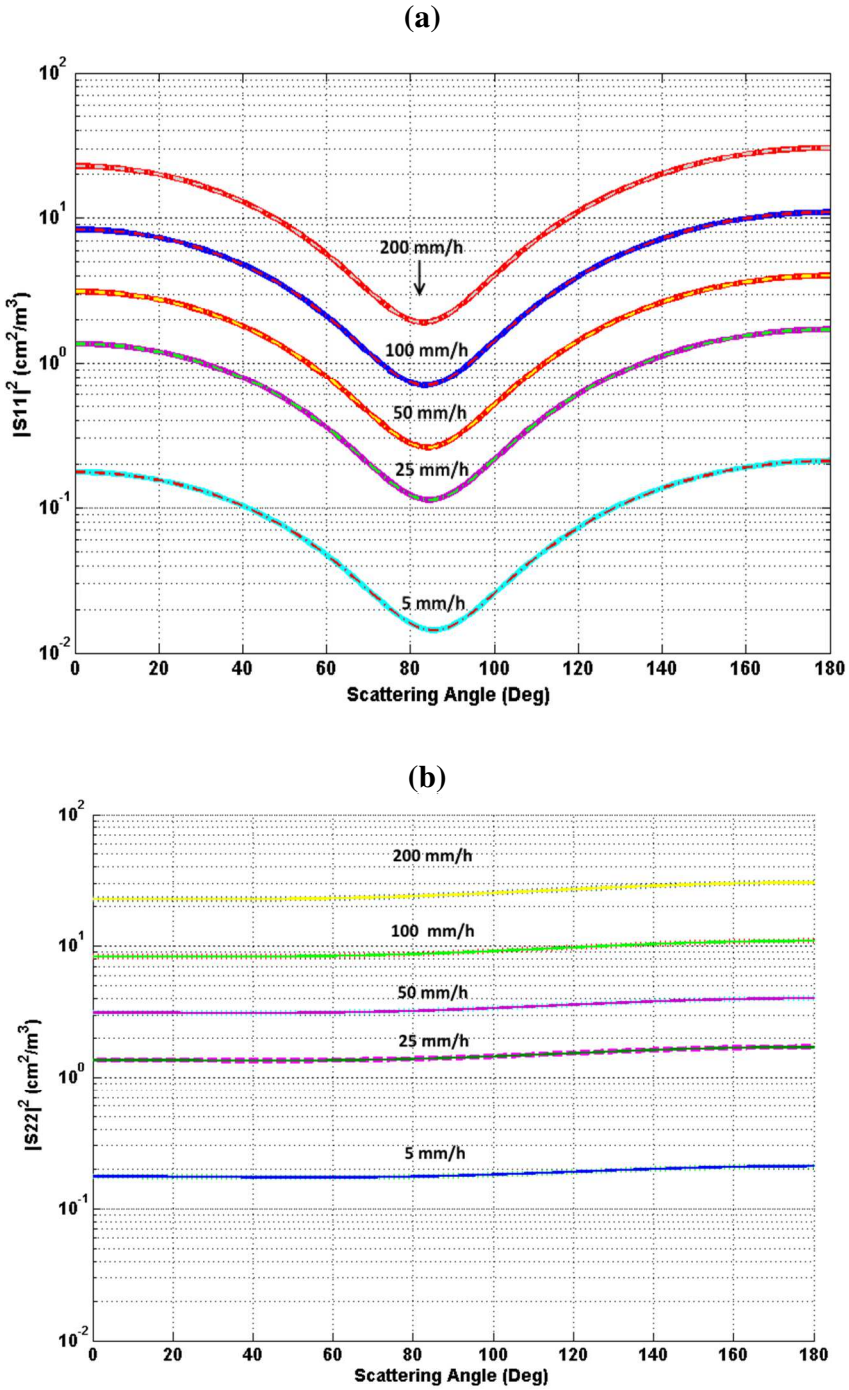

Figure 5.12: Scattering cross section components versus scattering angle at 19.5 GHz and 10° C for different rainfall rates: 5 mm/h, 25 mm/h, 50 mm/h, 100 mm/h, and 200 mm/h. Solid and dashed-dotted curves correspond to the EBCM and BHMIE (Mie Theory) codes, respectively: (a) $|\boldsymbol{S11}|^2$; (b) $|\boldsymbol{S22}|^2$.

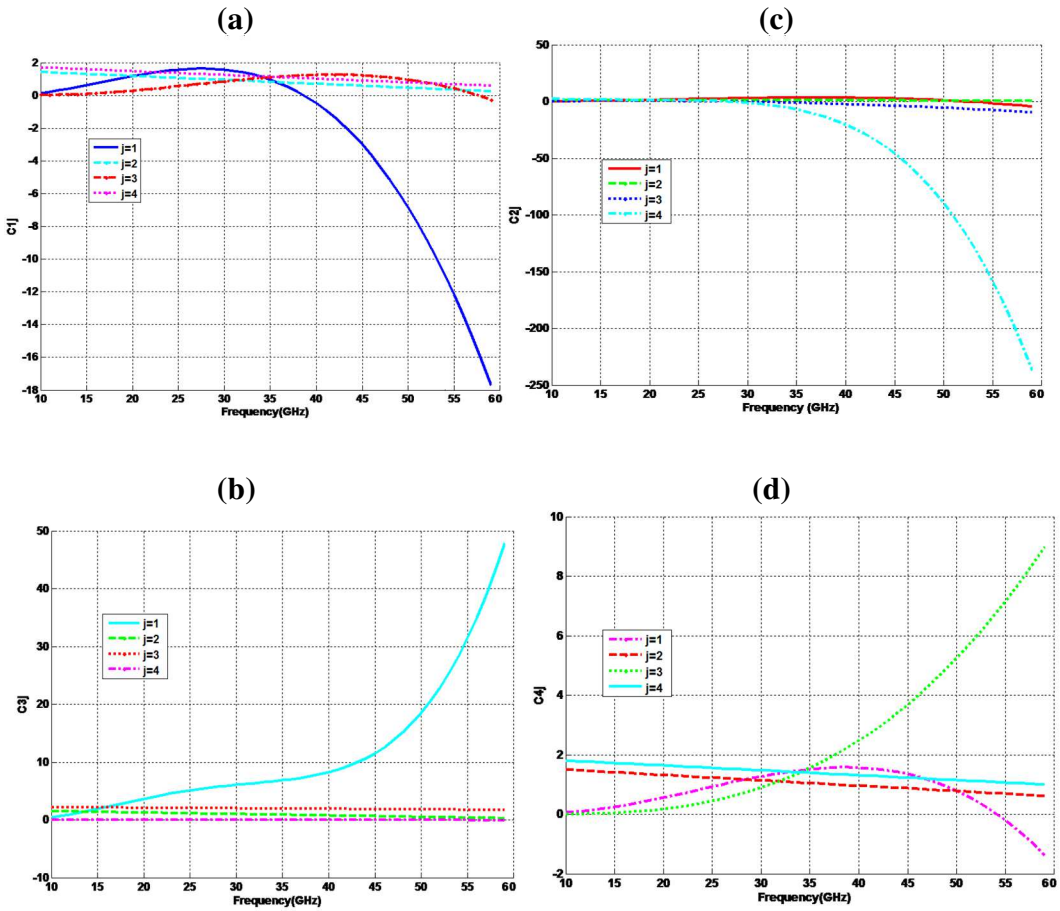

Figure 5.13: Coefficients of the Rayleigh approximation [74] in the range 10 GHz to 59 GHz.

On the other hand, the BHMIE scattering solution and the Extended Boundary Condition Method (EBCM) are applicable for frequencies higher than 30 GHz. This is demonstrated by the Figure 5.14, where the scattering cross section components $|S11|^2$ and $|S22|^2$ (cm^2/m^3) were computed at 40 GHz for a cluster of spherical drops conforming to the Marshall-Palmer DSD and the same rainfall rates: 5 mm/h, 25 mm/h, 50 mm/h, 100 mm/h, and 200 mm/h. Again, the corresponding results (solid and dashed-dotted curves for the EBCM and BHMIE codes, respectively) clearly overlap.

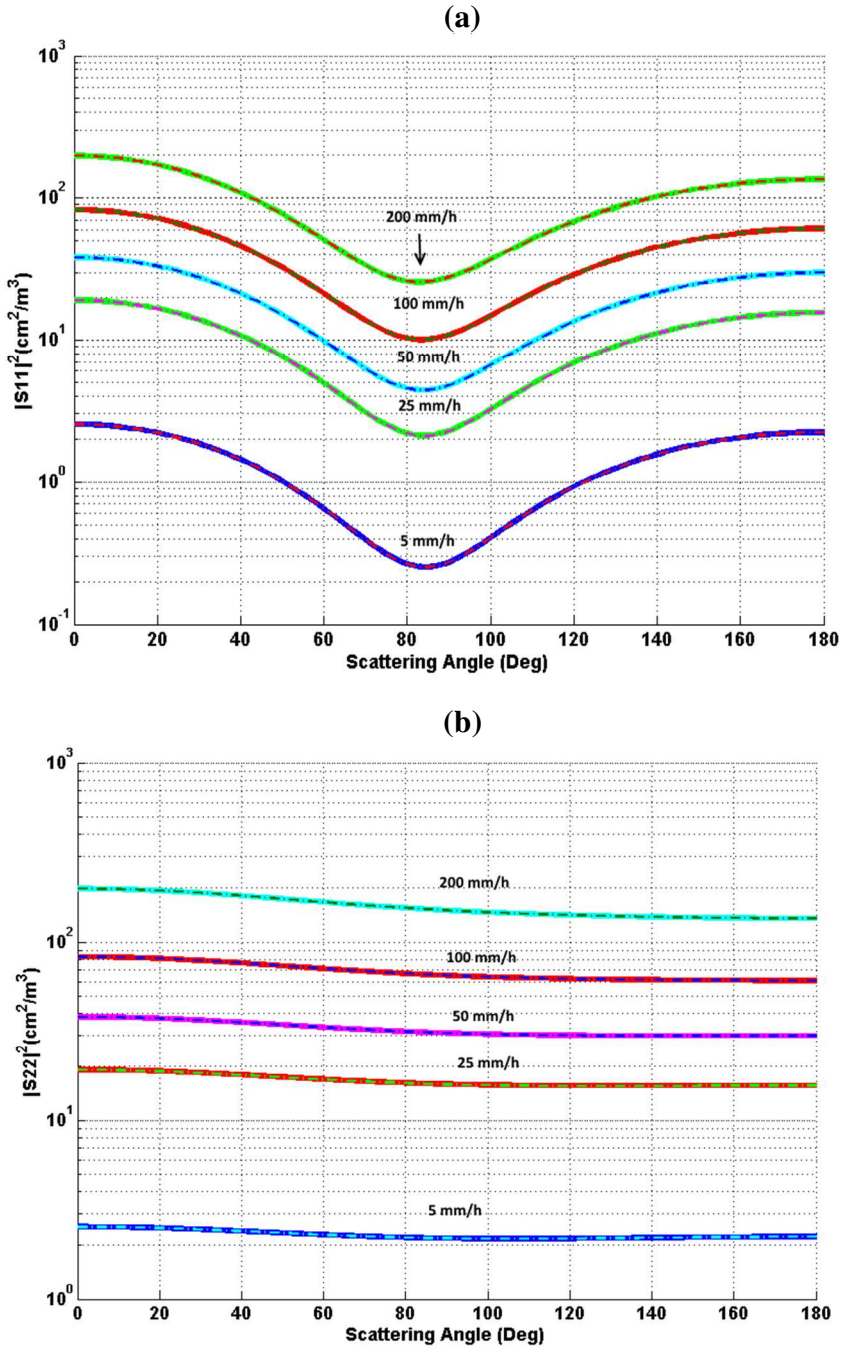

Figure 5.14: Scattering cross section components versus scattering angle at 40 GHz and 10° C for different rain rates: 5 mm/h, 25 mm/h, 50 mm/h, 100 mm/h, and 200 mm/h. Solid and dashed-dotted curves correspond to the EBCM and the BHMIE (Mie theory) codes, respectively: (a)$|\boldsymbol{S11}|^2$; (b)$|\boldsymbol{S22}|^2$.

To complete the verification of the present version of the EBCM code, the study described in reference [43] was reproduced. That is, the cross polarization discrimination of the coherently transmitted linearly polarized wave was computed for canting

spheroidal raindrops at 34.8 GHz. The scattering elements were computed assuming monodisperse oblate spheroidal raindrops with common radius of the equal-volume sphere equal to 3.5 mm, axial ratio equal to 1.6 and refractive index m = 5.048+i2.794. A density of 10 particles/m^3 was assumed. It should be noted that this density is substantially less than the one provided by the de Wolf DSD [12] (equal to 146.24 R$^{0.347}$, where the rainfall rate R is expressed in mm/h). Additionally, the orientation of the axes of the falling raindrops was assumed to conform to the following expression, identical to equation (36) of reference [43]

$$P(\beta) = \frac{1}{2} + P_2(\beta) = \frac{3}{2}\cos^2\beta \tag{5.2}$$

where β is the Eulerian angle which varies in the $[0, \pi]$ interval. Additionally, let Ω be the angle between the average symmetry axis of the particle and the vertical. The latter angle represents the canting angle in the equations (31) to (33) given in [43], which are used to compute the scattering elements. The corresponding results are shown in Figures 5.15 and 5.16 for Ω = 5^o and Ω = 10^o, respectively. The present results are in good agreement with the ones displayed by reference [43].

In summary, the above tests evidently show that the present version of the EBCM code is able to reproduce results available in the literature. Note that the EBCM code is based on a general formulation, which accommodates different axis-symmetric particle shapes, DSDs and distributions of the directions of the axes of symmetry. Even so, it was able to reproduce results from formulations that are "fine-tuned" to particular particle shapes (spherical and spheroidal) and that may not be easily generalized. It also shows the differences between the scattering properties of oblate spheroidal and Chuang and Beard [8] particles. This particular result indicates that, in combination with the realistic rain model proposed in this study, which considers raindrop sizes and associated shapes, their DSD, and distribution of orientations of their symmetry axes, the present version of the EBCM code can be applied to compute the scattering properties of rain at millimeter-wave frequencies.

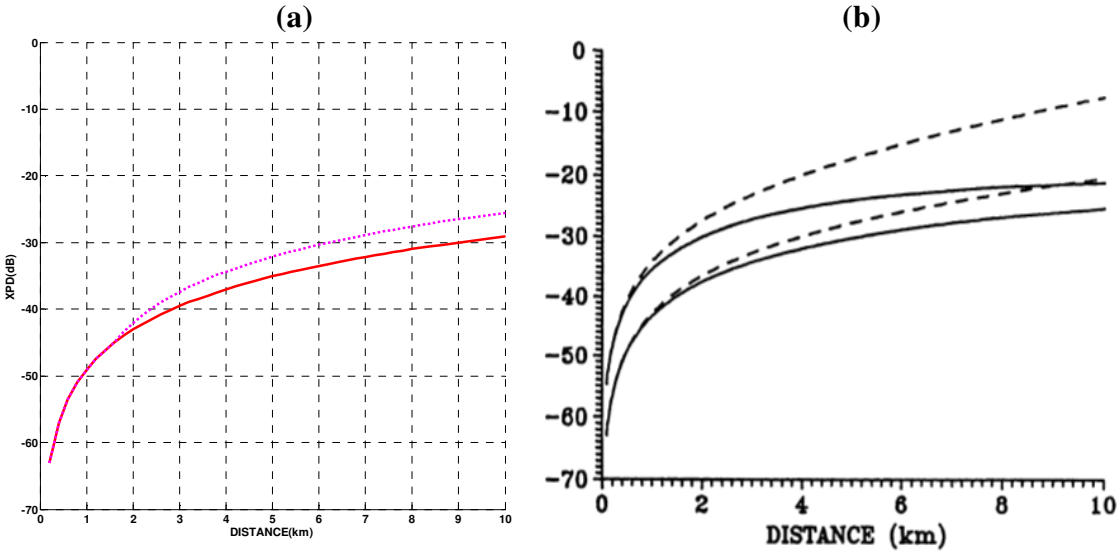

Figure 5.15: (a) Cross-polar discrimination XPD_V (solid line) and XPD_H (dashed line) versus distance for canted spheroidal raindrops with $\boldsymbol{\Omega = 5°}$. These results are in good agreement with the ones displayed by Figure 2 of reference [43], reproduced in panel (b).

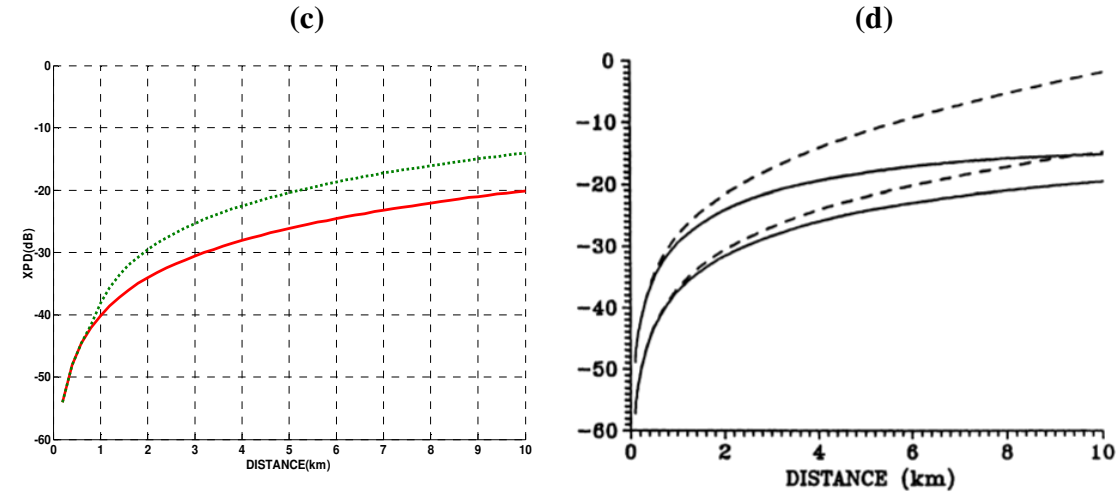

Figure 5.16: (c) Cross-polar discrimination XPD_V (solid line) and XPD_H (dashed line) versus distance for canted spheroidal raindrops with $\Omega = 10°$. These results are in good agreement with the ones displayed by Figure 2 of reference [43], reproduced in panel (d).

6 Estimation of the Rainfall Rate from Radar Measurements

This chapter presents the application of the proposed model described in Chapter 4 to the estimation of the rainfall rate from radar measurements. To test the rain model, the data collected by the CASA OTG X-radar located in Puerto Rico and the X-band radar located in Belém, Brazil are used.

Assume a radar with narrow beam that transmit pulses of duration τ. The received power P_r (watts) due to the scattering by a small volume can be represented by [83]

$$P_r = P_t \frac{\lambda_m^2}{(4\pi)^3} \frac{G^2}{r_m^4} \frac{\sigma_d \, V}{a_{gas} a_{rain}} \frac{1}{2\ln 2} = P_t \frac{\lambda_m^2}{(4\pi)^3} \frac{G^2}{r_m^4} \frac{\sigma_d \left[\pi \left(\frac{r\theta}{2}\right)^2 \left(\frac{c\tau}{2}\right)\right]}{a_{gas} a_{rain}} \frac{1}{2\ln 2} \tag{6.1}$$

$$P_r = \frac{P_t \, \lambda_m^2 \, G^2 \theta^2 c\tau \sigma_d}{1024\pi^2 \ln 2 \, r_m^2 a_{gas} a_{rain}} = \frac{C \, \sigma_d}{r_m^2 a_{gas} a_{rain}}$$

where $C = (P_t \lambda_m^2 \, G^2 \theta^2 c\tau / 1024\pi^2 \ln 2)$ summarizes the characteristics of the radar system, which includes the transmitted power P_t (watts), wavelength λ_m, the antenna gain G, pulse duration τ (s), and the half power beamwidth θ (radians). The differential backscattering cross section is represented by σ_d (m^2/m^3), range r_m , attenuation by the atmospheric gases a_{gas} and attenuation by rain a_{rain}, both dimensionless. The above equation takes attenuation effects into account.

In the Rayleigh scattering limit (particle sizes much less than the wavelength), the differential backscattering cross section σ_d (m^2/m^3) can be expressed by [82], [90]

$$\sigma_d = \frac{2}{3} \frac{\pi^5}{\lambda_m^4} \left| \frac{m^2 - 1}{m^2 + 2} \right|^2 \int_0^\infty D^6 N(D) dD = \frac{2}{3} \frac{\pi^5}{\lambda_m^4} \left| \frac{m^2 - 1}{m^2 + 2} \right|^2 Z \tag{6.2}$$

where m is the refractive index, D is the particle equivalent diameter (mm), $N(D)$ is the DSD ($mm^{-1}m^{-3}$), and Z is the reflectivity (mm^6/m^3). Assuming the exponential Marshall and Palmer DSD [53], [54], represented by expression (3.3) with $N_o = 6.62\times10^3\ R^{0.021}$ ($mm^{-1}m^{-3}$), $p = 0$, $q = 1$, and $\Lambda = 4.1\times10^3\ R^{-0.21}$ (m^{-1}), expression (6.2) yields [83]

$$Z = 200R^{1.6} \quad \rightarrow \quad \sigma_d = \frac{6.12\times10^{-14}}{\lambda_m^4}\left|\frac{m^2-1}{m^2+2}\right|^2 R^{1.6} \tag{6.3}$$

In the above expressions, R is the rainfall rate (mm/h). The right-hand side of expression (6.2) is commonly substituted for σ_d (m^2/m^3) in the radar equation (6.1) to convert the received power P_r into reflectivity Z. This can be trivially done when attenuation effects are neglected ($a_{gas} = a_{rain} = 1$). If necessary, Plan Position Indicator (*PPI*) reflectivity maps may then be converted into rainfall rates using the left-hand side of expression (6.3). Alternatively, the combination of the de Wolf DSD [54], represented by expressions (3.3) to (3.5), with $p = 2.93$ and $q = 1$, with expression (6.2) yields

$$Z = 339.95R^{1.463} \quad \rightarrow \quad \sigma_d = \frac{6.94\times10^{-14}}{\lambda_m^4}\left|\frac{m^2-1}{m^2+2}\right|^2 R^{1.463} \tag{6.4}$$

These expressions may play the same role of equations (6.3). Note that the right-hand sides of equations (6.3) and (6.4) can be expressed in the general form $Z = a_{ZR}R^{b_{ZR}}$.

Neglecting attenuation effects is a better approximation in the S band (around 2.5 GHz) than in the X band (around 10 GHz). To describe attenuation correction procedures, expressions (6.1) and (6.2) will be initially combined

$$Z^e(r_m) = \frac{P_r r_m^2}{\frac{2}{3}\frac{\pi^5}{\lambda_m^4}\left|\frac{m^2-1}{m^2+2}\right|^2 C} a_{gas}a_{rain} = Z^a(r_m)a_{gas}(r_m)a_{rain}(r_m) \tag{6.5}$$

where $Z^{e,a}$ are the estimated and apparent reflectivities (mm^6/m^3), considering or not attenuation effects, as functions of range r_m, for each fixed azimuth. The two-way attenuation due to atmospheric gases or rain along the propagation path between the radar and each rain volume can be written as

$$a_{gas,rain} = e^{2\int_0^r \gamma_{gas,rain}(s)ds} \tag{6.6}$$

where $\gamma_{gas,rain}$ are the specific attenuation factors (Np/km) and distances are measured in km. If the specific attenuation factors are specified in dB/km and distances are measured in m, the two-way attenuation can be expressed as

$$a_{gas,rain}(r_m) = e^{4.605\times10^{-4}\int_0^{rm} \gamma_{gas,rain}(s)ds} \tag{6.7}$$

While γ_{rain} is range-dependent, γ_{gas} is generally remains (or is considered to be) a constant, allowing expression (6.5) to be rearranged in the form

$$Z^e(r_m) = \left[Z^a(r_m)e^{4.605\times10^{-4}\gamma_{gas}r_m}\right]a_{rain}(r_m) = Z^{ag}(r_m)a_{rain}(r_m) \tag{6.8}$$

For each range, the $a_{gas}(r_m)$ term can be combined with $Z^a(r_m)$ by straightforward multiplication, yielding $Z^{ag}(r_m)$, equal to the term between square brackets, indicating the apparent reflectivity after corrections for attenuation by atmospheric gases. According to Hitschfeld and Bordan [75], the maximum value for γ_{gas} in the X band is 0.015 dB/km. This value is consistent with that provided by Annex 2 of the most recent version of Recommendation ITU-R P.676 [84]. Thus, the correction of the reflectivity due to the attenuation due to atmospheric gases in the X band on a two-way propagation along the range of 20 km, which should nonetheless be considered, corresponds to 0.6 dB. In linear units, it is typically less than 14.8 % for the same range.

6.1. Well-established Rain-attenuation Correction Methods

The combination of expressions (6.7) and (6.8) can be written in the alternative forms

$$Z^e(r_m) = Z^{ag}(r_m)e^{4.605\times10^{-4}\int_0^{rm} \gamma_{rain}(s)ds} \tag{6.9}$$

$$R^e(r_m) = R^{ag}(r_m)e^{\frac{4.605\times10^{-4}}{b_{ZR}}\int_0^{rm} \gamma_{rain}(s)ds} \tag{6.10}$$

Except for the coefficients in the exponential terms, these equations are equal. Hitschfeld and Bordan [75] assumed the relationship $\gamma_{rain}(s) = a_{\gamma R}[R^e(s)]^{b_{\gamma R}}$, which is well supported by the literature [55], [80]. Since $R^e(s) = (Z(s)/a_{ZR})^{1/b_{ZR}}$, the previous relationship can be mapped into $\gamma_{rain}(s) = \left(a_{\gamma R}/{a_{ZR}}^{1/b_{ZR}}\right)[Z(s)]^{b_{\gamma R}/b_{ZR}} = a_{\gamma Z}[Z(s)]^{b_{\gamma Z}}$ [86]. These relationships transform equations (6.9) and (6.10) into

$$Z^e(r_m) = Z^{ag}(r_m)e^{4.605\times10^{-4}a_{\gamma Z}\int_0^{r_m}[Z^e(s)]^{b_{\gamma Z}}ds} \tag{6.11}$$

$$R^e(r_m) = R^{ag}(r_m)e^{\frac{4.605\times10^{-4}a_{\gamma R}}{b_{ZR}}\int_0^{r_m}[R^e(s)]^{b_{\gamma R}}ds} \tag{6.12}$$

which can be inverted [75], [86]

$$Z^e(r_m) = \frac{Z^{ag}(r_m)}{\left\{1 - 4.605\times10^{-4}a_{\gamma Z}b_{\gamma Z}\int_0^{r_m}[Z^{ag}(s)]^{b_{\gamma Z}}ds\right\}^{1/b_{\gamma Z}}} \tag{6.13}$$

$$R^e(r_m) = \frac{R^{ag}(r_m)}{\left\{1 - \frac{4.605\times10^{-4}a_{\gamma R}b_{\gamma R}}{b_{ZR}}\int_0^{r_m}[R^{ag}(s)]^{b_{\gamma R}}ds\right\}^{1/b_{\gamma R}}} \tag{6.14}$$

Note that the Hitschfeld and Bordan (HB) method [75] described above diverges if the denominators of expressions (6.13) or (6.14) approach zero. In practice, $Z^{ag}(r_m)$ and $R^{ag}(r_m)$ are available, for each azimuth, as vectors of samples corresponding to range gates (away from the radar). Thus, discrete versions of equations (6.11) to (6.14) should be used. In particular,

$$Z^e_{n+1} = Z^{ag}_{n+1}e^{4.605\times10^{-4}a_{\gamma Z}\left[\sum_{k=1}^{n}\left(Z^e_k\right)^{b_{\gamma Z}}\right]\delta s_m} \tag{6.15}$$

$$R^e_{n+1} = R^{ag}_{n+1}e^{\frac{4.605\times10^{-4}a_{\gamma R}}{b_{ZR}}\left[\sum_{k=1}^{n}\left(R^e_k\right)^{b_{\gamma R}}\right]\delta s_m} \tag{6.16}$$

Assuming that the first sample (closest to the radar, where $n = 0$) is not corrected (that is, $Z^e_1 = Z^{ag}_1$ and $R^e_1 = R^{ag}_1$), as indicated by expressions (6.13) and (6.14), equations (6.15) and (6.16) can be recursively solved for $n \geq 1$ to estimate the desired variables.

The second attenuation correction procedure modifies a combination of the Hitschfeld–Bordan method [75] with the surface reference technique [86]. The original combined method (HB-SRT) was developed to analyze data from the precipitation radar (PR) onboard the Tropical Rainfall Measuring Mission (TRMM) satellite to observe three-dimensional storm structures over the ocean and land [76]. It initially defines the two-way path-integrated attenuation (PIA) to the surface PIA($r = r_s$) by

$$PIA = 10log[A(r_s)] = 10log\left[\frac{Z^e(r_s)}{Z^{ag}(r_s)}\right] \tag{6.17}$$

Allowing for variations of $a_{\gamma Z}$ along the slant path to account for transitions from solid (ice) and mixed to the water (hydrometeor) phases, expressions (6.13) and (6.17) yield the Hitschfeld and Bordan estimate of the PIA

$$PIA_{HB} = -\frac{10}{b_{\gamma Z}} log\left\{1 - 4.605 \times 10^{-4} b_{\gamma Z} \int_0^{r_s} a_{\gamma Z}(s)[Z^{ag}(s)]^{b_{\gamma Z}} ds\right\} \tag{6.18}$$

$$PIA_{HB} = -\frac{10}{b_{\gamma Z}} log(1 - \zeta)$$

where the constant ζ is defined by

$$\zeta = 4.605 \times 10^{-4} b_{\gamma Z} \int_0^{r_s} a_{\gamma Z}(s)[Z^{ag}(s)]^{b_{\gamma Z}} ds \tag{6.19}$$

The objective of the HB-SRT method is to find the best estimate of the PIA. Once this best estimate (PIA_E) is obtained, an attenuation correction factor ε is introduced to modify PIA_{HB} and the Hitschfeld–Bordan correction prescribed by the above expressions in such a way that

$$PIA_E = -\frac{10}{b_{\gamma Z}} log(1 - \varepsilon\zeta) \tag{6.20}$$

and

$$Z^e(r_m) = \frac{Z^{ag}(r_m)}{\left\{1 - 4.605 \times 10^{-4} b_{\gamma Z} \varepsilon \int_0^{r_m} a_{\gamma Z(s)} [Z^{ag}(s)]^{b_{\gamma Z}} ds\right\}^{1/b_{\gamma Z}}} \quad (6.21)$$

The PIA_E is initially equated to $\Delta\sigma$(dB), which represents the measured difference between the average of the surface cross section in rain-free conditions for a given incidence angle and the corresponding value in the presence of rain. From equation (6.20), one gets a superior value for ε

$$\varepsilon_S = \frac{1 - 10^{-b_{\gamma Z}\Delta\sigma/10}}{\zeta} \quad (6.22)$$

On the other hand, if the original ζ value is assumed to be exact, then $PIA_E = PIA_{HB}$ and equations (6.18) and (6.20) provide ε =1. An involved probabilistic formulation then determines PIA_E and the corresponding ε value between 1 and ε_S from ζ and $\Delta\sigma$.

A modified HB-SRT method was developed and implemented by Mora et al. [77] to meet weather-monitoring requirements in Puerto Rico. Currently, a WSR-88D S-band (λ = 10 cm) Doppler radar (better known as Next Generation Radar, NEXRAD), located in Cayey, central part of Puerto Rico, monitors the island´s weather (observation range of 460 km). This Federal Aviation Administration (FAA) radar is operated by the National Weather Service (NWS) office at San Juan. Although widely used over the United States of America, due to the Earth curvature, this type of long-range radar cannot observe 72 % of the lower atmosphere, under 3 km, which is where most dangerous weather events occur. It is also expensive and its spatial (typically 1 km) and temporal resolutions (typically 6 min) do not provide detailed weather data. To overcome these limitations, the National Science Foundation (NSF) Collaborative Adaptive Sensing of the Atmosphere (CASA) Engineering Research Center (ERC) developed a low-cost and reliable X-band dual polarized Doppler radar network [98]. Based on the results from the NSF ERC CASA, the UPRM modified a marine radar and developed an Off-The-Grid (OTG) X-band single-polarized radar network, deployed on Puerto Rico's west coast [81]. This network has three X-band radars that can cover up to 20.48 km in range, with spatial resolution of 20 m. Note that the distance between the Cayey (18º 6´ 43´´ N, 66º 9´ 58´´ W, S band) and Mayaguez (18º 12´ 5´´ N, 67º 8´ 43´´ W, X band) radars is approximately

104 km. On the other hand, while attenuation by atmospheric gases and rain has to be considered in the X band, it may be neglected in the S band (typically less than 1 dB). Considering the scenario described in the present paragraph, the modified HB-SRT method [76] still corrects reflectivity for attenuation effect by using expression (6.21).

Since the radar elevations are low, $a_{\gamma Z}$ can again be assumed to remain constant in expressions (6.19) and (6.21). Initially, $a_{\gamma Z}$ and $b_{\gamma Z}$ are set to 0.00048 and 0.6, respectively [87]. In equation (6.19), r_s now represents, for the associated azimuth, the maximum range of the OTG X-band radar with a volume that is also sampled by the NEXRAD S-band radar. The estimated ε value in the modified HB-SRT method is obtained from equation (6.22), with $\Delta\sigma$ substituted by

$$\Delta Z = Z(S-band) - Z(X-band) \tag{6.23}$$

where the right-hand side reflectivities are measured by the corresponding radars at the common volume located at the maximum range of the OTG X-band radar and ΔZ is also expressed in decibels. To account for the resolution difference between the two radars, the average from 50 last gates of the OTG radar is used in expression (6.23). Data from azimuths associated with non-positive ΔZ values are not corrected. Note that both the HB-SRT method and its modified version essentially adjust the $a_{\gamma Z}$ value adopted by the original HB method. Finally, the estimated reflectivity PPI can be mapped into rainfall rate through the general relationship between Z^e and R^e, with appropriate coefficients [92]

6.2. Application of the EBCM to the Estimation of the Rainfall Rate from Radar Measurements

The first application of the proposed model revisits the forecast by hydrologist and meteorologist through the use of meteorological X-band radars. To mitigate the effect of attenuation on the estimation of the rainfall rate field, a realistic model will be used to estimate the radar backscattering cross section and rain attenuation. This application is based on the Extended Boundary Condition Method (EBCM) and is compared with the HB and modified HB-SRT methods [75]-[77].

This application is based on the direct calculation of the backscattering cross section $\sigma_{duv}(\pi - \theta", \varphi" + \pi; \theta", \varphi")$ (m^2/m^3) of all particles in any unit volume, using the procedure described in Appendix G. In general, the radar scattering cross-section is defined as

$$\sigma_{duv}(\theta, \varphi; \theta'', \varphi'') = \int_0^\infty |\langle S_{uv}^D(\theta, \varphi; \theta'', \varphi'')\rangle|^2 N(D) dD, \quad uv = \theta\theta, \theta\varphi, \varphi\theta, \varphi\varphi \tag{6.24}$$

where uv indicates the polarization of the transmitted and received signal. This quantity is computed as a function of the rainfall rate *R* (mm/h), considering the realistic rain medium described in Chapter 3, specified by: (1) a cluster of raindrops with the shape-size relation proposed by Chuang and Beard [8]; (2) a raindrop size distribution given by de Wolf [12]; (3) the index of refraction of water for a given temperature and frequency suggested by Ray [13]; and (4) a distribution for the orientation of the symmetry axis of the particles. For the sake of completeness, the expressions for the elements *uv = θθ, φφ* of the average scattering matrix (with respect to the distribution of the orientation of the particle symmetry axis, for each equivalent diameter D) that will be used in the present chapter are repeated here:

$$\begin{aligned}\langle S_{\theta\theta}^D(\theta, \varphi; \theta'', \varphi'')\rangle = \frac{1}{k_o}\sum_{n=1}^{\infty}\sum_{n'=1}^{\infty} \alpha_{nn'}\{\tilde{T}_{0nn'}^{22D}\tau_{0n}(\theta)\tau_{0n'}(\theta'') + \\ +2\sum_{m=1}^{N_{min}}[\tilde{T}_{mnn'}^{11D}\pi_{mn'}(\theta'')\,\pi_{mn}(\theta) + \tilde{T}_{mnn'}^{12D}\tau_{mn'}(\theta'')\pi_{mn}(\theta) + \\ +\tilde{T}_{mnn'}^{21D}\pi_{mn'}(\theta'')\tau_{mn}(\theta) + \tilde{T}_{mnn'}^{22D}\tau_{mn'}(\theta'')\tau_{mn}(\theta)]\cos[m(\varphi - \varphi'')]\}\end{aligned} \tag{6.25}$$

$$\begin{aligned}\langle S_{\varphi\varphi}^D(\theta, \varphi; \theta'', \varphi'')\rangle = \frac{1}{k_o}\sum_{n=1}^{\infty}\sum_{n'=1}^{\infty} \alpha_{nn'}\{\tilde{T}_{0nn'}^{21D}\tau_{0n}(\theta)\tau_{0n'}(\theta'') + \\ +2\sum_{m=1}^{N_{min}}[\tilde{T}_{mnn'}^{11D}\tau_{mn'}(\theta'')\,\tau_{mn}(\theta) + \tilde{T}_{mnn'}^{12D}\pi_{mn'}(\theta'')\tau_{mn}(\theta) + \\ +\tilde{T}_{mnn'}^{21D}\tau_{mn'}(\theta'')\pi_{mn}(\theta) + \\ +\tilde{T}_{mnn'}^{22D}\pi_{mn'}(\theta'')\pi_{mn}(\theta)]\cos[m(\varphi - \varphi'')]\}\end{aligned} \tag{6.26}$$

In the above expressions, $\alpha_{nn'} = i^{n'-n-1}\sqrt{\frac{(2n+1)}{n(n+1)}\frac{(2n'+1)}{n'(n'+1)}}$, $N_{min} = \min(n, n')$, and the other terms are defined in Chapter 4.

Calculation of the backscattering cross-sections were made for all particles in a unit volume, as a function of rainfall rate *R*. Illustrative results at three different frequencies are shown in Figure 6.1, in which solid curves correspond to the backscattering cross-sections for vertically polarized incident and scattered field $\sigma_{d\theta\theta} = \sigma_{VV}$ and dashed curves for horizontally polarized incident and scattered field $\sigma_{d\varphi\varphi} = \sigma_{HH}$. These results are compared with predictions based on expression (6.3) (dotted curves). From this Figure, it is noted that σ_{HH} is larger than σ_{VV}. This is due to facts that the backscattering cross-section depends on: (1) the drop shape (with flattened larger particles); and (2) the orientations of their symmetry axes, which are mostly vertical, as was pointed out by [1] and [90].

The expression for the specific attenuation is derived using the same rain model based on the EBCM. The derivation is detailed in Appendix H, which indicates that the specific attenuation for a cluster or raindrops with specified DSD and distribution of random orientation of the symmetry axis, can be calculated by

$$\gamma_{\theta\theta\, rain}(Np/m) = 2\gamma = \frac{4\pi}{k_o^2} Im\left\{\int_0^\infty \sum_{n=1}^{\infty}\sum_{n'=1}^{\infty} \alpha_{nn'}\{\tilde{T}_{0nn'}^{22D}\tau_{0n}(\theta'')\tau_{0n'}(\theta'') + 2\sum_{m=1}^{N_{min}}[\tilde{T}_{mnn'}^{11D}\pi_{mn'}(\theta'')\,\pi_{mn}(\theta'') + \tilde{T}_{mnn'}^{12D}\tau_{mn'}(\theta'')\pi_{mn}(\theta'') + \tilde{T}_{mnn'}^{21D}\pi_{mn'}(\theta'')\tau_{mn}(\theta'') + \tilde{T}_{mnn'}^{22D}\tau_{mn'}(\theta'')\tau_{mn}(\theta'')]\}N(D)dD\right\} \quad (6.27)$$

$$\gamma_{\varphi\varphi\, rain}(Np/m) = 2\gamma = \frac{4\pi}{k_o^2} Im\left\{\int_0^\infty \sum_{n=1}^{\infty}\sum_{n'=1}^{\infty} \alpha_{nn'}\{\tilde{T}_{0nn'}^{22D}\tau_{0n}(\theta'')\tau_{0n'}(\theta'') + 2\sum_{m=1}^{N_{min}}[\tilde{T}_{mnn'}^{11D}\tau_{mn'}(\theta'')\,\tau_{mn}(\theta'') + \tilde{T}_{mnn'}^{12D}\pi_{mn'}(\theta'')\tau_{mn}(\theta'') + \tilde{T}_{mnn'}^{21D}\tau_{mn'}(\theta'')\pi_{mn}(\theta'') + \tilde{T}_{mnn'}^{22D}\pi_{mn'}(\theta'')\pi_{mn}(\theta'')]\}N(D)dD\right\} \quad (6.28)$$

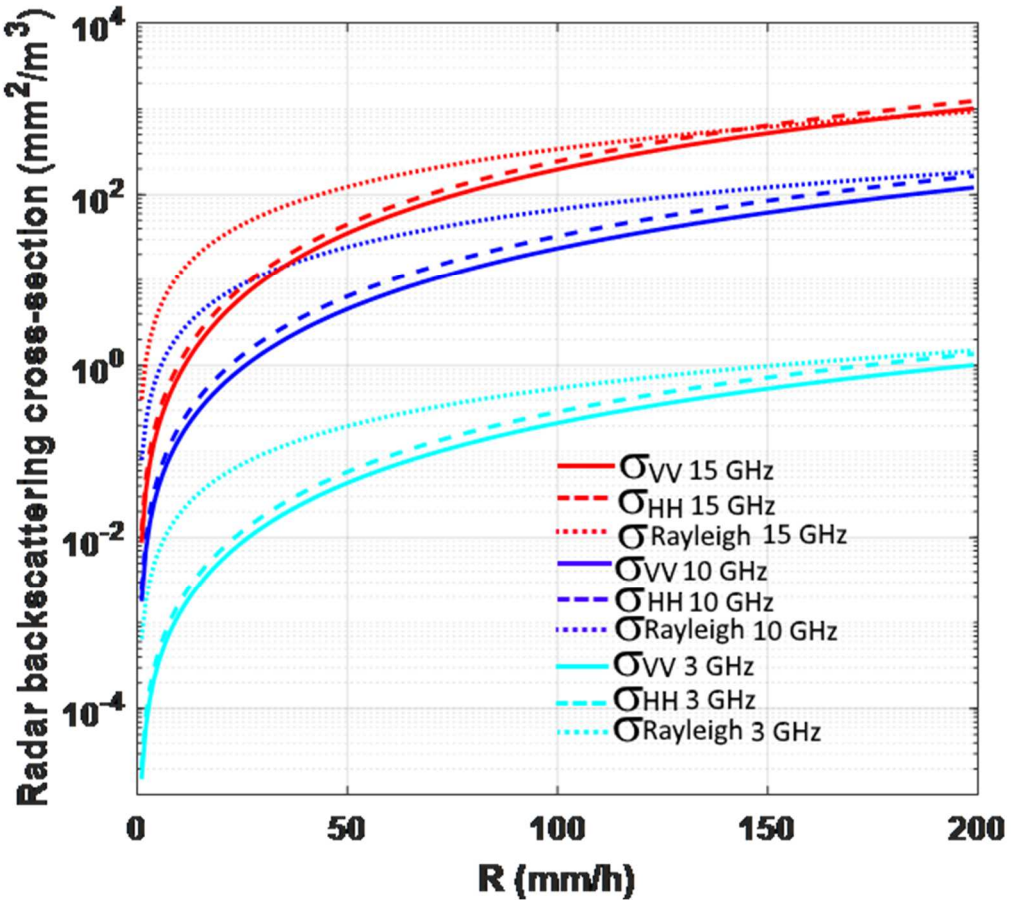

Figure 6.1: Backscattering cross-sections of a rain filled medium for vertical and horizontal polarization, σ_{vv} and σ_{HH}, as functions of the rainfall rates at different frequencies using the realistic rain model based on the EBCM and compared with predictions based on expression (6.3).

The specific attenuation of vertical and horizontal polarizations $\gamma_{uv\,rain}$ were calculated for three different frequencies and compared with results obtained using Recommendation ITU-R P.838-2 [80]. The results are displayed in Figure 6.2 (a) and (b) as functions of the rainfall rate, for different frequencies and polarizations, respectively. It is evident that the two models present differences that can reach 1 dB/km at rainfall rates close to 50 mm/h for the horizontal polarization at 15 GHz. On the other hand, they display a similar behavior for rainfall rates less than approximately 120 mm/h for the vertical polarization. For higher rainfall rates, it was found that the rain model from the Recommendation ITU-R P.838-2 may underestimate the attenuation, in comparison with the EBCM predictions. This results shows the attenuation is larger for horizontal polarization than vertical polarization, as expected.

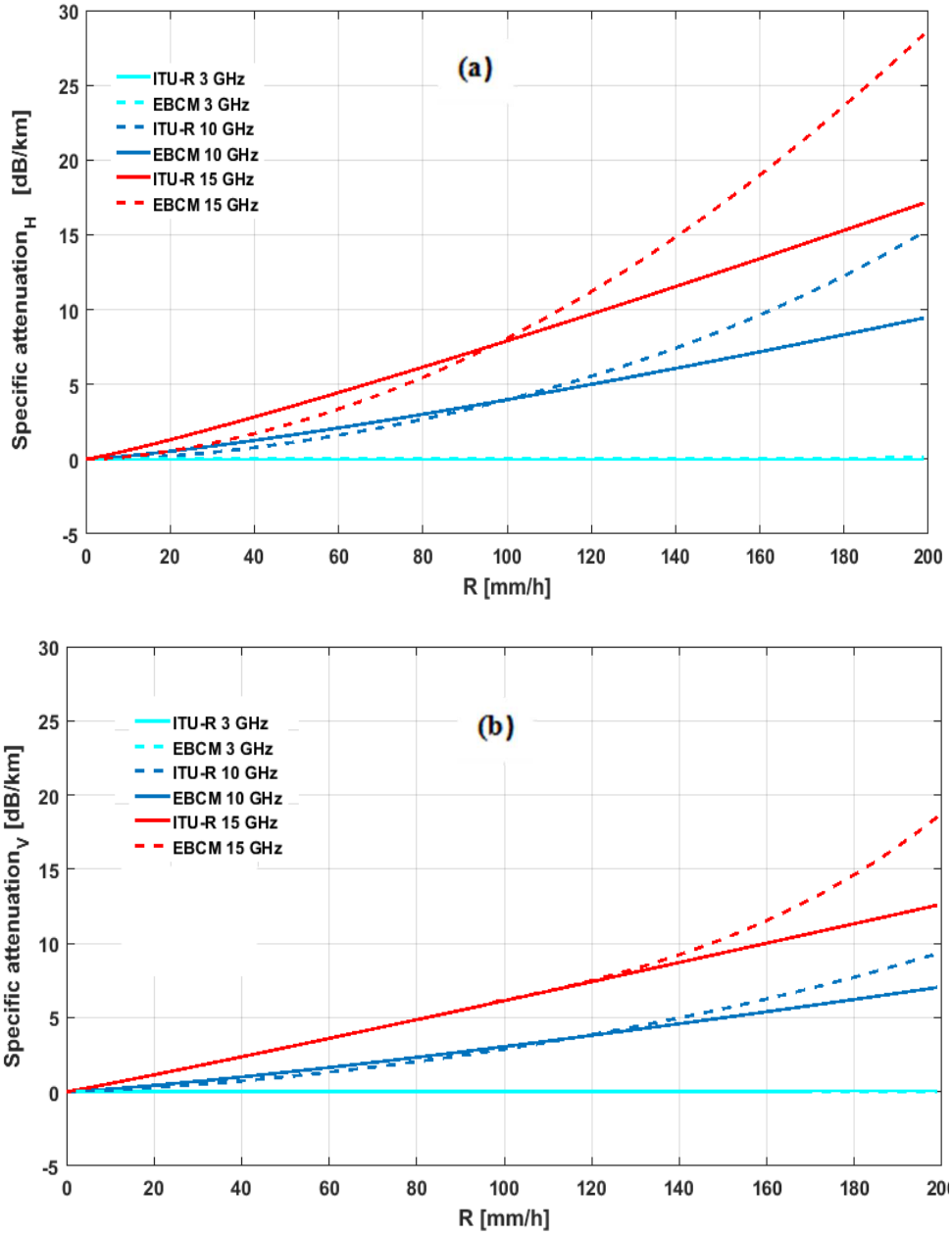

Figure 6.2: Comparison of the specific attenuations for: (a) horizontal and (b) vertical polarizations for different rainfall rates using the model proposed by Recommendation ITU-R P.838-2 [80] and the realistic rain model based on the EBCM.

Combining the formulation of the present section with the discrete version of the radar equation (6.1), one gets

$$\sigma_{duu}(r_{n+1}) = \\ = \frac{\left[P_r(r_{n+1}) r_{n+1}^2 e^{4.605\times10^{-4}\gamma_{gas} r_{n+1}}\right]}{C} e^{4.605\times10^{-4}\left[\sum_{k=1}^{n}\gamma_{rain,k}^{uu}\right]\delta s} \tag{6.29}$$

Assume again that the first sample (closest to the radar, where $n = 0$) is not corrected, as indicated by expression (6.7). Thus, $\sigma_{duu}(r_1) = P_r(r_1)r_1^2/C$ and the corresponding rainfall rate R_1 can be determined from the appropriate curve of Figures 6.1 or 6.2. The combination of equation (6.29) with the same curve can then be recursively solved for $n \geq 1$ to estimate the desired value of the corrected rainfall rate for each range gate.

6.3. Results from the Proposed Model and Comparisons with the Well-Established Methods using Radar Measurements

To test the proposed model, the procedure described immediately above is applied in the post-processing of the data from two different rain events. Subsequently, the estimated rainfall rates are compared with the predictions by the HB [75] and the modified HB-SRT [77] methods. The data were collected from two different X-band radars. The first is the CASA OTG X-band (λ = 3 cm). This single-polarized radar was developed by the Student Led Test Bed (STB) from the University of Puerto Rico, Mayaguez Campus (UPRM), which is part of the NSF Engineering Research Center CASA [81]. An overview of the system can be seen in Figure 6.3 and the main radar parameters are listed in Table 6.1. The radar constant C for this radar is 1850.3 watts/m^3.

Figure 6.3: Overview of the Mayaguez OTG X-band radar system.

Table 6.1: Technical data of the Mayaguez OTG X-band radar.

Frequency	9410 ± 30 MHz
Antenna Type	Parabolic
Antenna Gain	32.4 dB
Beam Width	3.8 degrees
Receiver Dynamic Range	70 dB
Transmitter Tube	Magnetron
Peak Power	4 kW
Pulse Length	0.8 µs
Pulse Repetition Frequency	511 Hz
Polarization	Vertical
Minimum Detectable Signal	-95 dBm
Observation Range	20.48 km

The second is the X-band (λ = 3 cm) METEOR 50DX–Selex radar sited in Belém, Brazil, which is operated by the research group Chuva Project, under the coordination of the Centro de Previsão de Tempo e Estudos Climáticos (CPTEC) do Instituto Nacional de Pesquisas Espaciais (INPE). The radar constant for this radar is 1667.3×10^2 watts/m^3.

Figure 6.4: METEOR 50DX X-band radar installed in Belém, Brazil.

Table 6.2: Technical data of the Belém METEOR 50DX X-band radar.

Frequency	9.375 ± 30 MHz
Antenna Type	Parabolic
Antenna Gain	38.5 dB
Beam Width	2 degrees
Receiver Dynamic Range	90 dB
Transmitter Tube	Magnetron
Peak Power	75 kW
Pulse Length	0.83 μs
Pulse Repetition Frequency	250-2500 Hz selectable
Polarization	Horizontal and Vertical
Minimum Detectable Signal	-110 dBm
Observation Range	100 km

The procedures described in the previous sections were implemented and applied to measurements provided by the two radars, to verify the efficiency of the models to estimate the rainfall rate field, considering the formulations for the backscattering cross section and attenuation correction. The following rain events were selected.

- **Case study: June 28th, 2012 event at 19:41:26 UTC**

The first case was obtained from the CASA OTG X-band radar and the received power data is provided in a binary format. This data is accessed with MATLAB and the received power was directly related with the rainfall rate through the procedure discussed above. This rain event was selected because the corrected data by the modified HB-SRT method was previously validated as explained in [77].

Figure 6.5 shows the comparison between PPIs (Plan Position Indicator) of the predicted rainfall rates: (a) before any attenuation correction; and (b) to (d) after the application of the three attenuation correction post-processing methods. The corrected rainfall rate was compared with the un-attenuated S-band data obtained from the WSR-88D NEXRAD Doppler radar, shown in Figure 6.5 (e). The areas inside the circles in the PPIs of Figures 6.5 (a) to (d) show the same area covered by the WSR-88D NEXRAD Doppler S-band radar. The area marked with a circle in the PPI of Figures 6.5 (e) shows the same area covered by the OTG X-band radar.

It is interesting to note that a visual comparison of Figures 6.5 (c) (the PPI scan of the corrected rainfall rate using the realistic rain model in combination with the EBCM) and 6.5 (b) (the PPI scan of the corrected rainfall rate using the modified HB-SRT method – validated method of attenuation correction) shows similar rain patterns in great part of the common area. However, the estimated values by the former are higher. Additionally, it is evident that the HB method [75], with results displayed by Figure 6.5 (d), underestimates the rainfall rate, in comparison with the other two approaches. On the other hand, the differences between the results obtained by the EBCM and the modified HB-SRT method are credited to fact that the latter also resort to a reference signal at the end of the beam provided by the NEXRAD S-band radar, as described by Mora [77]. Moreover, the two methods assume different rain models.

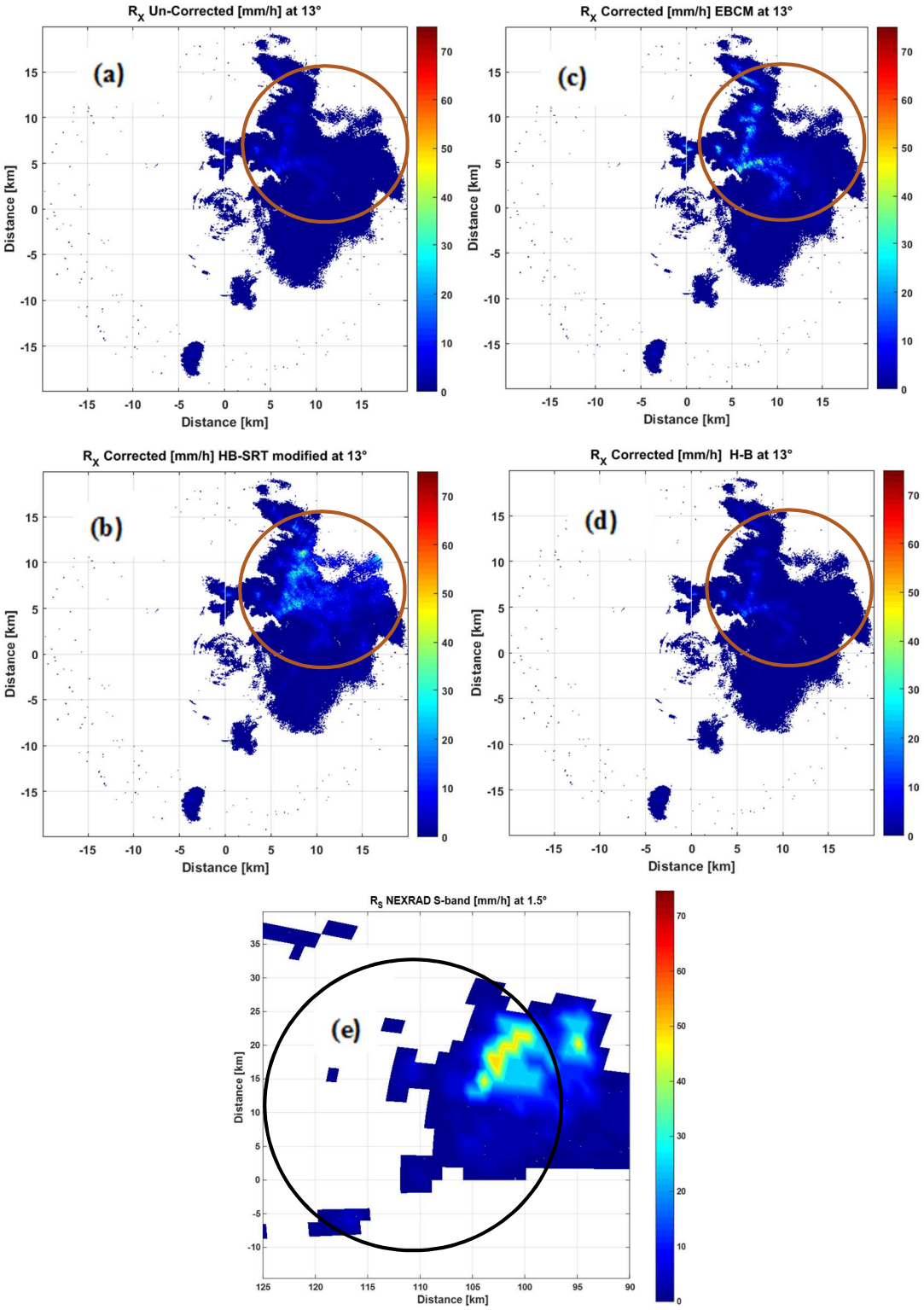

Figure 6.5: PPI scans of the rainfall rate: (a) before attenuation correction with vertical polarization at 13° elevation; (b) corrected by the modified HB-SRT method; (c) corrected by the EBCM; (d) corrected by the HB method; (e) PPI scan WSR-88D NEXRAD S-band measured rainfall rate at 1.5 °.

Figure 6.6 shows the range profiles of the measured and corrected rainfall rates along the propagation path at 13º in elevation and 30.6738 º in azimuth. It is evident that the highest attenuation corrections are obtained using the EBCM and the modified HB-SRT method.

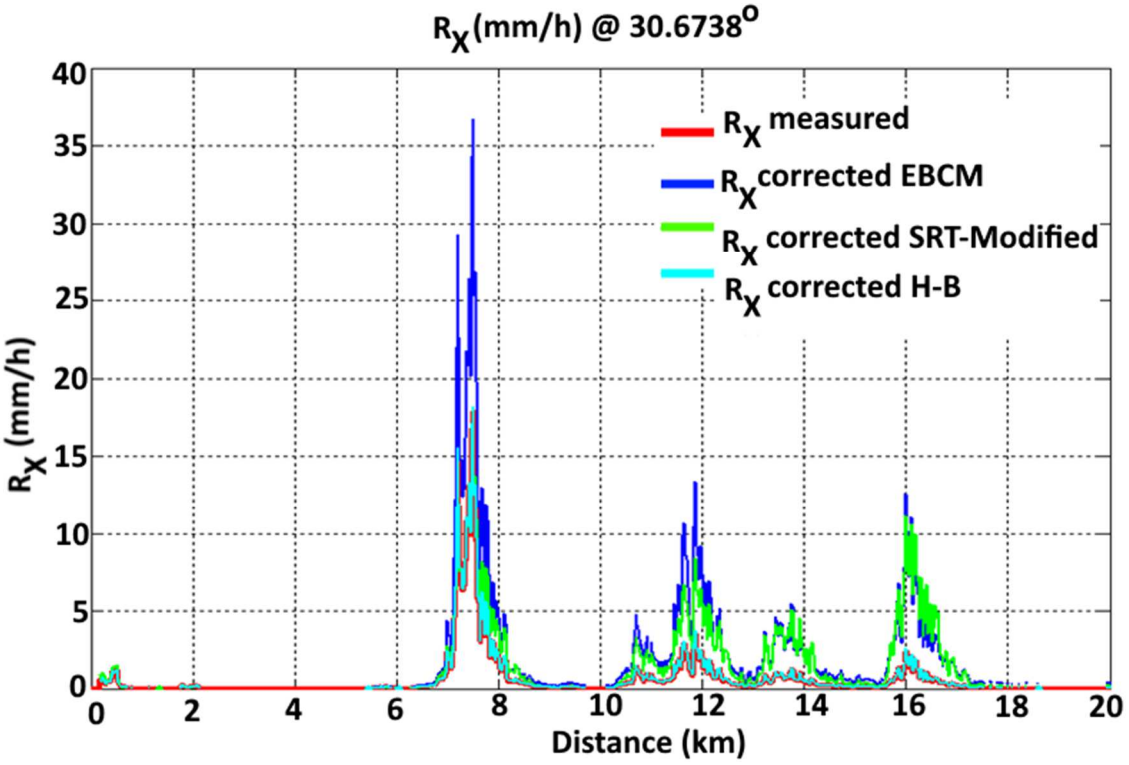

Figure 6.6: Comparison among range profiles of the uncorrected and corrected OTG X-band rainfall rate at 13º in elevation by the EBCM, modified HB-SRT and HB methods.

- **Case study: July 1th, 2011 event at 03:44:08 UTC**

The second case was obtained from the horizontally-polarized channel of the METEOR 50DX–Selex radar installed in Belém, Brazil. The radar data was retrieved from the database of the Chuva Project and is used with permission by the researchers. It is available in a compressed format called Universal Format (UF) and was accessed through a Python module. The data base only provides the uncorrected measured reflectivity, determined by the combination of expressions (6.1) and (6.2), which assumes the Marshall and Palmer DSD, spherical raindrops, as well as the Rayleigh scattering limit. Additionally, it adopts the HB method [75] to correct for rain attenuation effect only. The measured received power is not available. Figures 6.7 (a) and (c) show the

uncorrected and the HB-corrected rainfall rates, respectively. Note that the measured and corrected reflectivities, directly retrieved from the Chuva database, were only mapped into rainfall rates using the left-hand side of expression (6.3) and plotted.

Subsequently, the estimated (corrected) rainfall rate was used to estimate the rain specific attenuation for the horizontal polarization at each range gate, using equation (6.28), which resulted from the EBCM. For each azimuth, the vector of rain specific attenuation was then applied to equation (6.7) to correct the measured rainfall rate observed in Figure 6.7 (a). The EBCM-corrected rainfall rates are shown by Figure 6.7 (b). Note that the rainfall rates in this Figure are higher than those presented by Figure 6.7 (a), indicating that the attenuation correction algorithm based on EBCM is working properly. The red ovals inside the PPIs of Figures 6.7 (b) and (c) indicate areas where the attenuation correction by the HB method may be underestimating the effects of rain attenuation, with respect to the corrections by the EBCM. Indeed, Figure 6.8 plots the measured rainfall rates along the azimuth angle 70.5^{o}, as well as the results from the corrections by the EBCM and the HB method. The curves demonstrate that rainfall rate corrected by the EBCM may present higher values than the ones corrected by the HB method.

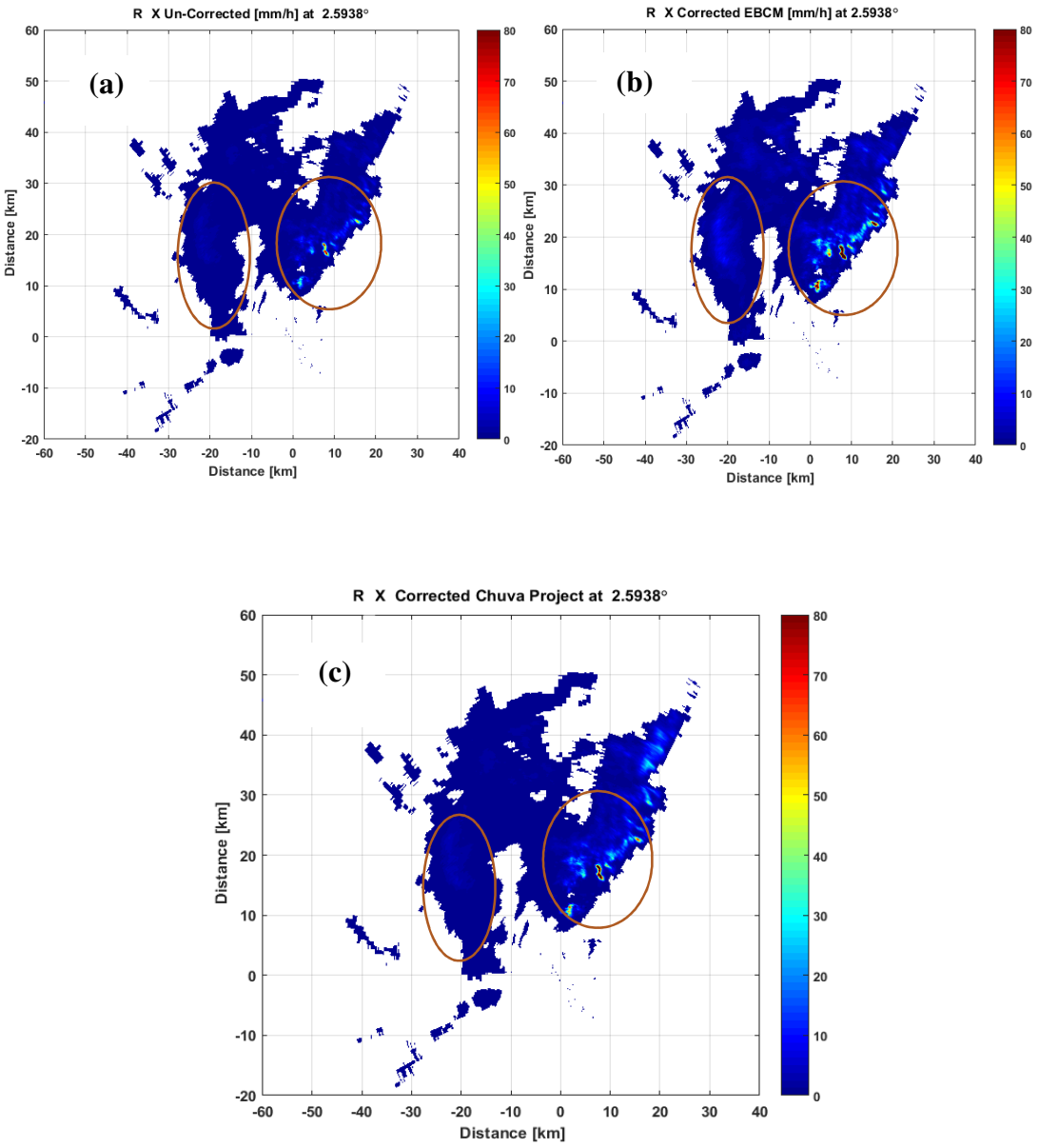

Figure 6.7: (a) PPI scan of the rainfall rate before attenuation correction with horizontal polarization at 2.6º in elevation; (b) PPI scan of the corrected rainfall rate by the EBCM; (c) PPI scan of the corrected rainfall rate by the HB method, adopted by the Chuva Project.

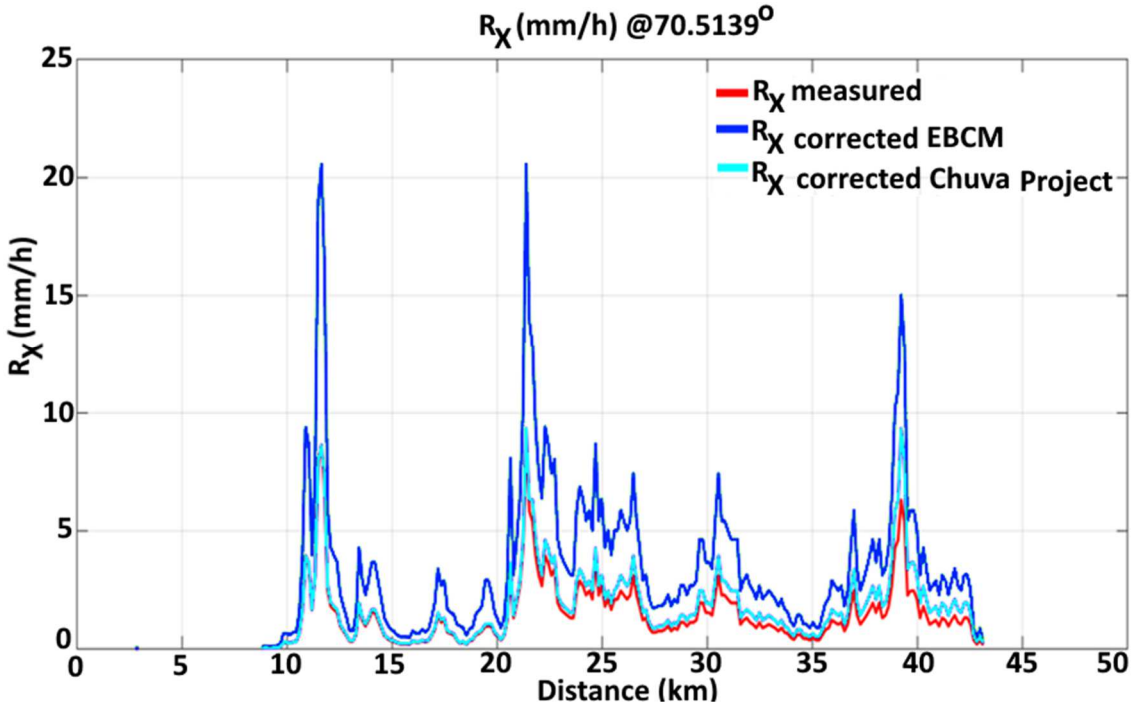

Figure 6.8: Comparison of range profiles of the uncorrected and corrected METEOR 50DX–Selex radar rainfall rate at 2.6° in elevation by the EBCM and the HB method. The latter is adopted by the Chuva Project.

7 The Interference Power into a Receiver Operating at Millimeter-Wave Frequencies

The use of millimeter-wave frequencies in radio links, although extremely promising, introduces many difficulties, particularly if the medium is filled with rain with the characteristics described in Chapter 3. The main difficulties are attenuation, scattering, depolarization and intersystem interference by precipitating particles along the propagation path that can affect the system performance and cause signal degradation. Thus, to design an efficient radio communication system, it is important to evaluate its performance. Among other factors, this evaluation is made through the knowledge of the (C/I) ratio, which is the ratio of the signal power received from the desired station to the interference power caused by the interfering station. In the present study it will be assumed that interference is mainly caused by rain scattering.

In this study, the interference level of systems using the same frequency is quantified by the Bistatic Radar Equation (BRE) and the rain effects are determined by implementing a realistic rain model based on Extended Boundary Condition Method (EBCM), which is detailed in Chapter 4. This realistic and improved model for analysis and quantification of rain-induced interference at 42 GHz and 70 GHz (two of the frequency bands under consideration for use by the fifth generation of cellular mobile communication systems) was implemented for two different urban scenarios. Thus, the signal to interference power ratios was computed for a transmitted signal with vertical and horizontal polarization, respectively.

Herein, the interfering element is formed by the intersection of two antenna beams, resulting in a common volume filled with precipitation particles. Figure 7.1 shows the rain scattering geometry used to compute interference. The transmitted signal is scattered from the direction of propagation, which leads to interference. The interfered power is represented by Pi.

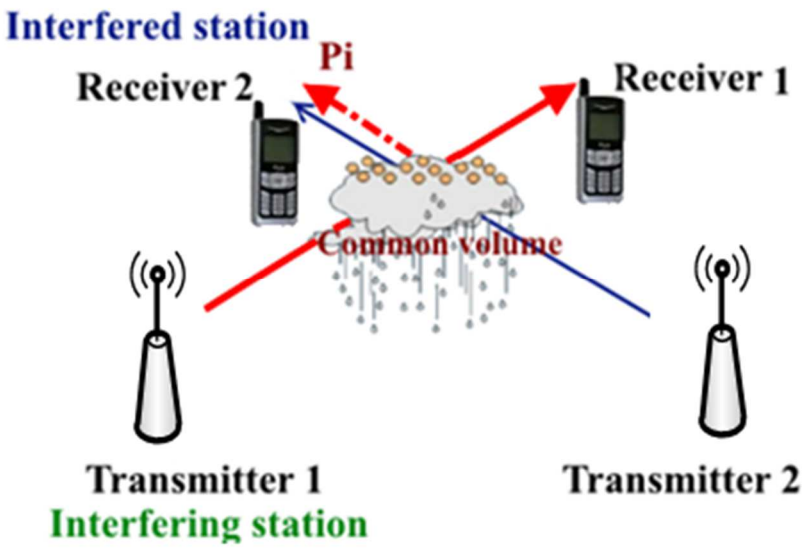

Figure 7.1: Scattering geometry for interference calculations, where Pi is the interference power.

7.1. Rain-Induced Interference Method

To study the effects of rain scattering interference caused by an undesired received signal, the signal to interference ratio (that is, the ratio between the power C of the desired signal and the aggregate interference power I at the desired receiver) is determined by

$$\frac{C}{I} = \frac{P_R}{\sum_{i=1}^{N} P_i} \tag{7.1}$$

where P_R is the received power from the desired station, P_i is the interference power caused by the interfering station i at the same receiver and N is the number of interfering stations. The desired power of a radio link is computed by the modified Friis transmission equation

$$P_R = P_T + G_T + G_R - L_S - L_G - L_R \tag{7.2}$$

where P_R(dB) is the desired power at the receiver, P_t(dB) is the transmitted power, G_t(dB) is the gain of the transmitting antenna, G_R(dB) is the gain of the receiving antenna, L_S(dB) is the free space loss, L_G (dB) is the attenuation by atmospheric gases and L_R (dB) is the attenuation due to rain.

The free space loss is obtained by the following equation

$$L_S = 20\log_{10}(d) + 20\log_{10}(f) + 92.45 \tag{7.3}$$

where d (km) is the distance between transmitter and receiver and f (GHz) is the system operating frequency.

The attenuation of the transmitted signals by gaseous absorption (water vapor and oxygen) L_G (dB) can be estimated by the model proposed by Recommendation ITU-R P.676-11 [84]. The total attenuation by gaseous absorption is based on the following formula

$$L_G = \gamma d = (\gamma_o + \gamma_w)d \tag{7.4}$$

where d (m) is the path length, γ_o (dB/m) is the specific attenuation due to oxygen and γ_w (dB/m) is the specific attenuation due to water vapor. Values of γ_o and γ_w can be estimated implementing the simplified algorithms given in Annex 2 of the Recommendation ITU-R 676-11[84].

Rain attenuation is estimated using the method based on the EBCM described in Appendix H. Thus, the co-polarized and cross-polarized components of the specific rain attenuation are given by

$$\begin{aligned}\gamma_{\theta\theta\,rain}(Np/m) = \frac{4\pi}{k_o^2} Im\Bigg\{\sum_{n=1}^{\infty}\sum_{n'=1}^{\infty} \alpha_{nn'}\{\langle\tilde{T}^{22}_{0nn'}\rangle\tau_{0n}(\theta'')\tau_{0n'}(\theta'') + \\ +2\sum_{m=1}^{N_{min}}[\langle\tilde{T}^{11}_{mnn'}\rangle\pi_{mn'}(\theta'')\,\pi_{mn}(\theta") + \langle\tilde{T}^{12}_{mnn'}\rangle\tau_{mn'}(\theta'')\pi_{mn}(\theta'') + \\ +\langle\tilde{T}^{21}_{mnn'}\rangle\pi_{mn'}(\theta'')\tau_{mn}(\theta'')+\langle\tilde{T}^{22}_{mnn'}\rangle\tau_{mn'}(\theta'')\tau_{mn}(\theta'')]\}\Bigg\}\end{aligned} \tag{7.5}$$

$$\gamma_{\theta\varphi\,rain}(Np/m) = \frac{4\pi}{k_o^2} Im\left\{\sum_{n=1}^{\infty}\sum_{n'=1}^{\infty}\alpha_{nn'}\left\{\frac{1}{i}\langle\tilde{T}_{mnn'}^{21D}\rangle\tau_{0n}(\theta'')\tau_{0n'}(\theta'') + \right.\right.$$

$$+2\sum_{m=1}^{N_{min}}[\langle\tilde{T}_{mnn'}^{11D}\rangle\pi_{mn'}(\theta'')\,\pi_{mn}(\theta'') + \langle\tilde{T}_{mnn'}^{12D}\rangle\tau_{mn'}(\theta'')\pi_{mn}(\theta'') + \tag{7.6}$$

$$\left.\left.+\langle\tilde{T}_{mnn'}^{21D}\rangle\tau_{mn'}(\theta'')\tau_{mn}(\theta'')+\langle\tilde{T}_{mnn'}^{22D}\rangle\pi_{mn'}(\theta'')\tau_{mn}(\theta'')]\right\}\right\}$$

$$\gamma_{\varphi\theta\,rain}(Np/m) = \frac{4\pi}{k_o^2} Im\left\{\sum_{n=1}^{\infty}\sum_{n'=1}^{\infty}\alpha_{nn'}\{\langle\tilde{T}_{mnn'}^{21D}\rangle\tau_{0n}(\theta'')\tau_{0n'}(\theta'') - \right.$$

$$-2\sum_{m=1}^{N_{min}}[\langle\tilde{T}_{mnn'}^{11D}\rangle\,\pi_{mn'}(\theta'')\tau_{mn}(\theta'') + \langle\tilde{T}_{mnn'}^{12D}\rangle\tau_{mn'}(\theta'')\tau_{mn}(\theta'') + \tag{7.7}$$

$$\left.\left.+\langle\tilde{T}_{mnn'}^{21D}\rangle\pi_{mn'}(\theta'')\pi_{mn}(\theta'')+\langle\tilde{T}_{mnn'}^{22D}\rangle\tau_{mn'}(\theta'')\pi_{mn}(\theta'')]\right\}\right\}$$

$$\gamma_{\varphi\varphi\,rain}(Np/m) = \frac{4\pi}{k_o^2} Im\left\{\sum_{n=1}^{\infty}\sum_{n'=1}^{\infty}\alpha_{nn'}\{\langle\tilde{T}_{0nn'}^{11}\rangle\tau_{0n}(\theta'')\tau_{0n'}(\theta'') + \right.$$

$$+2\sum_{m=1}^{N_{min}}[\langle\tilde{T}_{mnn'}^{11}\rangle\tau_{mn'}(\theta'')\,\tau_{mn}(\theta'') + \langle\tilde{T}_{mnn'}^{12}\rangle\pi_{mn'}(\theta'')\tau_{mn}(\theta'') + \tag{7.8}$$

$$\left.\left.+\langle\tilde{T}_{mnn'}^{21}\rangle\tau_{mn'}(\theta'')\pi_{mn}(\theta'')+\langle\tilde{T}_{mnn'}^{22}\rangle\pi_{mn'}(\theta'')\pi_{mn}(\theta'')]\right\}\right\}$$

$$\alpha_{nn'} = i^{n'-n-1}\sqrt{\frac{(2n+1)(2n'+1)}{n(n+1)n'(n'+1)}}$$

where the elements $\langle\tilde{T}_{mnn'}^{klD}\rangle$ are determined by using equation (F.19).

For a vertically polarized transmitted signal, rain attenuation L_R(dB) for a distance d (m) can be estimated by the following formula

$$L_R = \frac{\gamma_{\theta\theta\,rain}}{\ln(10)}d \tag{7.9}$$

For a horizontally polarized transmitted signal, rain attenuation L_R(dB) can be estimated for a distance d (m) by the following formula

$$L_R = \frac{\gamma_{\varphi\varphi\, rain}}{\ln(10)} d \tag{7.10}$$

The interference power due to rain scattering at the interfered station can be estimated by the Bistatic Radar Equation (BRE) [18],[82], which is expressed as:

$$P_i = P_T \frac{\lambda^2}{(4\pi)^3} \int_V \frac{G_T G_R A_T A_R}{{R_{Ti}}^2 {R_{Ri}}^2} \sigma_{bi}\, dV \tag{7.11}$$

where P_i is the received power at the interfered station due to rain scatter (watts), P_T is the power transmitted by the interfering station (watts), λ is the wavelength (meters), G_T antenna gain of the interfering station, G_R antenna gain of the interfered station, A_T is the attenuation along the path from the interfering station to an elementary volume dV inside the common volume, A_R is the attenuation from dV to the interfered station, R_{Ti} is the distance (meters)from the interfering station to dV, R_{Ri} is the distance from dV to the interfered station (meters), σ_{bi} is the scattering cross section per unit volume at each point in the common volume (m^2/m^3).

The scattering cross section per unit volume is estimated using the realistic rain model based on EBCM, which is explained in detail in Appendix G. The scattering cross section per unit volume can be expressed as

$$\sigma_{bi}(\theta, \varphi; \theta'', \varphi'') = \int_0^\infty |\langle S_{uv}^D(\theta, \varphi; \theta'', \varphi'')\rangle|^2 N(D) dD \tag{7.12}$$

$$uv = \theta\theta, \theta\varphi, \varphi\theta, \varphi\varphi$$

where the angles (θ'', φ'') represent the scattered direction due to an incident field in a given (θ, φ) direction, the subscripts uv indicate the polarization for the incident and scattered field, $\langle S_{uv}^D(\theta, \varphi; \theta'', \varphi'')\rangle$ are the elements of the orientationally averaged

scattering amplitude matrix for a particle of equivalent diameter D. The mentioned elements can be determined by using equations (G.27) - (G.30).

For urban environments, the common volume between two directional beams can be modeled as a rectangular prism, with area of the base given by the street corners shown in Figure 7.2 and height limited by the antenna sector-shaped radiation pattern. This common volume is subdivided in smaller volumes. As short distances (typically 200 m) are considered, a constant rainfall rate is assumed inside this scattering volume. It is assumed that the rain cell has a diameter that easily exceeds that of a street corner. That is, rain can assumed to be uniformly distributed within the region of interest, whithin the first approximation adopted here.

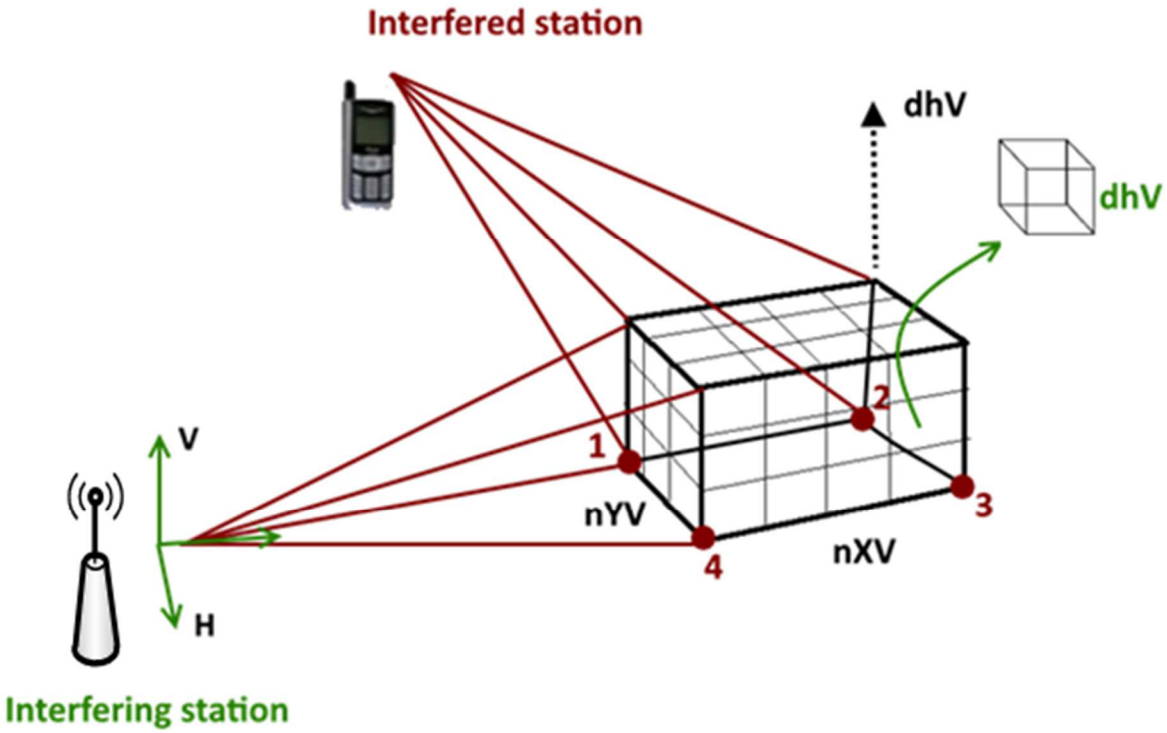

Figure 7.2: Common volume geometry.

7.2. Results of the Application of the Proposed Model to Rain Scatter Interference Calculations

The procedure explained above is applied for short-range radio communication systems operating at millimeter-wave frequencies in urban environments with the purpose of estimate the interference level on communication paths. In this study, it is assumed that the transmitter and receiver have the same technical characteristics, summarized in Table 7.1.

Table 7.1: Transmitter and receiver parameters.

Frequency	42 GHz and 70 GHz
Antenna Type	Sectorial array
Antenna Gain	20 dB
Beam Width	20 degrees
Transmitted Power	3 dB
Polarization	Vertical and Horizontal
Number of elements	7

The following urban scenarios are considered:

- **Case study: intersection between two perpendicular streets**

The first scenario used to evaluate the levels of interference for short path lengths is depicted in Figure 7.3, where two links are analyzed and the rain cell is centered at the intersection between two perpendicular streets. The red line represents the interfering link (Txk-Rxk), the blue line represents the interfered link due to rain (Txj-Rxj) and the red dashed line represents the direction of the scattered signal. For this case, the scattering angle was kept fixed at 90º. The yellow square represent the base of the common volume.

The transmitters, receivers and intersection corners are located at the coordinates listed in Tables 7.2 and 7.3, respectively. The coordinates were found on Google Earth for a particular area of Rio de Janeiro, Brazil. The heights *h* of the stations are assumed to be 5 m. To model the common volume Figure 7.2 was considered, where the following dimensions were used to subdivide in smaller volumes: nYV=100, nXV=100 and dhV=0.5 m. Thus, the common volume is subdivided until convergence is obtained. In

this study, it is assumed a directional beam that as far as go up the antenna gain decreases and it is no longer worthwhile to continue the summation. To obtain convergence, it was necessary 51 dhV.

Table 7.2: Location of the transmitters and receivers of the links for first scenario.

	Latitude	Longitude
Txk	22°59'6.20"S	43°13'31.37"W
Rxk	22°59'5.59"S	43°13'29.10"W
Txj	22°59'6.66"S	43°13'29.94"W
Rxj	22°59'4.62"S	43°13'30.71"W

Table 7.3: Location of the corners of the intersection between two perpendicular streets.

	Latitude	Longitude
Corner 1	22°59'5.18"S	43°13'30.69"W
Corner 2	22°59'4.97"S	43°13'29.96"W
Corner 3	22°59'5.93"S	43°13'29.60"W
Corner 4	22°59'6.16"S	43°13'30.32"W

This urban scenario was used to compute interference levels for 42 GHz and 70 GHz, rainfall rates of 30 mm/h and 75 mm/h, considering that the transmitted signal is vertically or horizontally polarized. It should be remembered that the above are two of the frequency bands under consideration for use by the fifth generation of cellular mobile communication systems and that the quoted rainfall rate are exceeded during 0.01 % of the average year in temprate climates and in the Rio de Janeiro/São Paulo region, respectively. Each case was analyzed individually.

The lengths of the interfering and interfered links are given in Table 7.4. These lengths are computed based on the location of the transmitters and receivers detailed in Table 7.2.

Table 7.4: Length of the interfered and interfering links

Links	Distance [m]
Distj (Interfered)	57.37
Distk (Interfering)	67.11

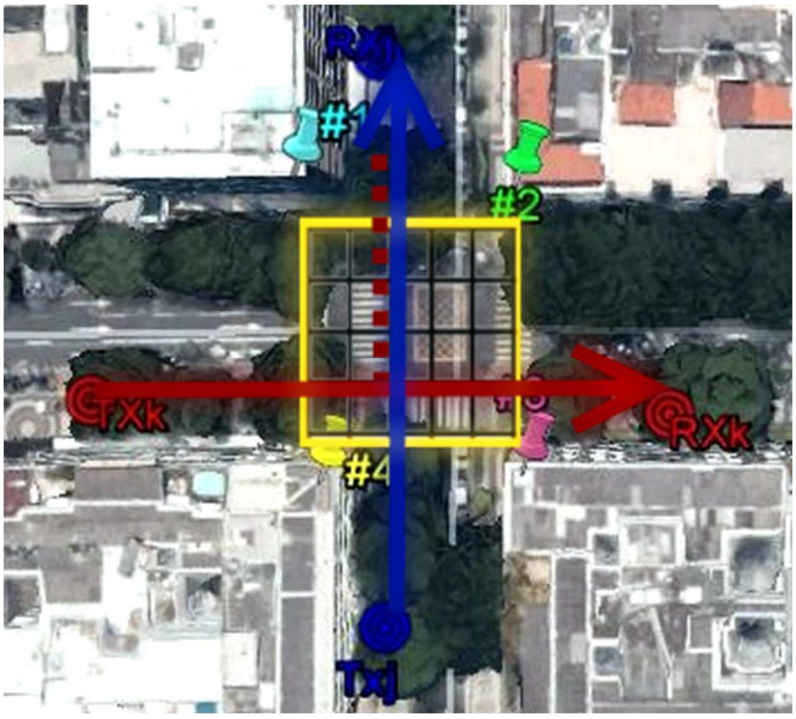

Figure 7.3: First urban scenario used to compute interference, showing the transmitter and receiver locations of the interfering and interfered-with links (adapted from Google Earth).

Following the procedure explained above, the desired power at the interfered station was computed using equation (7.2). The results are shown in Table 7.5 for 42 GHz and 70 GHz and different rainfall rates: 30 mm/h and 75 mm/h. In this Table, L_S is the free space loss, L_G is the attenuation of the transmitted signal by atmospheric gases, L_{RH} is the attenuation due to rain for a horizontally polarized signal, L_{RV} is the attenuation due to rain for a vertically polarized signal, P_{RV} is the desired power at the receiver for a vertically polarized signal and P_{RH} is the desired power at the receiver for a horizontally polarized signal. The desired power was computed for each of the vertically polarized and horizontally polarized transmitted signals, where the rain attenuation was estimated based on EBCM. Each case was analyzed independently. Table 7.6 shows the same

results but considering the rain attenuation was estimated based on the Recommendation ITU-R P.838-2. A comparison of Table 7.5 and 7.6 show the EBCM estimates higher attenuation at higher frequencies and rainfall rates, especially at 70 GHz.

Table 7.5: Results of the desired power for different frequencies, rainfall rates and polarizations of the transmitted signal (first scenario), where the rain attenuation is estimated based on EBCM.

f (GHz)	**R (mm/h)**	L_S **(dB)**	L_G **(dB)**	L_{RH} **(dB)**	L_{RV} **(dB)**	P_{RV} **(dBW)**	P_{RH} **(dBW)**
42	30	100.08	0.11	0.60	0.55	-57.74	-57.79
42	75	100.08	0.11	1.82	1.66	-58.85	-59.01
70	30	104.52	0.02	1.26	1.20	-62.74	-62.80
70	75	104.52	0.02	2.45	2.30	-63.84	-63.99

Table 7.6: Results of the desired power for different frequencies, rainfall rates and polarizations of the transmitted signal (first scenario), where the rain attenuation is estimated based on the Recommendation ITU-R P.838-2 [80].

f (GHz)	**R (mm/h)**	L_S **(dB)**	L_G **(dB)**	L_{RH} **(dB)**	L_{RV} **(dB)**	P_{RV} **(dBW)**	P_{RH} **(dBW)**
42	30	100.08	0.11	0.50	0.45	-57.64	-57.69
42	75	100.08	0.11	1.11	0.97	-58.16	-58.30
70	30	104.52	0.02	0.72	0.68	-62.22	-62.26
70	75	104.52	0.02	1.41	1.32	-62.86	-62.95

To estimate the interfering power, the Bistatic Radar Equation (BRE) given in equation (7.11) was implemented, where the rain cross-polarization effects were considered. The scattering cross section per unit volume was calculated based on the realistic rain model detailed in Chapter 4 and Appendix G. Figure 7.4 shows the scattering geometry used to compute the interference at the input of the interfered receiver, detailing only the transmission of the vertically-polarized interfering component. The received

vertical component due to the vertically-polarized interfering signal V is defined as follows:

$$V_{RI} = \sum_{i=1}^{4} V_{Ri} \tag{7.13}$$

In the above equation: (1) the component V_{R1} is initially attenuated (γ_{VV}) along the path from Tx1 to the common volume, scattered (σ_{VV}) by the common volume, and finally attenuated (γ_{VV}) along the path from the common volume to Rx2; (2) the component V_{R2} is initially attenuated (γ_{VV}) along the path from Tx1 to the common volume, scattered and depolarized (σ_{HV}) by the common volume, and finally attenuated and depolarized (γ_{VH}) along the path from the common volume to Rx2; (3) the component V_{R3} is initially attenuated and depolarized (γ_{HV}) along the path from Tx1 to the common volume, scattered and depolarized (σ_{VH}) by the common volume, and finally attenuated (γ_{VV}) along the path from the common volume to Rx2; and (4) the component V_{R4} is initially attenuated and depolarized (γ_{HV}) along the path from Tx1 to the common volume, scattered (σ_{HH}) by the common volume, and finally attenuated and depolarized (γ_{VH}) along the path from the common volume to Rx2. The received horizontal component due to the vertically-polarized interfering signal V is defined as follows:

$$H_{RI} = \sum_{i=1}^{4} H_{Ri} \tag{7.14}$$

In the above equation: (1) the component H_{R1} is initially attenuated (γ_{VV}) along the path from Tx1 to the common volume, scattered (σ_{VV}) by the common volume, and finally attenuated and depolarized (γ_{HV}) along the path from the common volume to Rx2; (2) the component H_{R2} is initially attenuated (γ_{VV}) along the path from Tx1 to the common volume, scattered and depolarized (σ_{HV}) by the common volume, and finally attenuated (γ_{HH}) along the path from the common volume to Rx2; (3) the component H_{R3} is initially attenuated and depolarized (γ_{HV}) along the path from Tx1 to the common volume, scattered (σ_{HH}) by the common volume, and finally attenuated (γ_{HH}) along the path from the common volume to Rx2; and (4) the component H_{R4} is initially attenuated and depolarized (γ_{HV}) along the path from Tx1 to the common volume, scattered and depolarized (σ_{VH}) by the common volume, and finally attenuated and depolarized (γ_{HV}) along the path from the common volume to Rx2.

A similar decomposition is applied to the horizontally-polarized interfering signal H. Thus, the interfering signal is composed by total vertical and horizontal interfering component V_{RI} and H_{RI}, respectively. Each one of these total components is subdivided into 8 partial components, described above.

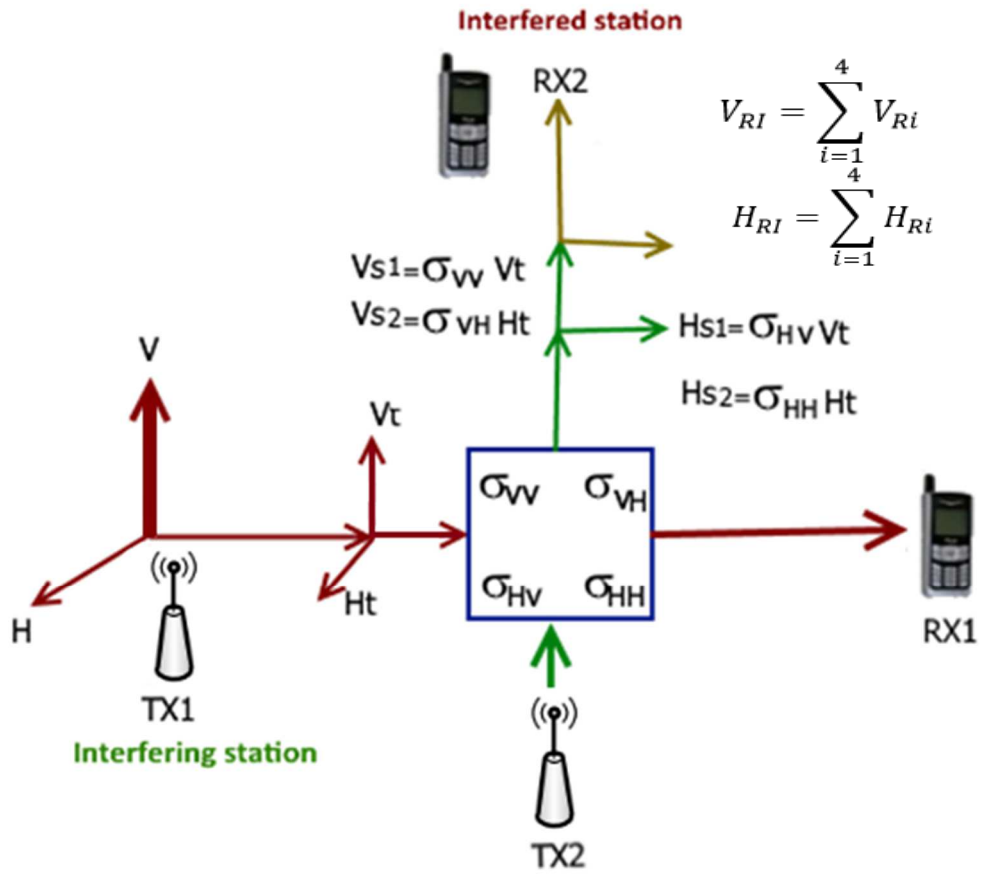

Figure 7.4: Scattering geometry used to compute interference.

The values of the co-polarized and cross-polarized components of the scattering cross section per unit volume of a rain-filled medium composed by rotationally symmetric raindrops at any position with the de Wolf DSD [12] for horizontally and vertically polarized transmitted signal are shown in Table 7.7. It is evident that the greatest contribution is provided by the co-polarized component of the transmitted signal. The contribution in the cross-polarized components shows the rain depolarization effects on the communication path.

The attenuation of the signal along the propagation path was calculated using the rain model based on EBCM. Equations (7.5)-(7.8) were implemented for the frequencies 42 GHz and 70 GHz and rainfall rates 30 mm/h and 75 mm/h. Table 7.8 shows the results for vertically- and horizontally-polarized transmitted signal, respectively.

Table 7.7: Values of the co- and cross-polarized components of the scattering cross section per unit volume (m^2/m^3) for the frequencies 42 GHz and 70 GHz and rainfall rates R = 30 mm/h and 75mm/h.

f (GHz)	**R (mm/h)**	σ_{VV}	σ_{VH}	σ_{HV}	σ_{HH}
42	30	5.01	0.006	0.0007	5.32
42	75	30.25	0.03	0.0006	32.78
70	30	112.17	0.13	0.037	117.2
70	75	406.83	0.51	0.24	435.9

Table 7.8: Values of co- and cross-polarized components of the specific attenuation (dB/km) for the frequencies 42 GHz and 70 GHz and rainfall rates R = 30 mm/h and 75mm/h.

f (GHz)	**R (mm/h)**	γ_{VV} **(dB/km)**	γ_{VH} **(dB/km)**	γ_{HV} **(dB/km)**	γ_{HH} **(dB/km)**
42	30	9.69	0.34	0.13	10.54
42	75	28.97	1.03	0.31	31.88
70	30	21.08	0.74	0.13	22.03
70	75	40.19	1.44	0.15	42.77

The results of the interfering power shown in Table 7.9 were obtained from equation (7.11) together with the complete versions of equations (7.13) and (7.14). The calculations were made for two different frequencies, polarizations of the transmitted signal and rainfall rates. Each case was studied separately. Subsequently, the signal to interference power ratio (dB) was calculated for the proper polarization as follow

$$\left(\frac{C}{I}\right)_{V,H} = P_{DV,H} - P_{IV,H} \tag{7.15}$$

where $P_{DV,H}$ (dB) is the desired power at the interfered-with receiver and $P_{IV,H}$ (dB) is the resultant interfered power at the same receiver, considering the appropriate polarization.

The results of Table 7.9 shows that the signal can experience the highest degradation and levels of interference at the interfered receiver for short path lengths for the frequency 70 GHz, rainfall rate of 75 mm/h. The results seem to indicate that value of the ratio C/I could become critically low for some configurations (depending on coding and modulation options), higher frequencies or rainfall rates. According to reference [6], the *C/I* ratios required at the receiver for a bit error rate (BER) equal to 10^{-6} (for link availability) are 18 dB (no Convolutional Coding – CC) and 14 dB (CC 2/3) for 4-QAM, 26 dB (no CC) and 24 dB (CC 7/8) for 16-QAM and 33 dB (no CC) and 31 dB (CC 5/6) for 64-QAM. In this study, a comparison between the results obtained from a horizontal and vertical polarized transmitted signal was also made. The results show that the ratio C/I seems insensitive to polarization.

Table 7.9: Values of the interfering power (dB) and signal to interference power ratio (C/I) (dB) for the frequencies 42 GHz and 70 GHz and rainfall rates R = 30 mm/h and 75mm/h.

f (GHz)	**R (mm/h)**	$\boldsymbol{P_{IH}}$ **(dBW)**	$\boldsymbol{P_{IV}}$ **(dBW)**	**(C/I)H (dB)**	**(C/I)V (dB)**
42	30	-84.31	-84.04	26.52	26.36
42	75	-78.63	-78.38	19.62	19.53
70	30	-84.75	-84.59	21.95	21.85
70	75	-79.63	-80.59	16.83	16.75

- **Case study: Two radio links located on the same street**

This second scenario (street in Rio de Janeiro) consists of two radio links with direct path between transmitting and receiving antennas. These radio links with short path lengths are located on the same street, as is shown in Figure 7.5, adapted from Google

Earth. The technical parameters of transmitting and receiving systems are assumed the same. The red line represents the interfering link (Txk-Rxk) and the blue line represents the interfered link (Txj-Rxj).

Figure 7.5: Second urban scenario used to compute interference, showing the transmitter and receiver locations of the interfering and interfered links (adapted from Google Earth).

The transmitters and receivers are located at the coordinates specified in Table 7.10.

Table 7.10: Location of the transmitters and receivers of the links for second scenario.

	Latitude	Longitude
Txk	22°59'5.28"S	43°13'39.58"W
Rxk	22°59'8.14"S	43°13'38.32"W
Txj	22°59'11.37"S	43°13'36.83"W
Rxj	22°59'14.57"S	43°13'35.34"W

The lengths of the interfering and interfered links are given in Table 7.11. These lengths are computed based on the location of the transmitters and receivers detailed in Table 7.10

Table 7.11: Length of the interfered and interfering links for second scenario.

Links	Distance [m]
Distj Interfered	107.19
Distk Interfering	95.01
Distz **Distance between Rxk and Txj**	108.03

To estimate the desired power levels at the interfered receiver, equation (7.2) was implemented. The free space loss L_s (dB) was calculated by equation (7.3), where d is the appropriate distance listed in Table 7.11.

The total atmospheric attenuation was calculated by the implementation of equation (7.4). Rain attenuation was calculated by the realistic rain model based on EBCM, where the scattering angle was kept fixed at 0^o. The values of the desired power are shown in Table 7.12 for the frequencies 42 GHz and 70 GHz, rainfall rates R = 30 mm/h and 75 mm/h, and different polarizations of the transmitted signal (vertical and horizontal). Table 7.13 shows the values of the desired power, where the rain attenuation is estimated based on the Recommendation ITU-R P.838-2. From the comparison of both Tables, it is evident that the rain attenuation estimated by the EBCM is significantly higher, especially for 70 GHz.

To calculate the interfering power along the direct path at the output of the interfered antenna, the scattering geometry shown in Figure 7.6 was used. The Friis transmission equation was used again, considering the contribution of the co-polarized and cross-polarized components of the attenuation due to rain.

Table 7.12: Values of the desired power for different frequencies, rainfall rates and polarizations of the transmitted signal (second scenario), where the rain attenuation is estimated based on EBCM.

f (GHz)	R (mm/h)	L_S (dB)	L_G (dB)	L_{RH} (dB)	L_{RV} (dB)	P_{RV} (dBW)	P_{RH} (dBW)
42	30	105.51	0.22	1.12	0.93	-63.66	-63.85
42	75	105.51	0.22	3.40	3.10	-65.83	-66.13
70	30	109.95	0.04	2.35	2.24	-69.23	-69.34
70	75	109.95	0.04	4.57	4.29	-71.28	-71.56

Table 7.13: Values of the desired power for different frequencies, rainfall rates and polarizations of the transmitted signal (second scenario), where the rain attenuation is estimated based on the Recommendation ITU-R P.838-2.

f (GHz)	R (mm/h)	L_S (dB)	L_G (dB)	L_{RH} (dB)	L_{RV} (dB)	P_{RV} (dBW)	P_{RH} (dBW)
42	30	105.51	0.22	0.93	0.83	-63.56	-63.66
42	75	105.51	0.22	2.07	1.81	-64.54	-64.80
70	30	109.95	0.04	1.34	1.27	-68.26	-68.33
70	75	109.95	0.04	2.63	2.46	-69.45	-69.62

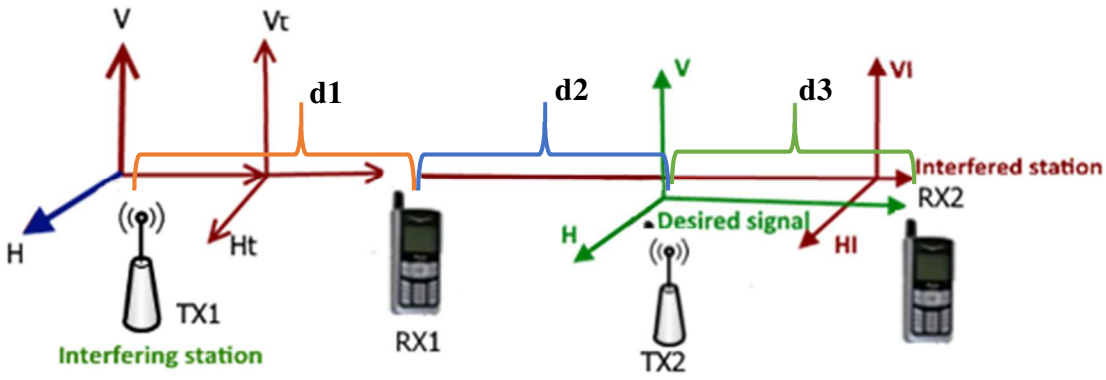

Figure 7.6: Scattering geometry used to compute interference for second urban scenario, where d1 = Distk, d2 = Distz, and d3 = Distj.

Table 7.14 shows the values of the attenuation of the transmitted signal by atmospheric gases, free space loss and attenuation due to rain for rainfall rates 30 mm/h and 75 mm/h along the interfering path. These values were computed for a vertically and horizontally polarized transmitted signal at the frequencies 42 GHz and 70 GHz.

Table 7.14: Values of the attenuation due to atmospheric gases, rain and free space loss along the interfering path for a vertically and horizontally polarized transmitted signal (second scenario).

f (GHz)	**R (mm/h)**	L_S **(dB)**	L_G **(dB)**	L_{RVV} **(dB)**	L_{RVH} **(dB)**	L_{RHV} **(dB)**	L_{RHH} **(dB)**
42	30	114.74	0.64	5.70	0.60	0.10	6.24
42	75	114.74	0.64	11.97	1.40	1.51	12.84
70	30	119.18	0.12	9.48	0.80	0.40	10.81
70	75	119.18	0.12	15.43	1.70	1.54	16.24

The values of the interfered power at the receiver and the signal to interference power ratio (C/I) were computed by implementing equation (7.15) for the proper polarization. The resulting values are shown in Table 7.15. For this second scenario, it is evident the highest level of interference is present at lower frequencies and rainfall rates, where the rain attenuation and cross-polarization is the main cause of interference. The present results indicate that the values of the C/I ratio could again become critically low

for some configurations (depending on coding and modulation options), higher frequencies or rainfall rates [6].

The results obtained from the second scenario, where two radio links are on the same street, present acceptable levels of signal to interference ratio (C/I) for higher rainfall rates, in comparison with the first scenario, where the main cause of interference is rain scatter.

Table 7.15: Values of the interfering power and power ratio (C/I) at the receiver (second scenario).

f (GHz)	R (mm/h)	P_{IH} (dBW)	P_{IV} (dBW)	$(C/I)_H$ (dB)	$(C/I)_V$ (dB)
42	30	-79.32	-78.78	15.47	15.12
42	75	-88.13	-87.26	24.28	22.72
70	30	-88.31	-86.98	17.75	18.97
70	75	-95.78	-94.97	23.69	24.22

In summary, the level of interference between short millimeter-wave links is dependent on their polarizations, common frequency and relative positions, as well as on the propagation medium. The above study, which is more detailed than previous assessments of the viability of systems based on millimeter waves, indicates that rain effects should not prevent them to work during a high percent of time. However, the present study should be extended to other configurations, frequencies and rainfall rates.

8 Conclusion and Future Work

8.1. Summary

Rain effects on microwave and millimeter-wave radio links were studied. Rain-induced attenuation, depolarization and scattering were analyzed by implementing a realistic rain medium in combination with the Extended Boundary Condition Method (EBCM). This includes a cluster of raindrops with the shape-size relation proposed by Chuang and Beard [8], combined with appropriate distributions for the drop size distribution and orientation of the symmetry axis of the particles. The characteristics of the rain medium were modeled, by developing a subroutine that describes the raindrop shapes for all equivalent diameters. The complex index of refraction of water was determined considering the frequency and temperature, according to the Ray model [13].

The developed model was validated through successful comparisons with corresponding results available in the literature. Additionally, results from the developed model were obtained for the scattering by an oblate spheroid, as well as by the corresponding Chuang and Beard particle [8], assuming different directions of incidence. Many cases [9], [28], [36], [45] of scattering calculations due to oblate spheroids can be found in the literature, implicitly assuming that this shape would provide a fair approximation to realistic particles and to the scattering properties of rain. However, the present results indicate that the scattering amplitudes of equal-volume (and relatively large) oblate spheroidal and Chuang and Beard particles may differ by non-negligible factors or even orders of magnitude for particular scattering angles. Combined with theoretical calculations and observations of realistic raindrop shapes, these results justify the adopted model of rainfall in the present work.

The proposed model based on the EBCM was initially used in the post-processing of X-band weather radar data from two different rain events to estimate backscattering cross sections and estimate rain attenuation corrections at each range gate. The results obtained from this model were compared with the HB and modified HB-SRT methods.

The comparison demonstrates this model is properly estimating the backscattering cross section and correcting the rain attenuation effects.

Next, the radar equation was applied in a first scenario to estimate the interference levels into a radio receiver operating in the millimeter-wave frequency band. The first scenario is characterized by perpendicular beams which intersect to define a common volume, assuming that the diameter of the rain cell is large enough to fill the environment of interest. The signal to interference power ratio (C/I) was evaluated for two different frequencies 42 GHz and 70 GHz; rainfall rates equal to 30 mm/h and 75 mm/h; and vertical and horizontal polarizations. It was found the rain-induced interference increases for higher frequencies and rainfall rates. The (C/I) ratio calculations did not show substantial sensitivity to the polarization, but it was observed the depolarization effects are predominant when a signal is transmitted with a horizontal polarization. This is due to facts that the backscattering cross-section depends on the drop shape (with flattened larger particles), and the orientations of their symmetry axes, which are mostly vertical, as was pointed out by [1] and [90]. Thus, it is recommended to use transmitters with vertical polarization to improve the performance of a communications system operating at the same millimeter wave frequencies. It was found that the main cause of signal degradation for this case study is due to rain scatter and the rain cross-polarization effects due to non-sphericity of raindrops is important to analyze the performance of a communication systems operating at the same frequency.

In the second case, two communication links operating at the same frequency under LOS (Line of Sight) were located on the same street. For this case, the interfered power under rainy conditions was calculated considering the attenuation effects along the path. The co-polarized and cross-polarized components were computed using the realistic rain model based on EBCM. The results obtained from the horizontal and vertical polarized transmitted wave were compared and it was found the signal transmitted with horizontal polarization is more susceptible to signal degradation at the desired receiver.

8.2. Future Work

It would be interesting to compare the rainfall rates estimated from the correction methods with those directly provided by a network of rain gauges, if available. This could provide an independent test on the effectiveness of the proposed attenuation-correction technique. It would also be interesting to apply the EBCM to dual-polarized weather radar data to extract more detailed information on the rain field.

The developed model could also be more extensively applied to the study of interferences between millimeter-wave link, assuming other configurations and frequencies.

Further studies of rain effects on microwave and millimeter-wave propagation could include multiple scattering effects on propagation in the presence of rain. It would be interesting to consider other realistic raindrop behaviors (different DSDs and distributions of orientations of symmetry axes of particles) to analyze the sensitivity of the scattering and attenuation properties computations to their parameters. Another aspect that should be considered is related with the scattering and attenuation properties of a cluster of raindrops, properly taking their relative positions into account.

References

[1] S. Okamura and T. Oguchi, **"Review: Electromagnetic wave propagation in rain and polarization effects,"** Proc. Jpn. Acad. Ser. B Phys. Biol. Sci., vol. 86, no. 6, pp. 539-562, June 2010.

[2] T. Oguchi, **"Scattering properties of Pruppacher-and-Pitter form raindrops and cross polarization due to rain: Calculations at 11,13,19.3,34.8 GHz,"** Radio Sci., vol. 12, no. 1, pp. 41-51, January 1977.

[3] T. Oguchi, **"Scattering from hydrometeors: A survey,"** Radio Sci., vol. 16, no. 5, pp. 691-730, October 1981.

[4] H. Barksdale and J. Bostian, **"Attenuation and depolarization due to rain scatter at millimeter wave frequencies,"** Proc. IEEE, vol. 3, no. 1, pp. 1033-1040, May 1988.

[5] T. Chu, **"Rain-Induced cross-polarization at centimeter and millimeter wavelengths,"** Bell Sys. Tech. J., vol. 53, no. 8, pp. 1557-1579, October 1974.

[6] C. Enjamio, E. Vilar, and F. Perez-Fontan, **"Rain scatter interference in mm-wave broadband fixed wireless access networks caused by a 2-D dynamic rain environment,"** IEEE Trans. Wireless Commun., vol. 6, no. 1, pp. 2497-2507, July 2007.

[7] C. Bohren and D. Huffman, **"Absorption and scattering by a sphere," in Absorption and Scattering of Light by Small Particles**, New York: John Wiley and Sons, 1983, pp. 82-129.

[8] C. C. Chuang and K. V. Beard, **"A numerical model for the equilibrium shape of electrified raindrops,"** J. Atmos. Sci., vol. 47, no. 11, pp. 1374-1389, June 1990.

[9] C. Gibbins, **"A new model for rain scatter interference for coordination between earth stations and terrestrial stations,"** Radio Sci., vol. 40, no. 4, pp. 1-16, July 2005.

[10] M. Mishchenko and L. Travis, **"Capabilities and limitations of a current Fortran implementation of the T-Matrix method for randomly oriented,**

rotationally symmetric scatteres," J. Quant. Spectr. Radiat. Transfer, vol. 60, no. 3, pp. 309-324, September 1998.

[11] M. I. Mishchenko, **"Calculation of the amplitude matrix for a nonspherical particle in a fixed orientation,"** Appl. Opt., vol. 39, no. 6, pp. 1026-1031, February 2000.

[12] D. A. de Wolf, **"On the Laws-Parsons distribution of raindrop sizes,"** Radio Sci., vol. 36, no. 4, pp. 639-642, July 2001.

[13] P. Ray, **"Broadband complex refractive indices of ice and water,"** Appl. Opt., vol. 11, no. 8, pp. 1836-1844, August 1972.

[14] G. Brussaard, **"A meteorological model for rain - induced cross polarization,"** IEEE Trans. Antennas Propagat., vol. 24, no. 1, pp. 5-11, January 1976.

[15] R. Olsen, D. Rogers, R. Hulays, and M. Kharadly, **"Interference due to hydrometeor scatter on satellite communication links,"** Proc. IEEE, vol. 81, no. 6, pp. 914-922, August 2002.

[16] L. Doherty and S. Stone, **"Forward scatter from rain,"** IEEE Trans. Antennas Propagat., vol. 8, no. 4, pp. 414-418, January 1960.

[17] D. Setzer, **"Anisotropic scattering due to rain at radio-relay frequencies,"** Bell Sys. Tech. J., vol. 50, no. 3, pp. 861-868, April 1971.

[18] R. Crane, **"Bistatic scatter from rain,"** IEEE Trans. Antennas Propagat., vol. 22, no. 2, pp. 312-320, January 1974.

[19] T. Chu, **"Rain-scatter interference on an earth-space path,"** IEEE Trans. Antennas Propagat., vol. 25, no. 2, pp. 287-288, April 1977.

[20] L. Tingye, W. Jakes, and J. Morrison, **"Forward scattering due to rain at 11 GHz,"** IEEE Trans. Antennas Propagat., vol. 25, no. 5 pp. 646-649, September 1977.

[21] P. Delogne and M. Lobelle, **"Numerical calculations on microwave propagation through rain,"** Ann. Telecommun., vol. 32, no. 11, pp. 386-391, July 1977.

[22] R. Bose, G. Bauer, and R. Jacoby, **"Two-dimensional line of sight interference analysis of LMDS network for the downlink and uplink,"** IEEE Trans. Antennas Propagat., vol. 52, no. 1, pp. 2464-2473, September 2004.

[23] A. Panagopoulos and J. Kanellopoulos, **"Statistics of differential rain attenuation on coverging terrestrial propagation path,"** IEEE Trans. Antennas Propagat., vol. 51, no. 9, pp. 2514-2517, September 2003.

[24] P. Waterman, **"Matrix formulation of electromagnetic scattering,"** Proc. IEEE, vol. 53, no. 8, pp. 805-812, August 1965.

[25] ITU-R, **"Proposed revision to the mode (2) rain scatter intereference prediction methodology in recommendation ITU-R P.452-16,"** in Radiocommunicatioin Study Groups, United Kingdom, Recommendation ITU-R P.452-16, 2002, pp. 1-24.

[26] H. C. van de Hulst, **Light scattering by small particles**, New York: Dover, 1981.

[27] M. Kerker, **The Scattering of light and other electromagnetic radiation**, New York: Academic, 1969.

[28] C. Magono, **"On the shape of water drops falling in stagnant air, "** J. Meteor., vol. 11, no. 1, pp. 77-79, February 1954.

[29] T. Oguchi, **"Attenuation and phase rotation of radio waves due to rain: calculation at 19.3 and 34.8 GHz, "** Radio Sci., vol. 8, no. 1, pp. 31-38, January 1973.

[30] T. Oguchi and Y. Hosoya, **"Scattering properties of oblate raindrops and cross polarization of radio waves due to rain II: Calculations at microwave and millimeter wave regions,"** Radio Research Laboratory, vol. 21, no. 105, pp. 191-259, 1974.

[31] M. Kahnert, **"Numerical methods in electromagnetic scattering theory,"** J. Quant. Spectr. Radiat. Transfer, vol. 111, no. 11, pp. 775-824, June 2003.

[32] T. Oguchi, **"Scattering properties of oblate raindrops and cross polarization of radio waves due to rain: Calculations at 19.3 and 34.8 GHz,"** Radio Research Lab., vol. 20, no. 102, pp. 79-118, 1973.

[33] S. Asano, **"Light scattering properties of spheroidal particles,"** Appl. Opt., vol. 18, no. 5, pp. 712-723, March 1979.

[34] S. Asano and G. Yamamoto, **"Light scattering by a spheroidal particle,"** Appl. Opt., vol. 14, no. 1, pp. 29-49, January 1975.

[35] O. Zienkiewicz, R. Taylor and J. Zhu, **The finite element method**, Columbia, Maryland: Butterworth-Heinemann, 2000.

[36] A. Taflove and S. Hagness, **Advances in computational electrodynamics: the finite difference time domain method**, Boston: Artech House, 1998.

[37] C. Bourlier, N. Pinel and G. Kubiche, **Method of moments for 2D scattering problems**, Hoboken, NJ: John Wiley and Sons, 2013.

[38] J. Morrison and M. Cross, **"Scattering of a plane electromagnetic wave by axisymmetric raindrops,"** Bell System Tech. J., vol. 53, no. 6, pp. 955-1019, July 1974.

[39] C. Yeh, **"Perturbation approach to the diffraction of electromagnetic waves by arbitrarily shaped dielectric obstacles,"** Phys. Rev., vol. 135, no. 5A, pp. A1193-A1201, August 1964.

[40] V. Erma, **"An exact solution for the scattering of electromagnetic waves from conductors of arbitrary shape:I. case of cylindrical symmetry,"** Phys. Rev., vol. 173, no. 5, pp. 1243-1257, September 1968.

[41] V. Erma, **"Exact solution for the scattering of electromagnetic waves from conductors of arbitrary shape: II general case,"** Phys. Rev., vol. 176, no. 5, pp. 1544-1553, December 1968.

[42] V. Erma, **"Exact solution for the scattering of electromagnetic waves from bodies of arbitrary shape: III. obstacle with arbitrary electromagnetic properites,"** Phys. Rev., vol. 179, no. 5, pp. 1238-1246, March 1969.

[43] M. I. Mishchenko, **"Coherent propagation of polarized millimeter waves through falling hydrometeors,"** J. Electromagn. Waves Appl., vol. 6, no. 10, pp. 1341-1351, April 1992.

[44] L. Tsang, J. A. Kong, and R. T. Shin , **Microwave remote sensing theory**, New York: John Wiley and Sons, 1985.

[45] M. I. Mishchenko, L. D. Travis and A. A. Lacis, **Scattering absortion and emission of light by small particles**, New York: Cambridge University Press, 2002.

[46] P. Barber and C. Yeh, **"Scattering of electromagnetic waves by arbitrarily shaped dielectric bodies,"** Appl. Opt., vol. 14, no. 12, pp. 2864-2872, December 1975.

[47] C. Warner and A. Hizal, **"Scattering and depolarization of microwaves by spheroidal raindrops,"** Radio Sci., vol. 11, no. 11, pp. 921-930, November 1976.

[48] H. Pruppacher and R. Pitter, **"A semi-empirical determination of the shape of cloud and rain drops,"** J. Atmos. Sci., vol. 28, no. 1, pp. 86-94, January 1971.

[49] M. I. Mishchenko, L. D. Travis and D. Mackowski, **"T-matrix computations of light scattering by nonspherical particles: A review,"** J. Quant. Spectr. Radiat.Transfer, vol. 55, no. 5, pp. 535-575, May 1996.

[50] M. I. Mishchenko, L. D. Travis and D. Mackowski, **"T-matrix method and its applications to electromagnetic scattering by particles: a current perspective,"** J. Quant. Spectr. Radiat. Transfer, vol. 115, no. 1, pp. 1700-1703, July 2010.

[51] M. Willis, **"Propagation in rain and clouds,"** in Propagation of Radiowaves, London: The Institution of Engineering and Technology, pp. 161-186, 2013.

[52] P. Watson and M. Arbabi, **"Rainfall crosspolarization at microwave frequencies,"** Proc. IEEE, vol. 120, no. 4, pp. 413-418, April 1973.

[53] J. Laws and D. Parson, **"The relation of raindrop-size to intensity,"** Trans. Amer. Gephys. Union., vol. 24, no. 2, pp. 452-460, October 1943.

[54] J. Marshall and W. Palmer, **"Shorter contributions: the distribution of raindrops with size,"** J. Meteor., vol. 5, no. 1, pp. 165-166, August 1948.

[55] R. Olsen, D. Rogers, and D. Hodge, **"The aRb relation in the calculation of rain attenuation,"** IEEE Trans. Antennas Propagat., vol. 26, no. 2, pp. 318-329, March 1978.

[56] B. Maher and P. Murphy, **"Variation of the canting angle distribution as a function of wind velocity,"** Elec. Letts., vol. 13, no. 19, pp. 567-568, September 1977.

[57] B. Maher, P. Murphy, and C. Sexton, **"A theoretical model of the effect of wind-gusting on rain-induced cross-polarization,"** Ann. Telecommun., vol. 32, no. 11, pp. 404-408, July 1977.

[58] J. Howard and M. Gerogiokas, **"A statistical raindrop canting angle model,"** IEEE Trans. Antennas Propagat., vol. 30, no. 1, pp. 141-147, January 1982.

[59] J. Howard, **"Application of statistical raindrop canting angle model on terrestrial and satellite links,"** Proc. IEEE, vol. 132, no. 2, pp. 119-125, April 1985.

[60] R. Gunn and G. Kinzer, **"The terminal velocity of fall for water droplets in stagnant air,"** J. Meteor., vol. 6, no. 4, pp. 243-248, August 1949.

[61] I. Dilworth and B. Evans, **"Cumulative crosspolarization and canting angle distributions,"** Elec. Letts., vol. 15, no. 19, pp. 603-604, September 1979.

[62] F. Moupfouma, **"Theoretical model for calculating rain-induced crosspolarisation,"** Elec. Letts., vol. 19, no. 13, pp. 465-469, June 1983.

[63] W. Vogel, B. Fanni, and A. Straiton, **"Some polarization effects for millimeter wave propagation in rain,"** Proc. Adv. Study Institute Program, vol. 27, no. 1, pp. 399-423, 1976.

[64] G. Brussaard and P. Watson, **Atmospheric modelling and millimetre wave propagation**, London: Chapman and Hall, 1995.

[65] J. Goldhirsh and B. Musiani, **"Rain cell size statistics derived from radar observations at wallops Island-Virginia,"** Trans. Geosci. Remote Sens., vol. 24, no. 6, pp. 947-948, November 1986.

[66] R. Crane, **"Comparative evaluation of several rain attenuation prediction models,"** Radio Sci., vol. 20, no. 4, pp. 843-863, July 1985.

[67] P. Misme and J. Fimbel, **"Theoretical and experimental determination of attenuation due to rain on a radio-path,"** Ann. Telecommun., vol. 30, no. 5, pp. 149-158, May 1975.

[68] A. Poggio, **"Integral equation solutions of three-dimensional scattering problems,"** in Computer Techniques for Electromagnetics, New York: Pergamon Press, pp. 159-260, 1973.

[69] C. T. Tai, **Dyadic green function in electromagnetic theory**, New Jersey: Institute of Electrical and Electronics Engineer, 1994.

[70] J. D. Jackson, **Classical electrodynamics**, New York : John Wiley and Sons, 1999.

[71] J. A. Stratton, **Electromagnetic theory**, New York: McGraw-Hill Book Company, 1941.

[72] D. Deirmendjian, **Electromagnetic scattering on spherical polydispersion**, Santa Monica, CA: Elsevier Publishing Company, 1969.

[73] M. I. Mishchenko, L. D. Travis and J. Hovenier, **Light scattering by nonspherical particles: theory, measurements and applications**, San Diego, CA: Academic Press, 2000.

[74] D. Tarducci and S. Tao, "**A simplified approach to bistatic radar reflectivity computations,"** Radio Sci*,* vol. 23, no. 3, pp. 443-449, June 1988.

[75] W. Hitschfeld and J. Bordan, **"Errors inherent in the radar measurement of rainfall at attenuating wavelenghts,"** J. Meteor., vol. 11, no. 1, pp. 58-66, February 1954.

[76] T. Iguchi, T. Kozu, R. Meneghini, J. Awaka, and K. Okamoto, **"Rain-profiling algorithm for the TRMM precipitation radar,"** J. Appl. Meteor., vol. 39, no. 12, pp. 2038-2052, December 2000.

[77] K. Mora, L. V. León and S. Cruz, **"Implementation and development of an attenuation correction algorithm for Off-The-Grid X-band radar,"** AMS Annual Student Conference, pp. 1-7, January 2013.

[78] A. Ishimaru, **Wave propagation and scattering in random media**, New York: Wiley - IEEE Press,February 1999.

[79] T. Ulaby and D. Long, **Microwave radar and radiometric remote sensing**, Massachussetts: Artech House Publishers, March 1986.

[80] International Telecommunication Union, "**Specific attenuation model for rain for use in prediction methods**," Recommendation ITU-R P.838-3, Geneva, Switzerland, 2005.

[81] G. A. Pablos-Vega et al., "**Development of an Off The Grid X-band radar for weather applications**," IEEE Int. Geosci. Remote Sens. Symposium, vol. 1, no. 1, pp. 1077-1080, July 2010.

[82] C. Capsoni and M. D'Amico, **"A physically based radar simulator,"** J. Atmos. Oceanic Technol., vol. 39, no. 15, pp. 593-598, April 1998.

[83] L. Battan, **Radar meteorology**, Chicago: University of Chicago Press, March 1973.

[84] International Telecommunication Union, "**Attenuation by atmospheric gases**," Recommendation ITU-R P.676-11, Geneva, Switzerland, 2016.

[85] Y. Liu, **The study and real-time implementation of attenuation correction for X-band dual polarization weather radars (Doctoral dissertation)**. Retrieved from Proquest. (Access No. 3321294) 2008.

[86] T. Iguchi and R. Meneghini, **"Intercomparison of single-frequency methods for retrieving a vertical rain profile from airborne of spaceborne radar data,"** J. Atmos. Oceanic Technol., vol. 11, no. 6, pp. 1507-1516, December 1994.

[87] J. Tutle and R. Rinehart, **"Attenuation correction in dual-wavelength analyses,"** J. Climate Appl. Meteor., vol. 22, no. 11, pp. 1914-1921, November 1983.

[88] J. Brotzge et al., **"CASA IP: Network operations and initial data,"** AMS Annual Student Conference, pp. 1-10, January 2007.

[89] K. Mora, L. León, J. Colom, S. Cruz and C. Demel, **"Polarization effects on a single polarized Off-The-Grid X-band radar,"** 2013 IEEE Int. Geosci. Remote Sens. Symposium, pp. 2216-2218, July 2013.

[90] V. Bringi and V. Chandrasekar, **Polarimetric doppler weather radar**, New York: Cambridge University Press, 2004

[91] P. Zhouyue and K. Farooq, **"An introduction to millimeter-wave mobile broadband systems,"** IEEE Communications Magazine, pp. 101-107, June 2011.

[92] G. E. Stout and E. A. Mueller, **"Survey of relationships between rainfall rate and radar reflectivity in the measurement of precipitation,"** J. Appl. Meteor., vol. 7, no. 1, pp. 465-474, Jun. 1968.

[93] M. Thurai, P. N. Gatlin and V.N. Bringi, **"Separating stratiform and convective rain types based on the drop size distribution characteristics using 2D video disdrometer data,"** Atmos. Res.,vol 169, pp. 416-423, March 2016.

[94] J. G. Andrews, S. Buzzi, W. Choi, S. Hanly, A. Lozano, A. C. K. Soong, and J. C. Zhang, **What will 5G be?**, IEEE Journal on Selected Areas in Communications, 32 (6), 1065 – 1082, 2014.

[95] T. Rappaport, S. Sun, R. Mayzus, H. Zhao, Y. Azar, K. Wang, G. Wong, J. Schulz, M. Samimi, and F. Gutierrez, **"Millimeter Wave Mobile Communications for 5G Cellular: It Will Work!,"** IEEE Access, vol. 1, pp. 335–349, 2013.

[96] International Telecommunication Union, **"Characteristics of precipitation for propagation modelling,"** Recommendation ITU-R P.837-6, Geneva, Switzerland, 2012.

[97] L. A. R. da Silva Mello, M. S. Pontes, N. R. Dhein and C. M. Einloft, **Radio Propagation Measurements In Brazil: Clear Air and Rainfall Effects**, Revista da Sociedade Brasileira de Telecomunicacoes Volume 9, número 1, pp. 27-43, Dezembro de 1994.

[98]]F. Juyent, V. Chandrasekar, D. McLaughlin, E. Insanic, and N. Bharadwaj, **"The CASA Integrated Project 1 Networked Radar System,"** *J. Atmos. Oceanic Technol.*, vol. 27, no. 1, pp. 61-78, Jan. 2010.

A.
Representation of the Fields in Terms of Surface Currents.

Let a known isotropic, homogeneous, and nonmagnetic particle centered at the origin, as shown in Figure A.1, be illuminated by an incident electromagnetic field. Figure A.1 also shows: (i) an internal region V_{int} bounded by the closed surface S that limits the particle; and (ii) the region V_{ext}, bounded by the surfaces S_∞ (of infinite radius) and *S*, representing the infinite region exterior to the particle, which is circumscribed by the sphere with radius $r_>$ and circumscribes another sphere with radius $r_<$.

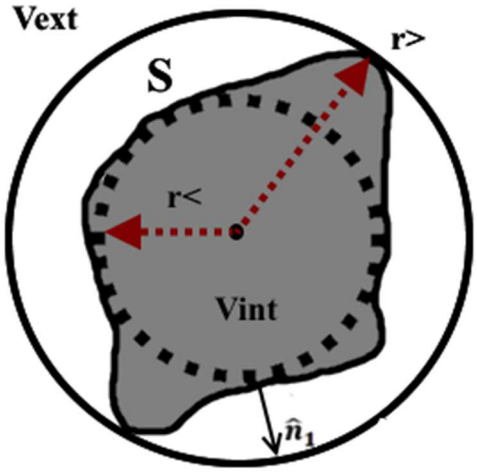

Figure A.1: Homogeneous scattering particle.

For each region, the electric field satisfies the following equations:

$$\begin{aligned} \nabla \times \nabla \times \vec{E} - {k_o}^2 \vec{E} = 0 \quad r \in V_{ext} \\ \nabla \times \nabla \times \vec{E} - {k_1}^2 \vec{E} = 0 \quad r \in V_{int} \end{aligned} \tag{A.1}$$

where k_o and k_1 are the wave number of the exterior and interior regions. Here, $k_o = \omega\sqrt{\mu_o \varepsilon_o}$ and $k_1 = k_o m$, where $m = \left[\varepsilon_r + i\left(\frac{\sigma}{\omega \varepsilon_o}\right)\right]^{1/2}$ is the complex index of refraction of water at the assumed frequency and temperature. The harmonic time variation $e^{-i\omega t}$ is implicitly assumed.

Next, the vector Green's theorem will be applied to the volume V_{ext}. The vector Green's theorem allows one to express the vector quantities $\vec{E}$ and $\vec{H}$ inside the volume V_{ext} as functions of the fields $\vec{E}$ and $\vec{H}$ over the limiting closed surface. The vector Green's theorem is given by

$$\int_{V_{ext}} \left[\vec{a}\cdot\left(\nabla\times\nabla\times\vec{b}\right)-\vec{b}\cdot\left(\nabla\times\nabla\times\vec{a}\right)\right]dV = \tag{A.2}$$

$$= \int_{S+S_\infty} \hat{n}\cdot\left[\vec{b}\times\left(\nabla\times\vec{a}\right)-\vec{a}\times\left(\nabla\times\vec{b}\right)\right]dS$$

where the unit vector $\hat{n}$ is perpendicular to surfaces S and S_∞ and directed away from V_{ext}. Thus, $\hat{n} = -\hat{n}_1$ along S. It should be noted that the integrals in equation (A.2) are performed with respect to the variable $\vec{r}$. Suppose $\vec{a} = \vec{E}(\vec{r})$ and $\vec{b} = \bar{\bar{G}}_o(\vec{r},\vec{r}')\cdot\vec{c}$, where $\vec{c}$ is an arbitrary constant vector and $\bar{\bar{G}}_o(\vec{r},\vec{r}')$ is the free-space dyadic Green´s function [69], which satisfy the following differential equation

$$\nabla\times\nabla\times\bar{\bar{G}}_o(\vec{r},\vec{r}') - {k_o}^2\bar{\bar{G}}_o(\vec{r},\vec{r}') = \bar{\bar{I}}\delta(r-r') \tag{A.3}$$

The left-hand side of equation (A.2) can be written in the form

$$LS = -\int_{V_{ext}} \left[\bar{\bar{G}}_o(\vec{r},\vec{r}')\cdot\vec{c}\cdot\left(\nabla\times\nabla\times\vec{E}\right)-\vec{E}\cdot\left(\nabla\times\nabla\times\bar{\bar{G}}_o(\vec{r},\vec{r}')\cdot\vec{c}\right)\right]dV$$

$$LS = -\int_{V_{ext}} \left\{\left[\bar{\bar{G}}_o(\vec{r},\vec{r}')\cdot\vec{c}\right]\cdot k_o^2\vec{E}-\vec{E}\cdot\left[k_o^2\bar{\bar{G}}_o(\vec{r},\vec{r}')\cdot\vec{c}+\bar{\bar{I}}\cdot\vec{c}\delta(r-r')\right]\right\}dV \tag{A.4}$$

Let $\bar{\bar{G}}_o = \vec{A}\vec{B}$. Thus

$$\bar{\bar{G}}_o\cdot\vec{c} = \vec{A}(\vec{B}\cdot\vec{c})$$

$$\left(\bar{\bar{G}}_o\cdot\vec{c}\right)\cdot\vec{E} = \left(\vec{A}\cdot\vec{E}\right)\left(\vec{B}\cdot\vec{c}\right)$$

$$\vec{E}\cdot\left(\bar{\bar{G}}_o\cdot\vec{c}\right) = \vec{E}\cdot\left[\left(\vec{A}\vec{B}\right)\cdot\vec{c}\right] = \left(\vec{E}\cdot\vec{A}\right)\left(\vec{B}\cdot\vec{c}\right)$$

and, since the first two terms mutually cancel each other, expression (A.4) reduces to

$$LS = \int_{V_{ext}} \left(\vec{E}\cdot\vec{c}\right)\delta(\vec{r}-\vec{r}')dV = \begin{cases}\vec{E}(\vec{r}')\cdot\vec{c} & \vec{r}'\epsilon\, V_{ext} \\ 0 & \vec{r}'\epsilon\, V_{int}\end{cases} \tag{A.5}$$

The surface integral on the right hand side of equation (A.2) represents the sum of two integrals. One of the integrals is over the spherical surface S_∞ bounding the exterior region at infinity and the other integral is over the surface particle S. Therefore, one has

$$RS = \left\{\int_{S_\infty} + \int_{S}\right\}\left\{\hat{n}\cdot\left\{\left[\bar{\bar{G}}_o(\vec{r},\vec{r}')\cdot\vec{c}\right]\times\left(\nabla\times\vec{E}\right) - \vec{E}\times\nabla\times\left[\bar{\bar{G}}_o(\vec{r},\vec{r}')\cdot\vec{c}\right]\right\}\right\}dS =$$

$$= \left\{-\int_{S_\infty} + \int_{S}\right\}\left\{\hat{n}_1\cdot\left\{\left(\nabla\times\vec{E}\right)\times\left[\bar{\bar{G}}_o(\vec{r},\vec{r}')\cdot\vec{c}\right] + \vec{E}\times\nabla\times\left[\bar{\bar{G}}_o(\vec{r},\vec{r}')\cdot\vec{c}\right]\right\}\right\}dS \tag{A.6}$$

The change of vectors $\hat{n} = \hat{n}_1$ in S_∞ and $\hat{n} = -\hat{n}_1$ in S should be noted in the immediately above equation. Taking the properties of the dyadic Green's function [69] into account

$$\bar{\bar{G}}_o = \vec{G}_{ox}\hat{x} + \vec{G}_{oy}\hat{y} + \vec{G}_{oz}\hat{z}$$

$$\bar{\bar{G}}_o\cdot\vec{c} = c_x\vec{G}_{ox} + c_y\vec{G}_{oy} + c_z\vec{G}_{oz}$$

$$\nabla\times\left(\bar{\bar{G}}_o\cdot\vec{c}\right) = c_x\nabla\times\vec{G}_{ox} + c_y\nabla\times\vec{G}_{oy} + c_z\nabla\times\vec{G}_{oz}$$

$$\nabla\times\left(\bar{\bar{G}}_o\cdot\vec{c}\right) = \left(\nabla\times\vec{G}_{ox}\right)(\hat{x}\cdot\vec{c}) + \left(\nabla\times\vec{G}_{oy}\right)(\hat{y}\cdot\vec{c}) + \left(\nabla\times\vec{G}_{oz}\right)(\hat{z}\cdot\vec{c}) =$$

$$= \left(\nabla\times\bar{\bar{G}}_o\right)\cdot\vec{c}$$

one gets

$$RS = \left\{ \left\{ -\int_{S_\infty} + \int_{S} \right\} \left\{ \left\{ i\omega\mu_o \left(\hat{n}_1 \times \vec{H}_+(\vec{r}) \right) \cdot \bar{\bar{G}}_o(\vec{r},\vec{r}') + \left(\hat{n}_1 \times \vec{E}_+(\vec{r}) \right) \cdot \nabla \right. \right. \right.$$

$$\left. \left. \left. \times \bar{\bar{G}}_o(\vec{r},\vec{r}') \right\} dS \right\} \right\} . \vec{c}$$

The integral over S_∞ is independent from the particle presence. Therefore, it represents the incident field $\vec{E}_i(\vec{r}')$. Thus, for $\vec{r}' \epsilon\, V_{ext}$

$$RS = \left\{ \vec{E}_i(\vec{r}') + \int_{S} \left\{ i\omega\mu_o \left(\hat{n}_1 \times \vec{H}_+(\vec{r}) \right) \cdot \bar{\bar{G}}_o(\vec{r},\vec{r}') + \left(\hat{n}_1 \times \vec{E}_+(\vec{r}) \right) \cdot \nabla \right. \right.$$

$$\left. \left. \times \bar{\bar{G}}_o(\vec{r},\vec{r}') \right\} dS \right\} \cdot \vec{c} \qquad \text{(A.7)}$$

The total field throughout the entire space is equal to the sum of the incident and scattered field

$$\vec{E}(\vec{r}') = \vec{E}_i(\vec{r}') + \vec{E}_s(\vec{r}') \qquad \text{(A.8)}$$

The combination of equations (A.5) and (A.7) finally provides

$$\vec{E}(\vec{r}') = \vec{E}_i(\vec{r}') + \qquad \text{(A.9)}$$

$$+ \int_S \left\{ i\omega\mu_o \left[\hat{n}_1 \times \vec{H}_+(\vec{r}) \right] \cdot \bar{\bar{G}}_o(\vec{r},\vec{r}') + \left[\hat{n}_1 \times \vec{E}_+(\vec{r}) \right] \cdot \nabla \times \bar{\bar{G}}_o(\vec{r},\vec{r}') \right\} dS$$

for $\vec{r}' \in V_{ext}$ and

$$\vec{E}_i(\vec{r}') = -\int_S \left\{ i\omega\mu_o \left[\hat{n}_1 \times \vec{H}_+(\vec{r}) \right] \cdot \bar{\bar{G}}_o(\vec{r},\vec{r}') + \left[\hat{n}_1 \times \vec{E}_+(\vec{r}) \right] \cdot \nabla \times \right.$$

$$\left. \times \bar{\bar{G}}_o(\vec{r},\vec{r}') \right\} dS \qquad \text{(A.10)}$$

for $\vec{r}' \in V_{int}$.

B.
Representation of a Plane Wave in Terms of Vector Spherical Wave Functions (VSWFs).

The incident field is represented by

$$\vec{E}_i(\vec{r}') = \vec{E}_o e^{ik_o \hat{n}_i \cdot \vec{r}'} \tag{B.1}$$

where $\vec{E}_o$ is the amplitude of the incident electric field, the wave number of free space is $k_o = 2\pi/\lambda = \omega\sqrt{\mu_o \varepsilon_o}$, and the position vector is $\vec{r}'$. The dot product $\vec{E}_o \cdot \hat{n}_i = 0$, and the unit vector $\hat{n}_i$ is given by

$$\hat{n}_i = -(\sin\theta'' \cos\varphi'' \hat{x} + \sin\theta'' \sin\varphi'' \hat{y} + \cos\theta'' \hat{z}) \tag{B.2}$$

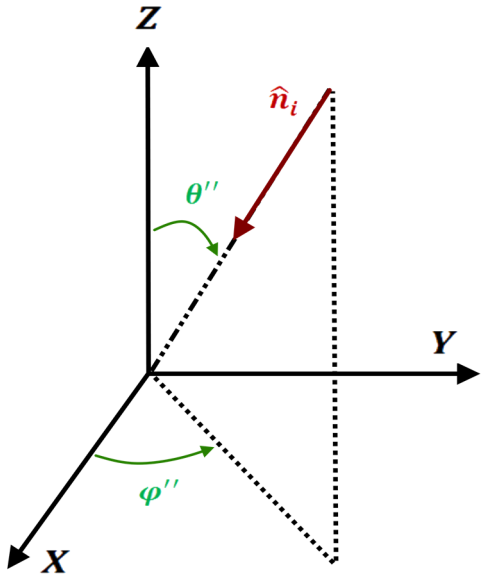

Figure B.1: Illustration of the scattering geometry.

Figure B.1 shows the direction of the incident field, as well as the spherical angles θ'' and φ'' in the Cartesian coordinate system.

The expansion of the incident field in vector spherical harmonics is represented by

$$\vec{E}_i(\vec{r}') = \sum_{n=1}^{\infty} \sum_{m=-n}^{+n} a_{mn} Rg\vec{M}_{mn}(k_o r', \theta', \varphi') + \\ + b_{mn} Rg\vec{N}_{mn}(k_o r', \theta', \varphi') \tag{B.3}$$

where a_{mn} and b_{mn} are the incident field expansion coefficients and $Rg\vec{M}_{mn}$ and $Rg\vec{N}_{mn}$ are the regular vector spherical harmonics functions defined by

$$Rg\vec{M}_{mn}(k_o r, \theta, \varphi) = \sqrt{\frac{(2n+1)}{4\pi n(n+1)}} j_n\,(k_o r)\{i\pi_{mn}(\theta)\hat{\theta} - \tau_{mn}(\theta)\hat{\varphi}\}e^{im\varphi}$$

or, equivalently

$$Rg\vec{M}_{mn}(k_o r, \theta, \varphi) = \gamma_{mn} j_n\,(k_o r)\vec{C}_{mn}(\theta, \varphi)$$

and

$$Rg\vec{N}_{mn}(k_o r, \theta, \varphi) = \\ = \sqrt{\frac{(2n+1)}{4\pi n(n+1)}}\left\{\left[\frac{j_n\,(k_o r)}{k_o r}\right] n(n+1) d_{om}^n(\theta)\hat{R} \right. \\ \left. + \frac{[u j_n\,(u)]'}{u}\bigg|_{k_o r} \left[\tau_{mn}(\theta)\hat{\theta} + i\pi_{mn}(\theta)\hat{\varphi}\right]\right\} e^{im\varphi}$$

or, equivalently

$$Rg\vec{N}_{mn}(k_o r, \theta, \varphi) = \gamma_{mn}\left\{n(n+1)\left[\frac{j_n\,(k_o r)}{k_o r}\right]\vec{P}_{mn}(\theta, \varphi) + \frac{[u j_n\,(u)]'}{u}\bigg|_{k_o r} \vec{B}_{mn}(\theta, \varphi)\right\}$$

In the above expressions

$$\pi_{mn}(\theta) = m\frac{d_{om}^n(\theta)}{\sin\theta}$$

$$\tau_{mn}(\theta) = \frac{d}{d\theta}[d^n_{om}(\theta)]$$

$$d^n_{0m}(\theta) = \sqrt{\frac{(n-m)!}{(n+m)!}} P^m_n(cos\theta)$$

and

$$\gamma_{mn} = \sqrt{\frac{(2n+1)}{4\pi n(n+1)} \frac{(n-m)!}{(n+m)!}}$$

where $j_n(x)$ is the Spherical Bessel function, $d^n_{0m}(\theta)$ is the Wigner d-function and $P^m_n(cos\theta)$ is the Associated Legendre function of the First Kind, defined in [44],[46], and [70].

Let the surface integral $I^{MM}_{mnm'n'}$ be defined by

$$I^{MM}_{mnm'n'} = \int_0^{2\pi} \int_0^{\pi} Rg\vec{M}_{mn}(kr,\theta,\varphi) \cdot Rg\vec{M}_{m'n'}(kr,\theta,\varphi) \sin\theta \, d\theta =$$

$$= \gamma_{mn}\gamma_{m'n'} j_n(kr) j_{n'}(kr) \int_0^{2\pi} e^{j(m+m')\varphi} d\varphi \int_0^{\pi} \left\{ (-mm') \frac{P^m_n(\cos\theta)}{\sin\theta} \frac{P^{m'}_{n'}(\cos\theta)}{\sin\theta} \right.$$

$$\left. + \frac{d}{d\theta}[P^m_n(\cos\theta)] \frac{d}{d\theta}[P^{m'}_{n'}(\cos\theta)] \right\} \sin\theta \, d\theta \qquad \text{(B.4)}$$

Equation (B.4) vanishes, except for $m' = -m$. In this case

$$I^{MM}_{mn(-m)n'} = 2\pi \, \gamma_{mn}\gamma_{-mn'} j_n(kr) j_{n'}(kr) \times$$

$$\times \int_0^{\pi} \left\{ m^2 \frac{P^m_n(\cos\theta)}{\sin\theta} \frac{P^{-m}_{n'}(\cos\theta)}{\sin\theta} \right.$$

$$\left. + \frac{d}{d\theta}[P^m_n(\cos\theta)] \frac{d}{d\theta}[P^{-m}_{n'}(\cos\theta)] \right\} \sin\theta \, d\theta \qquad \text{(B.5)}$$

The following relationship hold for the Associated Legendre function

$$P_n^{-m}(\cos\theta) = (-1)^m \frac{(n-m)!}{(n+m)!} P_n^m(\cos\theta) \tag{B.6}$$

Therefore, by substituting equation (B.6) into (B.5), and using the orthogonality relation (20) provided in section 7.13 of Stratton [71], one finds that $I^{MM}_{mn(-m)n'} = 0$ for $n' \neq n$ and

$$\begin{aligned} I^{MM}_{mn(-m)n} = (-1)^m \frac{(n-m)!}{(n+m)!} 2\pi\gamma_{mn}\gamma_{-mn} j_n(kr) j_n(kr) \cdot \\ \cdot \int_0^{\pi} \left\{ \frac{d}{d\theta}[P_n^m(\cos\theta)] \frac{d}{d\theta}[P_n^m(\cos\theta)] + \right. \\ \left. + m^2 \frac{P_n^m(\cos\theta)}{\sin\theta} \frac{P_n^m(\cos\theta)}{\sin\theta} \right\} \sin\theta d\theta = (-1)^m [j_n(kr)]^2 \end{aligned} \tag{B.7}$$

Similarly, let the integral $I^{NN}_{mnm'n'}$ be defined by

$$I^{NN}_{mnm'n'} = \int_0^{2\pi} \int_0^{\pi} Rg\vec{N}_{mn}(kr,\theta,\varphi) \cdot Rg\vec{N}_{m'n'}(kr,\theta,\varphi) \sin\theta \, d\theta$$

Again, one finds that $I^{NN}_{mnm'n'} = 0$ when $m' \neq -m$ and

$$\begin{aligned} I^{NN}_{mn(-m)n'} = 2\pi\gamma_{mn}\gamma_{-mn'} \left\{ \frac{j_n(kr)}{kr} \frac{j_{n'}(kr)}{kr} n(n+1)n'(n'+1) \times \right. \\ \times \int_0^{\pi} P_n^m(\cos\theta) P_{n'}^{-m}(\cos\theta) \sin\theta d\theta + \left. \frac{[uj_n(u)]'}{u}\bigg|_{kr} \frac{[uj_{n'}(u)]'}{u}\bigg|_{kr} \times \right. \\ \times \int_0^{\pi} \left\{ \frac{d}{d\theta}[P_n^m(\cos\theta)] \frac{d}{d\theta}[P_{n'}^{-m}(\cos\theta)] \right. \\ \left. \left. + m^2 \frac{P_n^m(\cos\theta)}{\sin\theta} \frac{P_{n'}^{-m}(\cos\theta)}{\sin\theta} \right\} \sin\theta d\theta \right\} \end{aligned} \tag{B.8}$$

Using expression (B.6) in combination with orthogonality relations (16) and (17) of section 7.3 and (20) of section 7.13 presented by Stratton [71], it follows that $I^{NN}_{mn(-m)n'} = 0$ for $n' \neq n$ and

$$I_{mn(-m)n}^{NN} = (-1)^m \frac{(n-m)!}{(n+m)!} 2\pi\gamma_{mn}\gamma_{-mn} \Bigg\{ n^2(n+1)^2 \left[\frac{j_n(kr)}{kr}\right]^2 \frac{2}{2n+1}\frac{(n+m)!}{(n-m)!} + \left\{\frac{[uj_n(u)]'}{u}\bigg|_{kr}\right\}^2 \frac{2}{2n+1}\frac{(n+m)!}{(n-m)!} n(n+1)\Bigg\} = \tag{B.9}$$

$$= (-1)^m \left\{ n(n+1)\left[\frac{j_n(kr)}{kr}\right]^2 + \left\{\frac{[uj_n(u)]'}{u}\bigg|_{kr}\right\}^2 \right\}$$

Finally, let the integral $I_{mnm'n'}^{MN}$ be defined by

$$I_{mnm'n'}^{MN} = \int_0^{2\pi}\int_0^{\pi} Rg\vec{M}_{mn}(kr,\theta,\varphi)\cdot Rg\vec{N}_{m'n'}(kr,\theta,\varphi)\sin\theta\, d\theta$$

As before, $I_{mnm'n'}^{MN} = 0$ for $m' \neq -m$. Thus

$$I_{mn(-m)n'}^{MN} =$$

$$= 2\pi\gamma_{mn}\gamma_{-mn'} j_n(kr)\frac{[uj_{n'}(u)]'}{u}\bigg|_{kr}(im)\int_0^{\pi}\Big\{P_n^m(\cos\theta)\frac{d}{d\theta}\left[P_{n'}^{-m}(\cos\theta)\right] + \frac{d}{d\theta}[P_n^m(\cos\theta)]P_{n'}^{-m}(\cos\theta)\Big\}d\theta = (-1)^m\frac{(n'-m)!}{(n'+m)!}2\pi\gamma_{mn}\gamma_{-mn'}\times \tag{B.10}$$

$$\times j_n(kr)\frac{[uj_{n'}(u)]'}{u}\bigg|_{kr}(im)\int_0^{\pi}\Big\{P_n^m(\cos\theta)\frac{d}{d\theta}\left[P_{n'}^{m}(\cos\theta)\right] + \frac{d}{d\theta}[P_n^m(\cos\theta)]P_{n'}^{m}(\cos\theta)\Big\}d\theta \tag{B.11}$$

Since $P_n^m(\pm 1) = 0$ when $m \neq 0$, one immediately obtains $I_{mnm'n'}^{MN} = I_{mnm'n'}^{NM} = 0$.

Based on the above results, expressions (B.1) and (B.3) provide

$$\int_0^{2\pi}\int_0^{\pi} \vec{E}_o e^{ik_o\vec{n}_i\cdot\vec{r}}\cdot$$

$$\cdot Rg\vec{M}_{m'n'}(k_o r,\theta,\varphi)\sin\theta d\theta d\varphi$$

$$= \vec{E}_o\cdot$$

$$\cdot\int_0^{2\pi}\int_0^{\pi} e^{ik_o\vec{n}_i\cdot\vec{r}} Rg\vec{M}_{m'n'}(k_o r,\theta,\varphi)\sin\theta d\theta d\varphi =$$

$$= \int_0^{2\pi}\int_0^{\pi}\left[\sum_{n=1}^{\infty}\sum_{m=-n}^{+n} a_{mn} Rg\vec{M}_{mn}(kr,\theta,\varphi) + b_{mn} Rg\vec{N}_{mn}(kr,\theta,\varphi)\right]\cdot \tag{B.12}$$

$$\cdot Rg\vec{M}_{m'n'}(k_o r,\theta,\varphi)\times$$

$$\times\sin\theta d\theta d\varphi = (-1)^{-m'}[j_{n'}(k_o r)]^2 a_{-m'n'}$$

Expression (23) on page 172 of Tsang et al. [44] can be written as follow

$$j_n(k_o r) Rg\vec{M}_{mn}(k_o r,\theta'',\varphi'') = \frac{(-i)^n}{4\pi}\int_{esf} e^{i(k_o r)(\hat{n}_i\cdot\hat{r}')} Rg\vec{M}_{mn}(k_o r,\theta',\varphi')\, d\Omega \tag{B.13}$$

where $\int_{esf}\ldots d\Omega$ is equivalent to $\int_0^{2\pi}\int_0^{\pi}\ldots\sin\theta d\theta d\varphi$. Thus, the combination of equations (B.12) and (B.13) yields

$$4\pi i^{n'}\vec{E}_o\cdot\left[j_{n'}(k_o r) Rg\vec{M}_{m'n'}(k_o r,\theta'',\varphi'')\right]$$

$$= (-1)^{-m'}[j_{n'}(k_o r)]^2 a_{-m'n'}$$

Therefore, the expansion coefficients a_{mn} of the incident field can be expressed in the following compact form

$$a_{mn} = (-1)^m i^n \frac{1}{\gamma_{mn}}\frac{(2n+1)}{n(n+1)}\vec{E}_o\cdot\vec{C}_{-mn}(\theta'',\varphi'') \tag{B.14}$$

A similar procedure leads to the expansion coefficients b_{mn} for the incident field. That is, equations (B.1) and (B.3) also provide

$$\vec{E}_o \cdot \int_{esf} e^{ik_o \vec{n}_i \cdot \vec{r}} Rg\vec{N}_{m'n'}(k_o r, \theta, \varphi)\, d\Omega =$$

$$= \int_{esf} \left[\sum_{n=1}^{\infty} \sum_{m=-n}^{+n} a_{mn} Rg\vec{M}_{mn}(kr, \theta, \varphi) + b_{mn} Rg\vec{N}_{mn}(kr, \theta, \varphi) \right]$$

$$\cdot\, Rg\vec{N}_{m'n'}(k_o r, \theta, \varphi) d\Omega$$

$$= (-1)^{-m'} \left\{ n'(n'+1) \left[\frac{j_{n'}(k_o r)}{k_o r} \right]^2 + \left\{ \left. \frac{[u j_{n'}(u)]'}{u} \right|_{kr} \right\}^2 \right\} b_{-m'n'} \qquad \text{(B.15)}$$

Substituting the initial expression for $Rg\vec{N}_{m'n'}(k_o r, \theta, \varphi)$ into the left-hand side of equation (B.15)and using expressions (22) and (24) on page 172 of Tsang et al. [44], one gets

$$(-1)^{-m'} \left\{ n'(n'+1) \left[\frac{j_{n'}(k_o r)}{k_o r} \right]^2 + \left\{ \left. \frac{[u j_n(u)]'}{u} \right|_{kr} \right\}^2 \right\} b_{-m'n'}$$

$$= \gamma_{m'n'} \vec{E}_o \cdot \left\{ n'(n'+1) \left[\frac{j_{n'}(k_o r)}{k_o r} \right] \cdot \right.$$

$$\left. \cdot \int_{esf} e^{ik_o r \hat{n}_i \cdot \hat{r}}\, \vec{P}_{m'n'}(\theta, \varphi) d\Omega + \left. \frac{[u j_n(u)]'}{u} \right|_{k_o r} \int_{esf} e^{ik_o r \hat{n}_i \cdot \hat{r}}\, \vec{B}_{m'n'}(\theta, \varphi) d\Omega \right\}$$

$$= \gamma_{m'n'} \vec{E}_o \cdot \left\{ n'(n'+1) \frac{4\pi}{\gamma'_{m'n'}} i^{n'-1} \left[\frac{j_{n'}(k_o r)}{k_o r} \right] Rg\vec{L}_{m'n'}(k_o r, \theta'', \varphi'') \right.$$

$$\left. + \frac{4\pi}{\gamma_{m'n'}} i^{n'-1} \left. \frac{[u j_n(u)]'}{u} \right|_{k_o r} Rg\vec{N}_{m'n'}(k_o r, \theta'', \varphi'') \right\}$$

Expressions (18) and (15) on page 171 of Tsang et al. [44] show that $Rg\vec{L}_{m'n'}$ and $Rg\vec{N}_{m'n'}$ have components that are proportional to $\vec{P}_{m'n'}(\theta,\varphi)$ and that this vector is aligned with the $\hat{r}$ direction. Since $\vec{E}_o$ does not have component in the $\hat{r}$ direction, the contribution from this term vanishes in the immediately above equation, which becomes

$$(-1)^{-m'}\left\{n'(n'+1)\left[\frac{j_{n'}(k_o r)}{k_o r}\right]^2+\left\{\frac{[uj_n(u)]'}{u}\bigg|_{kr}\right\}^2\right\}b_{-m'n'}=$$

$$=\gamma_{m'n'}\vec{E}_o\cdot\left\{n'(n'+1)\frac{4\pi}{\gamma'_{m'n'}}i^{n'-1}\left[\frac{j_{n'}(k_o r)}{k_o r}\right]\gamma'_{m'n'}\left[\frac{j_{n'}(k_o r)}{k_o r}\right]\vec{B}_{m'n'}(\theta'',\varphi'')+\right.$$

$$\left.+\frac{4\pi}{\gamma_{m'n'}}i^{n'-1}\frac{[uj_n(u)]'}{u}\bigg|_{k_o r}\gamma_{m'n'}\frac{[uj_n(u)]'}{u}\bigg|_{k_o r}\vec{B}_{m'n'}(\theta'',\varphi'')\right\}=$$

$$=4\pi\gamma_{m'n'}i^{n'-1}\left\{n'(n'+1)\left[\frac{j_{n'}(k_o r)}{k_o r}\right]^2+\left\{\frac{[\mu j_n(\mu)]'}{\mu}\right\}^2\right\}\vec{E}_o\cdot\vec{B}_{m'n'}(\theta'',\varphi'')$$

In the immediately above equation, $\gamma'_{m'n'}=\sqrt{n'(n'+1)}\gamma_{m'n'}$.Therefore, the expansion coefficients b_{mn} of the incident field can be expressed in the following compact form

$$b_{mn}=(-1)^m\frac{i^n}{i}\frac{1}{\gamma_{mn}}\frac{(2n+1)}{n(n+1)}\vec{E}_o.\vec{B}_{-mn}(\theta'',\varphi'') \qquad \text{(B.16)}$$

C.
Application of the Boundary Conditions to the Scattering Problem.

The boundary conditions that are used to solve the scattering problem can be written as follow

$$\hat{n} \times \vec{E}_+(\vec{r}) = \hat{n} \times \vec{E}_-(\vec{r}) \tag{C.1}$$

$$\hat{n} \times \vec{H}_+(\vec{r}) = \hat{n} \times \vec{H}_-(\vec{r}) \tag{C.2}$$

applicable at any arbitrary point $\vec{r} \epsilon\, S$ (at the particle surface). The plus (+) and minus $(-)$ signs indicate fields determined at then immediate exterior and interior of the particle, respectively. That is, continuity of the tangential electric and magnetic fields components across the boundary is required. To simplify notation in the present Appendix, $\hat{n}$ represents the unit vector orthogonal to S at any of its point and directed toward the exterior of the particle. The same vector is represented by $\hat{n}_1$ in Chapter 4. Expressions (4.15) and (4.16) provide the values of $\vec{E}_-(\vec{r})$ and $\vec{H}_-(\vec{r})$ when $\vec{r} \to S$

$$\hat{n} \times \vec{E}_+(\vec{r}) = \hat{n} \times \vec{E}_-(\vec{r}) = \\ = \sum_{n'=1}^{\infty} \sum_{m'=-n'}^{n'} c_{m'n'}\, \hat{n} \times Rg\vec{M}_{m'n'}(k_1 r, \theta, \varphi) + d_{m'n'}\, \hat{n} \\ \times Rg\vec{N}_{m'n'}(k_1 r, \theta, \varphi) \tag{C.3}$$

$$\hat{n} \times \vec{H}_+(\vec{r}) = \hat{n} \times \vec{H}_-(\vec{r}) = \\ = \frac{k_1}{i\omega\mu_o} \sum_{n'=1}^{\infty} \sum_{m'=-n'}^{n'} d_{m'n'} \hat{n} \times Rg\vec{M}_{m'n'}(k_1 r, \theta, \varphi) + c_{m'n'} \hat{n} \\ \times Rg\vec{N}_{m'n'}(k_1 r, \theta, \varphi) \tag{C.4}$$

Substituting equations (C.3) and (C.4) into equations (4.10) and (4.11) and using the vector identity $\vec{A} \times \vec{B} \cdot \vec{C} = \vec{A} \cdot \vec{B} \times \vec{C}$, one obtains

$$a_{mn} = (-1)^m k_o \sum_{n'=1}^{\infty} \sum_{m'=-n'}^{n'} \left\{ \left[(-ik_1) \int_S \hat{n} \cdot Rg\vec{M}_{m'n'}(k_1 r, \theta, \varphi) \times \vec{M}_{-mn}(k_o r, \theta, \varphi) \right] d_{m'n'} \right.$$

$$+ \left[(-ik_1) \int_S \hat{n} \cdot Rg\vec{N}_{m'n'}(k_1 r, \theta, \varphi) \times \vec{M}_{-mn}(k_o r, \theta, \varphi) dS \right] c_{m'n'} +$$

$$+ \left[(-ik_o) \int_S \hat{n} \cdot Rg\vec{M}_{m'n'}(k_1 r, \theta, \varphi) \times \vec{N}_{-mn}(k_o r, \theta, \varphi) dS \right] c_{m'n'} +$$

$$\left. + \left[(-ik_o) \int_S \hat{n} \cdot Rg\vec{N}_{m'n'}(k_1 r, \theta, \varphi) \times \vec{N}_{-mn}(k_o r, \theta, \varphi) dS \right] d_{m'n'} \right\}$$

Therefore

$$a_{mn} = \sum_{n'=1}^{\infty} \sum_{m'=-n'}^{n'} Q^{11}_{mnm'n'} c_{m'n'} + Q^{12}_{mnm'n'} d_{m'n'} \tag{C.5}$$

where

$$Q^{11}_{mnm'n'} = (-1)^m (-ik_o k_1) \int_S \hat{n} \cdot Rg\vec{N}_{m'n'}(k_1 r, \theta, \varphi) \times \vec{M}_{-mn}(k_o r, \theta, \varphi) dS + \tag{C.6}$$

$$+ (-1)^m \left(-ik_o{}^2\right) \int_S \hat{n} \cdot Rg\vec{M}_{m'n'}(k_1 r, \theta, \varphi) \times \vec{N}_{-mn}(k_o r, \theta, \varphi) dS$$

$$Q^{11}_{mnm'n'} = (-1)^m (-ik_o)(k_1 J^{21}_{mnm'n'} + k_o J^{12}_{mnm'n'}) \tag{C.7}$$

and

$$Q^{12}_{mnm'n'} = (-1)^m (-ik_o k_1) \int_S \hat{n} \cdot Rg\vec{M}_{m'n'}(k_1 r, \theta, \varphi) \times \vec{M}_{-mn}(k_o r, \theta, \varphi) dS + \tag{C.8}$$

$$+ (-1)^m (-ik_o{}^2) \int_S \hat{n} \cdot Rg\vec{N}_{m'n'}(k_1 r, \theta, \varphi) \times \vec{N}_{-mn}(k_o r, \theta, \varphi) dS$$

$$Q^{12}_{mnm'n'} = (-1)^m (-ik_o)(k_1 J^{11}_{mnm'n'} + k_o J^{22}_{mnm'n'}) \tag{C.9}$$

Similarly

$$b_{mn} = (-1)^m k_o \sum_{n'=1}^{\infty} \sum_{m'=-n'}^{n'} \left\{ \left[(-ik_1) \int_S \hat{n} \cdot Rg\vec{M}_{m'n'}(k_1 r, \theta, \varphi) \times \vec{N}_{-mn}(k_o r, \theta, \varphi) dS \right] d_{m'n'} + \right.$$

$$+ \left[(-ik_1) \int_S \hat{n} \cdot Rg\vec{N}_{m'n'}(k_1 r, \theta, \varphi) \times \vec{N}_{-mn}(k_o r, \theta, \varphi) dS \right] c_{m'n'} +$$

$$+ \left[(-ik_o) \int_S \hat{n} \cdot Rg\vec{M}_{m'n'}(k_1 r, \theta, \varphi) \times \vec{M}_{-mn}(k_o r, \theta, \varphi) dS \right] c_{m'n'} +$$

$$\left. + \left[(-ik_o) \int_S \hat{n} \cdot Rg\vec{N}_{m'n'}(k_1 r, \theta, \varphi) \times \vec{M}_{-mn}(k_o r, \theta, \varphi) dS \right] d_{m'n'} \right\}$$

$$b_{mn} = \sum_{n'=1}^{\infty} \sum_{m'=-n'}^{n'} Q^{21}_{mnm'n'} c_{m'n'} + Q^{22}_{mnm'n'} d_{m'n'} \tag{C.10}$$

where

$$Q^{21}_{mnm'n'} = (-1)^m (-ik_o k_1) \int_S \hat{n} \cdot Rg\vec{N}_{m'n'}(k_1 r, \theta, \varphi) \times \vec{N}_{-mn}(k_o r, \theta, \varphi) dS + \tag{C.11}$$

$$+ (-1)^m \left(-ik_o{}^2\right) \int_S \hat{n} \cdot Rg\vec{M}_{m'n'}(k_1 r, \theta, \varphi) \times \vec{M}_{-mn}(k_o r, \theta, \varphi) dS$$

$$Q^{21}_{mnm'n'} = (-1)^m (-ik_o)(k_1 J^{22}_{mnm'n'} + k_o J^{11}_{mnm'n'}) \tag{C.12}$$

and

$$Q^{22}_{mnm'n'} = (-1)^m (-ik_o k_1) \int_S \hat{n} \cdot Rg\vec{M}_{m'n'}(k_1 r, \theta, \varphi) \times \vec{N}_{-mn}(k_o r, \theta, \varphi) dS + \tag{C.13}$$

$$+(-1)^m\left(-ik_o{}^2\right)\int_S \hat{n}\cdot Rg\vec{N}_{m\prime n\prime}(k_1 r,\theta,\varphi) \times \vec{M}_{-mn}(k_o r,\theta,\varphi)dS$$

$$Q^{22}_{mnm\prime n\prime} = (-1)^m(-ik_o)(k_1 J^{12}_{mnm\prime n\prime} + k_o J^{12}_{mnm\prime n\prime}) \tag{C.14}$$

Similarly, substituting equations (C.3) and (C.4) into equations (4.13) and (4.14) and using the vector identity $\vec{A}\times\vec{B}\cdot\vec{C} = \vec{A}\cdot\vec{B}\times\vec{C}$, we obtain

$$p_{mn} = -(-1)^m k_o \sum_{n\prime=1}^{\infty}\sum_{m\prime=-n\prime}^{n\prime}\left\{\left[(-ik_1)\int_S \hat{n}\cdot Rg\vec{M}_{m\prime n\prime}(k_1 r,\theta,\varphi) \times Rg\vec{M}_{-mn}(k_o r,\theta,\varphi)\right]d_{m\prime n\prime} + \left[(-ik_1)\int_S \hat{n}\cdot Rg\vec{N}_{m\prime n\prime}(k_1 r,\theta,\varphi)\times Rg\vec{M}_{-mn}(k_o r,\theta,\varphi)dS\right]c_{m\prime n\prime} + \left[(-ik_o)\int_S \hat{n}\cdot Rg\vec{M}_{m\prime n\prime}(k_1 r,\theta,\varphi)\times Rg\vec{N}_{-mn}(k_o r,\theta,\varphi)dS\right]c_{m\prime n\prime} + \left[(-ik_o)\int_S \hat{n}\cdot Rg\vec{N}_{m\prime n\prime}(k_1 r,\theta,\varphi)\times Rg\vec{N}_{-mn}(k_o r,\theta,\varphi)dS\right]d_{m\prime n\prime}\right\}$$

Therefore

$$p_{mn} = -\sum_{n\prime=1}^{\infty}\sum_{m\prime=-n\prime}^{n\prime} RgQ^{11}_{mnm\prime n\prime}c_{m\prime n\prime} + RgQ^{12}_{mnm\prime n\prime}d_{m\prime n\prime} \tag{C.15}$$

where

$$RgQ^{11}_{mnm\prime n\prime} = (-1)^m(-ik_o k_1)\int_S \hat{n}\cdot Rg\vec{N}_{m\prime n\prime}(k_1 r,\theta,\varphi) \times Rg\vec{M}_{-mn}(k_o r,\theta,\varphi)dS + \tag{C.16}$$

$$+(-1)^m\left(-ik_o{}^2\right)\int_S \hat{n}\cdot Rg\vec{M}_{m\prime n\prime}(k_1 r,\theta,\varphi) \times Rg\vec{N}_{-mn}(k_o r,\theta,\varphi)dS$$

$$RgQ^{11}_{mnm\prime n\prime} = (-1)^m(-ik_o)(k_1 RgJ^{21}_{mnm\prime n\prime} + k_o RgJ^{12}_{mnm\prime n\prime}) \quad \text{(C.17)}$$

$$RgQ^{12}_{mnm\prime n\prime} = (-1)^m(-ik_o k_1)\int_S \hat{n}\cdot Rg\vec{M}_{m\prime n\prime}(k_1 r,\theta,\varphi) \times Rg\vec{M}_{-mn}(k_o r,\theta,\varphi)dS + \quad \text{(C.18)}$$

$$+(-1)^m\left(-ik_o{}^2\right)\int_S \hat{n}\cdot Rg\vec{N}_{m\prime n\prime}(k_1 r,\theta,\varphi) \times Rg\vec{N}_{-mn}(k_o r,\theta,\varphi)dS$$

$$RgQ^{12}_{mnm\prime n\prime} = (-1)^m(-ik_o)(k_1 RgJ^{11}_{mnm\prime n\prime} + k_o RgJ^{22}_{mnm\prime n\prime}) \quad \text{(C.19)}$$

Similarly

$$q_{mn} = -(-1)^m k_o \sum_{n\prime=1}^{\infty}\sum_{m\prime=-n\prime}^{n\prime}\left\{\left[(-ik_1)\int_S \hat{n}\cdot Rg\vec{M}_{m\prime n\prime}(k_1 r,\theta,\varphi) \times Rg\vec{N}_{-mn}(k_o r,\theta,\varphi)\right]d_{m\prime n\prime} + \right.$$

$$+\left[(-ik_1)\int_S \hat{n}\cdot Rg\vec{N}_{m\prime n\prime}(k_1 r,\theta,\varphi)\times Rg\vec{N}_{-mn}(k_o r,\theta,\varphi)dS\right]c_{m\prime n\prime} +$$

$$+\left[(-ik_o)\int_S \hat{n}\cdot Rg\vec{M}_{m\prime n\prime}(k_1 r,\theta,\varphi)\times Rg\vec{M}_{-mn}(k_o r,\theta,\varphi)dS\right]c_{m\prime n\prime} +$$

$$\left.+\left[(-ik_o)\int_S \hat{n}\cdot Rg\vec{N}_{m\prime n\prime}(k_1 r,\theta,\varphi)\times Rg\vec{M}_{-mn}(k_o r,\theta,\varphi)dS\right]d_{m\prime n\prime}\right\}$$

$$q_{mn} = -\sum_{n\prime=1}^{\infty}\sum_{m\prime=-n\prime}^{n\prime} RgQ^{21}_{mnm\prime n\prime}c_{m\prime n\prime} + RgQ^{22}_{mnm\prime n\prime}d_{m\prime n\prime} \quad \text{(C.20)}$$

$$RgQ^{21}_{mnm'n'} = (-1)^m(-ik_o k_1)\int_S \hat{n}\cdot Rg\vec{N}_{m'n'}(k_1 r,\theta,\varphi) \times Rg\vec{N}_{-mn}(k_o r,\theta,\varphi)dS + +(-1)^m\left(-ik_o{}^2\right)\int_S \hat{n}\cdot Rg\vec{M}_{m'n'}(k_1 r,\theta,\varphi) \times Rg\vec{M}_{-mn}(k_o r,\theta,\varphi)dS \quad \text{(C.21)}$$

$$RgQ^{21}_{mnm'n'} = (-1)^m(-ik_o)(k_1 RgJ^{22}_{mnm'n'} + k_o RgJ^{11}_{mnm'n'}) \quad \text{(C.22)}$$

$$RgQ^{22}_{mnm'n'} = (-1)^m(-ik_o k_1)\int_S \hat{n}\cdot Rg\vec{M}_{m'n'}(k_1 r,\theta,\varphi) \times Rg\vec{N}_{-mn}(k_o r,\theta,\varphi)dS + +(-1)^m\left(-ik_o{}^2\right)\int_S \hat{n}\cdot Rg\vec{N}_{m'n'}(k_1 r,\theta,\varphi) \times Rg\vec{M}_{-mn}(k_o r,\theta,\varphi)dS \quad \text{(C.23)}$$

$$RgQ^{22}_{mnm'n'} = (-1)^m(-ik_o)(k_1 RgJ^{12}_{mnm'n'} + k_o RgJ^{21}_{mnm'n'}) \quad \text{(C.24)}$$

D.
Expansion of the Surface Integrals in Vector Spherical Wave Functions.

The vector spherical wave functions are used in the expansion of the incident, scattered and internal fields. They are defined as follow

$$\vec{M}_{mn}(kr,\theta,\varphi) = \gamma_{mn} h_n^{(1)}(kr)\vec{C}_{mn}(\theta,\varphi)$$

$$\vec{M}_{mn}(kr,\theta,\varphi) = \gamma_{mn} h_n^{(1)}(kr)\left\{ im\frac{P_n^m(\cos\theta)}{\sin\theta}\hat{\theta} - \frac{d}{d\theta}[P_n^m(\cos\theta)]\hat{\varphi}\right\} e^{jm\varphi} \quad \text{(D.1)}$$

where $\gamma_{mn} = \sqrt{\frac{(2n+1)(n-m)!}{4\pi n(n+1)(n+m)!}}$.

The vector spherical wave function $\vec{M}_{mn}$ can also be expressed in terms of the Wigner d functions

$$\vec{M}_{mn}(kr,\theta,\varphi) = \sqrt{\frac{(2n+1)}{4\pi n(n+1)}} h_n^{(1)}(kr) \times \quad \text{(D.2)}$$

$$\left\{ im\frac{d_{om}^n(\theta)}{\sin\theta}\hat{\theta} - \frac{d}{d\theta}[d_{om}^n(\theta)]\hat{\varphi}\right\} e^{jm\varphi}$$

where

$$d_{om}^n(\theta) = \sqrt{\frac{(n-m)!}{(n+m)!}} P_n^m(\cos\theta) \quad \text{(D.3)}$$

Similarly

$$Rg\vec{M}_{mn}(kr,\theta,\varphi) = \sqrt{\frac{(2n+1)}{4\pi n(n+1)}} \times \quad \text{(D.4)}$$

$$\times j_n(kr)\left\{im\frac{d_{om}^n(\theta)}{\sin\theta}\hat{\theta}-\frac{d}{d\theta}[d_{om}^n(\theta)]\hat{\varphi}\right\}e^{jm\varphi}$$

The vector spherical wave function $Rg\vec{M}_{mn}$ can also be expressed in terms of associated Legendre functions

$$Rg\vec{M}_{mn}(kr,\theta,\varphi)=\gamma_{mn}j_n(kr)\times$$
$$\times\left\{im\frac{P_n^m(\cos\theta)}{\sin\theta}\hat{\theta}-\frac{d}{d\theta}[P_n^m(\cos\theta)]\hat{\varphi}\right\}e^{jm\varphi} \quad \text{(D.5)}$$

In terms of associated Legendre functions, the vector spherical wave function $\vec{N}_{mn}$ is given by

$$\vec{N}_{mn}(kr,\theta,\varphi)=\gamma_{mn}\left\{\left[\frac{h_n^{(1)}(kr)}{kr}\right]n(n+1)P_n^m(\cos\theta)\hat{R}+\right.$$
$$+\left.\frac{\left[uh_n^{(1)}(u)\right]'}{u}\right|_{u=kr}\frac{d}{d\theta}[P_n^m(\cos\theta)]\hat{\theta}+ \quad \text{(D.6)}$$
$$\left.+im\frac{\left[uh_n^{(1)}(u)\right]'}{u}\right|_{u=kr}\frac{P_n^m(\cos\theta)}{\sin\theta}\hat{\varphi}\right\}e^{jm\varphi}$$

$$\vec{N}_{mn}(kr,\theta,\varphi)=\sqrt{\frac{(2n+1)}{4\pi n(n+1)}}\left\{\left[\frac{h_n^{(1)}(kr)}{kr}\right]n(n+1)d_{om}^n(\theta)\widehat{R}+\right.$$
$$+\left.\frac{\left[uh_n^{(1)}(u)\right]'}{u}\right|_{u=kr}\frac{d}{d\theta}[d_{om}^n(\theta)]\hat{\theta}+ \quad \text{(D.7)}$$
$$\left.+im\frac{\left[\mu h_n^{(1)}(\mu)\right]'}{\mu}\right|_{\mu=kr}\frac{d_{om}^n(\theta)}{\sin\theta}\hat{\varphi}\right\}e^{jm\varphi}$$

Analogously, the vector spherical wave function $Rg\vec{N}_{mn}$ is defined by

$$Rg\vec{N}_{mn}(kr,\theta,\varphi) = \gamma_{mn}\left\{\left[\frac{j_n(kr)}{kr}\right] n(n+1)P_n^m(\cos\theta)\hat{R} + \right.$$
$$+\left.\frac{[uj_n(u)]'}{u}\right|_{u=kr}\frac{d}{d\theta}[P_n^m(\cos\theta)]\hat{\theta} +$$
$$\left. +im\frac{[uj_n(u)]'}{u}\right|_{u=kr}\frac{P_n^m(\cos\theta)}{\sin\theta}\hat{\varphi}\Bigg\} e^{jm\varphi} \quad \text{(D.8)}$$

$$Rg\vec{N}_{mn}(kr,\theta,\varphi) = \sqrt{\frac{(2n+1)}{4\pi n(n+1)}}\left\{\left[\frac{j_n(kr)}{kr}\right] n(n+1)d_{om}^n(\theta)\hat{R} + \right.$$
$$+\left.\frac{[uj_n(u)]'}{u}\right|_{u=kr}\frac{d}{d\theta}[d_{om}^n(\theta)]\hat{\theta} + \quad \text{(D.9)}$$
$$\left. +im\frac{[uj_n(u)]'}{u}\right|_{u=kr}\frac{d_{om}^n(\theta)}{\sin\theta}\hat{\varphi}\Bigg\} e^{jm\varphi}$$

Based on the above definitions, the surface integrals of Appendix C can be expanded as follows. It should be remembered that, in these integral (performed along the surface *S* of the axis-symmetric particle), vector products between two VSWFs are followed by a scalar product by $\hat{n}$. To simplify notation in the present Appendix, $\hat{n}$ again represents the unit vector orthogonal to *S* at any of its point and directed toward the exterior of the particle. The same vector is represented by $\hat{n}_1$ in Chapter 4. Since the particles of interest display axial symmetry, $\hat{n}$ has no azimuthal component $\hat{\varphi}$. Thus, the azimuthal component of the vector products between two VSWFs can be omitted from the following derivations.

The $J_{mnm'n'}^{11}$ integral

$$J_{mnm'n'}^{11} = (-1)^m \int_S \hat{n}(\vec{r}) \cdot \left[Rg\vec{M}_{m'n'}(k_1 r,\theta,\varphi) \times \vec{M}_{-mn}(k_o r,\theta,\varphi)\right] dS$$

where

$$Rg\vec{M}_{m'n'}(k_1 r,\theta,\varphi)\times\vec{M}_{-mn}(k_o r,\theta,\varphi)=\ \gamma_{m'n'}\gamma_{-mn}j_{n'}(k_1 r)h_n^{(1)}(k_o r).$$

$$.\left\{im'\frac{P_{n'}^{m'}(\cos\theta)}{\sin\theta}\hat{\theta}-\frac{d}{d\theta}\left[P_{n'}^{m'}(\cos\theta)\right]\hat{\varphi}\right\}\times$$

$$\times\left\{(-im)\frac{P_n^{-m}(\cos\theta)}{\sin\theta}\hat{\theta}-\frac{d}{d\theta}[P_n^{-m}(\cos\theta)]\hat{\varphi}\right\}e^{j(m'-m)\varphi}$$

$$=\gamma_{m'n'}\gamma_{-mn}j_{n'}(k_1 r)h_n^{(1)}(k_o r)\times$$

$$\times\left\{-(im')\frac{P_{n'}^{m'}(\cos\theta)}{\sin\theta}\frac{d}{d\theta}[P_n^{-m}(\cos\theta)]-\right.$$

$$\left.-(im)\frac{d}{d\theta}\left[P_{n'}^{m'}(\cos\theta)\right]\frac{P_n^{-m}(\cos\theta)}{\sin\theta}\right\}e^{j(m'-m)\varphi}\hat{R} \qquad \text{(D.10)}$$

Therefore

$$J_{mnm'n'}^{11}=2\pi(-1)^m\delta_{mm'}\gamma_{mn'}\gamma_{-mn}(-im)\times$$

$$\times\int_0^{\pi}j_{n'}(k_1 r)h_n^{(1)}(k_o r)\times$$

$$\left\{\frac{P_{n'}^{m}(\cos\theta)}{\sin\theta}\frac{d}{d\theta}[P_n^{-m}(\cos\theta)]+\right. \qquad \text{(D.11)}$$

$$\left.+\frac{P_n^{-m}(\cos\theta)}{\sin\theta}\frac{d}{d\theta}[P_{n'}^{m}(\cos\theta)]\right\}r^2\sin\theta\,d\theta$$

The $J_{mnm'n'}^{22}$ integral

$$\boldsymbol{J_{mnm'n'}^{22}}=(-1)^m\int_S\hat{n}(\vec{r})\cdot\left[Rg\vec{N}_{m'n'}(k_1 r,\theta,\varphi)\times\vec{N}_{-mn}(k_o r,\theta,\varphi)\right]dS$$

where

$$Rg\vec{N}_{m'n'}(k_1 r,\theta,\varphi)\times\vec{N}_{-mn}(k_o r,\theta,\varphi)=\gamma_{m'n'}\gamma_{-mn}\times$$

$$\times\left\{\frac{j_{n'}(k_1 r)}{k_1 r}n'(n'+1)P_{n'}^{m'}(\cos\theta)\hat{R}+\right.$$

$$+\frac{[uj_{n'}(u)]'}{u}\Bigg|_{u=k_1r}\frac{d}{d\theta}\left[P_{n'}^{m'}(\cos\theta)\right]\hat{\theta}+(im')\frac{[uj_{n'}(u)]'}{u}\Bigg|_{u=k_1r}\frac{P_{n'}^{m'}(\cos\theta)}{\sin\theta}\hat{\varphi}\Bigg\}\times$$

$$\times\left\{\frac{h_n^{(1)}(k_or)}{k_or}n(n+1)P_n^{-m}(\cos\theta)\,\hat{R}+\frac{\left[uh_n^{(1)}(u)\right]'}{u}\Bigg|_{u=k_or}\frac{d}{d\theta}[P_n^{-m}(\cos\theta)]\hat{\theta}+\right.$$

$$\left.+(-im)\frac{\left[uh_n^{(1)}(u)\right]'}{u}\Bigg|_{u=k_or}\frac{P_n^{-m}(\cos\theta)}{\sin\theta}\hat{\varphi}\right\}.e^{j(m'-m)\varphi}$$

$$Rg\vec{N}_{m'n'}(k_1r,\theta,\varphi)\times\vec{N}_{-mn}(k_or,\theta,\varphi)=\gamma_{m'n'}\gamma_{-mn}\times$$

$$\times\left\{(im)n'(n'+1)\frac{j_{n'}(k_1r)}{k_1r}\frac{\left[uh_n^{(1)}(u)\right]'}{u}\Bigg|_{u=k_or}P_{n'}^{m'}(\cos\theta)\frac{P_n^{-m}(\cos\theta)}{\sin\theta}\hat{\theta}+\right.$$

$$+\frac{\left[uj_{n'}(u)\right]'}{u}\Bigg|_{u=k_1r}\frac{d}{d\theta}\left[P_{n'}^{m'}(\cos\theta)\right](-im)\times$$

$$\times\frac{\left[uh_n^{(1)}(u)\right]'}{u}\Bigg|_{u=k_or}\frac{P_n^{-m}(\cos\theta)}{\sin\theta}\hat{R}$$

$$+(im')\frac{\left[uj_{n'}(u)\right]'}{u}\Bigg|_{u=k_1r}\frac{P_{n'}^{m'}(\cos\theta)}{\sin\theta}\frac{h_n^{(1)}(k_or)}{k_or}\times$$

$$\times n(n+1)P_n^{-m}(\cos\theta)\hat{\theta}-$$

$$-(im')\frac{[uj_{n'}(u)]'}{u}\Bigg|_{u=k_1r}\frac{P_{n'}^{m'}(\cos\theta)}{\sin\theta}\times$$

$$\left.\frac{\left[uh_n^{(1)}(u)\right]'}{u}\Bigg|_{u=k_or}\frac{d}{d\theta}[P_n^{-m}(\cos\theta)]\hat{R}\right\}e^{j(m'-m)\varphi}\qquad\text{(D.12)}$$

Therefore

$$J_{mnm'n'}^{22}=2\pi(-1)^m\delta_{mm'}\gamma_{mn'}\gamma_{-mn}(-im)\times$$

$$\times \int_0^{\pi} \left\{ \left. \frac{[uj_{n'}(u)]'}{u} \right|_{u=k_1 r} \left. \frac{\left[uh_n^{(1)}(u)\right]'}{u} \right|_{u=k_o r} \times \right.$$
$$\times \left[\frac{P_n^{-m}(\cos\theta)}{\sin\theta} \frac{d}{d\theta} P_{n'}^{m}(\cos\theta) + \right.$$
$$\left. + \frac{P_{n'}^{m}(\cos\theta)}{\sin\theta} \frac{d}{d\theta} P_n^{-m}(\cos\theta) \right] + \qquad \text{(D.13)}$$
$$+ \frac{1}{r}\frac{dr}{d\theta} \left[n'(n'+1) \frac{j_{n'}(k_1 r)}{k_1 r} \left. \frac{\left[uh_n^{(1)}(u)\right]'}{u} \right|_{u=k_o r} \right.$$
$$\left. + n(n+1) \left. \frac{[uj_{n'}(u)]'}{u} \right|_{u=k_1 r} \frac{h_n^{(1)}(k_o r)}{k_o r} \right] \cdot$$
$$\left. \cdot \frac{P_{n'}^{m}(\cos\theta)}{\sin\theta} P_n^{-m}(\cos\theta) \right\} r^2 \sin\theta \, d\theta$$

The $J_{mnm'n'}^{12}$ integral

$$J_{mnm'n'}^{12} = (-1)^m \int_S \hat{n}(\vec{r}) \cdot \left[Rg\vec{M}_{m'n'}(k_1 r, \theta, \varphi) \times \vec{N}_{-mn}(k_o r, \theta, \varphi) \right] dS$$

This integral can be expanded as follow

$$Rg\vec{M}_{m'n'}(k_1 r, \theta, \varphi) \times \vec{N}_{-mn}(k_o r, \theta, \varphi) =$$
$$= \gamma_{m'n'}\gamma_{-mn} j_{n'}(k_1 r) \left\{ (im') \frac{P_{n'}^{m'}(\cos\theta)}{\sin\theta} \hat{\theta} - \frac{d}{d\theta}\left[P_{n'}^{m'}(\cos\theta)\right] \hat{\varphi} \right\} \times$$
$$\times \left\{ \frac{h_n^{(1)}(k_o r)}{k_o r} n(n+1) P_n^{-m}(\cos\theta) \, \hat{R} + \right.$$
$$+ \left. \left. \frac{\left[uh_n^{(1)}(u)\right]'}{u} \right|_{u=k_o r} \frac{d}{d\theta}[P_n^{-m}(\cos\theta)] \hat{\theta} \right.$$
$$\left. + (-im) \left. \frac{\left[uh_n^{(1)}(u)\right]'}{u} \right|_{u=k_o r} \frac{P_n^{-m}(\cos\theta)}{\sin\theta} \hat{\varphi} \right\} e^{j(m'-m)\varphi}$$

$$Rg\vec{M}_{m'n'}(k_1r,\theta,\varphi)\times\vec{N}_{-mn}(k_or,\theta,\varphi)=\gamma_{m'n'}\gamma_{-mn}j_{n'}(k_1r)\times$$
$$\times\left\{m'm\frac{\left[uh_n^{(1)}(u)\right]'}{u}\Bigg|_{u=k_or}\frac{P_{n'}^{m'}(\cos\theta)}{\sin\theta}\frac{P_n^{-m}(\cos\theta)}{\sin\theta}\hat{R}-\right.$$
$$-\frac{h_n^{(1)}(k_or)}{k_or}n(n+1)\frac{d}{d\theta}\left[P_{n'}^{m'}(\cos\theta)\right]P_n^{-m}(\cos\theta)\,\hat{\theta}+ \quad (D.14)$$
$$\left.+\frac{\left[uh_n^{(1)}(u)\right]'}{u}\Bigg|_{u=k_or}\frac{d}{d\theta}\left[P_{n'}^{m'}(\cos\theta)\right]\frac{d}{d\theta}[P_n^{-m}(\cos\theta)]\hat{R}\right\}e^{j(m'-m)\varphi}$$

Therefore

$$J_{mnm'n'}^{12}=2\pi(-1)^m\delta_{mm'}\gamma_{mn'}\gamma_{-mn}\times$$
$$\times\int_0^\pi j_{n'}(k_1r)\left\{\frac{\left[uh_n^{(1)}(u)\right]'}{u}\Bigg|_{u=k_or}\left[m^2\frac{P_{n'}^m(\cos\theta)}{\sin\theta}\frac{P_n^{-m}(\cos\theta)}{\sin\theta}\right.\right. \quad (D.15)$$
$$\left.+\frac{d}{d\theta}\left[P_{n'}^m(\cos\theta)\right]\frac{d}{d\theta}[P_n^{-m}(\cos\theta)]\right]+$$
$$\left.+\frac{1}{r}\frac{dr}{d\theta}\frac{h_n^{(1)}(k_or)}{k_or}n(n+1)\frac{d}{d\theta}\left[P_{n'}^m(\cos\theta)\right]P_n^{-m}(\cos\theta)\right\}r^2\sin\theta d\theta$$

The $J_{mnm'n'}^{21}$ integral

$$J_{mnm'n'}^{21}=(-1)^m\int_S\hat{n}(\vec{r})\cdot\left[Rg\vec{N}_{m'n'}(k_1r,\theta,\varphi)\times\vec{M}_{-mn}(k_or,\theta,\varphi)\right]dS$$

This integral can be expanded as follow

$$Rg\vec{N}_{m'n'}(k_1r,\theta,\varphi)\times\vec{M}_{-mn}(k_or,\theta,\varphi)=$$
$$=\gamma_{m'n'}\gamma_{-mn}h_n^{(1)}(k_or)\left\{\left[\frac{j_{n'}(k_1r)}{k_1r}\right]n'(n'+1)P_{n'}^{m'}(\cos\theta)\,\hat{R}\right.$$
$$\left.+\frac{[uj_{n'}(u)]'}{u}\Bigg|_{u=k_1r}\frac{d}{d\theta}\left[P_{n'}^{m'}(\cos\theta)\right]\hat{\theta}\times\right.$$

$$\times (im')\frac{[uj_{n'}(u)]'}{u}\Big|_{u=k_1 r}\frac{P_{n'}^{m'}(\cos\theta)}{\sin\theta}\hat{\varphi}\Big\}$$
$$\times\Big\{(-im)\frac{P_n^{-m}(\cos\theta)}{\sin\theta}\hat{\theta}-\frac{d}{d\theta}[P_n^{-m}(\cos\theta)]\hat{\varphi}\Big\}e^{j(m'-m)\varphi}$$

$$Rg\vec{N}_{m'n'}(k_1 r,\theta,\varphi)\times\vec{M}_{-mn}(k_o r,\theta,\varphi)=$$

$$=\gamma_{m'n'}\gamma_{-mn}h_n^{(1)}(k_o r)\Big\{\Big[\frac{j_{n'}(k_1 r)}{k_1 r}\Big]n'(n'+1)P_{n'}^{m'}(\cos\theta)\frac{d}{d\theta}[P_n^{-m}(\cos\theta)]\hat{\theta}- \quad (D.16)$$

$$-\frac{[uj_{n'}(u)]'}{u}\Big|_{u=k_1 r}\frac{d}{d\theta}\Big[P_{n'}^{m'}(\cos\theta)\Big]\frac{d}{d\theta}[P_n^{-m}(\cos\theta)]\hat{R}-$$

$$-mm'\frac{[uj_{n'}(u)]'}{u}\Big|_{u=k_1 r}\frac{P_{n'}^{m'}(\cos\theta)}{\sin\theta}\frac{P_n^{-m}(\cos\theta)}{\sin\theta}\hat{R}\Big\}e^{j(m'-m)\varphi}$$

Therefore

$$J_{mnm'n'}^{21}=-2\pi(-1)^m\delta_{mm'}\gamma_{mn'}\gamma_{-mn}\times$$
$$\times\int_0^{\pi}h_n^{(1)}(k_o r)\Big\{\frac{[uj_{n'}(u)]'}{u}\Big|_{u=k_1 r}\Big[m^2\frac{P_{n'}^{m}(\cos\theta)}{\sin\theta}\frac{P_n^{-m}(\cos\theta)}{\sin\theta}+\frac{d}{d\theta}\Big[P_{n'}^{m}(\cos\theta)\Big]\frac{d}{d\theta}[P_n^{-m}(\cos\theta)]\Big]+ \quad (D.17)$$
$$+\frac{1}{r}\frac{dr}{d\theta}\frac{j_{n'}(k_1 r)}{k_1 r}n'(n'+1)P_{n'}^{m}(\cos\theta)\frac{d}{d\theta}[P_n^{-m}(\cos\theta)]\Big\}r^2\sin\theta d\theta$$

The expression for $RgJ_{mnm'n'}^{kl}$ can be obtained by substituting $j_\nu(kr)$ for $h_\nu^{(1)}(kr)$ in expressions (D.11), (D.13), (D.15), and (D.17).

The above expressions can be rewritten with basis on the following definitions and properties [44]

$$P_n^m(x) = \frac{(-1)^m}{2^n n!}(1-x^2)^{\frac{m}{x}}\frac{d^{n+m}}{dx^{n+m}}(x^2-1)^n \tag{D.18}$$

$$P_n^{-m}(x) = (-1)^m\frac{(n-m)!}{(n+m)!}P_n^m(x) \tag{D.19}$$

On the other hand, expressions in Appendix B, as well as equations (5.16) and (5.17) provided by [45], define

$$d_{om}^n(\theta) = \sqrt{\frac{(n-m)!}{(n+m)!}}P_n^m(x) = \sqrt{\frac{(n-m)!}{(n+m)!}}P_n^m(\cos\theta) \tag{D.20}$$

where $x = \cos\theta$ and

$$\pi_{mn}(\theta) = m\frac{d_{om}^n(\theta)}{\sin\theta}$$
$$\tau_{mn}(\theta) = \frac{d}{d\theta}d_{om}^n(\theta) \tag{D.21}$$

It should be noted that

$$\pi_{-mn}(\theta) = (-1)^{m+1}\pi_{mn}(\theta)$$
$$\tau_{-mn}(\theta) = (-1)^m\tau_{mn}(\theta)$$
$$\pi_{0n}(\theta) = 0$$

Therefore, equation (D.11) can be rearranged as

$$J_{mnm'n'}^{11} = 2\pi\delta_{mm'}\gamma_{mn'}\gamma_{-mn}\int_0^{\pi} j_{n'}(k_1 r)h_n^{(1)}(k_o r)\times$$

$$\times\left\{\frac{(-im)P_{n'}^{m}(\cos\theta)}{\sin\theta}\frac{d}{d\theta}\left[\frac{(n-m)!}{(n+m)!}P_{n}^{m}(\cos\theta)\right]+\right.$$
$$\left.+\frac{d}{d\theta}\left[P_{n'}^{m}(\cos\theta)\right]\left[\frac{(n-m)!}{(n+m)!}(-im)\frac{P_{n}^{m}(\cos\theta)}{\sin\theta}\sin\theta\right]\right\}r^{2}\sin\theta\,d\theta$$

$$J_{mnm'n'}^{11}=$$
$$=-\frac{i}{2}\delta_{mm'}\sqrt{\frac{(2n'+1)}{n'(n'+1)}\frac{(2n+1)}{n(n+1)}}\int_{-1}^{+1}j_{n'}(k_1r)h_{n}^{(1)}(k_or)\times \qquad \text{(D.22)}$$
$$\times\left[\pi_{mn}(\theta)\tau_{mn'}(\theta)+\tau_{mn}(\theta)\pi_{mn'}(\theta)\right]r^{2}dx$$

Similarly, from equation (D.13)

$$J_{mnm'n'}^{22}=2\pi(-im)\delta_{mm'}\sqrt{\frac{(2n'+1)}{4\pi n'(n'+1)}\frac{(n'-m)!}{(n'+m)!}}\cdot\sqrt{\frac{(2n+1)}{4\pi n(n+1)}\frac{(n+m)!}{(n-m)!}}\times$$
$$\times\int_{0}^{\pi}\left\{\frac{[uj_{n'}(u)]'}{u}\Big|_{u=k_1r}\frac{\left[uh_{n}^{(1)}(u)\right]'}{u}\Big|_{u=k_or}\left[\frac{d}{d\theta}\left[P_{n'}^{m}(\cos\theta)\right]\frac{(n-m)!}{(n+m)!}\frac{P_{n}^{m}(\cos\theta)}{\sin\theta}\right.\right.$$
$$\left.+\frac{P_{n'}^{m}(\cos\theta)}{\sin\theta}\frac{d}{d\theta}\left[\frac{(n-m)!}{(n+m)!}P_{n}^{m}(\cos\theta)\right]\right]+$$
$$+\frac{1}{r}\frac{dr}{d\theta}\left[\frac{j_{n'}(k_1r)}{k_1r}n'(n'+1)\frac{\left[uh_{n}^{(1)}(u)\right]'}{u}\Big|_{u=k_or}+\frac{[uj_{n'}(u)]'}{u}\Big|_{u=k_1r}\frac{h_{n}^{(1)}(k_or)}{k_or}n(n+1)\right].$$
$$\left.\cdot P_{n'}^{m}(\cos\theta)\frac{(n-m)!}{(n+m)!}\frac{P_{n}^{m}(\cos\theta)}{\sin\theta}\right\}r^{2}\sin\theta\,d\theta$$

$$J_{mnm'n'}^{22}=-\frac{i}{2}\delta_{mm'}\sqrt{\frac{(2n'+1)}{n'(n'+1)}\frac{(2n+1)}{n(n+1)}}\times$$
$$\times\int_{-1}^{+1}\left\{\frac{[uj_{n'}(u)]'}{u}\Big|_{u=k_1r}\frac{\left[uh_{n}^{(1)}(u)\right]'}{u}\Big|_{u=k_or}\left[\tau_{mn'}(\theta)\pi_{mn}(\theta)\right.\right. \qquad \text{(D.23)}$$
$$\left.+\pi_{mn'}(\theta)\tau_{mn}(\theta)\right]$$

$$+\frac{1}{r}\frac{dr}{d\theta}\left[\frac{j_{n'}(k_1 r)}{k_1 r}n'(n'+1)\frac{\left[uh_n^{(1)}(u)\right]'}{u}\Bigg|_{u=k_o r}\right.$$

$$\left.+\frac{[uj_{n'}(u)]'}{u}\Bigg|_{u=k_1 r}\frac{h_n^{(1)}(k_o r)}{k_o r}n(n+1)\right]\times$$

$$\times\pi_{mn}(\theta)d_{om}^{n'}(\theta)\Big\}r^2 dx$$

From equation (D.15), one has

$$J_{mnm'n'}^{12}=2\pi\delta_{mm'}\sqrt{\frac{(2n'+1)}{4\pi n'(n'+1)}\frac{(n'-m)!}{(n'+m)!}}.\sqrt{\frac{(2n+1)}{4\pi n(n+1)}\frac{(n+m)!}{(n-m)!}}\times$$

$$\times\int_0^{\pi}j_{n'}(k_1 r)\left\{\frac{\left[uh_n^{(1)}(u)\right]'}{u}\Bigg|_{u=k_o r}\left[m\frac{P_{n'}^m(\cos\theta)}{\sin\theta}\frac{(n-m)!}{(n+m)!}\frac{P_n^m(\cos\theta)}{\sin\theta}\right.\right.$$

$$\left.+\frac{d}{d\theta}\left[P_{n'}^m(\cos\theta)\right]\frac{d}{d\theta}\left[\frac{(n-m)!}{(n+m)!}P_n^{-m}(\cos\theta)\right]\right]+$$

$$\left.+\frac{1}{r}\frac{dr}{d\theta}\frac{h_n^{(1)}(k_o r)}{k_o r}n(n+1)\frac{d}{d\theta}\left[P_{n'}^{m'}(\cos\theta)\right]\frac{(n-m)!}{(n+m)!}P_n^m(\cos\theta)\right\}r^2\sin\theta d\theta$$

$$J_{mnm'n'}^{12}=\frac{1}{2}\delta_{mm'}\sqrt{\frac{(2n'+1)}{n'(n'+1)}\frac{(2n+1)}{n(n+1)}}\times$$

$$\times\int_{-1}^{+1}j_{n'}(k_1 r)\left\{\frac{\left[uh_n^{(1)}(u)\right]'}{u}\Bigg|_{u=k_o r}[\pi_{mn}(\theta)\pi_{m'}(\theta)+\tau_{mn}(\theta)\tau_{m'}(\theta)]+\right.$$

$$\left.+\frac{1}{r}\frac{dr}{d\theta}n(n+1)\frac{h_n^{(1)}(k_o r)}{k_o r}d_{om}^n(\theta)\tau_{mn'}(\theta)\right\}r^2 dx \qquad \text{(D.24)}$$

Finally, from the equation (B.17), one gets

$$J_{mnm'n'}^{21}=-2\pi\delta_{mm'}\sqrt{\frac{(2n'+1)}{4\pi n'(n'+1)}\frac{(n'-m)!}{(n'+m)!}}.\sqrt{\frac{(2n+1)}{4\pi n(n+1)}\frac{(n+m)!}{(n-m)!}}\times$$

$$\times \int_0^{\pi} h_n^{(1)}(k_o r)\left\{\left.\frac{[uj_{n'}(u)]'}{u}\right|_{u=k_1 r}\left[m\frac{P_{n'}^m(\cos\theta)}{\sin\theta}\frac{(n-m)!}{(n+m)!}m\frac{P_n^m(\cos\theta)}{\sin\theta}+\right.\right.$$

$$+\frac{d}{d\theta}\left[P_{n'}^m(\cos\theta)\right]\frac{d}{d\theta}\left[\frac{(n-m)!}{(n+m)!}P_n^m(\cos\theta)\right]\Bigg]+$$

$$\left.+\frac{1}{r}\frac{dr}{d\theta}\frac{j_{n'}(k_1 r)}{k_1 r}n'(n'+1)P_{n'}^m(\cos\theta)\frac{d}{d\theta}\left[\frac{(n-m)!}{(n+m)!}P_n^m(\cos\theta)\right]\right\}r^2\sin\theta d\theta$$

$$J_{mnm'n'}^{21}=-\frac{1}{2}\delta_{mm'}\sqrt{\frac{(2n'+1)}{n'(n'+1)}\frac{(2n+1)}{n(n+1)}}\times$$

$$\times\int_{-1}^{+1} h_n^{(1)}(k_o r)\left\{\left.\frac{[uj_{n'}(u)]'}{u}\right|_{u=k_1 r}[\pi_{mn}(\theta)\pi_{m'}(\theta)+\tau_{mn}(\theta)\tau_{m'}(\theta)]+\right. \tag{D.25}$$

$$\left.+\frac{1}{r}\frac{dr}{d\theta}\frac{j_{n'}(k_1 r)}{k_1 r}n'(n'+1)\tau_{mn}(\theta)d_{om}^{n'}(\theta)\right\}r^2 dx$$

The integrals in expressions (D.22) to (D.25), which agree with the ones provide by [45], are numerically determined using Gaussian quadrature formulas.

E.
Rotation of the T-matrix.

In the present Appendix, the rotation transformation rule for the T-matrix described by [44] and [45] is used to determine the scattering properties of the particle in the principal reference frame, characterized by the coordinates(r, θ, φ). The Eulerian angles α, β and γ specifies the rotation of the corresponding axes into those aligned with the symmetry axis of the raindrop characterized by the coordinates (r, θ_b, φ_b), where the b subscript indicates the body reference frame. Note that the distance from the common origin to any observation point is invariant under rotations of the reference frames. It has been shown by these authors that the vector spherical wave functions in the two reference frames can be related as follow

$$\vec{M}_{mn}(k_o r, \theta_b, \varphi_b) = \sum_{m'=-n}^{+n} \vec{M}_{m'n}(k_o r, \theta, \varphi) D^n_{m'm}(\alpha, \beta, \gamma) \tag{E.1}$$

$$\vec{N}_{mn}(k_o r, \theta_b, \varphi_b) = \sum_{m'=-n}^{+n} \vec{N}_{m'n}(k_o r, \theta, \varphi) D^n_{m'm}(\alpha, \beta, \gamma) \tag{E.2}$$

$$\vec{M}_{mn}(k_o r, \theta, \varphi) = \sum_{m'=-n}^{+n} \vec{M}_{m'n}(k_o r, \theta_b, \varphi_b) D^n_{m'm}(-\gamma, -\beta, -\alpha) \tag{E.3}$$

$$\vec{N}_{mn}(k_o r, \theta, \varphi) = \sum_{m'=-n}^{+n} \vec{N}_{m'n}(k_o r, \theta_b, \varphi_b) D^n_{m'm}(-\gamma, -\beta, -\alpha) \tag{E.4}$$

where $D^n_{m'm}(\alpha, \beta, \gamma)$ are the Wigner D functions

$$D^n_{m'm}(\alpha, \beta, \gamma) = e^{-im'\alpha} d^n_{m'm}(\beta) e^{-im\gamma} \tag{E.5}$$

and $d^n_{m'm}(\beta)$are the Wigner d functions. The regular vector spherical wave functions $Rg\vec{M}_{mn}(kr, \theta_b, \varphi_b)$ and $Rg\vec{N}_{mn}(kr, \theta_b, \varphi_b)$ can be similarly transformed using the Wigner D function.

Substituting the right-hand sides of expressions (E.1) and (E.2) into the representation of the incident field in the body frame of reference, one obtains

$$\vec{E}_i(\vec{r}) = \sum_{n=1}^{\infty}\sum_{m=-n}^{+n}\hat{a}_{mn}\sum_{m'=-n}^{+n} D^n_{m'm}(\alpha,\beta,\gamma)\,\vec{M}_{m'n}(k_o r,\theta,\varphi) + \hat{b}_{mn}\sum_{m'=-n}^{+n} D^n_{m'm}(\alpha,\beta,\gamma)\vec{N}_{m'n}(k_o r,\theta,\varphi)$$

$$= \sum_{n=1}^{\infty}\sum_{m'=-n}^{+n}\left\{\left[\sum_{m=-n}^{+n} D^n_{m'm}(\alpha,\beta,\gamma)\hat{a}_{mn}\right]\vec{M}_{m'n}(k_o r,\theta,\varphi) + \left[\sum_{m=-n}^{+n} D^n_{m'm}(\alpha,\beta,\gamma)\hat{b}_{mn}\right]\vec{N}_{m'n}(k_o r,\theta,\varphi)\right\}$$

Exchanging indices *m* and *m´*

$$\vec{E}_i(\vec{r}) = \sum_{n=1}^{\infty}\sum_{m=-n}^{+n}\left\{\left[\sum_{m'=-n}^{+n} D^n_{mm'}(\alpha,\beta,\gamma)\hat{a}_{m'n}\right]\vec{M}_{mn}(k_o r,\theta,\varphi) + \left[\sum_{m'=-n}^{+n} D^n_{mm'}(\alpha,\beta,\gamma)\hat{b}_{m'n}\right]\vec{N}_{mn}(k_o r,\theta,\varphi)\right\} \quad \text{(E.6)}$$

A similar development is carry out to express the scattered field as

$$\vec{E}_s(\vec{r}) = \sum_{n=1}^{\infty}\sum_{m=-n}^{+n}\left\{\left[\sum_{m'=-n}^{+n} D^n_{mm'}(\alpha,\beta,\gamma)\hat{p}_{m'n}\right]\vec{M}_{mn}(k_o r,\theta,\varphi) + \left[\sum_{m'=-n}^{+n} D^n_{mm'}(\alpha,\beta,\gamma)\hat{q}_{m'n}\right]\vec{N}_{mn}(k_o r,\theta,\varphi)\right\} \quad \text{(E.7)}$$

Remembering that the fields are also invariant under rotations of the reference frames, one gets

$$a_{mn} = \sum_{m'=-n}^{+n} D^n_{mm'}(\alpha,\beta,\gamma)\hat{a}_{m'n}$$
$$b_{mn} = \sum_{m'=-n}^{+n} D^n_{mm'}(\alpha,\beta,\gamma)\hat{b}_{m'n} \qquad \text{(E.8)}$$

$$p_{mn} = \sum_{m'=-n}^{+n} D^n_{mm'}(\alpha,\beta,\gamma)\hat{p}_{m'n}$$
$$q_{mn} = \sum_{m'=-n}^{+n} D^n_{mm'}(\alpha,\beta,\gamma)\hat{q}_{m'n} \qquad \text{(E.9)}$$

In the above expressions: (1) $\hat{a}_{m'n}, \hat{b}_{m'n}, \hat{p}_{m'n}$, and $\hat{q}_{m'n}$ are the coefficients of the expansions of the fields in the body reference frame; and (2) a_{mn}, b_{mn}, p_{mn}, and q_{mn} are the coefficients of the expansions of the fields in the principal reference frame. Similarly, substituting the right-hand sides of expressions (E.3) and (E.4) into the representation of the incident field in the principal frame of reference, one obtains

$$\vec{E}_i(\vec{r}) = \sum_{n=1}^{\infty}\sum_{m=-n}^{+n} a_{mn} \sum_{m'=-n}^{+n} D^n_{m'm}(-\gamma,-\beta,-\alpha)\,\vec{M}_{m'n}(k_o r,\theta_b,\varphi_b) + b_{mn}\sum_{m'=-n}^{+n} D^n_{m'm}(-\gamma,-\beta,-\alpha)\vec{N}_{m'n}(k_o r,\theta_b,\varphi_b)$$

where

$$D^n_{m'm}(-\gamma,-\beta,-\alpha) = D^{-1(n)}_{m'm=}(\alpha,\beta,\gamma) = D^{*n}_{m'm}(\alpha,\beta,\gamma)$$

$$\vec{E}_i(\vec{r}) = \sum_{n=1}^{\infty}\sum_{m'=-n}^{+n}\left\{\left[\sum_{m=-n}^{+n} D^n_{m'm}(-\gamma,-\beta,-\alpha)a_{mn}\right]\vec{M}_{m'n}(k_o r,\theta_b,\varphi_b) + \left[\sum_{m=-n}^{+n} D^n_{m'm}(-\gamma,-\beta,-\alpha)b_{mn}\right]\vec{N}_{m'n}(k_o r,\theta_b,\varphi_b)\right\}$$

Exchanging indices m and $m´$ again

$$\vec{E}_i(\vec{r}) = \sum_{n=1}^{\infty}\sum_{m=-n}^{+n}\left\{\left[\sum_{m´=-n}^{+n} D^n_{mm'}(-\gamma,-\beta,-\alpha)a_{m'n}\right]\vec{M}_{mn}(k_o r,\theta_b,\varphi_b) + \left[\sum_{m´=-n}^{+n} D^n_{mm'}(-\gamma,-\beta,-\alpha)b_{m'n}\right]\vec{N}_{mn}(k_o r,\theta_b,\varphi_b)\right\} \quad \text{(E.10)}$$

Similarly

$$\vec{E}_s(\vec{r}) = \sum_{n=1}^{\infty}\sum_{m=-n}^{+n}\left\{\left[\sum_{m'=-n}^{+n} D^n_{mm'}(-\gamma,-\beta,-\alpha)p_{m'n}\right]\vec{M}_{mn}(k_o r,\theta_b,\varphi_b) + \left[\sum_{m'=-n}^{+n} D^n_{mm'}(-\gamma,-\beta,-\alpha)q_{m'n}\right]\vec{N}_{mn}(k_o r,\theta_b,\varphi_b)\right\} \quad \text{(E.11)}$$

A second comparison between terms yields

$$\hat{a}_{mn} = \sum_{m´=-n}^{+n} D^n_{mm'}(-\gamma,-\beta,-\alpha)a_{m'n}$$
$$\hat{b}_{mn} = \sum_{m'=-n}^{+n} D^n_{mm'}(-\gamma,-\beta,-\alpha)b_{m'n} \quad \text{(E.12)}$$

$$\hat{p}_{mn} = \sum_{m'=-n}^{+n} D^n_{mm'}(-\gamma,-\beta,-\alpha)p_{m'n}$$
$$\hat{q}_{mn} = \sum_{m'=-n}^{+n} D^n_{mm'}(-\gamma,-\beta,-\alpha)q_{m'n} \quad \text{(E.13)}$$

Note that $n \geq |m|$ in equations (E.8), (E.9), (E.12), and (E.13).

It has been seen in equation (4.32) that, in the body reference frame

$$\begin{pmatrix}\hat{p}_{mn}\\ \hat{q}_{mn}\end{pmatrix}=\begin{pmatrix}\underline{\hat{T}}_{11} & \underline{\hat{T}}_{12}\\ \underline{\hat{T}}_{21} & \underline{\hat{T}}_{22}\end{pmatrix}\begin{pmatrix}\hat{a}_{mn}\\ \hat{b}_{mn}\end{pmatrix} \tag{E.14}$$

Similarly, in the principal reference frame

$$\begin{pmatrix}p_{mn}\\ q_{mn}\end{pmatrix}=\begin{pmatrix}\underline{T}_{11} & \underline{T}_{12}\\ \underline{T}_{21} & \underline{T}_{22}\end{pmatrix}\begin{pmatrix}a_{mn}\\ b_{mn}\end{pmatrix}$$

That is,

$$\hat{p}_{mn}=\sum_{n\prime=1}^{Nmax}\sum_{m\prime=-n\prime}^{+n\prime}\left[\hat{T}^{11}_{mnm\prime n\prime}\hat{a}_{m\prime n\prime}+\hat{T}^{12}_{mnm\prime n\prime}\hat{b}_{m\prime n\prime}\right] \tag{E.15}$$

$$\hat{q}_{mn}=\sum_{n\prime=1}^{Nmax}\sum_{m\prime=-n\prime}^{+n\prime}\left[\hat{T}^{21}_{mnm\prime n\prime}\hat{a}_{m\prime n\prime}+\hat{T}^{22}_{mnm\prime n\prime}\hat{b}_{m\prime n\prime}\right] \tag{E.16}$$

$$p_{mn}=\sum_{n\prime=1}^{Nmax}\sum_{m\prime=-n\prime}^{+n\prime}\left[T^{11}_{mnm\prime n\prime}a_{m\prime n\prime}+T^{12}_{mnm\prime n\prime}b_{m\prime n\prime}\right] \tag{E.17}$$

$$q_{mn}=\sum_{n\prime=1}^{Nmax}\sum_{m\prime=-n\prime}^{+n\prime}\left[T^{21}_{mnm\prime n\prime}a_{m\prime n\prime}+T^{22}_{mnm\prime n\prime}b_{m\prime n\prime}\right] \tag{E.18}$$

Combining equations (E.9) and (E.15), it follows that

$$p_{mn}=\sum_{m_2=-n}^{+n}D^{n}_{mm_2}(\alpha,\beta,\gamma)\sum_{n\prime=1}^{Nmax}\sum_{m\prime=-n\prime}^{+n\prime}\left[\hat{T}^{11}_{m_2nm\prime n\prime}\hat{a}_{m\prime n\prime}+\hat{T}^{12}_{m_2nm\prime n\prime}\hat{b}_{m\prime n\prime}\right]$$

$$p_{mn}=\sum_{n\prime=1}^{Nmax}\sum_{m\prime=-n\prime}^{+n\prime}\left\{\left[\sum_{m_2=-n}^{+n}D^{n}_{mm_2}(\alpha,\beta,\gamma)\,\hat{T}^{11}_{m_2nm\prime n\prime}\right]\hat{a}_{m\prime n\prime}+\left[\sum_{m_2=-n}^{+n}D^{n}_{mm_2}(\alpha,\beta,\gamma)\,\hat{T}^{12}_{m_2nm\prime n\prime}\right]\hat{b}_{m\prime n\prime}\right\} \tag{E.19}$$

Substituting equation (E.12) into (E.19), one obtains

$$p_{mn} = \sum_{n\prime=1}^{Nmax} \sum_{m\prime=-n\prime}^{+n\prime} \left\{ \left[\sum_{m_2=-n}^{+n} D^{n}_{mm_2}(\alpha,\beta,\gamma)\, \hat{T}^{11}_{m_2 n m\prime n\prime} \right] \left[\sum_{m_3=-n\prime}^{+n\prime} D^{n\prime}_{m\prime m_3}(-\gamma,-\beta,-\alpha) a_{m_3 n\prime} \right] + \left[\sum_{m_2=-n}^{+n} D^{n}_{mm_2}(\alpha,\beta,\gamma)\, \hat{T}^{12}_{m_2 n m\prime n\prime} \right] \left[\sum_{m_3=-n\prime}^{+n\prime} D^{n\prime}_{m\prime m_3}(-\gamma,-\beta,-\alpha) b_{m_3 n\prime} \right] \right\}$$

$$p_{mn} = \sum_{n\prime=1}^{Nmax} \sum_{m_3=-n\prime}^{+n\prime} \left\{ \sum_{m_2=-n}^{+n} \sum_{m\prime=-n\prime}^{+n\prime} \left\{ \left[D^{n}_{mm_2}(\alpha,\beta,\gamma) \hat{T}^{11}_{m_2 n m\prime n\prime} D^{n\prime}_{m\prime m_3}(-\gamma,-\beta,-\alpha) \right] + \left[D^{n}_{mm_2}(\alpha,\beta,\gamma) \hat{T}^{12}_{m_2 n m\prime n\prime} D^{n\prime}_{m\prime m_3}(-\gamma,-\beta,-\alpha) \right] b_{m_3 n\prime} \right\} \right. \quad \text{(E.20)}$$

By replacing the indices $m_3 \leftrightarrows m'$, equation (E.20) can be rewritten as follow

$$p_{mn} = \sum_{n\prime=1}^{Nmax} \sum_{m\prime=-n\prime}^{+n\prime} \left\{ \sum_{m_2=-n}^{+n} \sum_{m_3=-n\prime}^{+n\prime} \left\{ \left[D^{n}_{mm_2}(\alpha,\beta,\gamma) \hat{T}^{11}_{m_2 n m_3 n\prime} D^{n\prime}_{m_3 m\prime}(-\gamma,-\beta,-\alpha) \right] + \left[D^{n}_{mm_2}(\alpha,\beta,\gamma) \hat{T}^{12}_{m_2 n m_3 n\prime} D^{n\prime}_{m_3 m\prime}(-\gamma,-\beta,-\alpha) \right] b_{m\prime n\prime} \right\} \right. \quad \text{(E.21)}$$

An entirely analogous development leads to

$$q_{mn} = \sum_{n\prime=1}^{Nmax} \sum_{m\prime=-n\prime}^{+n\prime} \left\{ \sum_{m_2=-n}^{+n} \sum_{m_3=-n\prime}^{+n\prime} \left\{ \left[D^{n}_{mm_2}(\alpha,\beta,\gamma) \hat{T}^{21}_{m_2 n m_3 n\prime} D^{n\prime}_{m_3 m\prime}(-\gamma,-\beta,-\alpha) \right] + \left[D^{n}_{mm_2}(\alpha,\beta,\gamma) \hat{T}^{22}_{m_2 n m_3 n\prime} D^{n\prime}_{m_3 m\prime}(-\gamma,-\beta,-\alpha) \right] b_{m\prime n\prime} \right\} \right. \quad \text{(E.22)}$$

A comparison between expressions (E.17), (E.18), (E.21), and (E.22) provides the relationship between the T-matrices in the two reference frames

$$T_{mnm'n'}^{kl} = \sum_{m_2=-n}^{+n} \sum_{m_3=-n'}^{+n'} D_{mm_2}^{n}(\alpha,\beta,\gamma)\hat{T}_{m_2nm_3n'}^{kl} D_{m_3m'}^{n'}(-\gamma,-\beta,-\alpha) \qquad \text{(E.23)}$$

For an axially symmetric particle, which is the case of interest, one has

$$\hat{T}_{m_2nm_3n'}^{kl} = \delta_{m_2m_3}\hat{T}_{m_2nm_2n'}^{kl}$$

and equation (E.23) can be simplified as follow

$$T_{mnm'n'}^{kl} = \sum_{m_2=-N_{min}}^{+N_{min}} D_{mm_2}^{n}(\alpha,\beta,\gamma)\hat{T}_{m_2nm_2n'}^{kl} D_{m_2m'}^{n'}(-\gamma,-\beta,-\alpha) \qquad \text{(E.24)}$$

where $N_{min} = \min(n, n')$.

F.
Average T-matrix for a Particle of Equivalent Diameter D due to a Distribution of Orientations of the Symmetry Axis.

In the principal reference frame, the scattered field due to a particle of equivalent diameter D can be expressed as

$$\vec{E}_s^D(\vec{r}) = \sum_{n=1}^{\infty} \sum_{m=-n}^{+n} p_{mn}^D \vec{M}_{mn}(k_o\vec{r}) + q_{mn}^D \vec{N}_{mn}(k_o\vec{r}) \tag{F.1}$$

where

$$p_{mn}^D = \sum_{n\prime=1}^{\infty} \sum_{m=-n\prime}^{+n\prime} T_{mnm\prime n\prime}^{11D} a_{m\prime n\prime} + T_{mnm\prime n\prime}^{12D} b_{m\prime n\prime} \tag{F.2}$$

$$q_{mn}^D = \sum_{n\prime=1}^{\infty} \sum_{m=-n\prime}^{+n\prime} T_{mnm\prime n\prime}^{21D} a_{m\prime n\prime} + T_{mnm\prime n\prime}^{22D} b_{m\prime n\prime} \tag{F.3}$$

where $a_{m\prime n\prime}$ and $b_{m\prime n\prime}$ are the known and fixed coefficients of the expansion of the incident field in VSWFs in the principal reference frame, determined from expressions (B.14) and (B.16).

The average scattered field due a particle of equivalent diameter D and randomly-oriented symmetry axis is

$$\langle \vec{E}_s^D(\vec{r}) \rangle = \int_{\Omega"} \vec{E}_s^D(\vec{r}) p_{\mathrm{AB\Gamma}}^D(\alpha,\beta,\gamma) d\Omega" \tag{F.4}$$

where $p^{D}_{\mathrm{AB\Gamma}}(\alpha,\beta,\gamma)$ is the known probability density function of orientation of the symmetry axis of the particle with equivalent diameter D and the region of integration Ω' is limited by $0 \le \alpha \le 2\pi$, $0 \le \beta \le \pi$, and $0 \le \gamma \le 2\pi$.

It is evident from expressions (F.1) to (F.3) that the averaging procedure indicated in expression (F.4) will be finally applied to the T-matrix terms. That is,

$$\langle \vec{E}^{D}_{s}(\vec{r})\rangle = \sum_{n=1}^{\infty}\sum_{m=-n}^{+n} \langle p^{D}_{mn}\rangle \vec{M}_{mn}(k_o\vec{r}) + \langle q^{D}_{mn}\rangle \vec{N}_{mn}(k_o\vec{r}) \tag{F.5}$$

where

$$\langle p^{D}_{mn}\rangle = \sum_{n'=1}^{\infty}\sum_{m=-n'}^{+n'} \langle T^{11D}_{mnm'n'}\rangle a_{m'n'} + \langle T^{12D}_{mnm'n'}\rangle b_{m'n'} \tag{F.6}$$

$$\langle q^{D}_{mn}\rangle = \sum_{n'=1}^{\infty}\sum_{m=-n'}^{+n'} \langle T^{21D}_{mnm'n'}\rangle a_{m'n'} + \langle T^{22D}_{mnm'n'}\rangle b_{m'n'} \tag{F.7}$$

and

$$\langle T^{klD}_{mnm'n'}\rangle = \int_{\Omega''} T^{klD}_{mnm'n'} p^{D}_{\mathrm{AB\Gamma}}(\alpha,\beta,\gamma)\,d\Omega'' \tag{F.8}$$

Substituting the right-hand side of expression (E.24) for $T^{klD}_{mnm'n'}$ in the above result, one gets

$$\begin{aligned}\langle T^{klD}_{mnm'n'}\rangle = & \\ &= \sum_{m_1=-N_{min}}^{+N_{min}} \int_{\Omega''} D^{n}_{mm_1}(\alpha,\beta,\gamma)\hat{T}^{klD}_{m_1nm_1n'} \times \\ &\quad \times D^{n'}_{m_1m'}(-\gamma,-\beta,-\alpha) p^{D}_{\mathrm{AB\Gamma}}(\alpha,\beta,\gamma)\,\mathrm{d}\Omega'' \\ &= \sum_{m_1=-N_{min}}^{+N_{min}} \int_{\Omega''} \left[e^{-im\alpha} d^{n}_{mm_1}(\beta) e^{-im_1\gamma}\right]\left[e^{im_1\gamma} d^{n'}_{m_1m'}(-\beta) e^{im'\alpha}\right] \times\end{aligned} \tag{F.9}$$

$$\times \hat{T}^{klD}_{m_1 n m_1 n'} p^D_{\mathrm{AB\Gamma}}(\alpha,\beta,\gamma)\mathrm{d}\Omega"$$

$$= \sum_{m_1=-N_{min}}^{+N_{min}} \left\{ \left[\int_{\Omega"} e^{i(m'-m)\alpha}\, d^n_{m m_1}(\beta) d^{n'}_{m' m_1}(\beta) p^D_{\mathrm{AB\Gamma}}(\alpha,\beta,\gamma)\mathrm{d}\Omega" \right] \times \right.$$

$$\left. \times \hat{T}^{klD}_{m_1 n m_1 n'} \right\}$$

$$= \frac{\delta_{mm'}}{2\pi} \sum_{m_1=-N_{min}}^{+N_{min}} \left\{ \left[\int_{\Omega'} d^n_{m m_1}(\beta) d^{n'}_{m' m_1}(\beta) p^D_{\mathrm{B\Gamma}}(\beta,\gamma)\mathrm{d}\Omega' \right] \hat{T}^{klD}_{m_1 n m_1 n'} \right\}$$

where a uniform distribution in α has been assumed; that is, $p^D_{\mathrm{AB\Gamma}}(\alpha,\beta,\gamma) = p^D_{\mathrm{B\Gamma}}(\beta,\gamma)/2\pi$. Additionally, the well-known property $d^{n'}_{m_1 m'}(-\beta) = d^{n'}_{m' m_1}(\beta)$ has been used above [45]. Note that if $m \neq m'$, then $\langle \hat{T}^{klD}_{mnm'n'} \rangle = 0$. By use of the Clebsch-Gordan coefficients, the product of Wigner *d* functions can be expanded in such a way that the term between square brackets in the above expression becomes [43], [45]

$$SB^{Dm_1}_{mnm'n'} =$$

$$= (-1)^{m+m_1} \int_{\Omega'} \left[\sum_{n_1=|n-'|}^{n+'} C^{n_1 0}_{nmn'(-m)} C^{n_1 0}_{nm_1 n'(-m_1)} d^{n_1}_{00}(\beta) \right] p^D_{\mathrm{B\Gamma}}(\beta,\gamma)\mathrm{d}\Omega' \quad \text{(F.10)}$$

$$SB^{Dm_1}_{mnm'n'} =$$

$$= (-1)^{m+m_1} \sum_{n_1=|n-n'|}^{n+n'} C^{n_1 0}_{nmn'(-m)} C^{n_1 0}_{nm_1 n'(-m_1)} \int_{\Omega'} d^{n_1}_{00}(\beta) p^D_{\mathrm{B\Gamma}}(\beta,\gamma)\mathrm{d}\Omega'$$

where $d^{n_1}_{00}(\beta) = P_{n_1}(\cos\beta)$ and $C^{n_1 0}_{nmn'(-m)}$ are the Clebsch-Gordan coefficients specified in Appendix D of [45]. It follows that

$$\langle \hat{T}^{klD}_{mnm'n'} \rangle = \frac{\delta_{mm'}}{2\pi} \sum_{m_1=-N_{min}}^{+N_{min}} \left\{ (-1)^{m+m_1} \sum_{n_1=|n-n'|}^{n+n'} C^{n_1 0}_{nmn'(-m)} C^{n_1 0}_{nm_1 n'(-m_1)} \times \right.$$

$$\left. \times \left[\int_{\Omega'} d^{n_1}_{00}(\beta) p^D_{\mathrm{B\Gamma}}(\beta,\gamma)\mathrm{d}\Omega' \right] \hat{T}^{klD}_{m_1 n m_1 n'} \right\}$$

$$\langle \hat{T}^{klD}_{mnm'n'} \rangle = \frac{\delta_{mm'}}{2\pi}(-1)^m \sum_{n_1=|n-n'|}^{n+n'} C^{n_1 0}_{nmn'(-m)} \int_{\Omega'} d^{n_1}_{00}(\beta) p^{D}_{B\Gamma}(\beta,\gamma) \mathrm{d}\Omega' \times$$
$$\times \left[\sum_{m_1=-N_{min}}^{+N_{min}} (-1)^{m_1} C^{n_1 0}_{nm_1 n'(-m_1)} \hat{T}^{klD}_{m_1 n m_1 n'} \right] \tag{F.11}$$

The internal summation $\mathbb{S}$ (within square brackets) can be rewritten as follow

$$\mathbb{S} = \sum_{m_1=0}^{+N_{min}} (-1)^{m_1} \left(1 - \frac{1}{2}\delta_{m_1 0}\right) C^{n_1 0}_{nm_1 n'(-m_1)} \hat{T}^{klD}_{m_1 n m_1 n'} + \tag{F.12}$$
$$+ \sum_{m_1=-N_{min}}^{0} (-1)^{m_1} \left(1 - \frac{1}{2}\delta_{m_1 0}\right) C^{n_1 0}_{nm_1 n'(-m_1)} \hat{T}^{klD}_{m_1 n m_1 n'}$$

The last summation of the expression (F.12) can be rewritten as follow

$$\mathbb{S}_2 = \sum_{m_1=0}^{+N_{min}} (-1)^{-m_1} \left(1 - \frac{1}{2}\delta_{m_1 0}\right) C^{n_1 0}_{n(-m_1)n'm_1} \hat{T}^{klD}_{(-m_1)n(-m_1)n'} \tag{F.13}$$
$$= \sum_{m_1=0}^{+N_{min}} (-1)^{m_1}(-1)^{n+n'+n_1+k+l} \left(1 - \frac{1}{2}\delta_{m_1 0}\right) C^{n_1 0}_{nm_1 n'(-m_1)} \hat{T}^{klD}_{m_1 n m_1 n'}$$

Then

$$\mathbb{S} = \left[1 + (-1)^{n+n'+n_1+k+l}\right] \times$$
$$\times \sum_{m_1=0}^{+Nmin} (-1)^{m_1} \left(1 - \frac{1}{2}\delta_{m_1 0}\right) C^{n_1 0}_{nm_1 n'(-m_1)} \hat{T}^{klD}_{m_1 n m_1 n'} \tag{F.14}$$

Therefore

$$\langle \hat{T}^{klD}_{mnm'n'} \rangle = \frac{\delta_{mm'}}{2\pi}(-1)^m \sum_{n_1=|n-n'|}^{n+n'} \left[1 + (-1)^{n+n'+n_1+k+l}\right] C^{n_1 0}_{nmn'(-m)} \times$$

$$\times \int_{\Omega'} d_{00}^{n_1}(\beta) p_{B\Gamma}^{D}(\beta,\gamma)\mathrm{d}\Omega' \times \tag{F.15}$$

$$\times \left[\sum_{m_1=0}^{+N_{min}} (-1)^{m_1} \left(1 - \frac{1}{2}\delta_{m_1 0}\right) C_{nm_1 n'(-m_1)}^{n_1 0} \hat{T}_{m_1 n m_1 n'}^{klD} \right]$$

Using expression (3.16) for $p_{B\Gamma}^{D}(\beta,\gamma)$, the remaining integral in expression (F.15) can be rewritten as follow

$$\int_{\Omega'} d_{00}^{n_1}(\beta) p_{B\Gamma}^{D}(\beta,\gamma)\mathrm{d}\Omega' =$$

$$= \int_{\gamma_o - \frac{\delta\gamma}{2}}^{\gamma_o + \frac{\delta\gamma}{2}} \int_0^{\pi} \frac{1}{\sqrt{2\pi}\Delta\beta\mathcal{F}\delta\gamma} e^{-\frac{1}{2}\left(\frac{\beta-\beta_o}{\Delta\beta}\right)^2} P_{n_1}(\cos\beta)\, sin\beta d\beta d\gamma +$$

$$+ \int_{\gamma_o + \pi - \frac{\delta\gamma}{2}}^{\gamma_o + \pi + \frac{\delta\gamma}{2}} \int_0^{\pi} \frac{1}{\sqrt{2\pi}\Delta\beta\mathcal{F}\delta\gamma} e^{-\frac{1}{2}\left(\frac{\beta+\beta_o}{\Delta\beta}\right)^2} P_{n_1}(\cos\beta)\, sin\beta d\beta d\gamma =$$

$$= \frac{1}{\sqrt{2\pi}\Delta\beta\mathcal{F}} \left\{ \int_0^{\pi} \left[e^{-\frac{1}{2}\left(\frac{\beta-\beta_o}{\Delta\beta}\right)^2} + e^{-\frac{1}{2}\left(\frac{\beta+\beta_o}{\Delta\beta}\right)^2} \right] P_{n_1}(\cos\beta)\, sin\beta d\beta \right\} = \underline{P}_{n_1} \tag{F.16}$$

Therefore, expression (F.16) can be rewritten in a more compact form

$$\langle \hat{T}_{mnm'n'}^{klD} \rangle = \frac{\delta_{mm'}}{2\pi} (-1)^m \sum_{n_1=|n-n'|}^{n+n'} \left[1 + (-1)^{n+n'+n_1+k+l}\right] C_{nmn'(-m)}^{n_1 0} \times \tag{F.17}$$

$$\times \underline{P}_{n_1} \left[\sum_{m_1=0}^{+N_{min}} (-1)^{m_1} \left(1 - \frac{1}{2}\delta_{m_1 0}\right) C_{nm_1 n'(-m_1)}^{n_1 0} \hat{T}_{m_1 n m_1 n'}^{klD} \right]$$

$$= \delta_{mm'} \tilde{T}_{mnn'}^{klD}$$

It should be noted that

$$
\begin{aligned}
&\left[1+(-1)^{n+n'+n_1+k+l}\right] C^{n_1 0}_{n(-m)n'm} \\
&= \left[1+(-1)^{n+n'+n_1+k+l}\right](-1)^{n+n'+n_1} C^{n_1 0}_{nmn'(-m)} \\
&= \left[(-1)^{n+n'+n_1}+(-1)^{k+l}\right] C^{n_1 0}_{nmn'(-m)} \\
&= (-1)^{k+l}(-1)^{k+l}\left[(-1)^{n+n'+n_1}+(-1)^{k+l}\right] C^{n_1 0}_{nmn'(-m)} \\
&= (-1)^{k+l}\left[1+(-1)^{n+n'+n_1+k+l}\right] C^{n_1 0}_{nmn'(-m)}
\end{aligned}
\tag{F.18}
$$

Thus

$$
\tilde{T}^{klD}_{-mnn'} = (-1)^{k+l}\tilde{T}^{klD}_{mnn'} \tag{F.19}
$$

G.
Average Scattering Amplitude due to a Particle with Equivalent Diameter D and Randomly Oriented Symmetry Axis.

It is well known that the following approximations are valid in the limit $k_o r \to \infty$

$$h_n^{(1)}(k_o r) \approx (-i)^{n+1} \frac{e^{ik_o r}}{k_o r} \tag{G.1}$$

$$\left.\frac{\left[u h_n^{(1)}(u)\right]'}{u}\right|_{k_o r} \approx (-i)^n \frac{e^{ik_o r}}{k_o r} = (-i)^{n+1} i \frac{e^{ik_o r}}{k_o r} \tag{G.2}$$

Thus, applying the same limit $k_o r \to \infty$ to the definitions of the VSWFs in Appendix B, one obtains

$$\vec{M}_{mn}(k_o r, \theta, \varphi) = \gamma_{mn} h_n^{(1)}(k_o r) \vec{C}_{mn}(\theta, \varphi) \tag{G.3}$$

$$\approx \gamma_{mn} (-i)^{n+1} \vec{C}_{mn}(\theta, \varphi) \frac{e^{ik_o r}}{k_o r}$$

$$\vec{N}_{-mn}(k_o r, \theta, \varphi) =$$

$$= \gamma_{mn} \left\{ n(n+1) \frac{h_n^{(1)}(k_o r)}{k_o r} \vec{P}_{mn}(\theta, \varphi) \right. \tag{G.4}$$

$$\left. + + \left.\frac{\left[u h_n^{(1)}(u)\right]'}{u}\right|_{k_o r} \vec{B}_{mn}(\theta, \varphi) \right\}$$

$$\approx \gamma_{mn} (-i)^{n+1} i \vec{B}_{mn}(\theta, \varphi) \frac{e^{ik_o r}}{k_o r}$$

The average scattered field due to a distribution of random orientations of the symmetry axis of a particle of equivalent diameter D can be rearrange by substituting equations (G.3) and (G.4) into equation (F.5)

$$\langle \vec{E}_s^D(\vec{r}) \rangle \approx \left\{ \sum_{n=1}^{\infty} \sum_{m=-n}^{+n} (-i)^{n+1} \gamma_{mn} \times \right. \tag{G.5}$$

$$\left. \times \left[\langle p_{mn}^D \rangle \vec{C}_{mn}(\theta, \varphi) + i \langle q_{mn}^D \rangle \vec{B}_{mn}(\theta, \varphi) \right] \right\} \frac{e^{ik_o r}}{k_o r}$$

where, according to expressions (F.6) and (F.7),

$$\langle p_{mn}^D \rangle = \sum_{n'=1}^{\infty} \sum_{m=-n'}^{+n'} \langle \hat{T}_{mnm'n'}^{11D} \rangle a_{m'n'} + \langle \hat{T}_{mnm'n'}^{12D} \rangle b_{m'n'} \tag{G.6}$$

$$\langle q_{mn}^D \rangle = \sum_{n'=1}^{\infty} \sum_{m=-n'}^{+n'} \langle \hat{T}_{mnm'n'}^{21D} \rangle a_{m'n'} + \langle \hat{T}_{mnm'n'}^{22D} \rangle b_{m'n'} \tag{G.7}$$

In the above expressions, $a_{m'n'}$ and $b_{m'n'}$ are the known and fixed coefficients of the expansion of the incident field in VSWFs in the principal reference frame, determined from expressions (B.14) and (B.16). The elements $\langle \hat{T}_{mnm'n'}^{klD} \rangle$ are determined by using equation (F.17), which can be combined with expressions (G.5) to (G.7) to provide

$$\langle \vec{E}_s^D(\vec{r}) \rangle \approx$$

$$\approx \frac{e^{ik_o r}}{k_o r} \sum_{n=1}^{\infty} \sum_{m=-n}^{+n} (-i)^{n+1} \gamma_{mn} \left\{ \left[\sum_{n'=1}^{\infty} \sum_{m'=-n'}^{+n'} \left(\langle \hat{T}_{mnm'n'}^{11D} \rangle a_{m'n'} + \right. \right. \right. \tag{G.8}$$

$$\left. + \langle \hat{T}_{mnm'n'}^{12D} \rangle b_{m'n'} \right] \vec{C}_{mn}(\theta, \varphi) +$$

$$\left. + i \left[\sum_{n'=1}^{\infty} \sum_{m'=-n'}^{+n'} \langle \hat{T}_{mnm'n'}^{21D} \rangle a_{m'n'} + \langle \hat{T}_{mnm'n'}^{22D} \rangle b_{m'n'} \right] \vec{B}_{mn}(\theta, \varphi) \right\}$$

$$\langle \vec{E}_s^D(\vec{r}) \rangle \approx$$

$$\approx \frac{e^{ik_o r}}{k_o r} \sum_{n=1}^{\infty} \sum_{m=-n}^{+n} (-i)^{n+1} \gamma_{mn} \left\{ \left[\sum_{n'=1}^{\infty} \tilde{T}_{mnn'}^{11D} a_{m'n'} + \tilde{T}_{mnn'}^{12D} b_{m'n'} \right] \times \right. \tag{G.9}$$

$$\times \left[(-1)^m \sqrt{\frac{(n+m)!}{(n-m)!}} \left[i \pi_{mn}(\theta) \hat{\theta} - \tau_{mn}(\theta) \hat{\varphi} \right] e^{im\varphi} \right] \times$$

$$\left. + i \left[\sum_{n'=1}^{\infty} \tilde{T}_{mnn'}^{21D} a_{m'n'} + \tilde{T}_{mnn'}^{22D} b_{m'n'} \right] \times \right.$$

$$\times\left[(-1)^m\sqrt{\frac{(n+m)!}{(n-m)!}}\left[\tau_{mn}(\theta)\hat{\theta}+i\pi_{mn}(\theta)\hat{\varphi}\right]e^{im\varphi}\right]\Bigg\}$$

In expressions (G.8) and (G.9), one should have $|m|\leq \min(n,n')$. Thus,

$$\begin{aligned}\langle\vec{E}_s^D(\vec{r})\rangle \approx &\left\{\frac{e^{ik_o r}}{k_o r}\sum_{n=1}^{\infty}\sum_{m=-n}^{+n}(-i)^{n+1}(-1)^m\gamma_{mn}\sqrt{\frac{(n+m)!}{(n-m)!}}\times\right.\\ &\times\left\{i\left[\sum_{n'=1}^{\infty}\tilde{T}^{11D}_{mnn'}a_{m'n'}+\tilde{T}^{12D}_{mnn'}b_{m'n'}\right]\pi_{mn}(\theta)+\right.\\ &\left.+i\left[\sum_{n'=1}^{\infty}\tilde{T}^{21D}_{mnn'}a_{m'n'}+\tilde{T}^{22D}_{mnn'}b_{m'n'}\right]\tau_{mn}(\theta)\right\}e^{im\varphi}\Bigg\}\hat{\theta}-\\ &-\left\{\frac{e^{ik_o r}}{k_o r}\sum_{n=1}^{\infty}\sum_{m=-n}^{+n}(-i)^{n+1}(-1)^m\gamma_{mn}\sqrt{\frac{(n+m)!}{(n-m)!}}\times\right.\\ &\times\left\{\left[\sum_{n'=1}^{\infty}\tilde{T}^{11D}_{mnn'}a_{m'n'}+\tilde{T}^{12D}_{mnn'}b_{m'n'}\right]\tau_{mn}(\theta)+\right.\\ &\left.+\left[\sum_{n'=1}^{\infty}\tilde{T}^{21D}_{mnn'}a_{m'n'}+\tilde{T}^{22D}_{mnn'}b_{m'n'}\right]\pi_{mn}(\theta)\right\}e^{im\varphi}\Bigg\}\hat{\varphi}\end{aligned} \tag{G.10}$$

Substituting equation (B.14) and (B.16) into (G.10), one gets

$$\begin{aligned}\langle\vec{E}_s^D(\vec{r})\rangle \approx &\left(E_o\frac{e^{ik_o r}}{k_o r}\right)\times\\ &\times\sum_{n=1}^{\infty}\sum_{m=-n}^{+n}(-i)^{n+1}(-1)^m\gamma_{mn}\sqrt{\frac{(n+m)!}{(n-m)!}}\times\\ &\times 4\pi(-1)^m\left\{iA_{\theta mn}\hat{\theta}-A_{\varphi mn}\hat{\varphi}\right\}e^{im(\varphi-\varphi'')}\end{aligned} \tag{G.11}$$

where

$$A_{\theta mn} = \sum_{n'=1}^{\infty} i^{n'} d_{n'} \left\{ \tilde{T}^{11D}_{mnn'} \hat{e}_i \cdot \left[-i\pi_{mn'}(\theta'')\hat{\theta} - \tau_{mn'}(\theta'')\hat{\varphi} \right] + \right.$$
$$\left. + \tilde{T}^{12D}_{mnn'} \frac{1}{i} \hat{e}_i \cdot \left[\tau_{mn'}(\theta'')\hat{\theta} - i\pi_{mn'}(\theta'')\hat{\varphi} \right] \right\} \pi_{mn}(\theta) +$$
$$+ \sum_{n'=1}^{\infty} i^{n'} d_{n'} \left\{ \tilde{T}^{21D}_{mnn'} \hat{e}_i \cdot \left[-i\pi_{mn'}(\theta'')\hat{\theta} - \tau_{mn'}(\theta'')\hat{\varphi} \right] + \right.$$
$$\left. + \tilde{T}^{11D}_{mnn'} \frac{1}{i} \hat{e}_i \cdot \left[\tau_{mn'}(\theta'')\hat{\theta} - i\pi_{mn'}(\theta'')\hat{\varphi} \right] \right\} \tau_{mn}(\theta) \tag{G.12}$$

$$A_{\varphi mn} = \sum_{n'=1}^{\infty} i^{n'} d_{n'} \left\{ \tilde{T}^{11D}_{mnn'} \hat{e}_i \cdot \left[-i\pi_{mn'}(\theta'')\hat{\theta} - \tau_{mn'}(\theta'')\hat{\varphi} \right] + \right.$$
$$\left. + \tilde{T}^{12D}_{mnn'} \frac{1}{i} \hat{e}_i \cdot \left[\tau_{mn'}(\theta'')\hat{\theta} - i\pi_{mn'}(\theta'')\hat{\varphi} \right] \right\} \tau_{mn}(\theta) +$$
$$+ \sum_{n'=1}^{\infty} i^{n'} d_{n'} \left\{ \tilde{T}^{21D}_{mnn'} \hat{e}_i \cdot \left[-i\pi_{mn'}(\theta'')\hat{\theta} - \tau_{mn'}(\theta'')\hat{\varphi} \right] + \right.$$
$$\left. + \tilde{T}^{22D}_{mnn'} \frac{1}{i} \hat{e}_i \cdot \left[\tau_{mn'}(\theta'')\hat{\theta} - i\pi_{mn'}(\theta'')\hat{\varphi} \right] \right\} \pi_{mn}(\theta) \tag{G.13}$$

Therefore, the orientationally averaged scattered field can be written in the following compact form

$$\begin{bmatrix} \langle E^D_{S\theta}(\vec{r}) \rangle \\ \langle E^D_{S\varphi}(\vec{r}) \rangle \end{bmatrix}_{(r,\theta,\varphi)} = \frac{e^{ik_o r}}{k_o r} \times$$
$$\times \begin{bmatrix} k_o \langle S^D_{\theta\theta}(\theta,\varphi;\theta'',\varphi'') \rangle & k_o \langle S^D_{\theta\varphi}(\theta,\varphi;\theta'',\varphi'') \rangle \\ k_o \langle S^D_{\varphi\theta}(\theta,\varphi;\theta'',\varphi'') \rangle & k_o \langle S^D_{\varphi\varphi}(\theta,\varphi;\theta'',\varphi'') \rangle \end{bmatrix} \begin{bmatrix} E^i_\theta(\vec{r}) \\ E^i_\varphi(\vec{r}) \end{bmatrix} \tag{G.14}$$

where $\langle S^D_{uv}(\theta,\varphi;\theta'',\varphi'') \rangle$ are the elements of the orientationally averaged scattering amplitude matrix for a particle of equivalent diameter D. The angles (θ'',φ'') represent the scattered direction of the incident field. The subscripts *uv* *($\theta\theta,\theta\phi,\phi\theta,\phi\phi$)* indicate the polarization components for the linearly incident and scattered fields.

Based on expressions (G.11) to (G.13), one obtains

$$\langle S^D_{\theta\theta}(\theta,\varphi;\theta'',\varphi'')\rangle = \frac{4\pi}{k_o}\sum_{n=1}^{\infty}\sum_{m=-n}^{+n}(-i)^n\,\gamma_{mn}\sqrt{\frac{(n+m)!}{(n-m)!}}\times$$

$$\times\left\{\left[\sum_{n'=1}^{\infty} i^{n'-1}\,d_{n'}[\tilde{T}^{11D}_{mnn'}\pi_{mn'}(\theta'')+\tilde{T}^{12D}_{mnn'}\tau_{mn'}(\theta'')]\right]\pi_{mn}(\theta)\right. \tag{G.15}$$

$$+$$

$$\left.+\left[\sum_{n'=1}^{\infty} i^{n'-1}\,d_{n'}[\tilde{T}^{21D}_{mnn'}\pi_{mn'}(\theta'')+\tilde{T}^{22D}_{mnn'}\tau_{mn'}(\theta'')]\right]\times\right.$$

$$\left.\times\,\tau_{mn}(\theta)\right\}e^{im(\varphi-\varphi'')}$$

$$\langle S^D_{\theta\varphi}(\theta,\varphi;\theta'',\varphi'')\rangle = -\frac{4\pi}{k_o}\sum_{n=1}^{\infty}\sum_{m=-n}^{+n}(-i)^n\,\gamma_{mn}\sqrt{\frac{(n+m)!}{(n-m)!}}\times$$

$$\times\left\{\left[\sum_{n'=1}^{\infty} i^{n'}\,d_{n'}[\tilde{T}^{11D}_{mnn'}\tau_{mn'}(\theta'')+\tilde{T}^{12D}_{mnn'}\pi_{mn'}(\theta'')]\right]\pi_{mn}(\theta)+\right. \tag{G.16}$$

$$\left.+\left[\sum_{n'=1}^{\infty} i^{n'}\,d_{n'}[\tilde{T}^{21D}_{mnn'}\tau_{mn'}(\theta'')+\tilde{T}^{22D}_{mnn'}\pi_{mn'}(\theta'')]\right]\times\right.$$

$$\left.\times\,\tau_{mn}(\theta)\right\}e^{im(\varphi-\varphi'')}$$

$$\langle S^D_{\varphi\theta}(\theta,\varphi;\theta'',\varphi'')\rangle = \frac{4\pi}{k_o}\sum_{n=1}^{\infty}\sum_{m=-n}^{+n}(-i)^n\,\gamma_{mn}\sqrt{\frac{(n+m)!}{(n-m)!}}\times$$

$$\times\left\{\left[\sum_{n'=1}^{\infty} i^{n'}\,d_{n'}[\tilde{T}^{11D}_{mnn'}\pi_{mn'}(\theta'')+\tilde{T}^{12D}_{mnn'}\tau_{mn'}(\theta'')]\right]\tau_{mn}(\theta)+\right. \tag{G.17}$$

$$\left.+\left[\sum_{n'=1}^{\infty} i^{n'}\,d_{n'}[\tilde{T}^{21D}_{mnn'}\pi_{mn'}(\theta'')+\tilde{T}^{22D}_{mnn'}\tau_{mn'}(\theta'')]\right]\times\right.$$

$$\left.\times\,\pi_{mn}(\theta)\right\}e^{im(\varphi-\varphi'')}$$

$$\langle S^D_{\varphi\varphi}(\theta,\varphi;\theta'',\varphi'')\rangle = \frac{4\pi}{k_o}\sum_{n=1}^{\infty}\sum_{m=-n}^{+n}(-i)^{n+1}\,\gamma_{mn}\sqrt{\frac{(n+m)!}{(n-m)!}}\times \tag{G.18}$$

$$\times\left\{\left[\sum_{n'=1}^{\infty} i^{n'}\,d_{n'}[\tilde{T}^{11D}_{mnn'}\tau_{mn'}(\theta'')+\tilde{T}^{12D}_{mnn'}\pi_{mn'}(\theta'')]\right]\tau_{mn}(\theta)+\right.$$

$$+\left[\sum_{n'=1}^{\infty} i^{n'}\, d_{n'}[\tilde{T}^{21D}_{mnn'}\tau_{mn'}(\theta'') + \tilde{T}^{22D}_{mnn'}\pi_{mn'}(\theta'')]\right]\times$$

$$\times\, \pi_{mn}(\theta)\}e^{im(\varphi-\varphi'')}$$

where $\tilde{T}^{klD}_{mnn'}$ is defined by the expression (F.17),

$$d_{n'} = \sqrt{\frac{(2n'+1)}{4\pi n'(n'+1)}} \qquad \gamma_{mn} = \sqrt{\frac{(2n+1)(n-m)!}{4\pi n(n+1)(n+m)!}} \tag{G.19}$$

$$4\pi\gamma_{mn}\sqrt{\frac{(n+m)!}{(n-m)!}}\,d_{n'} = \sqrt{\frac{(2n+1)(2n'+1)!}{n(n+1)n'(n'+1)!}} \tag{G.20}$$

The summations in expressions (G.15) to (G.18) can be rearranged in the general form

$$\langle S^D_{uv}(\theta,\varphi;\theta'',\varphi'')\rangle = \frac{4\pi}{k_o}\sum_{n=1}^{\infty}\sum_{n'=1}^{\infty}\sum_{m=-N_{min}}^{+N_{min}}\{\ldots\}$$

where $N_{min} = \min(n, n')$. It has been seen in Appendix D and equation (F.19) that

$$\pi_{-mn}(\theta) = (-1)^{m+1}\pi_{mn}(\theta)$$

$$\tau_{-mn}(\theta) = (-1)^{m}\tau_{mn}(\theta) \tag{G.21}$$

$$\tilde{T}^{klD}_{-mnn'} = (-1)^{k+l}\tilde{T}^{klD}_{mnn'} \tag{G.22}$$

Substituting expressions (G.19) to (G.22) into the rearranged versions of expressions (G.15) to (G.18), it is seen that the inner summation terms of $\langle S^D_{uv}(\theta,\varphi;\theta'',\varphi'')\rangle$ that involve negative m values can be rewritten as follows

$$\langle \Sigma^D_{\theta\theta}(\theta,\varphi;\theta'',\varphi'')\rangle_- = \sum_{m=1}^{N_{min}}[\tilde{T}^{11D}_{mnn'}\pi_{mn'}(\theta'')\,\pi_{mn}(\theta) +$$

$$+\tilde{T}^{12D}_{mnn'}\tau_{mn'}(\theta'')\pi_{mn}(\theta) + \tilde{T}^{21D}_{mnn'}\pi_{mn'}(\theta'')\tau_{mn}(\theta) +$$

$$+\tilde{T}^{22D}_{mnn'}\tau_{mn'}(\theta'')\tau_{mn}(\theta)]e^{-im(\varphi-\varphi'')} \tag{G.23}$$

$$\langle \Sigma^D_{\theta\varphi}(\theta,\varphi;\theta'',\varphi'')\rangle_- = -\sum_{m=1}^{N_{min}} \Big[[\tilde{T}^{11D}_{mnn'}\tau_{mn'}(\theta'')\pi_{mn}(\theta) + \\ +\tilde{T}^{12D}_{mnn'}\pi_{mn'}(\theta'')\pi_{mn}(\theta) + \tilde{T}^{21D}_{mnn'}\tau_{mn'}(\theta'')\tau_{mn}(\theta) \\ +\tilde{T}^{22D}_{mnn'}\pi_{mn'}(\theta'')\tau_{mn}(\theta)]e^{-im(\varphi-\varphi'')} \tag{G.24}$$

$$\langle \Sigma^D_{\varphi\theta}(\theta,\varphi;\theta'',\varphi'')\rangle_- = -\sum_{m=1}^{N_{min}} [\tilde{T}^{11D}_{mnn'}\pi_{mn'}(\theta'')\tau_{mn}(\theta) + \\ +\tilde{T}^{12D}_{mnn'}\tau_{mn'}(\theta'')\tau_{mn}(\theta) + \tilde{T}^{21D}_{mnn'}\pi_{mn'}(\theta'')\pi_{mn}(\theta) + \\ +\tilde{T}^{22D}_{mnn'}\tau_{mn'}(\theta'')\pi_{mn}(\theta)]e^{-im(\varphi-\varphi'')} \tag{G.25}$$

$$\langle \Sigma^D_{\varphi\varphi}(\theta,\varphi;\theta'',\varphi'')\rangle_- = \sum_{m=1}^{N_{min}} [\tilde{T}^{11D}_{mnn'}\tau_{mn'}(\theta'')\,\tau_{mn}(\theta) + \\ +\tilde{T}^{12D}_{mnn'}\pi_{mn'}(\theta'')\tau_{mn}(\theta) + \tilde{T}^{21D}_{mnn'}\tau_{mn'}(\theta'')\pi_{mn}(\theta) + \\ +\tilde{T}^{22D}_{mnn'}\pi_{mn'}(\theta'')\pi_{mn}(\theta)]e^{-im(\varphi-\varphi'')} \tag{G.26}$$

Combining the inner summation terms of $\langle S^D_{uv}(\theta,\varphi;\theta'',\varphi'')\rangle$ that involve positive m values with the corresponding ones in expressions (G.23) to (G.26), one gets

$$\langle S^D_{\theta\theta}(\theta,\varphi;\theta'',\varphi'')\rangle = \frac{1}{k_o}\sum_{n=1}^{\infty}\sum_{n'=1}^{\infty}\alpha_{nn'}\{\tilde{T}^{22D}_{0nn'}\tau_{0n}(\theta)\tau_{0n'}(\theta'') + \\ +2\sum_{m=1}^{N_{min}}[\tilde{T}^{11D}_{mnn'}\pi_{mn'}(\theta'')\,\pi_{mn}(\theta) + \tilde{T}^{12D}_{mnn'}\tau_{mn'}(\theta'')\pi_{mn}(\theta) + \\ +\tilde{T}^{21D}_{mnn'}\pi_{mn'}(\theta'')\tau_{mn}(\theta)+\tilde{T}^{22D}_{mnn'}\tau_{mn'}(\theta'')\tau_{mn}(\theta)]\cos[m(\varphi \\ -\varphi'')]\} \tag{G.27}$$

$$\langle S^D_{\theta\varphi}(\theta,\varphi;\theta'',\varphi'')\rangle = \\ = \frac{1}{k_o}\sum_{n=1}^{\infty}\sum_{n'=1}^{\infty}\alpha_{nn'}\Big\{\frac{1}{i}\tilde{T}^{21D}_{0nn'}\tau_{0n}(\theta)\tau_{0n'}(\theta'') + \\ +2\sum_{m=1}^{N_{min}}\Big[[\tilde{T}^{11D}_{mnn'}\tau_{mn'}(\theta'')\pi_{mn}(\theta) + \tilde{T}^{12D}_{mnn'}\pi_{mn'}(\theta'')\pi_{mn}(\theta) + \\ +\tilde{T}^{21D}_{mnn'}\tau_{mn'}(\theta'')\tau_{mn}(\theta) \\ +\langle\hat{T}^{22D}_{mnn'}\rangle\pi_{mn'}(\theta'')\tau_{mn}(\theta)\Big]\sin[m(\varphi-\varphi'')]\Big\} \tag{G.28}$$

$$\langle S^D_{\varphi\theta}(\theta,\varphi;\theta'',\varphi'')\rangle$$

$$= \frac{1}{k_o}\sum_{n=1}^{\infty}\sum_{n'=1}^{\infty}\alpha_{nn'}\{i\tilde{T}^{21D}_{0nn'}\tau_{0n}(\theta)\tau_{0n'}(\theta'') - \tag{G.29}$$

$$-2\sum_{m=1}^{N_{min}}[\tilde{T}^{11D}_{mnn'}\pi_{mn'}(\theta'')\tau_{mn}(\theta) + \tilde{T}^{12D}_{mnn'}\tau_{mn'}(\theta'')\tau_{mn}(\theta) +$$

$$+\tilde{T}^{21D}_{mnn'}\pi_{mn'}(\theta'')\pi_{mn}(\theta)$$

$$+ \tilde{T}^{22D}_{mnn'}\tau_{mn'}(\theta'')\pi_{mn}(\theta)]\sin[m(\varphi-\varphi'')]\}$$

$$\langle S^D_{\varphi\varphi}(\theta,\varphi;\theta'',\varphi'')\rangle = \frac{1}{k_o}\sum_{n=1}^{\infty}\sum_{n'=1}^{\infty}\alpha_{nn'}\{\tilde{T}^{11D}_{0nn'}\tau_{0n}(\theta)\tau_{0n'}(\theta'') + \tag{G.30}$$

$$+2\sum_{m=1}^{N_{min}}[\tilde{T}^{11D}_{mnn'}\tau_{mn'}(\theta'')\,\tau_{mn}(\theta) + \tilde{T}^{12D}_{mnn'}\pi_{mn'}(\theta'')\tau_{mn}(\theta) +$$

$$+\tilde{T}^{21D}_{mnn'}\tau_{mn'}(\theta'')\pi_{mn}(\theta)$$

$$+ \tilde{T}^{22D}_{mnn'}\pi_{mn'}(\theta'')\pi_{mn}(\theta)]\cos[m(\varphi-\varphi'')]\}$$

where

$$\alpha_{nn'} = i^{n'-n-1}\sqrt{\frac{(2n+1)(2n'+1)}{n(n+1)n'(n'+1)}} \tag{G.31}$$

The above theoretical development remains applicable to a particle of equivalent diameter D and average orientation of the symmetry axis. Thus, expression (G.14) that relates incident and scattered intensities agrees with the upper sub-matrix 2x2 of representation (2.85) in reference [78].

Finally, according to Ishimaru [78], the elements of the differential scattering cross section matrix are

$$\sigma_{duv}(\theta,\varphi;\theta'',\varphi'') = \int_0^{\infty}|S^D_{uv}(\theta,\varphi;\theta'',\varphi'')|^2 n(D)dD \tag{G.32}$$

$$uv = \theta\theta, \theta\varphi, \varphi\theta, \varphi\varphi$$

Note that $\sigma_{duv}(\theta,\varphi;\theta'',\varphi'')$ has units of (m^2/m^3).

H.
Derivation of the Specific Attenuation using the Realistic Rain Model.

Here, a spherical electromagnetic wave propagating perpendicularly to a plane interface with $e^{-i\omega t}$ time variation will be assumed. The plane interface separates the free space from a rain cell (represented by a layer with finite and constant conductivity). The electric field of a spherical electromagnetic wave in the far field region at a distance *r* from the source is written as

$$\vec{E}(\vec{r}) = \vec{E}_o \frac{e^{ikr}}{r} \tag{H.1}$$

where k is propagation constant

$$k = \sqrt{\omega^2 \mu\varepsilon + i\omega\mu\sigma} \tag{H.2}$$

ε is the permittivity, μ is the permeability and σ is the conductivity of the medium. In free space, $\varepsilon = \varepsilon_o$, $\mu = \mu_o$ and $\sigma = 0$. Thus $k_o = \omega\sqrt{\mu_o \varepsilon_o} = 2\pi/\lambda$ is real and the electric field decreases with the distance *r*.

As a result of the incidence on the interface, the transmitted wave propagates in the rain layer, with conductivity $\sigma \neq 0$. For this medium, the propagation constant $k = k_R + ik_I$ becomes complex. Equation (H.1) can be written as

$$\vec{E}(\vec{r}) = \vec{E}_o \frac{e^{ik_o(Re(m)+iIm(m))r}}{r} = \vec{E}_o e^{-k_o Im(m) r} \frac{e^{ik_o Re(m) r}}{r} \tag{H.3}$$

The above expression indicates the attenuation is no longer caused only by free space. Rain causes an additional attenuation of the electromagnetic wave. As previously seen in equation (H.3)

$$e^{ikr} = e^{ik_o\left(Re(m)+iIm(m)\right)r} = e^{-k_oIm(m)r}e^{ik_oRe(m)r} \tag{H.4}$$

$$e^{ikr} = e^{-\gamma r}\, e^{ik_oRe(m)r}$$

The specific attenuation due to a cluster of particles with a DSD and a distribution of random orientation of the symmetry axis can be defined as

$$\gamma = k_oIm(m) = \frac{2\pi}{k_o^2} Im\left\{\int_0^\infty \langle k_o S_{uv}^D(\theta",\varphi";\theta",\varphi")\rangle N(D)dD\right\} \tag{H.5}$$

$$\gamma_{rain} = 2\gamma = \frac{4\pi}{k_o^2} Im\left\{\int_0^\infty \langle k_o S_{uv}^D(\theta",\varphi";\theta",\varphi")\rangle N(D)dD\right\} \tag{H.6}$$

$$uv = \theta\theta, \varphi\varphi$$

where $\langle S_{uv}^D(\theta",\varphi";\theta",\varphi")\rangle$ are the elements of the orientationally averaged scattering amplitude defined in Appendix G. Note that expressions (H.5) and (H.6) considers attenuations in the field and corresponding power, respectively.

According to the method based on EBCM and considering the expressions given in Appendix G, expression (H.6) for the elements *uv = θθ, φφ* of the scattering matrix can be written as

$$\gamma_{\theta\theta\, rain}(Np/m) = \frac{4\pi}{k_o^2} Im\left\{\int_0^\infty \sum_{n=1}^{\infty}\sum_{n'=1}^{\infty} \alpha_{nn'}\{\tilde{T}_{0nn'}^{22D}\tau_{0n}(\theta'')\tau_{0n'}(\theta'') + \right. \tag{H.7}$$

$$+2\sum_{m=1}^{N_{min}}[\tilde{T}_{mnn'}^{11D}\pi_{mn'}(\theta'')\,\pi_{mn}(\theta") + \tilde{T}_{mnn'}^{12D}\tau_{mn'}(\theta'')\pi_{mn}(\theta'') +$$

$$\left.+\tilde{T}_{mnn'}^{21D}\pi_{mn'}(\theta'')\tau_{mn}(\theta'')+\tilde{T}_{mnn'}^{22D}\tau_{mn'}(\theta'')\tau_{mn}(\theta'')]\right\}N(D)dD\}$$

$$\gamma_{\varphi\varphi\, rain}(Np/m) = \frac{4\pi}{k_o^2} Im\left\{\int_0^\infty \sum_{n=1}^{\infty}\sum_{n'=1}^{\infty} \alpha_{nn'}\{\tilde{T}_{0nn'}^{11D}\tau_{0n}(\theta'')\tau_{0n'}(\theta'') + \right. \tag{H.8}$$

$$+2\sum_{m=1}^{N_{min}}[\tilde{T}^{11D}_{mnn'}\tau_{mn'}(\theta'')\,\tau_{mn}(\theta'')+\tilde{T}^{12D}_{mnn'}\pi_{mn'}(\theta'')\tau_{mn}(\theta'')+$$
$$+\tilde{T}^{21D}_{mnn'}\tau_{mn'}(\theta'')\pi_{mn}(\theta'')+\tilde{T}^{22D}_{mnn'}\pi_{mn'}(\theta'')\pi_{mn}(\theta'')]\}N(D)dD\}$$

where the elements $\tilde{T}^{klD}_{mnn'}$ are defined by expression (F.17). Note that the averaging process due to the DSD is only applied to these elements. Defining

$$\langle\tilde{T}^{kl}_{mnn'}\rangle=\int_0^\infty\tilde{T}^{klD}_{mnn'}N(D)dD$$

expressions (H.7) and (H.8) can be rewritten in the final formats

$$\gamma_{\theta\theta\,rain}(Np/m)=\frac{4\pi}{k_o^2}Im\left\{\sum_{n=1}^{\infty}\sum_{n'=1}^{\infty}\alpha_{nn'}\{\langle\tilde{T}^{22}_{0nn'}\rangle\tau_{0n}(\theta'')\tau_{0n'}(\theta'')+\right. \tag{H.9}$$
$$+2\sum_{m=1}^{N_{min}}[\langle\tilde{T}^{11}_{mnn'}\rangle\pi_{mn'}(\theta'')\,\pi_{mn}(\theta")+\langle\tilde{T}^{12}_{mnn'}\rangle\tau_{mn'}(\theta'')\pi_{mn}(\theta'')+$$
$$\left.+\langle\tilde{T}^{21}_{mnn'}\rangle\pi_{mn'}(\theta'')\tau_{mn}(\theta'')+\langle\tilde{T}^{22}_{mnn'}\rangle\tau_{mn'}(\theta'')\tau_{mn}(\theta'')]\}\right\}$$

$$\gamma_{\varphi\varphi\,rain}(Np/m)=\frac{4\pi}{k_o^2}Im\left\{\sum_{n=1}^{\infty}\sum_{n'=1}^{\infty}\alpha_{nn'}\{\langle\tilde{T}^{11}_{0nn'}\rangle\tau_{0n}(\theta'')\tau_{0n'}(\theta'')+\right. \tag{H.10}$$
$$+2\sum_{m=1}^{N_{min}}[\langle\tilde{T}^{11}_{mnn'}\rangle\tau_{mn'}(\theta'')\,\tau_{mn}(\theta'')+\langle\tilde{T}^{12}_{mnn'}\rangle\pi_{mn'}(\theta'')\tau_{mn}(\theta'')+$$
$$\left.+\langle\tilde{T}^{21}_{mnn'}\rangle\tau_{mn'}(\theta'')\pi_{mn}(\theta'')+\langle\tilde{T}^{22}_{mnn'}\rangle\pi_{mn'}(\theta'')\pi_{mn}(\theta'')]\}\right\}$$

I.
Summary of T-Matrix formulation.

For the sake of completeness, the expressions for the elements $\langle S_{uv}^{D}(\theta,\varphi;\theta'',\varphi'')\rangle$ with $uv = \theta\theta,\ \theta\varphi,\ \varphi\theta,\ \varphi\varphi$ of the scattering matrix will be fully specified below:

$$\langle S_{\theta\theta}^{D}(\theta,\varphi;\theta'',\varphi'')\rangle = \frac{1}{k_o}\sum_{n=1}^{\infty}\sum_{n'=1}^{\infty}\alpha_{nn'}\{\tilde{T}_{0nn'}^{22D}\tau_{0n}(\theta)\tau_{0n'}(\theta'') +$$
$$+2\sum_{m=1}^{N_{min}}[\tilde{T}_{mnn'}^{11D}\pi_{mn}(\theta)\pi_{mn'}(\theta'') + \tilde{T}_{mnn'}^{12D}\pi_{mn}(\theta)\tau_{mn'}(\theta'') + \quad \text{(I.1)}$$
$$+\tilde{T}_{mnn'}^{21D}\tau_{mn}(\theta)\pi_{mn'}(\theta'') + \tilde{T}_{mnn'}^{22D}\tau_{mn}(\theta)\tau_{mn'}(\theta'')]\cos[m(\varphi-\varphi'')]\}$$

$$\langle S_{\theta\varphi}^{D}(\theta,\varphi;\theta'',\varphi'')\rangle = \frac{1}{k_o}\sum_{n=1}^{\infty}\sum_{n'=1}^{\infty}\alpha_{nn'}\left\{\frac{1}{i}\tilde{T}_{0nn'}^{21D}\tau_{0n}(\theta)\tau_{0n'}(\theta'') +\right.$$
$$+2\sum_{m=1}^{N_{min}}\left[[\tilde{T}_{mnn'}^{11D}\pi_{mn}(\theta)\tau_{mn'}(\theta'') + \tilde{T}_{mnn'}^{12D}\pi_{mn}(\theta)\pi_{mn'}(\theta'') + \quad \text{(I.2)}\right.$$
$$\left.+\tilde{T}_{mnn'}^{21D}\tau_{mn}(\theta)\tau_{mn'}(\theta'') + \tilde{T}_{mnn'}^{22D}\tau_{mn}(\theta)\pi_{mn'}(\theta'')]\sin[m(\varphi-\varphi'')]\right\}$$

$$\langle S_{\varphi\theta}^{D}(\theta,\varphi;\theta'',\varphi'')\rangle = \frac{1}{k_o}\sum_{n=1}^{\infty}\sum_{n'=1}^{\infty}\alpha_{nn'}\{i\tilde{T}_{0nn'}^{12D}\tau_{0n}(\theta)\tau_{0n'}(\theta'') -$$
$$-2\sum_{m=1}^{N_{min}}[\tilde{T}_{mnn'}^{11D}\tau_{mn}(\theta)\pi_{mn'}(\theta'') + \tilde{T}_{mnn'}^{12D}\tau_{mn}(\theta)\tau_{mn'}(\theta'') + \quad \text{(I.3)}$$
$$+\tilde{T}_{mnn'}^{21D}\pi_{mn}(\theta)\pi_{mn'}(\theta'') + \tilde{T}_{mnn'}^{22D}\pi_{mn}(\theta)\tau_{mn'}(\theta'')]\sin[m(\varphi-\varphi'')]\}$$

$$\langle S_{\varphi\varphi}^{D}(\theta,\varphi;\theta'',\varphi'')\rangle = \frac{1}{k_o}\sum_{n=1}^{\infty}\sum_{n'=1}^{\infty}\alpha_{nn'}\{\tilde{T}_{0nn'}^{11D}\tau_{0n}(\theta)\tau_{0n'}(\theta'') +$$
$$+2\sum_{m=1}^{N_{min}}[\tilde{T}_{mnn'}^{11D}\tau_{mn}(\theta)\tau_{mn'}(\theta'') + \tilde{T}_{mnn'}^{12D}\tau_{mn}(\theta)\pi_{mn'}(\theta'') + \quad \text{(I.4)}$$
$$+\tilde{T}_{mnn'}^{21D}\pi_{mn}(\theta)\tau_{mn'}(\theta'') + \tilde{T}_{mnn'}^{22D}\pi_{mn}(\theta)\pi_{mn'}(\theta'')]\cos[m(\varphi-\varphi'')]\}$$

Note that only the main diagonal elements are used in Chapter 6 and 7. In the above expressions, $N_{min} = min(n, n')$ and

$$\pi_{mn}(\theta) = m\frac{d^n_{om}(\theta)}{\sin\theta} \tag{I.5}$$

$$\tau_{mn}(\theta) = \frac{d}{d\theta}[d^n_{om}(\theta)] \tag{I.6}$$

$$d^n_{0m}(\theta) = \sqrt{\frac{(n-m)!}{(n+m)!}}P^m_n(cos\theta) \tag{I.7}$$

$$\alpha_{nn'} = i^{n'-n-1}\sqrt{\frac{(2n+1)}{n(n+1)}\frac{(2n'+1)}{n'(n'+1)}} = i^{n'-n-1}\alpha'_{nn'} \tag{I.8}$$

where $d^n_{0m}(\theta)$ is the Wigner d-function and $P^m_n(cos\theta)$ is the associated Legendre function of the first kind. The terms $\tilde{T}^{klD}_{mnn'}$ (*k,l = 1,2*) result from averaging the T-matrix elements over the distribution of orientations of the symmetry axis of a particle with equivalent diameter *D* in the principal reference frame (vertical *z*-axis and wave vector of the incident field in *xz*-plane). That is,

$$\langle T^{klD}_{mnm'n'}\rangle = \int_\Omega T^{klD}_{mnm'n'}p^D_{\mathrm{AB\Gamma}}(\alpha,\beta,\gamma)d\Omega = \delta_{mm'}\tilde{T}^{klD}_{mnn'} \tag{I.9}$$

where $\delta_{mn'} = 1$ for equal indices and zero otherwise. It should be observed that expression (I.9) could accommodate orientation distributions that vary with the equivalent diameter *D*. However, as explained in Chapter 6, expression (3.16) is adequate for the present development. The combination of the two expressions leads to

$$\begin{aligned}\tilde{T}^{klD}_{mnn'} = {} & \frac{(-1)^m}{2\pi}\sum_{n_1=|n-n'|}^{n+n'}\left[1+(-1)^{n+n'+n_1+k+l}\right]C^{n_1 0}_{nmn'(-m)}\times \\ & \times \underline{P}_{n_1}\left[\sum_{m_1=0}^{+N_{min}}(-1)^{m_1}\left(1-\frac{1}{2}\delta_{m_1 0}\right)C^{n_1 0}_{nm_1n'(-m_1)}\hat{T}^{klD}_{m_1nm_1n'}\right]\end{aligned} \tag{I.10}$$

In the immediately above expression, $C^{n_1 0}_{nm_1n'(-m_1)}$ are the Clebsch-Gordan coefficients [45] and

$$\begin{aligned}\underline{P}_{n_1} &= \int_\Omega d^{n_1}_{00}(\beta)p^D_{\mathrm{B\Gamma}}(\beta,\gamma)\mathrm{d}\Omega = \\ &= \frac{1}{\sqrt{2\pi}\Delta\beta\mathcal{F}}\left\{\int_0^\pi\left[e^{-\frac{1}{2}\left(\frac{\beta-\beta_o}{\Delta\beta}\right)^2}+e^{-\frac{1}{2}\left(\frac{\beta+\beta_o}{\Delta\beta}\right)^2}\right]P_{n_1}(\cos\beta)\,sin\beta d\beta\right\}\end{aligned} \tag{I.11}$$

where $P_{n_1}(\cos\beta)$ is the Legendre polynomial of degree n_1. The elements $\hat{T}^{klD}_{mnm'n'}$ of the T-matrix of a single particle of equivalent diameter *D* in the body reference frame (*z*-axis aligned with the particle symmetry axis) result from

$$\begin{pmatrix} \underline{\hat{T}}^{11D} & \underline{\hat{T}}^{12D} \\ \underline{\hat{T}}^{21D} & \underline{\hat{T}}^{22D} \end{pmatrix} = -\begin{pmatrix} Rg\underline{Q}^{11D} & Rg\underline{Q}^{12D} \\ Rg\underline{Q}^{21D} & Rg\underline{Q}^{22D} \end{pmatrix}\begin{pmatrix} \underline{Q}^{11D} & \underline{Q}^{12D} \\ \underline{Q}^{21D} & \underline{Q}^{22D} \end{pmatrix}^{-1} \tag{I.12}$$

where the elements $Q^{klD}_{mnm'n'}$ of the square-block submatrices $\underline{Q}^{klD}$ are

$$Q^{11D}_{mnm'n'} = (-1)^m(-ik_o)\left(k_1 J^{21D}_{mnm'n'} + k_o J^{12D}_{mnm'n'}\right) \tag{I.13}$$

$$Q^{12D}_{mnm'n'} = (-1)^m(-ik_o)\left(k_1 J^{11D}_{mnm'n'} + k_o J^{22D}_{mnm'n'}\right) \tag{I.14}$$

$$Q^{21D}_{mnm'n'} = (-1)^m(-ik_o)\left(k_1 J^{22D}_{mnm'n'} + k_o J^{11D}_{mnm'n'}\right) \tag{I.15}$$

$$Q^{22D}_{mnm'n'} = (-1)^m(-ik_o)\left(k_1 J^{12D}_{mnm'n'} + k_o J^{21D}_{mnm'n'}\right) \tag{I.16}$$

In expressions (I.13) to (I.16), $k_o = 2\pi/\lambda$ is the free-space wavenumber, λ is the wavelength, $k_1 = \mathrm{m}k_o$, and m is the complex index of refraction of water. The terms $J^{klD}_{mnm'n'}$ are numerically determined by the application of Gaussian quadrature formulas to

$$J^{11}_{mnm'n'} = -\frac{i\delta_{mm'}}{2}\alpha'_{nn'}\int_{-1}^{+1} j_{n'}(u_1)h^{(1)}_n(u_o)\left[\pi_{mn}(\theta)\tau_{mn'}(\theta) + \tau_{mn}(\theta)\pi_{mn'}(\theta)\right]r^2 dx \tag{I.17}$$

$$J^{12}_{mnm'n'} = \frac{\delta_{mm'}}{2}\alpha'_{nn'}\int_{-1}^{+1} j_{n'}(u_1)\left\{\left.\frac{\left[uh^{(1)}_n(u)\right]'}{u}\right|_{u_o}\left[\pi_{mn}(\theta)\pi_{m'}(\theta) + \tau_{mn}(\theta)\tau_{m'}(\theta)\right] + \right. \tag{I.18}$$

$$\left. + n(n+1)\frac{1}{r}\frac{dr}{d\theta}\frac{h^{(1)}_n(u_o)}{u_o}d^n_{om}(\theta)\tau_{mn'}(\theta)\right\}r^2 dx$$

$$J^{21}_{mnm'n'} = -\frac{\delta_{mm'}}{2}\alpha'_{nn'}\int_{-1}^{+1} h_n^{(1)}(u_o)\left\{\left.\frac{[uj_{n'}(u)]'}{u}\right|_{u_1}[\pi_{mn}(\theta)\pi_{m'}(\theta)+\tau_{mn}(\theta)\tau_{m'}(\theta)]+\right.$$
$$\left.+n'(n'+1)\frac{1}{r}\frac{dr}{d\theta}\left.\frac{j_{n'}(u_1)}{u_1}\right|\tau_{mn}(\theta)d^{n'}_{om}(\theta)\right\}r^2dx \qquad \text{(I.19)}$$

$$J^{22}_{mnm'n'} = -\frac{i\delta_{mm'}}{2}\alpha'_{nn'}\int_{-1}^{+1}\left\{\left.\frac{[uj_{n'}(u)]'}{u}\right|_{u_1}\left.\frac{\left[uh_n^{(1)}(u)\right]'}{u}\right|_{u_o}[\pi_{mn}(\theta)\tau_{mn'}(\theta)\right.$$
$$+\tau_{mn}(\theta)\pi_{mn'}(\theta)]+$$
$$+\frac{1}{r}\frac{dr}{d\theta}\left[n'(n'+1)\left.\frac{j_{n'}(u_1)}{u_1}\right|\left.\frac{\left[uh_n^{(1)}(u)\right]'}{u}\right|_{u_o}+n(n+1)\left.\frac{[uj_{n'}(u)]'}{u}\right|_{u_1}\frac{h_n^{(1)}(u_o)}{u_o}\right]\times \qquad \text{(I.20)}$$
$$\left.\times\pi_{mn}(\theta)d^{n'}_{om}(\theta)\right\}r^2dx$$

In these four expressions, $j_n(u)$ and $h_n^{(1)}(u)$ represent the spherical Bessel and first kind Hankel functions. Primes above square brackets indicate derivatives of the internal terms with respect to *u*. The ratios between the derivatives and *u* are evaluated at $u_{o,1} = k_{o,1}r$ as indicated. Additionally, $x = cos\theta$, where θ is the central angle with the symmetry axis of the particle, observed in the outer scale of Figure 1, and r depends on θ, according to the raindrop shape described in Section 4 for the equivalent diameter *D*.

Similarly, the elements $RgQ^{klD}_{mnm'n'}$ of the square-block submatrices $Rg\underline{Q}^{klD}$ in expression (I.12) are

$$RgQ^{11D}_{mnm'n'} = (-1)^m(-ik_o)\left(k_1RgJ^{21D}_{mnm'n'} + k_oRgJ^{12D}_{mnm'n'}\right) \qquad \text{(I.21)}$$

$$RgQ^{12D}_{mnm'n'} = (-1)^m(-ik_o)\left(k_1RgJ^{11D}_{mnm'n'} + k_oRgJ^{22D}_{mnm'n'}\right) \qquad \text{(I.22)}$$

$$RgQ^{21D}_{mnm'n'} = (-1)^m(-ik_o)\left(k_1RgJ^{22D}_{mnm'n'} + k_oRgJ^{11D}_{mnm'n'}\right) \qquad \text{(I.23)}$$

$$RgQ^{22D}_{mnm'n'} = (-1)^m(-ik_o)\left(k_1RgJ^{12D}_{mnm'n'} + k_oRgJ^{21D}_{mnm'n'}\right) \qquad \text{(I.24)}$$

where the terms $RgJ^{klD}_{mnm'n'}$ are obtained from $J^{klD}_{mnm'n'}$ by the substitution of $j_n(u)$ for $h_n^{(1)}(u)$ in expressions (A17) to (A20).

In summary, the T-Matrix formulation described in general terms in [44], [45] was specialized in Chapter 6 to the realistic rain medium specified in Chapter 4 and applied to weather radar measurements of the rainfall rate to correct the results for the effects of rain attenuation along the paths between the radar and each sampled volume.